Karlsruhe Institute of Technology

KATRIN "First Light"

—

Commissioning and Modelling of the Beamline

Zur Erlangung des akademischen Grades eines

Doktors der Naturwissenschaften

von der Fakultät für Physik
des Karlsruher Instituts für Technologie

genehmigte

Dissertation

von

M.Sc. Moritz Thomas Hackenjos

aus Villingen-Schwenningen

Erstgutachter:	Prof. Dr. G. Drexlin Institut für Experimentelle Teilchenphysik, KIT
Zweitgutachter:	Prof. Dr. B. Holzapfel Institut für Technische Physik, KIT

Tag der mündlichen Prüfung: 15.12.2017

Declaration of authorship

With this declaration I declare that I have written this dissertation on my own and have not used any other sources and tools than those indicated. All passages of the work which have been taken over literally or analogously from other sources are marked as such. This thesis has not yet been submitted to any audit authority in the same or similar form.

Erklärung zur Selbständigkeit

Mit dieser Erklärung versichere ich, dass ich die vorliegende Dissertation selbstständig verfasst und keine anderen als die angegebenen Quellen und Hilfsmittel benutzt habe. Alle Stellen der Arbeit, die wörtlich oder sinngemäß aus anderen Quellen übernommen wurden, sind als solche kenntlich gemacht. Diese Arbeit wurde in gleicher oder ähnlicher Form noch keiner Prüfungsbehörde vorgelegt.

Moritz Thomas Hackenjos

Karlsruhe, den 17. Januar 2018

Contents

CHAPTER 0

Zusammenfassung

Die vorliegende Arbeit beschreibt Untersuchungen mit dem Karlsruhe Tritium Neutrino (KATRIN) Experiment, welche während der "First Light" Messkampagne durchgeführt wurden. Diese ermöglichte es erstmals, Elektronen am flussaufwärts gerichteten Ende des Experiments zu erzeugen und diese mit Hilfe eines magnetischen Führungsfeldes adiabatisch durch die gesamte 70 m lange Anlage zum Detektor zu leiten, um transmittierte Elektronen mit einem Silizium-Detektor zu zählen. Ziel war es, die erforderliche kollisionsfreie Führung von Elektronen in einem magnetischen Flussschlauch von $210\,\mathrm{Tcm}^2$ durch das gesamte KATRIN Strahlsystem zu demonstrieren. Die gewonnenen Ergebnisse sind für die Bestimmung der absoluten Neutrinomasse mit einer bisher unerreichten Sensitivität von $m_\nu = 200\,\mathrm{meV}$ (90 % C.L.) von entscheidender Bedeutung.

Das Standardmodell der Teilchenphysik beschreibt die drei bekannten Neutrinos als masselose, elektrisch neutrale und rein schwach wechselwirkende Teilchen. Die Entdeckung von Neutrinooszillationen lieferte jedoch den eindeutigen Beweis, dass Neutrinos eine nicht verschwindende Masse besitzen. Neutrinos sind damit das am häufigsten vorkommende massive Teilchen im Universum, da jeder Kubikzentimeter 339 Neutrinos enthält. Mit ihrer nicht verschwindenden Masse hatten sie somit direkten Einfluss auf die Bildung großräumiger Strukturen im frühen Universum. Eine direkte und modellunabhängige Bestimmung der Neutrinomasse würde es erlauben, einen der wichtigen Fit-Parameter in kosmologischen Modellen festzulegen. Zusätzlich könnte die Beobachtung der absoluten Neutrinomasse einen Hinweis geben, wie Massen jenseits des Higgs-Mechanismus erzeugt werden. Daher ist es für die Kosmologie und Teilchenphysik von essentieller Bedeutung, die absolute Neutrinomasse zu bestimmen. Die hochpräzise Spektroskopie der Energie von Elektronen aus dem Tritium β-Zerfall ist eine bewährte Methode, um im Bereich des kinematischen Endpunkts die Masse des Neutrinos direkt und modellunabhängig zu bestimmen. Die Neutrinomasse manifestiert sich dabei in einer geringfügigen Änderung der spektralen Form nahe des Endpunkts. Das KATRIN Experiment ist das führende Tritium Neutrino-Massen-Experiment der nächsten Generation, da es die Sensitivität der bisherigen Experimente in Mainz und Troitsk um eine Größenordnung übertreffen wird. Dieses ehrgeizige Ziel erfordert insbesondere eine Erhöhung der statistischen Präzision bei gleichzeitiger Verringerung aller systematischen Unsicherheiten. Dies wird durch die Kombination der hierfür besonders geeigneten Technik einer fensterlosen gasförmigen Tritiumquelle mit Auslese durch ein retardierendes Spektrometer erreicht. Dies entspricht der bekannten MAC-E Filtertechnologie.

Die Quelle des KATRIN Experiments ist so konzipiert, dass sie eine Aktivität von 10^{11} β-Elektronen pro Sekunde liefert. Da nur ein winziger Bruchteil von 2×10^{-13} aller β-Zerfälle im letzten 1 eV-Intervall unterhalb des Endpunkts E_0 des Energiespektrums auf-

treten, wird eine Signalzählrate von einigen mcps[1] erwartet. Daher sind drei Nettojahre an Datenaufnahme, die fünf Kalenderjahren experimenteller Laufzeit entsprechen, notwendig, um die erforderliche Statistik für die angestrebte Sensitivität zu erreichen. Schwankungen der Aktivität der fensterlosen gasförmigen Tritiumquelle (WGTS) führen zu systematischen Unsicherheiten, daher muss diese auf einem bisher unerreichten Niveau von 0.1 % stabilisiert werden. Die Quellstabilität wird von folgenden Parametern direkt beeinflusst: der Reinheit des Tritiumgases, dem Einlassdruck des Tritiumgases in das Quellrohr, der Pumpleistung der Turbomolekularpumpen (TMPs) und der Temperatur der Quelle. Dementsprechend muss die Temperatur des Quellrohrs auf dem gleichen Niveau wie die Quellaktivität stabilisiert werden. Um den Effekt der thermischen Dopplerverbreiterung der β-Elektronenenergien durch molekulare Bewegung zu minimieren, wird die gasförmige Quelle durch das umgebende Quellrohr auf 30 K gekühlt. Ein wesentliches Ziel dieser Arbeit war es festzustellen, ob der geforderte Temperaturbereich sowie die spezifizierte Temperaturstabilität erreicht werden kann.

Im Herbst 2015 wurde der Zusammenbau des WGTS Kryostaten durch einen industriellen Partner abgeschlossen und an den Campus Nord des KIT geliefert, wo er das KATRIN Strahlrohrsystem der Quell- und Transportsektion (STS) mit den bereits vorhandenen Komponenten der differentiellen Pumpstrecke (DPS) und kryogenen Pumpstrecke (CPS) vervollständigte. Die Inbetriebnahme der WGTS umfasste den Betrieb des Zwei-Phasen-Kühlsystems des Quellrohrs und des Temperaturmesssystems. Die Temperaturmessungen des Quellrohrs konnten zeigen, dass der Temperaturbereich von 30 K zuverlässig und ohne technische Probleme erreicht wurde. Eine durchschnittliche Temperaturstabilität von $(3{,}28 \pm 1{,}68)$ mK/h wurde über einen Zeitraum von 16 Tagen ermittelt. Dieses Ergebnis übertrifft die spezifizierte Temperaturstabilität von 30 mK/h um eine Größenordnung. Dies ist ein wichtiges Ergebnis im Hinblick auf das Budget der systematischen Unsicherheiten, um die angestrebte Sensitivität auf die Neutrinomasse zu erreichen. Die Temperatur am hinteren äußeren Ende des Quellrohrs ist dabei jedoch 500 mK höher im Vergleich zur Mitte und dem vorderen Ende. Die Spezifikation der Temperaturhomogenität von 30 mK kann somit nicht erreicht werden. Im Hinblick auf die ausgezeichneten Ergebnisse der Temperaturstabilität kann aber die Temperaturinhomogenität in das Quellmodell integriert werden. Dieses modifizierte Quellmodell ermöglicht es den Einfluss der Temperaturinhomogenität zu berücksichtigen, ohne die Sensitivität auf die Neutrinomasse zu beeinträchtigten.

Um die erforderliche Statistik zu erreichen und Systematiken zu minimieren, muss das Magnetfeld, welches einen Flussschlauch innerhalb des Strahlrohrs erzeugt, die β-Elektronen kollisionsfrei von ihrem Ursprungspunkt durch die 70 m lange Anordnung leiten, um sie schließlich am Detektor zu zählen. Hierbei sind zwei magnetische Flussschläuche von Relevanz. Der erste hat einen kreisförmigen Querschnitt von 191 Tcm^2 um die Längsachse des Strahlrohrs und führt die relevanten β-Elektronen für die Neutrinomassen-Analyse von der Quelle zum Detektor. Der zweite hat eine Größe von 210 Tcm^2 und bildet eine ringförmige Struktur um den ersten magnetischen Flussschlauch. Die Hauptaufgabe dieses erweiterten Flussschlauchs ist es, einen Pufferbereich zu definieren, der frei von Kollisionen mit der Wand des Strahlrohrs ist, und somit für den engeren 191 Tcm^2 Flussschlauchbereich sicher stellt, dass damit einhergehende Änderungen der kinetischen Energie der relevanten β-Elektronen bei hohen Energien verhindert wird. Im Strahlrohrabschnitt der CPS befindet sich außerdem der *forward beam monitor* (FBM), welcher die Quellaktivität am äußersten Rand des 210 Tcm^2 Flussschlauchs überwacht. Das Hauptziel dieser Arbeit war es, die Ausrichtung des magnetischen Flussschlauchs innerhalb des gesamten Strahlrohrs zu untersuchen. Dies beinhaltet damit die detaillierte Bestimmung, ob die β-Elektronen kollisionsfrei geführt werden können und ob die Quellaktivität mittels des FBM überwacht werden kann.

[1] milli counts per second (Ereignisse pro 1000 s)

Die Kombination der STS Komponenten zu einer durchgehenden Strahlführung wurde Anfang 2016 abgeschlossen. Dies beinhaltete eine simultane Inbetriebnahme aller Strahlrohrkomponenten. Das Hauptspektrometer und das Detektorsystem (FPD), die einen Teil des Spektrometer- und Detektorsektion (SDS) bilden, wurden bereits zwischen 2012 und 2016 im Rahmen von zwei Messkampagnen, SDS-I und SDS-II, in Betrieb genommen. Den letzten fehlenden Bestandteil von SDS bildete das Vorspektrometer, welches im Sommer 2016 den SDS Bereich komplettierte und damit das KATRIN Strahlrohrsystem vervollständigte. Durch die erfolgreiche Inbetriebnahme der einzelnen Komponenten konnten die supraleitenden Magnete erstmals gemeinsam betrieben werden und erzeugten dadurch den ersten durchgängigen magnetischen Flussschlauch innerhalb des 70 m langen Strahlrohrs. Im Herbst 2016 wurden zwei künstliche Elektronenquellen, welche einen schmalen und einen breiten Elektronenstrahl generieren, am flussaufwärts gerichtetem Ende des KATRIN Strahlrohrs installiert, um die Ausrichtung des magnetischen Flussschlauchs relativ zum Strahlrohr zu messen.

Durch einhergehende mechanische Positionsmessungen der einzelnen KATRIN Komponenten während der Konstruktion und Inbetriebnahme war es möglich, ein realistisches Modell des gesamten KATRIN Strahlrohrsystems mit dem Kassiopeia Softwarepaket zu erstellen. Dieses Modell wurde um die "As-Built" Geometrien der Magnete erweitert. Dies ermöglicht eine realitätsnahe Simulation des Verlaufs der Magnetfeldlinien im Strahlrohr. In Kombination mit der implementierten Elektronenstrahlquelle konnten umfangreiche Simulationen zur Teilchenbewegung entlang der Magnetfeldlinien durchgeführt werden. Dadurch war es möglich, eine Abtastung des Flussschlauchs mit Elektronen über die supraleitenden Dipolmagnete der WGTS durchzuführen. Das Ergebnis ist eine lineare Abhängigkeit zwischen der Auslenkung des Elektronenstrahls auf dem Detektorwafer und dem Dipolstrom. Diese Korrelation ermöglicht eine sehr genaue Bestimmung des Zentrums des Elektronenstrahls auf dem Detektorwafer, da dieser unabhängig von der Pixelauflösung bestimmt werden kann.

Im Hinblick auf die First Light Messkampagne war es möglich, durch die lokale Absenkung des Magnetfeldes den Flussschlauch aufzuweiten und mit Hilfe der Elektronenstrahlabtastung des entstandenen Engpasses zur Wand gezielt nach Kollisionspunkten zu suchen, um die Ausrichtung des magnetischen Flussschlauchs im STS-Bereich zu überprüfen. Mit Hilfe der Elektronenstrahlabtastung wurden Engpässe auf dem Detektorwafer abgebildet, so dass die Ausrichtung der untersuchten Komponente im Bezug auf den FPD ermittelt werden konnte. Die begleitende Simulationen zeigen, dass der 191 Tcm^2 Flussschlauch in der Tat kollisionsfrei durch das gesamte Strahlrohr geführt werden kann. Allerdings kollidierte der 210 Tcm^2 Flussschlauch horizontal innerhalb des DPS Strahlrohrs. Durch den Betrieb der DPS Magnete bei einem moderat höheren Magnetfeld können die Kollisionen des 210 Tcm^2 Flussschlauchs vermieden werden. Die Ausrichtung der Strahlführung zwischen Spektrometer und Detektor wurde mit der in Vorgängerarbeiten entwickelten asymmetrischen Magnetfeldmethode untersucht. Dazu wird der flussaufwärts gerichtete Magnet des zu untersuchenden Spektrometers abgeschaltet. Dies führt zu einer Aufweitung des magnetischen Flussschlauchs, wodurch Elektronen, die durch Feldemission nahe der inneren Oberfläche des Spektrometers emittiert werden, auf den Detektor geleitet und detektiert werden konnten. Das Ergebnis ist ein ringförmiges Abbild auf dem Detektor, welches die Ausrichtung zwischen der inneren Elektrodenstruktur des Spektrometers und dem FPD beinhaltet. Da das globale Magnetfeld für die First Light Ausrichtungsmessungen reduziert werden musste, wurden Simulationen für verschiedene Feldeinstellungen durchgeführt. Dadurch konnte gezeigt werden, dass die Ausrichtungsmessungen magnetfeldunabhängig sind. Die aufgeführten komplexen Messstrategien wurden anschließend im Rahmen der First Light Messkampagne zur Bestimmung der Ausrichtung des magnetischen Flussschlauchs eingesetzt.

Mit Hilfe einer Elektronenquelle, die den gesamten Querschnitt des Flussschlauchs beleuchtet, konnten erstmals die Transporteigenschaften des magnetischen Flussschlauchs auf einer gesamten Länge von 70 m gemessen werden. Das Ergebnis für niederenergetische Elektronen war die Beobachtung eines Schattens, der auf dem unteren Teil des Detektorwafers sichtbar war. Weitere Untersuchungen ergaben, dass der Schatten durch ein elektrostatisches Blockierungspotential am Klappenventil zwischen dem Vor- und Hauptspektrometer verursacht wird. Dieses Potential reflektiert sehr niederenergetische Elektronen mit Energien unter 100 eV. Die relevanten β-Elektronen für die Neutrinomassenmessung besitzen aber Energien im multi-keV Bereich und werden somit nicht von dem beobachteten elektrostatischen Potential beeinflusst. Dieses verhindert jedoch die Beobachtung von niederenergetischen Untergrundereignissen, welche im STS-Strahlrohrbereich als auch im Vorspektrometer erzeugt werden. Weitere Untersuchungen müssen daher durchgeführt werden, um das Bauteil zu identifizieren welches das Potential erzeugt. Dieses Bauteil muss anschließend modifiziert werden, um eine erneute Bildung des elektrostatischen Potentials zu verhindern.

Ein wesentliches Ergebnis der First Light Messkampagne war die Verifizierung der erwarteten linearen Abhängigkeit zwischen der geometrischen Verschiebung des Elektronenstrahls auf dem Detektor und dem Strom in den Dipolspulen der WGTS. Leider wurde die Messung durch Beobachtung eines Elektronenhalos um den Elektronenstrahl beeinflusst, was zu einem einen störenden systematischen Effekt verursacht und zum anderen zu einer signifikanten Unsicherheit in den Ausrichtungsergebnissen führt. Dennoch sind die erzielten Ausrichtungsergebnisse den Simulationsergebnissen sehr ähnlich, da nur der DPS-Bereich den magnetischen Flussschlauch horizontal so weit einengt, dass nur der 191 Tcm^2 Flussschlauch kollisionsfrei bei nominalen Magnetfeldeinstellungen geführt werden kann. Durch den Betrieb der DPS Magnete bei höherem Magnetfeld verschwinden die Kollisionen des 210 Tcm^2 Flussschlauchs fast vollständig. Dementsprechend sollte es möglich sein, die Quellaktivität mit dem FBM im äußeren Bereich des 210 Tcm^2 Flussschlauchs zuverlässig zu überwachen. Die Ausrichtung der einzelnen Komponenten von STS und SDS untereinander und zum FPD zeigte keine signifikante Abweichung vom Design. Eine mechanische Neuausrichtung einer Komponente der DPS-Strahlführung oder eine Verschiebung des magnetischen Flussschlauchs unter Verwendung der supraleitenden Dipolmagnete der WGTS ist daher nicht erforderlich. Somit können die β-Elektronen dort kollisionsfrei und ungestört geführt werden.

Die bevorstehende Inbetriebnahmephase III des gesamten KATRIN Experiments zu Anfang 2018 wird es ermöglichen, die Ausrichtung des magnetischen Flussschlauchs noch genauer zu untersuchen. Dies wird durch die Elektronenkanone der Rear Section ermöglicht, welche ab diesem Zeitpunkt zur Verfügung stehen wird. Dieser Emitter erzeugt einen halofreien und scharfkantigem Elektronenstrahl mit einem Durchmesser im sub-mm-Bereich. Dieser wohldefinierte Elektronenstrahl ermöglicht es, ein sehr detailliertes Bild der Ausrichtung der magnetischen Flussschlauchs im Strahlrohr unter Verwendung der etablierten magnetischen Engpassmethode zu erzeugen. Zusätzlich wird der Aufbau der gesamten Strahlrohrinstrumentierung abgeschlossen sein. Dies erlaubt es, zudem die Ausrichtung zwischen der Instrumentierung und dem magnetischen Flussschlauch exakt zu bestimmen. Basierend auf den Ergebnissen dieser Arbeit erfüllt der magnetische Flussschlauch damit alle Anforderungen, um die effektive Neutrinomasse mit einer Empfindlichkeit von 200 meV bei 90 % C.L. über fünf Kalenderjahre zu messen, wenn die DPS, wie vorgeschlagen, mit einem höheren Magnetfeld betrieben wird.

CHAPTER 1

Introduction

This thesis presents the results of the "First Light" measurement campaign of the Karlsruhe Tritium Neutrino (KATRIN) experiment. For the first time a configuration was implemented which has allowed to create electrons at one end of the experiment and to guide these electrons through the entire 70-m-long setup to the detector to be counted. The goal was to verify that electrons can be guided collision-free through the setup, thereby allowing to minimize systematic effects from energy losses. This is essential for KATRIN to reach the absolute neutrino mass scale with an unreached sensitivity of $m_\nu = 200\,\mathrm{meV}$ (90 % C.L.) [Ang05].

The Standard Model of particle physics describes the neutrinos as massless, electrically neutral and purely weakly interacting particles. However, the discovery of the neutrino oscillation has provided unambiguous evidence that neutrinos have a non-vanishing mass [Fuk98b, Ahm01, Ahm02, Aha05, Wen10, Aha13]. Thus, neutrinos are the most abundant massive particle in the universe, with each cubic centimeter containing 339 neutrinos [Les12]. Due to their non-vanishing mass, they have a direct influence on the formation of large-scale structures in the early universe. Additionally, their non-zero mass has a major impact on particle physics since the Standard Model of particle physics offers no explanation about the mechanism behind neutrino masses and oscillation. The strong influence of massive neutrinos on cosmology and particle physics is the motivating raison d'être for to realize the next-generation direct neutrino mass experiment, KATRIN.

The KATRIN experiment makes use of the kinematics of tritium β-decay to measure the neutrino mass in a direct and model-independent way. The neutrino mass has a direct influence on the shape of the spectrum only near the endpoint. Therefore, KATRIN will investigate the electron energy spectrum of β-electrons in the region close to the endpoint with unprecedented precision. The unique sensitivity of the KATRIN experiment can only be achieved by combining a high-luminosity gaseous tritium source with a large spectrometer that is based on the MAC-E filer principle. Since only a small fraction of β-electrons originates from the region close the endpoint of the spectrum, KATRIN requires a stable source activity on the 0.1 % level to obtain the required statistics while simultaneously reducing systematic effects. The huge flux of β-electrons has to be guided adiabatically and collision-free from the source through the 70-m long beamline of the experiment to the detector.

The entire beamline is surrounded by a series of superconducting solenoids which provide a magnetic field to guide the β-electrons. Due to the cylindrical geometry of the beamline, the magnetic guiding field can be described as a magnetic flux tube of specific size. To avoid collisions, the superconducting magnets and thus the magnetic flux tube are coaxially aligned with the beamline. The rather stringent specifications have to be verified by

dedicated alignment measurements and the actual geometry data have to be implemented into a sophisticated simulation model of the KATRIN beamline to scrutiny the magnetic flux tube alignment. With the help of simulation results it is possible to develop specific alignment strategies. During the First Light campaign, these complex measurement strategies are used to determine the alignment of the magnetic flux tube in the beamline, forming the main objective of this thesis.

To minimize the source-related systematic uncertainties, the β-activity has to be stabilized on a 0.1 % level. Several parameters influence the activity, such as the pressure and purity of the gas, and the temperature of the source tube, containing the gaseous tritium. Since the source activity is directly correlated with the temperature of the source tube, it has to be stabilized on a 0.1 % level as well. In addition, to limit the effect of thermal broadening of the β-electron energies due to molecular motion, the source tube and hence the gaseous tritium source is cooled to a temperature regime of 30 K. Another objective of this thesis is to determine whether the specified temperature regime as well as the corresponding stability and homogeneity requirements can be achieved.

Chapter 2 gives a summary of the history and status of neutrino physics. Current results of neutrino experiments are outlined with the focus on neutrino oscillation, since these provide evidence for a non-vanishing neutrino mass. It concludes with outlining and contrasting the different-model dependent and independent methods to determine the absolute neutrino mass scale.

The underlying principles of β-spectroscopy using MAC-E filters is presented in chapter 3. It outlines the technical setup of the KATRIN experiment while giving an overview of individual KATRIN components and their technical realization. The statistic and systematic performance with regard to source activity and magnetic flux tube alignment are discussed as well. The chapter is completed by a detailed description of the objectives of this thesis.

Chapter 4 presents the works performed during STS beamline commissioning. The focus of this chapter is on the commissioning of the source tube cooling system and on the achieved level of temperature homogeneity and stability. The determination of the position of the superconducting inside the cryostats of the STS beamline and with respect to the global KATRIN coordinate system is outlined as well as the achieved magnetic field stability. Finally the commissioning of the cryogenic pumping section with regard on the 3-K cryogenic beamline trap is discussed.

The First Light measurement campaign is described in detailed in chapter 5. It includes the objectives of the measurement campaign as well as the hardware status of KATRIN experiment during this crucial measurement period. It explains the technical setup behind the use of a pencil beam and a wide beam electron source that were used for alignment measurements. The chapter concludes with an overview of the underlying principles of the alignment measurement methods.

Chapter 6 details the simulation efforts of this thesis for the global KATRIN beamline, including the careful investigation of the magnetic field. At first the simulation software Kassiopeia is presented, which allows to create a detailed model of the geometry and the electromagnetic fields of the entire beamline for particle tracking. The simulation allows to assess the merits of the two implemented electron sources. The main focus here is on the pencil beam to scan the magnetic flux tube by making use of superconducting dipole magnets of the source section. Finally, the pros and cons of different measurement methods as well as the best-suited magnetic field configurations are presented.

The experimental results obtained during the First Light campaign are discussed in chapter 7. It presents the alignment parameters for each KATRIN section with respect to the

detector. The main task was to identify if the magnetic flux tube can be guided collision-free through the entire KATRIN beamline. The outcome is discussed together with options to further improve the flux tube alignment. Finally, the implications for the neutrino mass measurement are outlined and complemented by suggestions for future alignment measurements.

The last chapter summarizes the performed measurements and the results obtained and will give an outlook on the upcoming neutrino mass measurement starting in 2018.

CHAPTER 2

Neutrino physics

Being the most abundant massive particle in nature, neutrinos have a key role in elementary particle physics with strong links to the formation of large scale structures in the early universe. With its non-vanishing mass and large-scale oscillation effects, neutrinos could be central to answer the fundamental questions:

1. Are neutrino oscillations violating CP-symmetry? Could this potentially explain the matter-antimatter asymmetry in the universe?
2. What is the absolute mass of the neutrino? Could this be a hint on how masses are generated beyond the Higgs mechanism?
3. What type of particles are neutrinos Dirac or Majorana particles?
4. In which way did neutrinos influence the structure formation in the early universe?

Since W. Pauli has postulated the neutrino in 1930 [Pau30b, Pau30a] in a letter to a conference in Tübingen, they have fundamentally changed our understanding not only of the β-decay but also in understanding the interactions of elementary particles. Due to their weak interaction, a direct detection seemed to be impossible at these times. However, in 1956, a mile-stone in neutrino physics was achieved when Reines and Cowan finally discovered neutrinos in the Savannah River reactor experiment [Rei56a, Rei56b, Cow56]. Since then neutrino physics has continuously gained pace and two more types of neutrinos, the μ-neutrino and the τ-neutrino were found in 1962 [Dan62] and 2001 [DON01]. A breakthrough observation in 1998 [Fuk98a, Fuk98b] and 2001 [Ahm01, Ahm02] has provided unambiguous evidence for the phenomenon of neutrino oscillations, which was already described by Pontecorvo in 1968 [Pon68]. Neutrino oscillations give incontrovertible proof that the masses of neutrinos are non-zero. Due to this fact neutrinos clearly point to physics beyond the standard model of particles, which assumes neutrinos to be massless.

The hierarchy of neutrino masses is still unknown, but the mass splittings between the three neutrino types have been determined with high accuracy. The observed mass splittings allow to define at least a lower mass limit [Ber12]. Upper mass limits have been set by using cosmological models and direct neutrino mass measurements using β-spectroscopy. To determine the neutrino mass in a model-independent way, high-precision β-spectroscopy is used to investigate the endpoint energy region of the tritium β-spectrum, where the neutrino mass has a measurable influence on the shape [Kra05, Ase11].

Neutrino masses are one of the fundamental yet still unknown parameters in the Standard Model (SM). Being the lightest and most abundant fermionic particles in the universe, the influence of neutrinos on the structure formation in the early universe is of specific

importance. Therefore, a precision determination of its mass is a key motivation for the leading next-generation neutrino mass experiment: the Karlsruhe Tritium Neutrino (KATRIN) experiment. The target of KATRIN is to improve the neutrino mass sensitivity by one order of magnitude compared to the present neutrino mass results. The sensitivity goal is 200 meV at 90 % C.L., which will be achieved by using high-precision tritium β-spectroscopy.

A brief overview of the history of the neutrinos with milestone observations will be given in the next section of this chapter. Afterwards the theoretical description of neutrinos in the SM of particle physics will be explained in section 2.2. The observation of neutrino oscillations and the underlying physics beyond the SM will be shown in section 2.3. The different techniques used in precision neutrino mass investigations will be given in section 2.4. In the last section 2.5, the current status of direct and model independent neutrino mass experiments will be detailed.

2.1 A summary of the neutrino history

It took more then 10 years after the first discovery of radioactivity by Henri Becquerel in 1896 until N. R. Campbell showed that β-rays are identical with electrons emitted by the radioactive decay of a nucleus [Rut10]. At the beginning β-decay investigation on the decay properties were incorrectly described, implying simply that a mother nucleus X decays into a daughter nucleus Y under the emission of an electron e^-:

$$ {}^{A}_{Z}\mathrm{X} \;\rightarrow\; {}^{A}_{Z+1}\mathrm{Y} + e^- . \tag{2.1} $$

The consequence of this two-body decay should be a discrete spectrum of electron energies. First investigations of the β-electrons in an external magnetic field however gave a hint to a continous energy distribution [Bae11b, Bae11a, Mei13]. In 1914, J. Chadwick finally proved that the energy spectrum of the β-emitter ^{214}Pb and ^{214}Bi is indeed continuous [Cha14], as shown in figure 2.1. Two additional experiments confirmed Chadwicks result of a continuous β-spectrum [Ell27, Mei30].

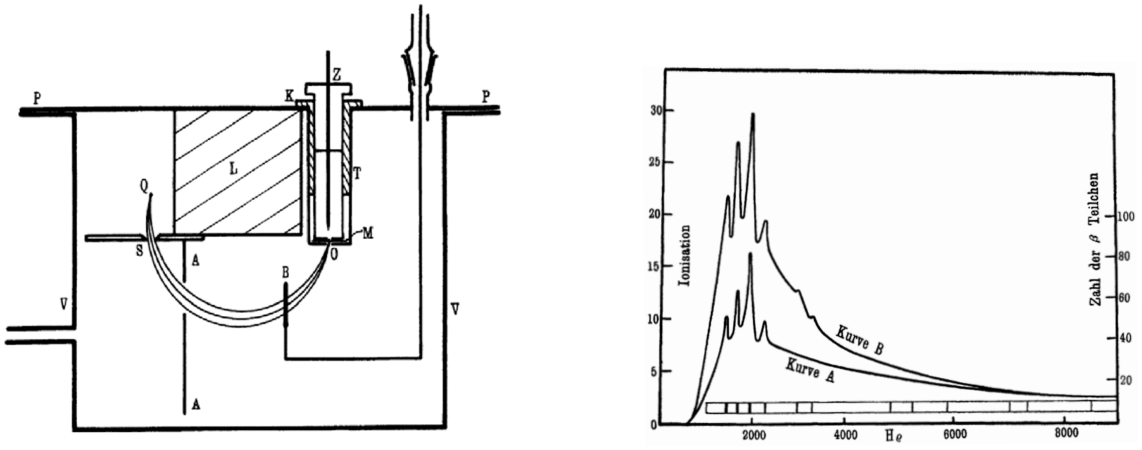

Figure 2.1: Electron energy distribution curve of the radium β-decay. Chadwick used a RaB and RaC β-emitter within a vacuum chamber in a magnetic field to study the energy distribution of the β-ray, shown in the left figure. The energy distribution showed 4 linies, but the most important insight was the continous energy spectrum, shown on the right figure. Twenty years later F. Scott repeated the measurement and confirmed Chadwicks result [Sco35, Cha14]. Figures adapted from [Cha14].

Although, this result seemingly violates conservation of energy, momentum and angular momentum it took more than a decade until the β-decay reaction was extended to a three-body-decay by W. Pauli [Pau30b]. Pauli postulated a then hypothetical stable, interacting only weakly, described as an electrically neutral, spin $-1/2$ particle ($\overline{\nu}_e$), which carries away the missing angular momentum and the energy. This explains the continuous energy spectrum:

$$ {}^{A}_{Z}X \quad \rightarrow \quad {}^{A}_{Z+1}Y + e^- + \overline{\nu}_e. \tag{2.2} $$

Furthermore, Pauli concluded that the shape of the β-spectrum could only be explained if neutrinos have a non-vanishing mass [Pau30b]. The first β^+-decay was detected by F. Joliot and I. Curie in 1932 [Jol34], completing the radioactive decay processes which produce β-rays (not taking into account electron capture):

$$ \beta^-\text{-decay:} \quad n \quad \rightarrow \quad p + e^- + \overline{\nu}_e, \tag{2.3} $$

$$ \beta^+\text{-decay:} \quad p \quad \rightarrow \quad n + e^+ + \nu_e. \tag{2.4} $$

In 1934, E. Fermi formulated the theory of a three-body β-decay by assuming a point-like weak interaction [Fer34], and renamed the new neutral particle to neutrino. His calculation of the transition rate $\Gamma_{i\rightarrow f}$ of the β-spectrum from the initial state i to the final state f:

$$ \Gamma_{i\rightarrow f} = 2\pi \cdot G_F^2 \cdot |\langle f|M_{fi}|i\rangle^2| \cdot \frac{dN}{dE}, \tag{2.5} $$

was named in his honor and today is called "Fermi's Golden Rule" [Dir27, Fer34]. Here G_F denotes the coupling constant, followed by M_{fi} which describes the transition matrix element, and the final-state density ($\frac{dN}{dE}$). For weak interactions between neutrinos and matter, H. Bethe and R. Peierls calculated a cross section of $\sigma = 10^{-44}\,\mathrm{cm}^2$ in the same year [Bet34].

A variety of novel phenomena improvements during the last decades have required to describe the differential spectrum of the β-electrons $\frac{d^2N}{dtdE}$ as a function of the kinetic energy of the electron as follows:

$$ \frac{d^2N}{dtdE} = \frac{G_F^2 \cdot \cos^2\theta_C}{2\pi^3}|M|^2 F(Z+1,E) \cdot \sqrt{(E^2+m_e^2)^2 - m_e^2c^4} \cdot (E + m_ec^2) \cdot $$
$$ (E_0 - E) \cdot \sqrt{(E_0-E)^2 - m_{\overline{\nu}_e}^2 c^4} \cdot \Theta(E_0 - E - m_{\overline{\nu}_e}c^2). \tag{2.6} $$

Here, we have integrated over all possible discrete and continuous final states [Bel03, Wei05, Ott08, Dre13]. The elements of "Fermi's Golden Rule" are listed in table 2.1.

Table 2.1: Physical quantities of "Fermi's Goldener Regel".

physical quantities	description
G_{F}	Fermi's coupling constant
θ_{C}	Cabibbo-angle
M_{fi}	transition matrix element
$F(Z+1,E)$	Fermi-function with nucleus charge value Z of the daughter nucleus
E	energy of the electron
m_{e}	mass of the electron
E_0	end-point energy of the β-spectrum
p	momentum of the electron
$m_{\overline{\nu}_{\mathrm{e}}}$	mass of the electron anti-neutrino

A major experimental breakthrough was achieved in 1956, when C. Cowan and F. Reines finally could prove the existence of neutrinos with their now famous series experiments, among them "project poltergeist" [Rei53, Rei56b, Cow56]. Predecessor experiments were first located at the Hanford Site, but to allow a more definitive conclusion, the experimental location had to moved to the P Reactor of the Savanna River Plant. With a maximal distance of 11 m to the reactor core, a reactor-neutrino flux of $5 \times 10^{13}\,\mathrm{cm}^{-2}\mathrm{s}^{-1}$ was calculated [Gri04]. Furthermore, the detector was buried 12 m below ground to provide adequate shielding against the soft component of cosmic rays. This last implementation of the "poltergeist" experiment consists of a sandwich configuration where two target tanks are placed between three scintillator modules. These scintillator modules are equipped with 110 PMTs to collect the scintillation light and produce electric signals. Each tank was filled with $100\,\ell$ water including a total of 40 kg of dissolved cadmium chloride ($CdCl_2$). The classical inverse β-decay was used to detect electron antineutrinos ($\overline{\nu}_{\mathrm{e}}$):

$$\mathrm{p} + \overline{\nu}_e \quad \rightarrow \quad \mathrm{n} + \mathrm{e}^+. \tag{2.7}$$

The target protons are provided by the largest number of water molecules inside the tanks. The positrons annihilate quickly with electrons into two 511-keV photons. The heavy recoil neutron propagates a few microseconds through the target until being thermalized by scattering processes with protons of the water to finally be captured by a cadmium nuclei. The excited cadmium nuclei after capture immediately deexcites via emission of several γ-photons with an overall energy in the MeV range:

$$^{113}\mathrm{Cd} + \mathrm{n} \quad \rightarrow \quad ^{114}\mathrm{Cd}^*, \tag{2.8}$$

$$^{114}\mathrm{Cd}^* \quad \rightarrow \quad ^{114}\mathrm{Cd} + \gamma. \tag{2.9}$$

The short time delays of typically $< 17\,\mu\mathrm{s}$ between the 511-keV photons and the MeV γ-photons were used to distinguish neutrino signals from the background [Cow56]. This is the so-called delayed coincidence method still in use today in many reactor ν-experiments.

A second type of neutrino, the so-called muon-neutrino (ν_μ), was discovered at the Brookhaven National Laboratory in 1962. There, at the Alternating Gradient Synchrotron (AGS), 15 GeV protons were striking a beryllium target to produce pions (π). Nowadays it is well-known that these pions can decay via the following channels:

$$\pi^+ \quad \rightarrow \quad \mu^+ + \nu_\mu, \tag{2.10}$$

$$\pi^- \quad \rightarrow \quad \mu^- + \overline{\nu}_\mu. \tag{2.11}$$

The pion beam from AGS was focused onto a massive 13.5 m thick iron block for absorption. Some of the pions decayed in flight to neutrinos, which penetrate the massive block, while

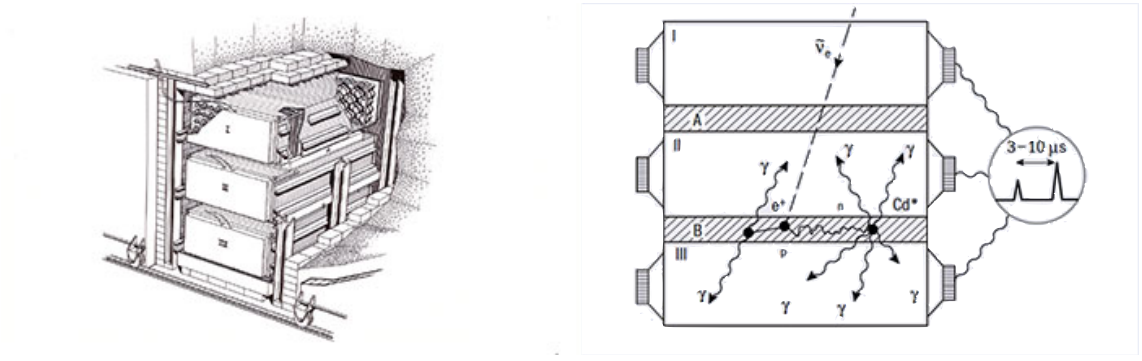

Figure 2.2: Configuration of the neutrino experiment poltergeist. The left picture shows the sandwich configuration of project poltergeist. On the right side the measurement principle is demonstrated. The target tanks (A and B) are highlighted with lines. The scintillator modules (I – III) which are covered with the photo multipliers are highlighted in transparent. A time delay of $3 - 10\,\mu s$ is mentioned. The time delay shown on the right side of the figure, depends on the cadmium concentration in the water of the target tanks [Cow56, Rei56b]. This figure is adapted from [Sut16]

all other particles were blocked off. The outcome was a pure beam of neutrinos. A 10 t aluminum spark chamber was placed inside this beam path. The aim was to prove that the muon neutrinos (ν_μ) can be distinguished from electron neutrinos (ν_e). Experiments were able to detect 29 muon events, being identified by their straight tracks. These straight tracks could clearly be discriminated from six electron events, which had produced a wide electromagnetic shower. Accordingly, it could be demonstrated that the muon-neutrino and the electron-neutrino are two different particles [Dan62].

In 1975, the tau-lepton (τ) and hence, the third leptonic generation was detected [Per75]. Although the existing of tau-neutrinos (ν_τ) was expected since then, it took another 25 years until the first τ-neutrinos were detected at the DONUT experiment. High-energy protons with 800 GeV from the Tevatron accelerator were guided onto a tungsten beam dump. The particles created did contain an unstable part of D_S-mesons, which immediately decayed to:

$$D_S \quad \rightarrow \quad \tau + \overline{\nu}_\tau. \tag{2.12}$$

This tau-neutrino beam was focused on a detector, consisting of stainless steel sheets, separated from each other by nuclear emulsion plates. A shield of concrete, lead and iron was used to absorb all other particles. The unique track of the produced τ-leptons in the fiducial volume resulted in a typical kink in its trajectory. With these characterizations it was possible to identify four τ-neutrino events [DON01].

Already in 1989 the Apparatus for LEP Physics (ALEPH) experiment investigated the total width of the Z^0-resonance at the Large Electron-Positron (LEP) collider at CERN. The analysis of the Z^0-resonance showed about three ($N_\nu = 3.27 \pm 0.30$) light neutrino species with a mass $m_\nu < 45$ GeV [DeC89], twelve years before the τ-neutrino was detected. In 2006 the combined analysis of the LEP and the SLC data provided a light neutrino number of $N_\nu = 2.9840 \pm 0.0082$ [The06].

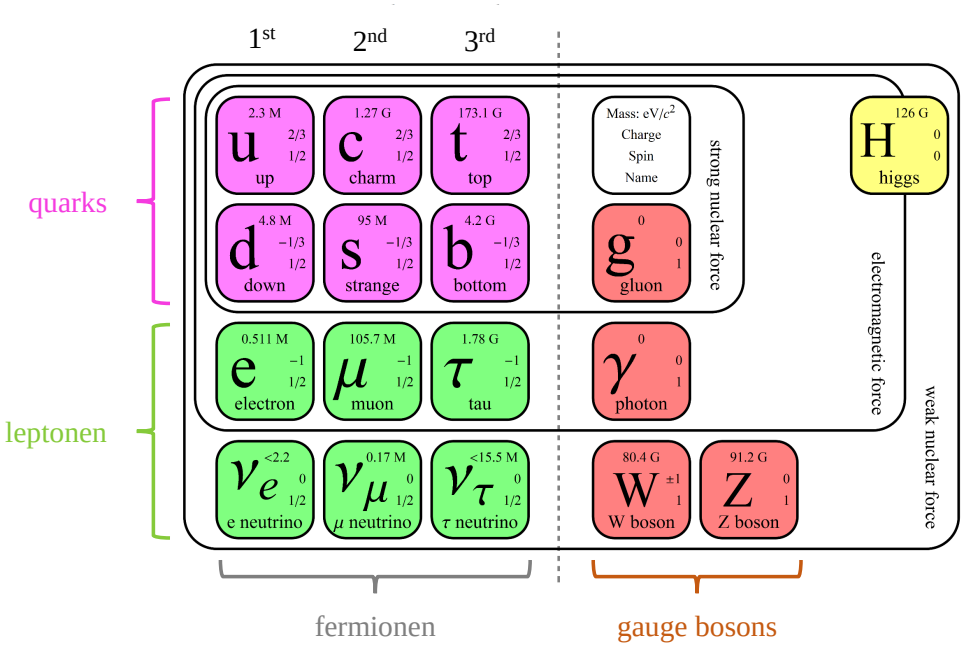

Figure 2.3: The standard model of particle physics. The left side of the figure shows the three generations of the quarks and the leptons, which form together the fermions. The fermions are classified as spin 1/2 particles. On the right side of the figure the bosons are presented, classified as spin 1 particles, excluded the higgs boson which has a spin 0. Figure is adapted from [Lub17].

2.2 Neutrinos in the standard model of particle physics

Today the SM of particle physics describes the three discovered light neutrino generations, which can be distinguished by their different flavor (ν_e, ν_μ and ν_τ), see figure 2.3. With their spin 1/2, neutrinos are classified as fermions, and, together with their corresponding partners (e^-, μ^- and τ^-), they form a distinct subcategory of fermions, the leptons, see figure 2.3. In the SM leptons are arranged in doublets, transforming under the weak isospin SU(2) gauge symmetry, while its weak hypercharge Y describes transformations under U(1). A unification of these symmetries forms the gauge group $SU(2) \otimes U(1)$, creating the electroweak interaction. The Higgs mechanism allows this gauge group to contain three massive gauge bosons, the $W^\pm$ & Z^0 which mediate the weak interaction and a massless vector boson γ mediating the electromagnetic interaction.

Based on the spectacular successes of quantum electrodynamics (QED) in the 1950s, major efforts have been undertaken to construct a similar theory for the weak interaction. First descriptions in the 1960s by S. Glashow [Gla61], A. Salam and J. Ward [Sal64] were expanded in a formulation in 1967 which was simultaneously achieved by S. Weinberg and A. Salam [Wei67, Sal68]. Around 1968 this culminated in the unified electroweak theory by S. Glashow, S. Weinberg and A. Salam. Key to their theory was the so-called Higgs mechanism which gives mass to the gauge bosons $W^\pm$ & Z^0. As early as 1964, this mechanism was formulated by P. Higgs, F. Englert, and R. Brout in the *PRL symmetry breaking papers* [Hig64, Eng64].

These authors implemented a scalar Higgs field into the $SU(2) \otimes U(1)$ Lagrangian, which couples to the gauge fields of U(1), giving mass to the gauge bosons $W^\pm$ & Z^0 by spontaneous symmetry breaking. The remaining gauge boson γ remains massless. In doing so, three unphysical massless Goldstone bosons were eliminated, while one massive boson remains [Hig64]. In 2012 the theoretically predicted scalar Higgs boson was observed in the CMS and ATLAS experiments at LHC [Aad12, Cha12].

In 1955, one year before the first neutrinos were detected by Cowan and Reines, R. Davis set out to measure reactor neutrinos, based on Pontecorvo's original idea by the radiochemical reaction [Dav55]:

$$^{37}\mathrm{Cl} + \overline{\nu} \quad \not\rightarrow \quad ^{37}\mathrm{Ar} + \mathrm{e}^{-}. \tag{2.13}$$

Accordingly, a large amount of carbon tetra-chloride next to the Savannah river reactor was used as a target. The underlying theoretical model in these days assigned the same identity to neutrinos and antineutrinos ($\nu = \overline{\nu}$). At present, a detection of $\overline{\nu}_\mathrm{e}$ from a reactor is impossible due to the fact that conservation of lepton number 2.12 is violated. Consequently, R. Davis experiment had to yield a negative result.

In 1956, Lee and Yang suggested violation of parity conservation in weak interactions [Lee56]. An experimental breakthrough was achieved in the same year by C. Wu as she could prove maximal violation of parity conservation in weak reactions [Wu 57]. The resulting fundamental left-right asymmetry in weak interactions, gives couplings between the weak gauge bosons and left-handed particles, and right-handed antiparticles. The investigated physical observable was the handedness of a particle, so-called helicity:

$$h = \frac{\vec{s} \cdot \vec{p}}{|\vec{s}| \cdot |\vec{p}|}, \tag{2.14}$$

which is the projection of the particle spin $\vec{s}$ on its momentum $\vec{p}$. Due to the fact that the helicity operator depends on the reference frame, it is not Lorentz-invariant. Hence, in the case of creating a massive particle by the weak interaction, this can be detected with right- and left-handed helicities. However, massless particles will only be detected with a left-handed helicity.

The first determination of the neutrino helicity was achieved in 1958 by M. Goldhaber [Gol58]. Helicity of neutrinos was determined by measuring the polarization of photons, produced by the electron capture (EC) of $^{152\mathrm{m}}$Eu and the ensuing fast deexcitation of the daughter nucleus $^{152\mathrm{m}}\mathrm{Sm}^{*}$ ($\tau = 30\,\mathrm{fs}$):

$$^{152\mathrm{m}}\mathrm{Eu} + \mathrm{e}^{-} \quad \rightarrow \quad ^{152\mathrm{m}}\mathrm{Sm}^{*} + \nu_\mathrm{e} + 950\,\mathrm{keV}, \tag{2.15}$$

$$^{152\mathrm{m}}\mathrm{Sm}^{*} \quad \rightarrow \quad ^{152\mathrm{m}}\mathrm{Sm} \; + \gamma \; + 961\,\mathrm{keV}. \tag{2.16}$$

Goldhaber finally determined the neutrino helicity to be $h = -1.0 \pm 0.3$ [Gol58]. The conclusion is that the direction of neutrino spin and momentum are opposite. The achieved result is in good agreement with maximum parity violation of weak interactions, discovered earlier in the Wu experiment.

Hence, the corresponding V–A theory [Fey58, Sud58] implies the existence of massless left-handed neutrinos and massless right-handed antineutrinos, a central asset of the SM.

2.3 Neutrino physics beyond the standard model

Since the postulation of neutrinos by Pauli in 1930, major efforts were undertaken to disclose its secrets. For along period of time, the theoretical description of the neutrino was in good agreement with the experimental results starting in the 1980s and 1990s, a series of neutrino experiments found more and more stringent indications for flavor transformation between all three neutrino generations. The consequence of this oscillation results is that at least two neutrino generations are not massless and the flavor number conservation is violated. Furthermore, the 3×3 neutrino mixing matrix comes with a factor which could violate the CP-symmetry. This could be the key element to explain the evident asymmetry between matter and anti-matter in the universe. The following sections give a short introduction to the history of neutrino oscillation physics, followed by a brief discussion of the theoretical framework and concluding with recent results.

2.3.1 The solar neutrino problem

Combining the inconclusive experiment of Davis in 1955 with the landmark discovery of the electron antineutrino by Reines and Cowan, it seemed evident that neutrinos are non-identical to their anti-particles [Dav55, Rei56b, Cow56]. Although Pontecorvo's first idea to measure the neutrinos via an inverse β-decay was not successful, neutrino-iduced n-p transpormations can be used to measure neutrinos from fusion processes that occur in the core of the sun [Dav64, Bet14b]. Here, the radio-chemical transformation of chloride into argon via an inverse β-decay and vice versa was proposed to detect solar neutrinos [Pon91]:

$$^{37}\mathrm{Cl} + \nu_e \quad \underset{\text{capture}}{\overset{\text{decay}}{\rightleftharpoons}} \quad ^{37}\mathrm{Ar} + e^- . \tag{2.17}$$

Already in the same year Bahacall published his detailed estimates of solar fusion processes and nuclear β-decays, to establish the Standard Solar Model (SSM) [Bah64a, Bah64b].

The then new results in neutrino physics gave Davis a strong impetus to realize his famous Homestake experiment to measure solar neutrinos [Dav64]. A tank filled with 615 tons of liquid perchloroethylene C_2Cl_4 was used as target, placed in the Homestake gold mine 1478 m underground. Interactions of solar neutrinos with ^{37}Cl transforms it to ^{37}Ar, is a radioactive isotope of argon with a half-life of about 35 days. After a few weeks, small quantities of the argon isotope have formed and can be purged out of perchloroethylene with gaseous helium. Afterwards, a few tens of atoms of ^{37}Ar were separated from the process gas helium by using a cold trap. Finally, a small proportional counter was filled to detect the decay of ^{37}Ar via K-electron capture to excited ^{37}Cl*. During the deexcitation, a 2.8-keV Auger electron is emitted and was detected with proportional counter [Dav68]:

$$^{37}\mathrm{Ar} + e^- \quad \rightarrow \quad ^{37}\mathrm{Cl}^* + \nu_e, \tag{2.18}$$

$$^{37}\mathrm{Cl}^* \quad \rightarrow \quad ^{37}\mathrm{Cl} \; + e^- . \tag{2.19}$$

With this radio-chemical method, the real-time information about neutrino interactions, such as time of reaction and neutrino energy, get lost. With an energy threshold of 814 keV, Davis was able to detect ^{7}Be and ^{8}B neutrinos, see figure2.4. Already in the seventies, first results were consistently at a value of only one third of Bahcall's calculated solar neutrino flux [Bah76, Dav79]. This result established the so-called "solar neutrino problem". Between 1970 and 1994, more than 108 extractions were performed. This gave a solar neutrino induced production rate of $r = 0.48 \pm 0.03\,(\text{stat.}) \pm 0.03\,(\text{syst.})$ ^{37}Ar per day [Dav94].

The solar neutrino problem seemed at first to be an issue related to uncertainties related to the SSM, nuclear cross sections, or even Davis' experiment. Bahcall's calculations and Davis' experiment were checked repeatedly, but both were indeed correct [Bah82]. Subsequently, a series of successor experiments, using the transformation of gallium ^{71}Ga into germanium ^{71}Ge, such as GALLEX [Ham99], SAGE [Abd02] and GNO [Alt05], confirmed the deficit of solar neutrinos. However, these experiments could not deliver real-time information about neutrino fluxes. A significant milestone was achieved in the nineteen-nineties, when the water Cherenkov-based Kamiokande experiment delivered first real-time information and confirmed the deficit again [Fuk96].

The next-generation Cherenkov experiments like Super-Kamiokande [Fuk98a] and SNO [Ahm01] are based on light and heavy water as a target, respectively. These experiments were designed to investigate the solar neutrino problem in more detail. A water Cherenkov

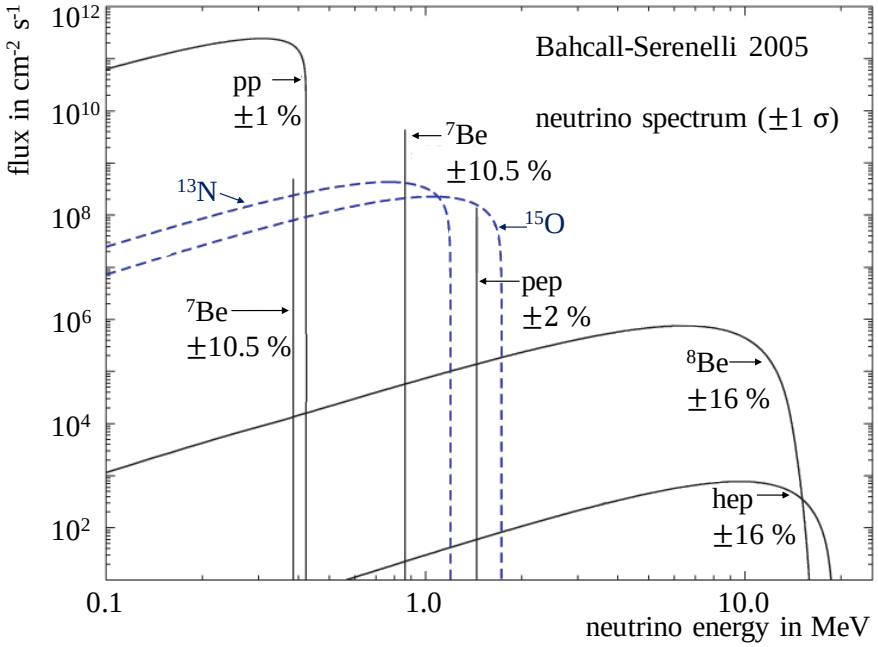

Figure 2.4: The solar neutrino flux. The energy spectrum of solar neutrinos as predicted by the standard solar model. Figure is adapted from [Bah05].

detector makes use of the principle that neutrinos can interact with matter via elastic scattering off atomic shell electrons:

$$\nu_\alpha + e^- \quad \rightarrow \quad \nu_\alpha + e^- \qquad (\alpha = e, \mu, \tau). \tag{2.20}$$

The result of a neutrino interaction in this channel is an electrically charged particle with a rather high energy of up to several MeV, produces characteristic Cherenkov light cones in the target medium. The shape and alignment of theses cones include information about the direction of the incident neutrino, its kinetic energy, the arrival time and the point of interaction inside the target mass. To detect the Cherenkov light cones, the surface of a vessel is completely covered with a large number of photomultipliers.

Located in the Kamioka mine in Japan, the Super-Kamiokande is the largest real-time neutrino detector so far, with a target mass of 50000 t of high-purity water. More than 13000 PMTs tubes allow a high-resolution Cherenkov light detection. Based on the elastic scattering process (see equation 2.20), the Super-Kamiokande detector allows to observe all neutrino flavors, in principle. A landmark discovery was achieved in 1998 by observation of an up-down asymmetry of high-energy atmospheric muon neutrinos. Although the primary cosmic ray flux is nearly isotropic, a discrepancy between the measured and the expected number of atmospheric muon neutrinos (ν_μ), as a function of the zenith angle and hence the propagation length through the earth, was observed (see figure 2.5). This gave the first indication that the measured neutrinos flavor depends on the distance between the production point and the detection point, which could only be explained by neutrino oscillations.

The new era of precision neutrino oscillation studies culminated in the results of the Sudbury Neutrino Observatory (SNO) experiment. Here, the same Cherenkov technology was used, however with a target mass of 1000 t heavy water (D_2O). The vessel was surrounded by 10000 PMTs to detect the Cherenkov light from reaction of ^{8}B-neutrinos. For the first time it was possible to measure the elastic scattering reaction, see equation

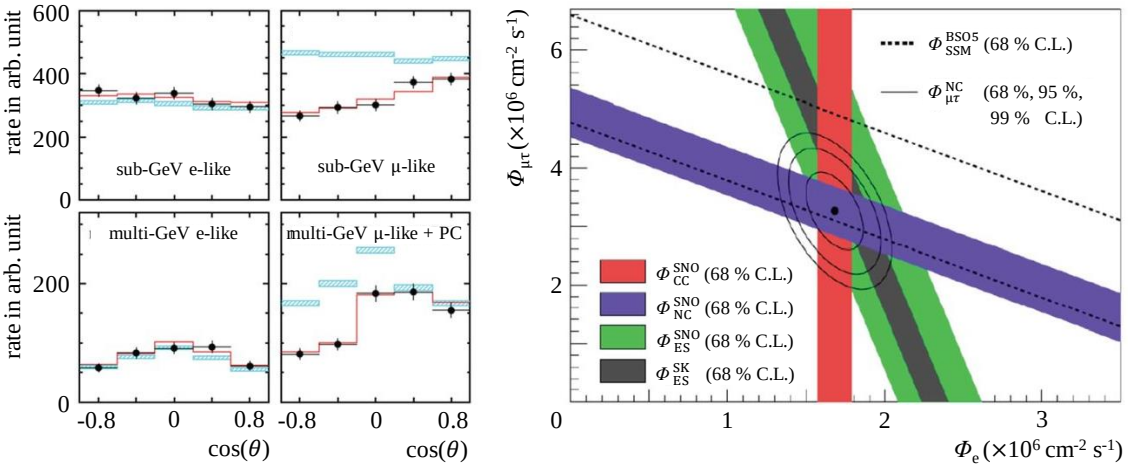

Figure 2.5: Observation of the neutrino oscillation. On the left site the measured atmospheric neutrino flux by Super-Kamiokande is shown. The measured results are highlighted with black points and complemented by the expected rate considering the oscillation theory, marked in red. Shown in blue is the expected rate without oscillation. On the right picture the measured solar neutrino flux $\phi_{\mu,\tau}$ versus the neutrino flux ϕ_e is shown. The colors denote the CC-, NC-, and ES-reactions. Furthermore, the Super-Kamiokande results are shown as brown band [Fuk02, Fuk03]. The predicted neutrino flux of ^{8}B is highlighted in black dashed lines [Bah05]. Figures are adapted from [Vir16] and [Aha05].

2.19, and simultaneously the neutral (NC) and charged current (CC) reactions:

$$\text{CC:}\quad \nu_e + d \rightarrow p + p + e^-, \tag{2.21}$$

$$\text{NC:}\quad \nu_\alpha + d \rightarrow n + p + \nu_\alpha \qquad (\alpha = e, \mu, \tau). \tag{2.22}$$

Due to their origin from fusion processes, solar neutrinos have a limited energy (E_ν), see figure 2.4, so that CC reactions are energetically possible for electron neutrinos only ($m_\mu \gg m_e$ and $m_\mu > E_\nu$). Consequently, the true flux of ν_e can be measured via this reaction. In contrast, the NC reaction is flavor blind, allowing an overall neutrino flux measurement. The thermalized neutron of this process from deuteron break-up is captured by a suitable nucleus resulting in the emission of photons with known energies to be detected with PMTs. This breakthrough discovery was published in 2001, where the total rate of NC reactions was found to be in excellent agreement with the predicted rate of solar neutrinos gained from the SSM (see figure 2.5). Furthermore, the electron neutrino fraction of one third confirmed the results of the previous experiments [Ahm02]. As predicted by Bahcall, the solar core is an electron neutrino source only. Both results give unambiguous evidence that neutrinos can transform their flavor during propagation. Moreover, the Super-Kamiokande atmospheric neutrino oscillation result gives clear evidence for the oscillatory character therein [Aha05, Zub11].

2.3.2 The theory to describe the neutrino oscillation

The idea for neutrino oscillations was put forward in the fifties by Pontercovo, however, then as a neutrino-to-antineutrino oscillation channel [Pon57, Pon58]. Further developments in the framework on the theory by Maki, Nakagawa and Sakata have completed

the theory of flavor oscillation put forward by Pontercorvo and Gribov [Mak62, Dan62, Pon68, Gri69]. Key reason for the theory development was the observation of the solar neutrino deficit. The basic framework of this theory will be briefly outlined and be based on [Pon68, Zub11].

Neutrino mixing

Based on the theory of weak interaction, neutrinos interact as flavor eigenstates $|\nu_\alpha\rangle$ ($\alpha = e, \mu, \tau$). Each of these flavor eigenstates can be written as a linear superposition of three light, stationary mass eigenstates $|\nu_i\rangle$ ($i = 1, 2, 3$), and vice versa. In the simplest form, neutrino mixing can be expressed as a unitary transformation relating the three flavor eigenstates and their mass eigenstates. The transformation is defined by a unitary n × n mixing matrix U ($U^\dagger_{i\alpha} = U^*_{\alpha i}$) according to:

$$|\nu_\alpha\rangle = \sum_i U_{\alpha i} |\nu_i\rangle \qquad \text{and} \qquad |\nu_i\rangle = \sum_\alpha U^*_{\alpha i} |\nu_\alpha\rangle . \tag{2.23}$$

A convenient parametrization of the unitary 3×3 mixing matrix U is given:

$$U = \begin{pmatrix} c_{12}c_{13} & s_{12}c_{13} & s_{12}e^{-i\delta} \\ -s_{12}c_{23} - c_{12}s_{23}s_{13}e^{i\delta} & c_{12}c_{23} - s_{12}s_{23}s_{13}e^{i\delta} & s_{23}c_{13} \\ s_{12}s_{23} - c_{12}c_{23}s_{13}e^{i\delta} & -c_{12}s_{23} - s_{12}s_{23}s_{13}e^{i\delta} & c_{23}c_{13} \end{pmatrix} \cdot \begin{pmatrix} 1 & 0 & 0 \\ 0 & e^{i/2 \cdot \alpha_{21}} & 0 \\ 0 & 0 & e^{i/2 \cdot \alpha_{31}} \end{pmatrix}, \tag{2.24}$$

which is called the Pontecorvo-Maki-Nakagawa-Sakata (PMNS) matrix. The matrix includes $c_{ij} = \cos(\theta_{ij})$, $s_{ij} = \sin(\theta_{ij})$, a Dirac CP-violation phase $\delta = [0, 2\pi]$, three weak mixing angles $\theta_{ij} = [0, \pi/2]$ and two Majorana CP-violation phases α_{21} and α_{31} (the latter are of no relevance here). The contribution of a mass eigenstate to a specific flavor eigenstate, and vice versa, is given by the mixing angle. At the writing this thesis, it is not known if neutrinos are Majorana or Dirac particles, therefore it is possible to introduce CP violation with one or, in the Majorana case, of three phases. Under the assumption that the three neutrino generation theory is consistent, the neutrino mixing is characterized by seven or nine parameters ($\theta_{12}, \theta_{23}, \theta_{13}, m_1, m_2, m_3, \delta$ and α_{21}, α_{31}). However, oscillation experiments are not sensitive on these Majorana phases and they can be safety ignored for the extended description below.

Neutrino oscillation

The stationary mass eigenstates are physical eigenstates of the free Hamiltonian $\mathcal{H}$ with eigenvalue E. As a solution of the time-independent Schrödinger equation, the temporal propagation along a one-dimensional coordinate (x) can be described by plane waves:

$$|\nu_i(x,t)\rangle = e^{-i(E_i t - p_i x)/\hbar} |\nu_i\rangle . \tag{2.25}$$

Although neutrinos are produced and detected in pure flavor states, during their propagation they develop into a superposition of flavor states according to:

$$|\nu_\alpha(x,t)\rangle = \sum_i U_{\alpha i} |\nu_i(x,t)\rangle , \tag{2.26}$$

$$|\nu_\alpha(x,t)\rangle = \sum_i U_{\alpha i} e^{-i(E_i t - p_i x)/\hbar} |\nu_i\rangle , \tag{2.27}$$

$$|\nu_\alpha(x,t)\rangle = \sum_{i,\beta} U_{\alpha i} U^*_{\beta i} e^{-i(E_i t - p_i x)/\hbar} |\nu_\beta\rangle . \tag{2.28}$$

For a flavor conversion $\nu_\alpha \to \nu_\beta$, the transition amplitude is given by:

$$A(\nu_\alpha \to \nu_\beta)(x,t) = \langle \nu_\beta | \nu_\alpha(x,t) \rangle = \sum_i U^*_{\beta i} U_{\alpha i} \mathrm{e}^{-i(E_i t - p_i x)/\hbar}, \tag{2.29}$$

resulting in the transition probability:

$$P(\nu_\alpha \to \nu_\beta)(x,t) = |A(\nu_\alpha \to \nu_\beta)(x,t)|^2 = \sum_{i,j} U_{\alpha i} U^*_{\alpha j} U^*_{\beta i} U_{\beta j} \mathrm{e}^{-i(E_i t - p_i x)/\hbar} \mathrm{e}^{i(E_j t - p_j x)/\hbar}. \tag{2.30}$$

In case of ultra-relativistic neutrinos ($v \approx c$) with total energy of $E_i \approx p_i c \gg m_i c^2$, the energy eigenstate can be approximated to:

$$E_i = \sqrt{p_i^2 c^2 + m_i^2 c^4} \approx p_i c + \frac{m_i^2 c^4}{2E}. \tag{2.31}$$

With $v \approx c$, $m_{ij}^2 = m_i^2 - m_j^2$ and the length L between the neutrino source and the point of detection, equation 2.30 respectively yields to:

$$P(\nu_\alpha \to \nu_\beta)(x,t) = P(\nu_\alpha \to \nu_\beta)(L,E) \tag{2.32}$$

$$= \sum_{i,j} U_{\alpha i} U^*_{\alpha j} U^*_{\beta i} U_{\beta j} \mathrm{e}^{-i/\hbar \frac{\Delta m_{ij}^2 c^3}{2} \frac{L}{E}} \tag{2.33}$$

$$= \sum_i |U_{\alpha i} U^*_{\beta i}|^2 + 2\mathrm{Re} \sum_{j>i} U_{\alpha i} U^*_{\alpha j} U^*_{\beta i} U_{\beta j} \mathrm{e}^{-i/\hbar \frac{\Delta m_{ij}^2 c^3}{2} \frac{L}{E}}. \tag{2.34}$$

The final equation 2.34 presents the quantum mechanical nature of neutrino oscillation as interference phenomenon. In addition, the formula demonstrates how the oscillatory behavior of the transition probability depends on the parameter m_{ij}^2, and the experimental variables L and E. This result in an oscillatory behavior of the transition probability non-diagonal terms in U, and at least one mass eigenstate which is non-zero. Accordingly, neutrino oscillations are sensitive to m_{ij}^2 only, and not on the absolute scale.

Simplified neutrino oscillation

If neutrino oscillations are simplified within a two-neutrino flavors model (ν_α, ν_β) with two massive neutrinos (ν_1, ν_2), the unified mixing matrix reduces to a simpler 2×2 form, containing one mixing angle θ only:

$$\begin{pmatrix} \nu_\alpha \\ \nu_\beta \end{pmatrix} = \begin{pmatrix} \cos(\theta) & \sin(\theta) \\ -\sin(\theta) & \cos(\theta) \end{pmatrix} \cdot \begin{pmatrix} \nu_1 \\ \nu_2 \end{pmatrix}. \tag{2.35}$$

For the two-flavor case the transition probability is:

$$P(\nu_\alpha \to \nu_\beta) = \sin^2(2\theta) \sin\left(\frac{\Delta m^2}{4} \frac{L}{E}\right) = 1 - P(\nu_\alpha \to \nu_\alpha). \tag{2.36}$$

The result of the oscillation theory is that neutrino oscillations occurs only if θ and Δm^2 are non-vanishing parameters. The characteristic oscillation length of a full oscillation cycle is given by [Zub11]:

$$L_0 = 4\pi\hbar c \cdot \frac{E}{\Delta m^2}. \tag{2.37}$$

Further, the matter-caused MSW-effect requires to modify the flavor transformation [Wol78, Mik86]. A variety of oscillation experiments over the past years has allowed to obtain parameters in the PMNS matrix. Depending on the specific neutrino source, the baseline

to the detector and the energy range of neutrinos, these experiments were sensitive on different parameters $(\theta, \Delta m^2)$ of the matrix. A large variety of oscillation experiments has improved our understanding of the PMNS parameters. In the next section, different neutrino sources and corresponding experiments will be summarized briefly and selected results will be presented.

2.3.3 Detailed study of the neutrino oscillation

Neutrino oscillation experiments make use of two fundamental detection scenarios: the appearance of a new flavor (appearance channel) and the disappearance of an initial flavor (disappearance channel) to measure θ_{ij}, Δm^2_{12} and Δm^2_{32}. To achieve the best sensitivity, the flux rate has to be measured one scales similar to the oscillation length, where the oscillation effect is most pronounced. The most important neutrino sources to study oscillation effects are nuclear reactors, particle accelerators, astrophysical sources and the sun [Zub11].

Solar neutrino experiments

Various nuclear fusion reactions produce solar neutrinos in the core of the sun with characteristic rates and energies up to 15 MeV, yielding the solar neutrino spectrum (see figure 2.4). The first solar neutrino experiments such as Homestake were sensitive only to electron neutrinos. Due to the huge 1.5×10^8 km baseline between the solar core and detection on earth and in view of the MSW effect ($E_\nu > 5$ MeV), a component of the electron neutrino flux is transformed into myon and tau neutrinos. Early solar neutrino experiments, thus only observed the disappearance channel of ν_e, and interpreted the result as a deficit of the solar neutrino flux.

As mentioned in section 2.3.1, the solar neutrino deficit is explained by neutrino transformation as proven by the results of the SNO experiment [Ahm01, Ahm02], which was sensitive to all flavors [Zub11]. In its second phase, two tons of dissolved salt (NaCl) enabled the detection of two channels, the exclusive CC channel, and the inclusive NC channel. For the first time the bolometric ^{8}B neutrino flux was measured and compared to the flavor-selective channel to discriminate between the ν_e and (ν_μ, ν_τ) contributions. A total ^{8}B neutrino flux rate of $\phi = (5.25 \pm 0.16(\text{stat.})^{+0.11}_{-0.13}(\text{syst.})) \times 10^6\,\text{cm}^{-2}\text{s}^{-1}$ verified the standard solar model [Aha13]. The following oscillation parameters have been determined [Aha13]:

$$\Delta m^2_{21} = (5.6^{+1.9}_{-1.4}) \times 10^{-5}\,\text{eV}^2 \tag{2.38}$$

$$\tan^2\theta_{12} = 0.427^{+0.033}_{-0.029}. \tag{2.39}$$

In 2012, the Borexino experiment detected for the first time neutrinos from the pep fusion reaction [Bel12]. Furthermore, by combining results for different solar neutrino branches, it could be demonstrated that the MSW effect reduces the survival probability of electron neutrinos from the ^{8}B reaction with energies above 3 MeV [Bel10, Mik85, Wol78].

Atmospheric neutrino oscillation

A persistent and isotropic flux of high-energy charged particles from the galaxy, so-called cosmic rays, is penetrating the upper atmosphere of earth, producing a cascade of lighter particles. This cascade typically consists of hadrons, in particular of positive or negative pions and kaons. Some of these subsequently decay into muons and neutrinos [Zub11]:

$$\pi^+ \to \mu^+ + \nu_\mu, \tag{2.40}$$

$$\mu^+ \to e^+ + \nu_e + \overline{\nu}_\mu, \tag{2.41}$$

and

$$\pi^- \to \mu^- + \overline{\nu}_\mu, \tag{2.42}$$
$$\mu^- \to e^- + \overline{\nu}_e + \nu_\mu. \tag{2.43}$$

The flavor ratio of this decay is expected as $R = (\nu_\mu + \overline{\nu}_\mu)/(\nu_e + \overline{\nu}_e) \approx 2$ over a large energy range and thus is suitable to investigate oscillations of atmospheric neutrinos.

For a detailed probe it is necessary to obtain information of the energy (E), the baseline (L) of the neutrino and its direction of motion. Water-Cherenkov detectors like Super-Kamiokande are ideally suited to make use of this information. This enables to discriminate between down-going neutrinos, which are produced in the atmosphere above the detector ($L \approx 10\,\text{km}$), and upward-going neutrinos, produced in the atmosphere on the opposite side of the earth ($L \approx 10^4\,\text{km}$) [Zub11]. When measuring the flavor ratio R as a function of direction (zenith angle of the neutrino), it is possible to investigate the oscillation probability P as function of L/E. First indications of atmospheric neutrino oscillation were published by the Kamiokande experiment in 1994, as they observed a smaller ratio than expected [Fuk94]. Further examination in 1998 by the Super-Kamiokande experiment confirmed these results and provided definite evidence for $\nu_\mu \to \nu_\alpha$ oscillations [Fuk98a, Fuk98b]. In 2011, the following results for oscillation parameters were published in [Abe11]:

$$1.2 \cdot 10^{-3}\,\text{eV}^2 \leqslant |\Delta m^2_{23}| \leqslant 4 \cdot 10^{-3}\,\text{eV}^2 \qquad (90\,\%\ \text{C.L.}), \tag{2.44}$$
$$0.78 \leqslant \sin^2 2\theta_{23} \qquad (90\,\%\ \text{C.L.}). \tag{2.45}$$

In comparison to the solar neutrino mass splitting, this value is significantly higher. In this context it is important to note that the sign of Δm^2_{23} is still unknown.

Reactor neutrino oscillation

Nuclear fission reactors play a key role in experimental neutrino physics since they are the most intense man-made (anti)neutrino source on earth. Plutonium isotopes are bred during the "burning" process of uranium isotopes. The latter undergo a decay chain, which is specific for each isotop, $^{235}_{92}$U, $^{238}_{92}$U, $^{239}_{94}$Pu and $^{241}_{94}$Pu [Men11, Cha15]. Each fission produces $\sim 200\,\text{MeV}$ of energy and isotropically emittes neutrinos with energies below 10 MeV, resulting in a large number of $\sim 10^{20}$ $\overline{\nu}_e$ per second for one GW of thermal power. Reactor oscillation experiments only look for the disappearance channel of $\overline{\nu}_e$, due to the low energy scale, which is below the threshold to create μ- or τ-leptons. The detection principle of the reactor electron antineutrino is identical to "project poltergeist" from 1957, using a large-volume organic liquid scintillator as target.

One of the most important oscillation experiments is KamLAND in Japan, using a mean baseline of about 180 km to all Japanese nuclear reactors. This led to a precise measurement of the following parameters [Abe08]:

$$\Delta m^2_{12} = 7.58^{+0.14}_{-0.13}(\text{stat.})^{+0.15}_{-0.15}(\text{syst.}) \times 10^{-5}\,\text{eV}^2, \tag{2.46}$$
$$\tan^2\theta_{12} = 0.56^{+0.10}_{-0.07}. \tag{2.47}$$

Finally, in 2012, the third mixing angle θ_{13} was observed by the Daya Bay experiment, using a baseline of 1.7 km [An 12]. The results are in agreement with the RENO and DoubleChooz experiments [Ahn12, Abe12]. To minimize reactor-related systematic effects, all three experiments use a near detector ($L \sim 0.4\,\text{km}$) and a far detector ($L \sim 1 - 2\,\text{km}$). This principle allows to use the near detector to verify the predicted $\overline{\nu}_e$-flux to obtain a precise rate of the disappearance strength at the far detector [Dwy15].

In 2015 the Daya Bay collaboration puplished the following results [Hu 15, Col17]:

$$\sin^2(2\theta_{13}) = 0.084 \pm 0.005. \tag{2.48}$$

This is in good agreement with the independent $\overline{\nu}_e$ detection channel using signals based on neutrons captured on hydrogen [An 14]:

$$\sin^2(2\theta_{13}) = 0.083 \pm 0.018. \tag{2.49}$$

Accelerator neutrino oscillation

A man-made neutrino source with great promise to study neutrino oscillations in detail are particle accelerators. A ν_μ-neutrino beam on the GeV-scale produced by irradiating a fixed target (e.g. graphite or aluminium) with high energetic protons [Zub11]. The aim is to produce pions and focus them with a so-called magnetic horn. A well-focused neutrino beam results from the decay of these poins inside a decay tunnel. A shield at the end of the tunnel stops all particles except neutrinos, producing a pure beam of ν_μ or $\overline{\nu}_\mu$. Oscillation experiments use the disappearance channel of ν_μ to study $\nu_\mu \rightarrow \nu_\tau$. A near detector, typically located directly behind the shield, detects the undistorted energy spectrum, the overall neutrino flux and its radial profile. Using a long baseline (250 km up to 730 km) between the neutrino source and the main detector is key to measure θ_{13} and the CP violating phase δ in the appearance channel $\nu_\mu \rightarrow \nu_e$. Simultaneously, the disappearance channel $\nu_\mu \rightarrow \nu_\mu$ is sensitive on Δm^2_{23} and θ_{23} [Zub11]. Important results have been achieved by the T2K experiment, which uses Super-Kamiokande as far detector [Ahn06]:

$$\Delta m^2_{32} = (2.51 \pm 0.10) \times 10^{-3}\,\mathrm{eV}^2, \tag{2.50}$$

$$\sin^2\theta_{23} = 0.514^{+0.055}_{-0.056}, \tag{2.51}$$

at 68 % C.L. for normal mass ordering [Abe15], which confirms previous results from other accelerator experiments like MINOS or OPERA [Ada13]. As already mentioned, by using a ν_μ-beam and an $\overline{\nu}_\mu$-beam allows to measure the CP-violating phase δ. The T2K experiment has published a value of [Abe15]:

$$\delta = [0.15, 0.83]\pi \qquad \text{(normal mass hirarchy)}, \tag{2.52}$$

$$\delta = [-0.08, 1.09]\pi \qquad \text{(inverted mass hirarchy)}. \tag{2.53}$$

This will be further scrutinized by the acceleration oscillation experiment NOνA, with a baseline of 810 km, which aims to resolve θ_{13} and δ, and furthermore the mass hierarchy of neutrinos. For detailed information see some of the latest puplications [Ada17, Ada16a, Ada16b].

2.4 Determination of the neutrino mass

The previously discussed discovery of neutrino oscillations has provided evidence that neutrinos are massive particles. However, the technique of neutrino oscillations does not allow to study the absolute neutrino mass scale. To determine this, two different methods, a direct and an indirect method, are used. The direct method is based on the kinematics of β-decays (see section 2.4.4), while the indirect method uses specific theoretical assumptions on rare decays or the imprint of cosmological neutrinos. Both methods are outlined in the following.

2.4.1 Cosmological approach

The very early universe is successfully described by the "Big Bang" model, which describes many thermal processes in the then hot dense state. Since that time the univers expands and simultaneously cools down [Per09]. Observations have demonstrated that its structure is isotropic and homogeneous on large scales [Zub11]. Quantum fluctuations in the early universe were amplified during the proposed inflationary stage of the universe. Subsequently, gravitational overdensities from density inhomogeneities evolved into galaxy clusters that exist in the present [Per09]. During this early time of the universe neutrinos being produced in thermal processes were relativistic and free streaming. Accordingly, they damped gravitational clustering on small scales. The strength of the damping depends on the total neutrino density [Per09], which is proportional to:

$$m_{\mathrm{tot}} = \sum_i m_i. \tag{2.54}$$

An example of the influence of different neutrino masses on the structure formation in the early universe is presented in figure 2.6. These relic neutrinos, however, have not been detected until now. Due to their large number of $339\,\mathrm{cm}^{-3}$ they have to be taken into account for the overall matter and energy content of the universe [Les12].

The Friedmann equations, which connect the energy contributions of radiation, matter and dark energy to the expansion of the universe can be used in the standard cosmological model, the so-called "ΛCDM" model, to investigate the impact of matter and energy on cosmic evolution. In the case of an Euclidean geometry, the critical energy density is given by [Zub11]

$$\varrho_{\mathrm{crit.}} = \frac{3 \cdot H_0^2}{\pi G}, \tag{2.55}$$

with the gravitational constant G, and the Hubble constant H_0, first measured by E. Hubble 1929 [Hub29]. The density parameters

$$\Omega_{\mathrm{x}} = \frac{\varrho_{\mathrm{x}}}{\varrho_{\mathrm{crit.}}}, \tag{2.56}$$

are given by the critical energy density $\varrho_{\mathrm{crit.}}$ and energy densities ϱ_{x} of each contributor x. Neutrinos contribute to this as so-called hot dark matter. This comes from their characteristics, in particular their relativistic free-streaming after decoupling from thermal equilibrium in the early universe [Per09]. In the ΛCDM model, neutrino mass eigenstates m_i are linked to the energy density Ω_ν of the relic neutrinos by:

$$\sum_i m_i = \Omega_\nu \cdot 93h^2\,\mathrm{eV}, \tag{2.57}$$

where h is the dimensionless Hubble parameter. By assuming a flat and neutrino dominated universe, and by using the Hubble parameter $h = 0.678 \pm 0.009$ [Ade16], a very conservative upper limit on the sum of all neutrino masses can be estimated of:

$$\sum_i m_i \lesssim 42.75 \pm 0.01\,\mathrm{eV}. \tag{2.58}$$

A much more stringent limit on neutrino masses was published in 2015 by the Planck collaboration, in the form of a model–dependent upper limit of the sum of all neutrino masses:

$$\sum_i m_i \leq 0.23\,\mathrm{eV} \qquad (95\,\%\ \mathrm{C.L.}). \tag{2.59}$$

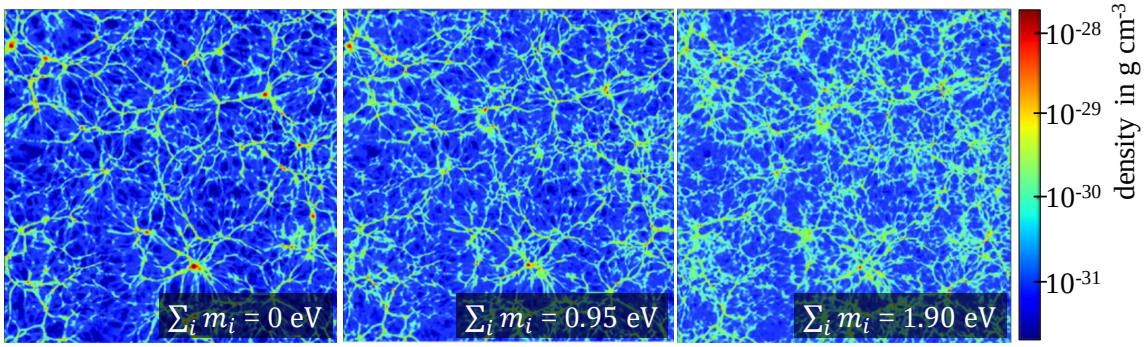

Figure 2.6: The effect of massive neutrinos on the baryon density distribution in the universe. As it is shown, the massive neutrinos smear out the small scale structures. The figure is adapted from [Aga11].

This limit includes the latest Planck data, as well as the results of investigations of baryon acoustic oscillations, supernova-light curve analysis from SNLS, results of the SDSS supernova sky survey and several other shift supernova data [Beu11, Bet14a]. The model to obtain this upper limit is thus based on a large variety of parameters in the ΛCDM model, some of which have only been measured in a model-dependent way yet. At present, neutrino masses are an input parameter to cosmological models. A direct and model-independent measurement of neutrino masses would thus supplement cosmological models.

2.4.2 Time-of-flight method using supernova neutrinos

A core-collapse supernova of type II, Ib or Ic occurs, when the stellar core collapses under its own gravitational force as the core cannot produce any further energy by fusion processes. Neutrinos produced by thermal processes with energies in the MeV range carry away about 99 % of the released gravitational energy. The mass of neutrinos can then be determined by measuring their time-of-flight [Zub11]:

$$T = \frac{L}{v} \approx L \cdot \left(1 + \frac{m_\nu^2}{2E_\nu^2}\right). \tag{2.60}$$

To determine m_ν, one has to determine the spread of arrival times for neutrinos with different energies E_1, E_2. The observed temporal delay Δt then depends on the time difference Δt_0 between their emission time t_1 and t_2. Hence the delay is given by:

$$\Delta t = t_2 - t_1 = \Delta t_0 + \frac{m_\nu^2}{2} \cdot \left(\frac{1}{E_{\nu,2}^2} - \frac{1}{E_{\nu,2}^1}\right). \tag{2.61}$$

Supernova neutrino detectors can measure the parameters Δt, $E_{\nu,1}^2$ and $E_{\nu,2}^2$, while other astrophysical observations provide the distance L. Since the neutrino pulse is model-dependent, however this leads to significant uncertainties on the neutrino mass m_ν [Fis10].

In 1987 the famous supernova SN1987A was observed by water-based Cherenkov detectors [Bio87, Hir88]. Within 13 seconds two experiments, Kamiokande and IBM, counted a total of 19 neutrinos. This was the first direct observation of supernova neutrinos and the beginning of the neutrino astronomy. The corresponding result on the antineutrino mass is an upper limit of:

$$m_{\overline{\nu}_e} \leq 5.7\,\text{eV} \qquad (95\,\%\ \text{C.L.}), \tag{2.62}$$

and up to date still represents the first and last observed galactic neutrino burst [Lor02].

2.4.3 Double β-decay

In the case of a double beta decay, two protons of one nucleus are simultaneously transformed into two neutrons, or vice versa:

$$ {}^{\mathrm{A}}_{\mathrm{Z}}\mathrm{X} \rightarrow {}^{\mathrm{A}}_{\mathrm{Z+2}}\mathrm{Y} + \mathrm{e}^- + \mathrm{e}^- + \overline{\nu}_\mathrm{e} + \overline{\nu}_\mathrm{e}, \tag{2.63} $$

$$ {}^{\mathrm{A}}_{\mathrm{Z}}\mathrm{X} \rightarrow {}^{\mathrm{A}}_{\mathrm{Z-2}}\mathrm{Y} + \mathrm{e}^+ + \mathrm{e}^+ + \nu_\mathrm{e} + \nu_\mathrm{e}. \tag{2.64} $$

This process occurs if single β-decay is energetically forbidden according to the Bethe-Weizsäcker equation [Wei35]. The long half-lifes time of about $\sim 10^{20}$ years [Zub11], results from the fact that ββ-decay is a second order process of weak interactions. In 1935, this process was postulated first [Goe35]. The first observation of double β-decay was achieved in 1969 by a geochemical experiment using the decay of ^{82}Se into ^{82}Kr [Kir69].

Postulating that neutrinos could be their own antiparticles in 1937, E. Majorana proposed a second type of double β-decay process, with the distinction of being neutrino-less due to the exchange of a virtual Majorana-like neutrino [Maj37, Rac37, Fur39]. In this process two neutrons can transform into two protons and vice versa:

$$ {}^{\mathrm{A}}_{\mathrm{Z}}\mathrm{X} \rightarrow {}^{\mathrm{A}}_{\mathrm{Z+2}}\mathrm{Y} + \mathrm{e}^- + \mathrm{e}^-, \tag{2.65} $$

$$ {}^{\mathrm{A}}_{\mathrm{Z}}\mathrm{X} \rightarrow {}^{\mathrm{A}}_{\mathrm{Z-2}}\mathrm{Y} + \mathrm{e}^+ + \mathrm{e}^+. \tag{2.66} $$

This processes violates lepton number conservation by two units and is thus forbidden in the SM of particle physics. An observation of this rare decay would indicate physics beyond the SM. As neutrino-less double β-decay is characterized by two electrons carrying away all decay energy, it manifests as a tiny peak at the decay endpoint of the β-spectrum. By investigating such a peak, the effective Majorana mass is measured:

$$ \langle m_{\beta\beta} \rangle^2 = \left| \sum_i U_{ei}^2 m_i \right|^2 = \left| \sum_i |U_{ei}|^2 e^{i\alpha_i} m_i \right|^2 , \tag{2.67} $$

where α_i are CP violating Majorana phases.

This can lead to a cancellation of the coherent sum, so that

$$ \langle m_{\beta\beta} \rangle^2 < m_k. \tag{2.68} $$

A variety of neutrino-less double β-decay experiments like GERDA [Ack13], EXO [Alb14] or KamLAND-Zen [Asa16] determiend half-lifes of specific even-even isotopes, typical limit is given by [Ago13]:

$$ t_{1/2}^{0\nu} > 2.1 \times 10^{25}\,\mathrm{y} \qquad (90\,\%\ \mathrm{C.L.}). \tag{2.69} $$

The effective mass can be obtained via:

$$ \langle m_{\beta\beta} \rangle^2 = \left(t_{1/2}^{0\nu} \cdot G^{0\nu}(E_0, Z) \cdot \left| M_{\mathrm{GT}}^{0\nu} - \frac{g_\mathrm{V}^2}{g_\mathrm{A}^2} M_\mathrm{F}^{0\nu} \right|^2 \right)^{-1} . \tag{2.70} $$

Since the nuclear matrix element $M_{\mathrm{GT}}^{0\nu}$ in equation 2.70 depends on the theoretical nuclear model, the determined half-life in 2.69 corresponds to a upper limit of :

$$ m_{\beta\beta} < (0.2 - 0.4)\,\mathrm{eV}, \tag{2.71} $$

for the effective mass of Majorana neutrinos.

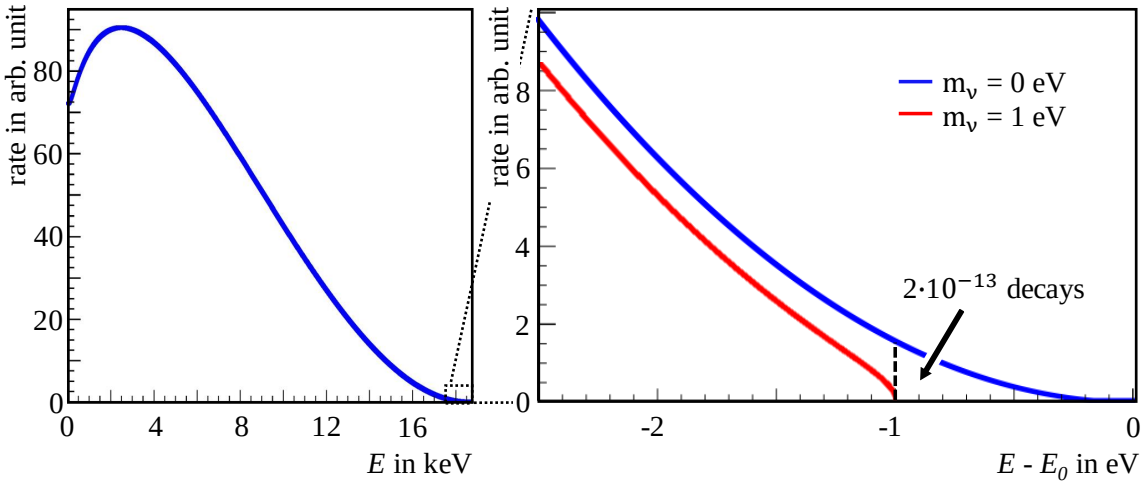

Figure 2.7: The tritium β-spectrum. The left figure shows the entire β-spectrum. The influence of a neutrino mass of about 1 eV on the spectrum shape near the endpoint E_0 of the spectrum is presented in the right figure.

2.4.4 Single β-decay

The most straightforward and unique way prominent principle to determine neutrino masses independent of further assumptions is the investigation of single β-decay. This principle only relies on the kinematics of three body decay reactions such as

$$\mathrm{n} \quad \rightarrow \quad \mathrm{p} + \mathrm{e}^- + \overline{\nu}_\mathrm{e}, \tag{2.72}$$

exploiting energy and momentum conservation. The theoretical description of this decay reaction is given by Fermi's golden rule (see equation 2.5). A precise spectroscopy of the kinetic energy of β-electrons allows to determine the effective mass of the electron antineutrino as a non-vanishing mass has a tiny influence on the shape of the energy spectrum. A visualization of the influence of a neutrino with a mass of 1 eV on the spectrum of the tritium β-decay is presented in figure 2.7. The differential rate of the electron energy spectrum is described by equation 2.6, including the observable of interest: the squared mass of the electron antineutrino m_ν^2. Although it is a superposition of three neutrino mass eigenstates:

$$m_\nu^2 = \sum_{i=1}^{3} |U_{ei}|^2 m_i^2, \tag{2.73}$$

and the incoherent weighted sum causes a fine structure at the endpoint of the energy spectrum, the effect is much smaller than the energy resolution of the current experiment. For this reason, the current experiments observe the effective mass of the electron antineutrino. In the following, different measurement techniques are presented to obtain a precise measurement of the β-spectrum.

Bolometer experiments

Cryogenic bolometers, similar to those often used for investigation of neutrino-less double β-decay, represent a well-known technique for investigations of single β-decay. In such a calorimeter setup the β-source and detector are combined. Hence, the entire decay energy is released into the detector. Such a setup minimizes systematic effects from energy losses of the signal particles on their way from the source to the detector.

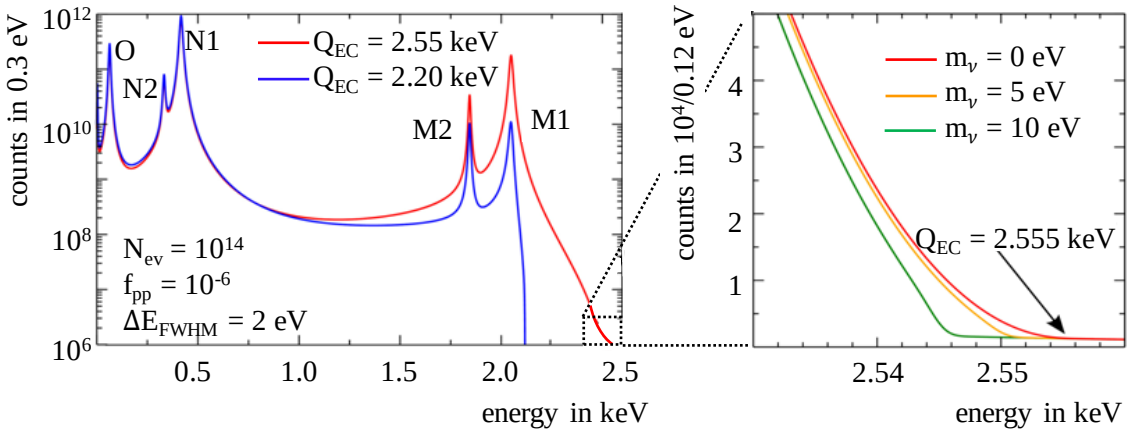

Figure 2.8: The energy spectrum of the ^{163}Ho electron capture. The figure on the left side shows the entire energy spectrum of the ^{163}Ho electron capture. The influence of different neurino masses on the shape of the energy spectrum near the endpoint, is presented in the right figure. The figure is adapted from [Tel15].

With a low endpoint energy of Q = 2.67 keV, rhenium ^{187}Re was long considered to be a favorable isotope, despite its long half-life of $t_{1/2} = 4.3 \times 10^{10}$ y. To reach a high source activity, a large amount of ^{187}Re is required. The MILANO experiment made use of about $2.5 - 3.0\,\mu$g of $AgReO_4$ crystals, allocated in an array of 10 micro-calorimeters. In 2004 an upper limit on the electron antineutrino mass of

$$m_{\bar{\nu}_e} < 15\,\text{eV} \qquad (90\,\%\ \text{C.L.}), \tag{2.74}$$

was published [Sis04]. However, this β-emitter has been abandoned in favour of another isotope, ^{163}Ho, which decays by an EC process:

$$^{163}\text{Ho} + e^- \rightarrow {}^{163}\text{Dy}^* + \nu_e, \tag{2.75}$$

with the resulting ^{163}Dy* deexciting via the emission of electrons and radiation (see figure 2.8). Its half-life of $t_{1/2} \approx 4570$ y is relatively short in comparison to ^{187}Re. Another benefit is the low Q_{EC}-value of $2.858 \pm 0.010(\text{stat}) \pm 0.05(\text{syst})$ keV [Ran17].

The ECHo experiment is designed to measure the energy released in the deexcitation process as a small temperature increase, mediated by phonons. It is planned to measure the mass difference between ^{163}Ho and ^{163}Dy in a dedicated penning trap [Gas14]. The aim of ECHo is to eventually reach a sub-eV sensitivity with a large array of cryogenic bolometers.

Synchrotron radiation experiment

A new approch to measure the neutrino mass is in developement by the Project 8 collaboration [Asn15]. Here, tritium β-electrons are guided by a strong magnetic field to emit synchrotron radiation on the GHz scale. An antenna array measures the frequency of synchrotron radiation for energy measurement. A first demonstration of the measuring principle was performed by using ^{83m}Kr as a source of monoenergetic electrons, as shown in figure 2.9 [Asn15]. This technique has the potential to eventually reach sensitivities of $m_{\bar{\nu}_e} \lesssim 40$ meV by using an atomic tritium source in absence of systematics [Ash17].

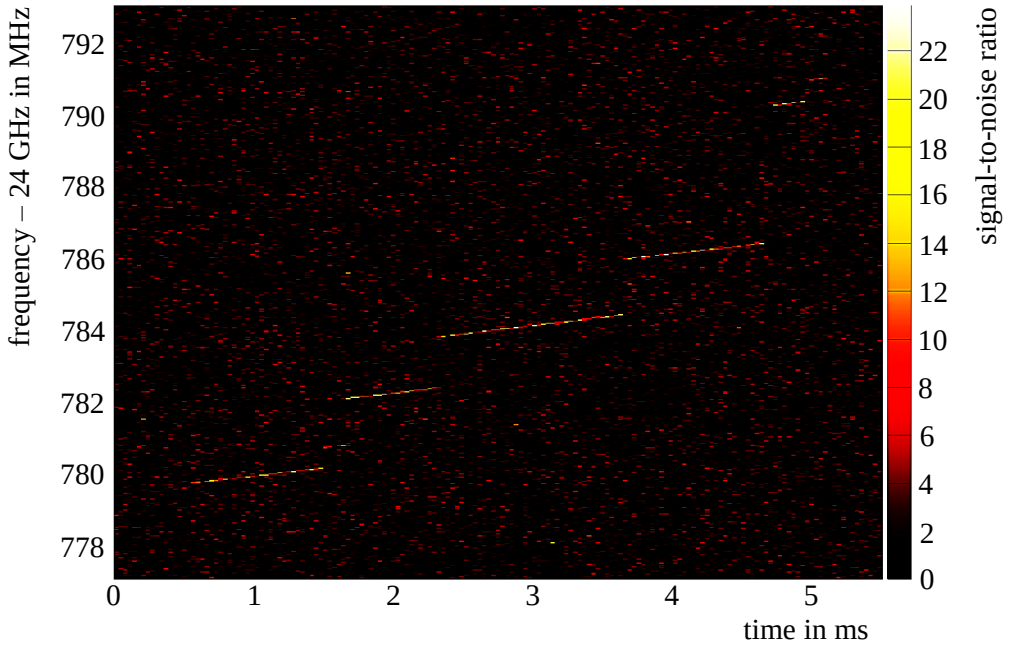

Figure 2.9: Electron cyclotron spectrum of the Project 8 collaboration. A typical signal from the decay of ^{83m}Kr characterized by an abrupt onset of narrow-band power over the thermal noise of the system. The measured frequency reflects the kinetic energy of the electron, in this case 30 keV. The frequency-time window shown represents only a portion of an extended event lasting more than 15 ms. The frequency increases slowly as the electron loses energy by emission of cyclotron radiation. RThe spectrum shows six or possibly seven frequency jumps before the electron is ejected from the trap. The jumps result from the energy loss and pitch-angle changes caused by collisions with the residual gas, predominantly hydrogen. The most probable size of the energy jump, as determined from many events, is 14 eV. The figure and the text is adapted from [Asn15, Ash17].

MAC-E filter experiments

The best model-independent neutrino mass limits have been achieved by the Magnetic Adiabatic Collimation with Electrostatic (MAC-E) filter technology. The most stringent results have been achieved by the Mainz [Bar98] and Troitsk [Lob85] experiments. The Mainz experiment mode use of a solid quenched tritium source, and achieved an upper limit of

$$m_{\overline{\nu}_e} < 2.3\,\text{eV} \qquad (95\,\%\ \text{C.L.}), \tag{2.76}$$

[Kra05]. The Troitsk experiment is based on a windowless source of molecular tritium, and has reported an upper limit of

$$m_{\overline{\nu}_e} < 2.05\,\text{eV} \qquad (95\,\%\ \text{C.L.}), \tag{2.77}$$

[Ase11]. The outcome of a combined analysis leads to a slightly more stringent upper limit of

$$m_{\overline{\nu}_e} < 2.0\,\text{eV} \qquad (95\,\%\ \text{C.L.}), \tag{2.78}$$

[Pat16]. This result is currently the most sensitive model-independent upper limit on neutrino masses. These experiments have, however, reached their intrinsic limit due to statistics and systematics.

2.5 Current generation of neutrino mass experiments

Reaching a sub-eV neutrino mass sensitivity is the target of the new generation of β-decay experiments, with the Karlsruhe Tritium Neutrino (KATRIN) Experiment leading the field. It is currently under construction and commissioning and will improve the current sensitivities by one order of magnitude. KATRIN is designed to reach a sensitivity of 200 meV (90 % C.L.) [Ang05]. Therefore, the source luminosity has to be increased by a factor of 100 while at the same time decreasing the systematic uncertainties by two orders of magnitude in comparison to the Mainz and Troitsk experiments. To do so, KATRIN will exploit the concept of a windowless gaseous tritium source, which was successfully used at the Troitsk experiment. The MAC-E filter principle will be used for precision β-spectroscopy, a well-known technique to investigate the endpoint region of tritium β-decay at 18.6 keV. In the following chapter, the MAC-E filter principle is discussed in detail with focus on the KATRIN experiment.

CHAPTER 3

Determination of the neutrino mass with KATRIN

This chapter will detail the working principle and main components of the Karlsruhe Tritium Neutrino (KATRIN) experiment which is currently under construction at KIT [Ang05, Dre13]. It is designed to investigate the shape of the electron spectrum of tritium β-decay with unprecedented precision, resulting in a measurement of the effective electron antineutrino mass with a sensitivity of $m_{\overline{\nu}_e} = 200\,\mathrm{meV}$ at 90 % C.L.. The discovery potential for $m_{\overline{\nu}_e} = 350\,\mathrm{meV}$ at $5\,\sigma$ is reached after five years of operation. Pushing forward into the sub-eV level, and exceeding the sensitivity of previous direct neutrino mass experiments by a factor of 10, KATRIN represents the leading next-generation neutrino mass experiment. In brief, KATRIN relies on the combination of a high-luminosity Windowless Gaseous Tritium Source (WGTS) and a high-resolution spectrometer, based on the Magnetic Adiabatic Collimation combined with an Electrostatic (MAC-E) filter technologies.

The measurement principle as well as fundamentals of precision tritium β-spectroscopy are outlined in section 3.1. The ensemble of components forming the 70-m long KATRIN beamline, is presented in section 3.2. The single units are outlined in-depth together with its specific task. Each unit is designed at the extreme limit of technological feasibility, to operate at a precision level well above previous efforts to guarantee a reliable neutrino mass measurement.

The magnetic flux tube characterization is the main part of this thesis. Therefore, the principle of β-electron guiding as well as specific properties of the magnetic flux tube are explained in section 3.2.7. The unrivaled neutrino mass sensitivity of KATRIN evidently is limited by systematic and statistic uncertainties, which then are outlined in section 3.3. Since the magnetic flux tube is used to guide β-electrons, a collision-free alignment is key to achieve the required small systematics by avoiding energy losses. The statistic performance as well as details of the sweeping process are explained in section 3.3.1. As a main part of systematic uncertainties are source-related, these are presented in section 3.3.2. Here, the source stability with focus on the source temperature is discussed in great detail. Finally, this chapter summarizes the objectives of this thesis in section 3.4.

3.1 Principle of precise β-spectroscopy with a MAC-E filter

The MAC-E filter principle is leading technique to determine the absolute neutrino mass scale in a direct and model-independent way at present [Wei99, Ang05, Thu11, Dre13]. Since only a minute fraction 2×10^{-13} of all decays fall into the last 1-eV region of the β-spectrum, a high-luminosity tritium source is needed together with a high-precision MAC-E filter to achieve the desired sensitivity of $m_{\overline{\nu}_e} = 200\,\mathrm{meV}$. These two main components are outlined in the following.

3.1.1 Concept of a high luminosity gaseous tritium source

Previous neutrino mass experiments based on tritium sources have corroberated the fact that tritium (^{3}H) is the ideal β-emitter for a direct and model independent neutrino mass determination [Ott08, Dre13]. Here, the endpoint region of the β-spectrum of tritium was investigated using precision β-spectroscopy. Since ^{3}H is an unstable isotope of hydrogen, it decays via the weak interaction process into a daughter nucleus (^{3}He$^+$), an β-electron and the particles of interest, the electron antineutrino $\overline{\nu}_e$:

$$^3\mathrm{H} \rightarrow {}^3\mathrm{He}^+ + \mathrm{e}^- + \overline{\nu}_e. \tag{3.1}$$

Several unique characteristics of tritium β-decay provide key advantage in view of high resolution MAC-E filter read-out:

- **low endpoint energy:** Tritium has the second lowest endpoint energy of $E_0 \approx 18.6\,\mathrm{keV}$, after ^{187}Re [Nag06]. This leads to a rather large event rate close to E_0 in comparision to other β-emitters. In combination with the well-established concept of a MAC-E filter the low retarding voltage allows to investigate the tritium β-spectrum endpoint region [Bea80, Kru83].
- **short half-life:** With a half-life of $\tau_{1/2} = (12.32 \pm 0.02)$ years [Luc00], small amounts of gaseous tritium can be used to create a high-luminosity source. This is necessary in view of the tiny fraction of 2×10^{-13} decays contributing to the 1-eV endpoint region. Additionally, the amount of source material is minimized, reducing the probability of inelastic scattering processes for β-electrons at 18.6 keV.
- **super-allowed decay:** The nuclear matrix element of the transition is energy-independent, since the mother ^{3}H, and the daughter ^{3}He, are mirror nuclei. Thus, the spectrum is completely determined by the available phase space. Additionally, the matrix element is rather large $|M|^2 = 5.55$, close to the free neutron decay [Rob88, Dre13].
- **atomic shell structure:** The atomic shell structures of the daughter ^{3}He and the mother necleus ^{3}H are rather simple due to the low nuclear charge. Consequently, this minimizes required corrections caused by inelastic scattering prozesses or excited electron final states in case that a gaseous tritium source is used [Bel03]. This allows to calculate electronic exitations and their propabilites [Dos06, Dos08]. Further, the Fermi function allows to quantify interactions between daughter nucleus and emitted β-electrons.
- **recoil correction:** The daughter nucleus experiences a recoil of $E_{\mathrm{rec}} = 1.72\,\mathrm{eV}$, the variation in the electron region-of-interest of about 30 eV below E_0 results in a variation of to $\Delta E_{\mathrm{rec}} = 3.5\,\mathrm{meV}$. This leads to a quasi fixed enpoint energy [Mas07].
- **gaseous phase:** Solid state effects have not to be considered in a gaseous tritium source, on condition that it remains fully gaseous at temperatures of 30 K without formation of clusters.

In the temperature regime of 30 K, the tritium source is based on molecular tritium (T_2), implying the more complex decay reaction:

$$T_2 \rightarrow (^3HeT)^+ + e^- + \overline{\nu}_e. \tag{3.2}$$

Accordingly, molecular effects such as excitation, rotation or vibration have to be taken in account for final states as these effects lead to a systematic uncertainty in the neutrino mass analysis.

The design of a high-luminosity gaseous tritium source has to fulfill several tasks. Foremost, a source activity of $\sim 10^{11}$ β-electrons per second with a stability of 0.1 % is required. For this activity, and aspired tritium gas purity of 95 %, an effective source column density of 5×10^{17} molecules/cm^2 results. Higher column densities would lead to increased scattering processes and more frequent energy losses of signal electrons and an increase of systematic effects. This results in a delicate trade-off between improving systematic effects and increasing the statistics.

The maximum acceptance angle $\theta_{max} = 50.8°$ in combination with the detector efficiency results in an expected signal rate in the endpoint region, ranging from a few counts per second (cps) to a few mcps [Ang05, Dre13].

3.1.2 Measurement principle of the MAC-E filter

After the first implementation as a high-resolution method for electron energy analysis by Beamson, Porter and Turner [Bea80], the MAC-E filter principle was advanced further by the work of Kruit and Read [Kru83]. This method for analyzing electron energies was finally adapted for the neutrino experiments at Mainz [Pic92] and Troitsk [Lob85]. The MAC-E filter principle combines high energy resolution with a very large angular acceptance. This allows to investigate the tiny distortion at the endpoint of the tritium β-spectrum caused by the non-vanishing neutrino mass. Simultaneously, it uses a large fraction of the source luminosity.

Magnetic adiabatic collimation

The MAC-E filter principle makes use of a large retarding spectrometer, formed by an evacuated large-volume vessel, which is located between two superconducting solenoids. An axially symmetric magnetic field guides signal electrons from the source on the upstream side of the spectrometer to the detector, where they are counted, as displayed in figure 3.1. The isotropically emitted electrons have an individual starting angle θ_{textS} with respect to the direction of the guiding magnetic field line. Due to the starting angle, and the Lorentz force, the electrons are propagated through the spectrometer on spiral-shaped cyclotron trajectories. Hence, the kinetic energy is a composition of longitudinal component $E_\parallel$ and a transversal component $E_\perp$ which can be described as:

$$E_{kin} = E_\parallel + E_\perp. \tag{3.3}$$

Since the superconducting solenoids are localized at the two ends of the spectrometer, the magnetic field in between decreases by several orders of magnitude, reaching the minimum at the so-called analyzing plane located mid-point. The superconducting solenoids generate a magnetic field which guides the electrons adiabatically through the spectrometer, so that an invariant can be used to discuss the motion:

$$\gamma \cdot \mu = \frac{\gamma + 1}{2} \cdot \frac{E_\perp}{B} = \text{const.} \tag{3.4}$$

with the relativistic Lorentz factor γ and the orbital magnetic moment μ of the electron. The adiabatic invariant of the motion is the magnetic moment $\gamma = 1.04$, which can be approximated to 1, so that:

$$\mu = \frac{E_\perp}{B} = \text{const.}. \tag{3.5}$$

The decrease of the magnetic field B thus causes a reduction of the transversal energy component $E_\perp$, according to equations 3.4 and 3.5, so that to keep the adiabatic invariant of the electron constant. Hence, adiabaticity of this process is only guaranteed in case that the gradient of the magnetic field is sufficiently small. From the conservation of kinetic energy, the decrease of the transversal energy component $E_\perp$ leads to an increase of the longitudinal component $E_\parallel$ according to equation 3.3. Consequentially, the magnetic field gradient causes an energy transformation $E_\perp \rightarrow E_\parallel$. This process is completely reversible, and re-transforms the almost parallel beam of electrons with $E_\parallel \gg E_\perp$ on the way from the analyzing plane to the detector side via $E_\parallel \rightarrow E_\perp$, as shown in figure 3.1. Since the minimum magnetic field at the analyzing plane is non-zero, a small fraction of the kinetic energy remains in the transversal component. This fraction can not be analyzed and limits the "energy resolution" (or better filter width) of the MAC-E filter:

$$\Delta E = \frac{B_{\text{min}}}{B_{\text{max}}} \cdot E_{\text{kin}}. \tag{3.6}$$

Electrostatic filtering

The MAC-E filter principle is based on applying a retarding potential U_0 to perform precision energy analysis of β-electrons. A careful field design guarantees that the spectrometer connected to negative potential is characterized by an electric field parallel to the magnetic field lines. Only electrons with a sufficiently large longitudinal energy $E_\parallel > |qU_0|$ can overcome this potential barrier $|qU_0|$ at the analyzing plane. Electrons with a longitudinal energy $E_\parallel < |qU_0|$ are reflected by the electrostatic potential back to the upstream direction. As mentioned above, magnetic adiabatic collimation ensures that the kinetic energy is almost completely transformed into longitudinal energy $E_\parallel$ at the analyzing plane, which is highly important, since only electrons with an longitudinal energy greater than the retarding voltage can pass this barrier, as seen in figure 3.1. After passing the analyzing plane, the electrons are reaccelerated by the decreasing potential and are finally counted at the detector. By repeatedly varying the retarding potential, the β-electron energy spectrum is scanned in an integral way.

Magnetic-mirror effect

The magnetic adiabatic collimation has one drawback in the form of the magnetic mirror effect. Thereby, background or scattering signal electrons at the center can be reflected when traveling from the weak into the strong magnetic field. The KATRIN setup is designed so that the maximum magnetic field does not occur at the source B_{S}, but at the downstream part of the spectrometer ($B_{\text{S}} < B_{\text{max}}$). This implies that signal electrons at larger angles are reflected at this magnetic mirror, as their longitudinal energy component has been completely transformed into transverse energy $E_\parallel \rightarrow E_\perp$ ($E_\parallel = 0$ and $E_\perp = E_{\text{kin}}$). If the starting angle θ_{S} of a β-electrons in the source is greater than the maximum acceptance angle

$$\theta_{\text{max}} = \arcsin\left(\sqrt{\frac{B_{\text{S}}}{B_{\text{max}}}}\right), \tag{3.7}$$

this electron will be reflected. A large starting angle also implies a longer trajectory through the experimental setup. Thus, the probability of energy losses as a result of scattering processes and emission of synchrotron radiation is increased. To limit the maximum

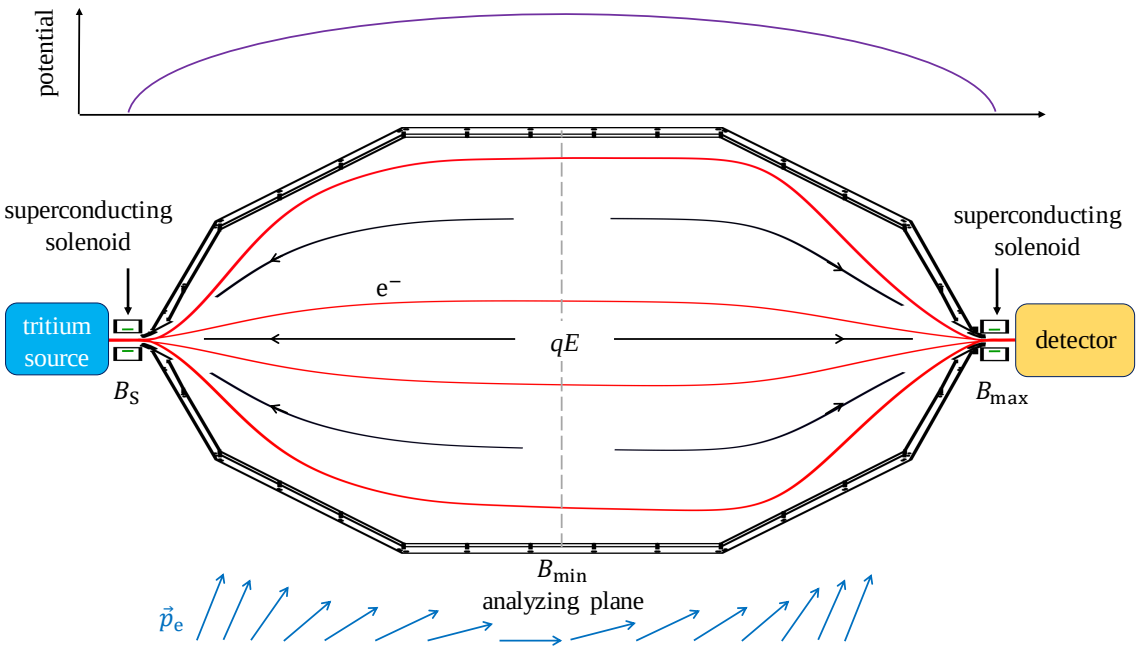

Figure 3.1: Principle of the MAC-E filter technology. The sketch shows the signal electrons, isotropically emitted in the tritium source, which are guided by the magnetic field (red) through the spectrometer. Two superconducting solenoids, one on each side of the spectrometer, provide this magnetic field. The momentum of the electrons is transformed adiabatic towards the analyzing plan, shown in the lower part of the figure. In the center of the spectrometer, where the magnetic field reaches the minimum, the momentum of the electrons is parallel to the magnetic field direction. The electric field, shown as the retarding potential on the top of the figure, acts as a high-pass filter. Thereby, signal electrons with lower energies as the retarding potential are reflected back to the source. The signal electrons which can pass the analyzing plane, are accelerated afterwards by leaving the electric field. Finally these electrons are counted at the detector.

acceptance angle consequently has the benefit of suppressing less-favorable trajectories for precision β-spectroscopy [Hig07, Hig08]. The magnetic mirrors on both side of the spectrometer most importantly traps background electrons which are generated inside the spectrometer. More information about background processes and its composition can be found in [Sch14, Har15]. In addition, effects such as scattering processes of signal electrons with residual gas molecules can change the energy or angle of the electron. To increase the possibility for a store electron to leave the spectrometer in upstream direction, the pinch magnet is operated at the highest magnetic field in the setup.

3.2 Technical setup of the KATRIN beamline

In view of implementing a high-luminosity gaseous tritium source, the source components of KATRIN are located inside the Tritium Laboratory Karlsruhe (TLK). It is the only laboratory which offers the infrastructure as well as the handling and process technologies and the license to operate the gaseous tritium source of KATRIN [Pen00, Sch13a]. Therefore, and due to safety reasons, all tritium containing parts of the setup are located at the TLK. In 2016 the entire beamline was assembled, and the first global superconducting solenoid and vacuum commission of the beamline was realized.

The commissioning measurements of the beamline as well as of single STS (source and transport section) components are the main objective of this thesis and are outlined in the following chapters. A detailed description of each KATRIN section, with focus on their unique tasks, is outlined in the following parts, starting with a general overview of the global KATRIN setup.

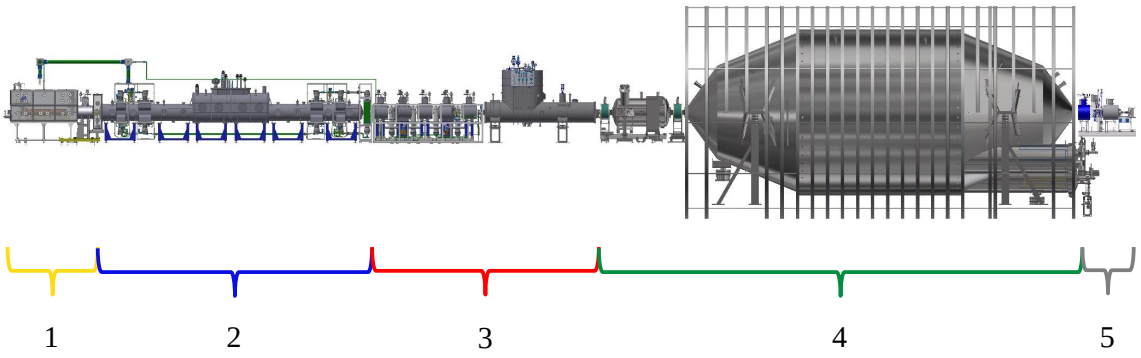

Figure 3.2: Setup of the KATRIN experiment. The rear section (1) forms the upstream end of the experiment followed by the 16-m long WGTS cryostat which includes the gaseous tritium source (2). The transport section (3) consisting of the DPS and the CPS is used to guide the signal electrons from the source to the spectrometer section (4). Simultaneously the transport section reduces the tritium gas flow by 14 orders of magnitude between the source section and the spectrometer section to prevent a tritium introduced background. Finally, the signal electrons which passed the spectrometer potential are counted by the detector wafer of the FPD (5).

3.2.1 Overview

A unique feature of the 70-m long KATRIN beamline is the windowless combination of a gaseous tritium source with a high resolution spectrometer system of very large size, which allows precision analysis of the kinetic energy of signal electrons. To achieve the required statistics, high purity tritium gas is injected with a rate of 1.853 mbar ℓ/s into the central part of the windowless gaseous tritium source (WGTS). The coaxial beamline is surrounded by a system of 24 superconducting solenoids to create a strong magnetic field to guide signal electrons from the source to the detector. A major challenge is to reduce the tritium gas rate between injectionat the source and the spectrometer to prevent tritium-induced background there, without disturbing the kinetic energy of the electrons. This task is being fulfilled by the transport section, located between the WGTS and the spectrometers, reducing the tritium gas flow by more than 14 orders of magnitude. The source and transport section (STS) is the tritium-containing part of the whole setup, which is followed by the tritium-free spectrometer and detector section (SDS). The latter consists of two MAC-E filters and the focal plane detector (FPD). The pre-spectrometer (PS) is used as a pre-filter close to E_0 at 18.3 keV, reducing the flux of low-energy electrons into the main spectrometer (MS). There, high-precision analysis of the kinetic energy of signal electrons is implemented to investigate the shape of the tritium β-spectrum . Signal electrons which pass the spectrometer system are counted at FPD system in a Si-detector array. This system provides the end of the beamline in downstream direction. The opposite end of the beamline, in upstream direction, is formed by the rear section (RS). This system allows to monitor the source activity and to perform regular calibrations.

3.2.2 Windowless gaseous tritium source (WGTS) cryostat

The windowless gaseous tritium source is formed by the 10-m long stainless steel beam tube, the so-called source tube with radius of 45 mm. To restrict energy losses of tritium β-electrons to scattering processes of source gas molecules only, the source tube is windowless on both sides. Molecular tritium gas is injected in the center of the source tube through a set of capillaries. An inlet pressure of about 3×10^{-3} mbar results in an injection rate of 5×10^{19} tritium molecules per second. The source tube is located between the two differential pumping sections WGTS-R on the upstream side and WGTS-F

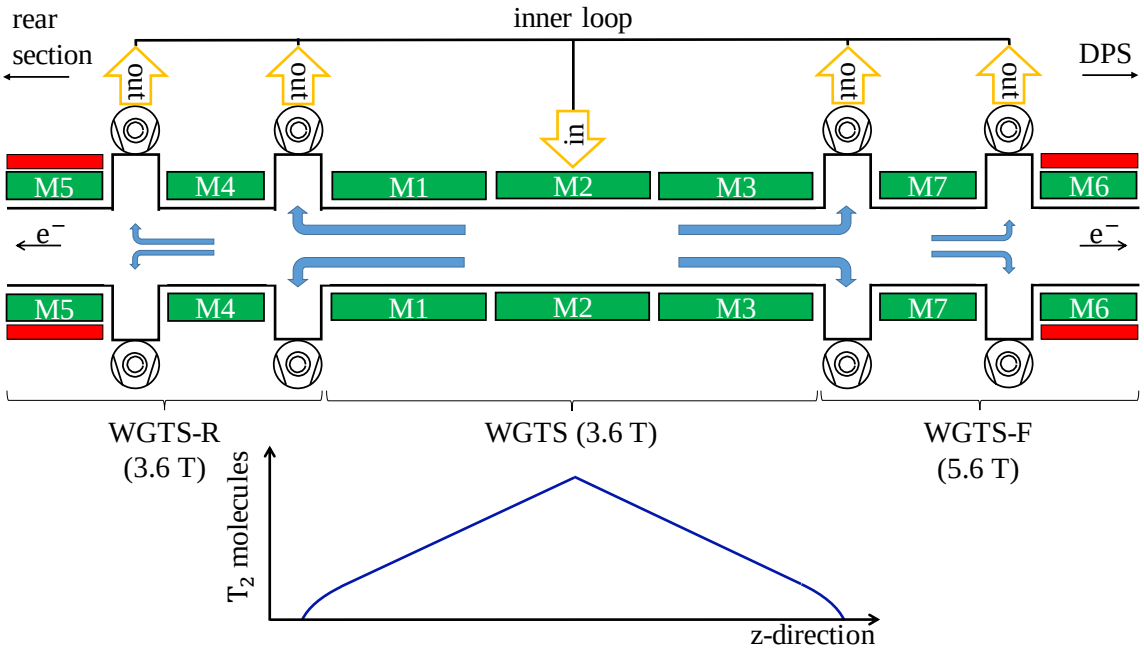

Figure 3.3: Sketch of the WGTS beamline and the source density profile. The upper part of the figure shows a sketch of the WGTS beamline surrounded by the superconducting solenoid system M1 - M7 (green) and a simplified representation of the inner loop system. Both ends of the WGTS beamline include a system of vertical and horizontal superconducting dipoles (red). This dipole system can be used to align the magnetic flux tube inside the beamline. The 10-m long source tube contains the WGTS. The density profile of this source is simplified presented in the lower part of the figure.

on the downstream side. Each consists of six turbo molecular pumps (TMPs). They reduce the tritium gas flow into the adjacent systems, the DPS and RS, as displayed in figure 3.3. A closed inner loop system collects the processed gas after the pumping sections. There, a permeator separates the small fraction of impurities. To obtain a constant tritium gas amount with the required tritium purity of $\epsilon_T > 95\,\%$ in the inner loop cycle, it is feeded batch-wise with high-purity tritium from the TLK infrastructure [Ang05, Stu10, Bab12]. To monitor the isotopic composition of the gas before re-injection into the source tube, a so-called LARA setup is used, based on Laser-Raman spectroscopy [Fis11, Sch11, Sch13a, Sch13c, Sch13b, Fis14, Sch15]. This inner loop system is designed to achieve the required column density of $\rho d = 5 \times 10^{17}$ molecules/cm^2, corresponding to a source activity of $\sim 10^{11}$ decays per second [Ang05, Bab12]. To minimize systematic effects on the neutrino mass, a source stability of 0.1 % is required [Ang05]. The following parameters have to be stabilized on this level: gas purity, inlet-pressure, pumping performance of the TMPs, and source tube temperature stability and homogeneity. A key feature of the source tube is its two-phase neon (argon) cooling system mounted on the outer side of the tube in beam direction. It is designed to cool the source tube and operate it at a temperature of 30 K (100 K) with the required stability of 0.1 % [Ang05, Bab12]. This temperature regime was identified, as it minimizes distortions of the β-spectrum due to thermal Doppler-broadening. Also, it reduces the tritium gas flow and hence the tritium throughput. More information about systematic effects in this system is presented in section 3.3.2.

The source tube is surrounded by three superconducting solenoids operated at 3.6 T, as well as the WGTS-R solenoids to generate a magnetic field to guide the β-electrons adiabatically, see figure 3.3. To prevent collisions of the electron flux in downstream direction the WGTS-F solenoids are operated at 5.6 T, compressing the diameter of the magnetic

flux tube. A vertical and horizontal superconducting dipole magnet system, placeded around the outermost solenoids M5 on the rear side and M6 on the front side, is used to adjust the magnetic flux tube to avoid collisions with the beamline, as detailed in figure 3.3. The kinetic energy of signal electrons can be influenced by plasma-related phenomena, as well as by collisions between the β-electrons and beamline elements. To prevent these effect, and to compensate possible misalignment of the magnetic flux tube inside the global KATRIN beamline, only the inner part of the gaseous tritium source with a radius of 41 mm is used for the neutrino mass analysis. Accordingly, the source cross section of $\sim 53\,\mathrm{cm}^2$ and the magnetic field of 3.6 T, generate a magnetic flux tube of $191\,\mathrm{Tcm}^2$, relevant to the neutrino mass analysis.

The windowless gaseous tritium source (WGTS) cryostat was assembled at *RI GmbH*[1] at Bergisch Gladbach and delivered to KIT on September 10$^{\mathrm{th}}$ 2015. Since then the cryostat has been commissioned, the works therein form a significant part of this thesis and are outlined in section 4.1.

3.2.3 Rear section

The rear section is the concluding component of the KATRIN beamline in upstream direction, behind the WGTS-R, with the rear wall chamber. A gold-coated disc, the so-called rear wall (RW) with an almost uniform work function is located inside this chamber, which for tritium condition, defines the source potential. It also provides a wide electron beam generated by illumination with a strong UV light source. This low-energy electrons are required to maintain quasi-neutrality of the plasma potential of the source [Bab12, Bab14, Sch16, Kuc16]. Additionally, a customized beta-induced X-ray spectrometer (BIXS) monitors in-situ the tritium activity of the WGTS on the 0.1 % level [Bab12, Roe13, Bab14, Roe15]. The column density of the gaseous tritium source is measured in regular intervals via inelastic scattering, via angular-resolved electron gun (EGUN) [Bab12, Bab14]. Before starting the regular KATRIN neutrino mass measurements, the EGUN system is used to determine and optimize the magnetic flux tube alignment of the beamline. First measurements of the magnetic flux tube alignment by using a comparable and a very broad electron beam constitute a major part of this thesis and are outlined in chapter 7. An other key task of the EGUN during the start-up of the KATRIN neutrino mass measurement will be to determine the energy-loss function and the inelastic scattering cross section of 18.6-keV signal electrons [Gro15].

3.2.4 Transport section

The transport section features two essential design cornerstones: the first one is to guide β-electrons collision-free and adiabatically up to the SDS elements, and the second one is to reduce the tritium gas flow up to the SDS part by more than 14 orders of magnitude [Ang05, Kos12, Jan15]. This reduction factor is required, since tritium-induced background within the spectrometer system has to be prevented with respect to the reference background rate of 10^{-2} cps. This leads to a maximum allowed tritium gas flow of about $10^{-14}\,\mathrm{mbar}\,\ell/\mathrm{s}$ at the entry of the SDS [Ang05]. As demonstrated by equation 3.2, tritium molecules are left in an ionized state after β-decay. Due to their charge (T^+, $T_3{}^+$) they are guided by the magnetic field like signal electrons. Another essential task of the transport section is thus to block these ionized tritium molecules from reaching the SDS part of KATRIN, since these would generate background in the spectrometer by collisions.

[1] RI Research Instruments GmbH, Friedrich-Ebert-Strasse 75, 51429 Bergisch Gladbach, Germany

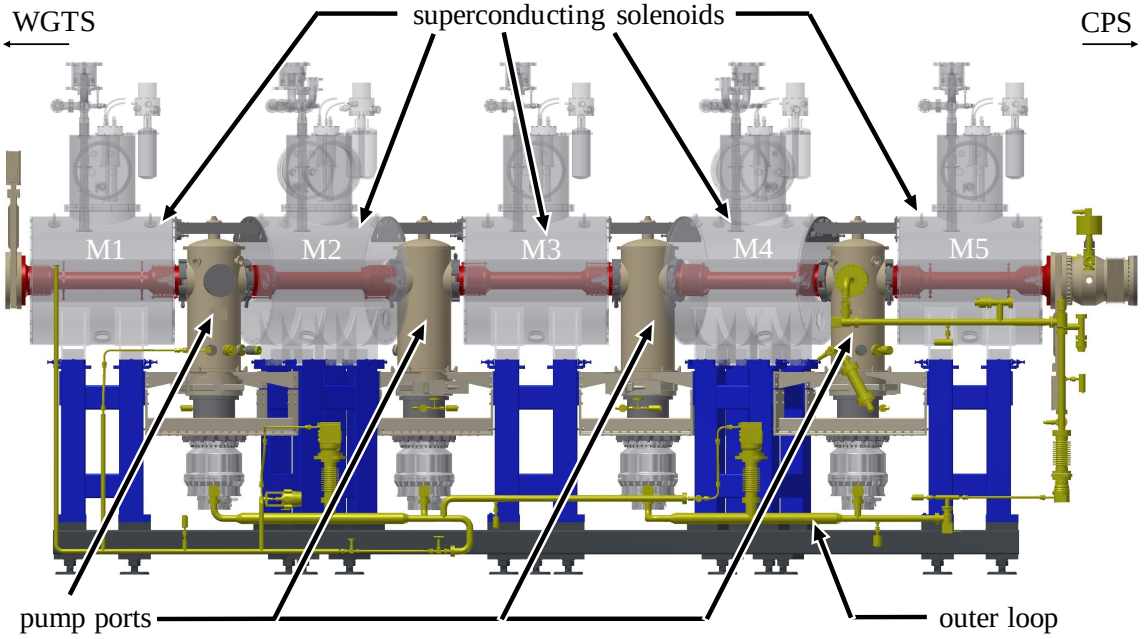

Figure 3.4: The differential pumping section of the KATRIN experiment. The figure shows a CAD drawing of the DPS. The modular superconducting solenoid system is highlighted in a transparent grey. Therefore, it is possible to see the single beam tubes (red) inside the warm bore of each magnet. The beam tubes are connected via the pump ports (brown) to the entire DPS beamline. Four TMPs (silver) are located at the lower part of the pump ports. A part of the loop system (yellow) is connecting the gas outlet of all TMPs to guide the collected process gas back to the TLK infrastructure.

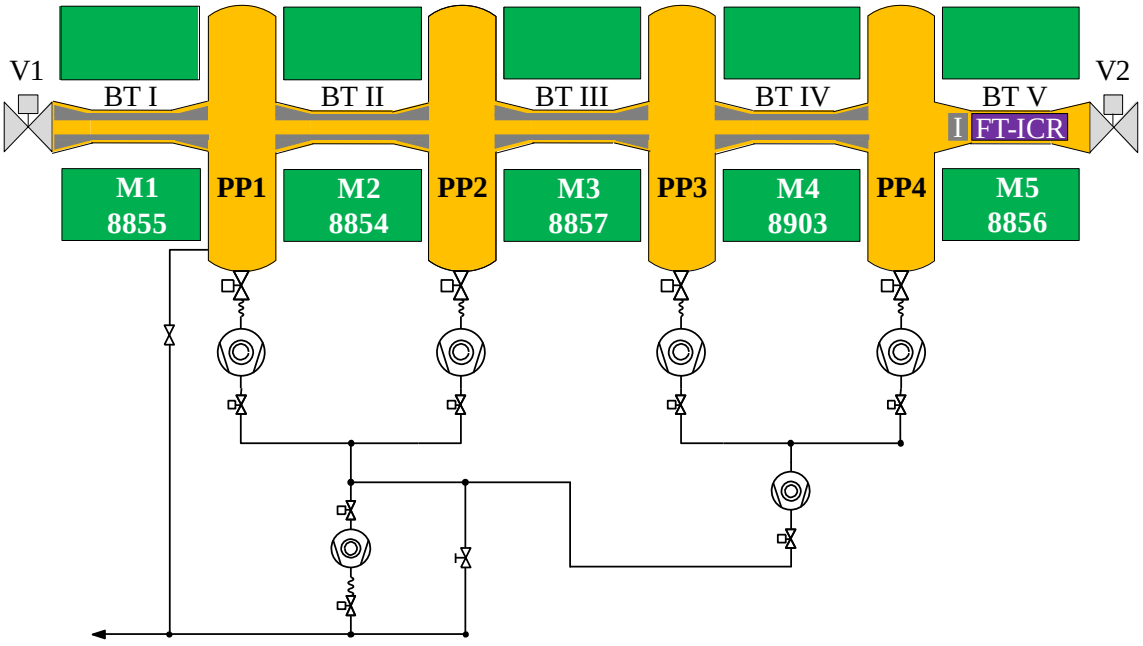

Figure 3.5: Beamline instrumentation and pumping concept of the DPS. The beamline of the DPS is highlighted in yellow and can be separated to WGTS by the beamline valve (V1) and to the CPS by the beamline valve (V2). The beamline includes four dipole electrodes consisting of two half-shells with conically ends (grey) implemented in beam tubes 1 – 4 (BT I – IV). Beam tube five (BT V) includes a ring electrode in upstream direction to block the ions. An FT-ICR device is implemented to measure the ion flux composition. The DPS loop system with the TMPs is arranged in a quasi cascade configuration.

The first part of the transport section is found by the WGTS-F, being integrated into the WGTS cryostat, as detailed in 3.2.2. Two large components form the main part of the transport section after the WGTS cryostat, the differential pumping section (DPS), and the cryogenic pumping section (CPS). The DPS reduces the tritium gas flow with TMP by five orders of magnitude down to 10^{-7} mbar ℓ/s at the entry of the CPS. A total of five superconducting solenoids (M1 – M5) creates the required magnetic guiding field of up to 5.0 T inside the DPS beamline. It consists of five beam tubes located in the warm bore of each solenoid, attached to each other via four pump ports. One TMP is located at each pump port at the bottom, see figure 3.4. The extra pump port 0 is located at the beamline connection between the WGTS and DPS units, and pump port 5 at the beamline connection between DPS and CPS, shown in figure 3.4. Since the pumping efficiency of TMPs decreases at very low gas flows, an other pumping technique has to be used after the DPS to reduce the tritium gas flow even more. To achieve the required gas flow reduction factor, the CPS traps the remaining tritiated molecules by cryosorption. Therefore, the CPS beam tube elements 2 – 5 are cooled down to 3 K, see figure 3.6. The gold coated inner surface of the beam tubes has to be prepared with a thin layer of argon frost to increase the effective sorption surface, as well as to increase the sticking coefficient, resulting in an enhanced pumping efficiency. Seven superconducting solenoids (M1 – M7) are surrounding the CPS beamline, providing magnetic guiding fields up to 5.6 T. The beamline of the DPS as well as the beamline of the CPS include Ω-shaped chicanes, which are formed by beam tube elements arranged in a tilt of 20° in the DPS, and of 15° in the CPS, see figure 3.4 and 3.6. This shape prevents the so-called molecular beaming effect, which corresponds to a collimated gas flux directed strongly forward [Luk12]. Additionally, the pump efficiency is increased by this chicanes.

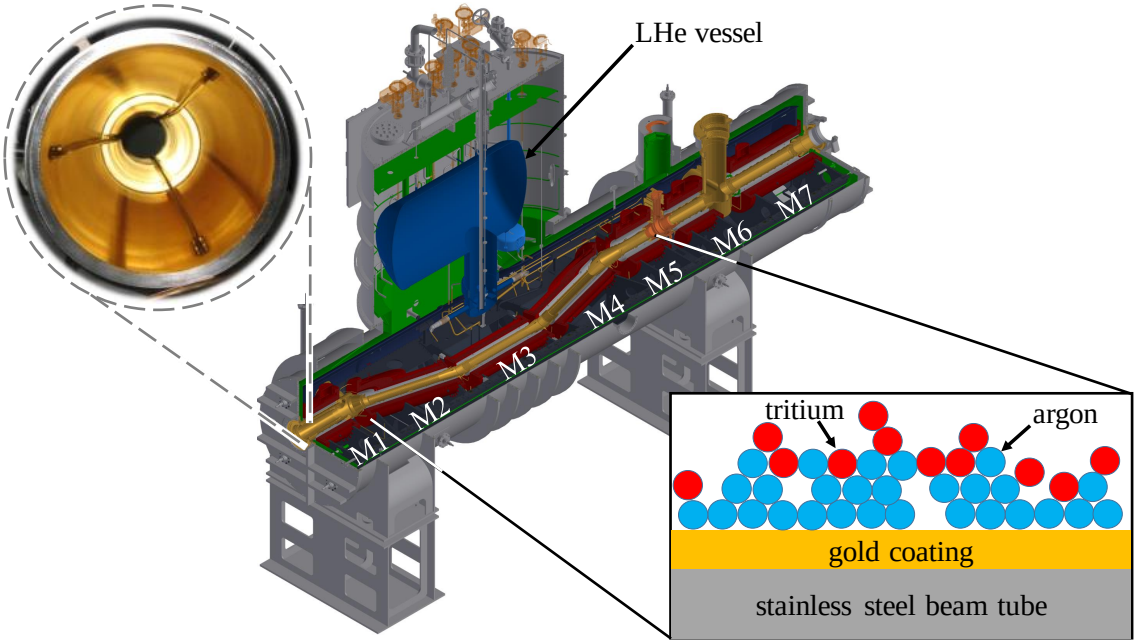

Figure 3.6: The cryogenic pumping section. The stainless steal beamline (yellow) of the CPS is gold coated. A picture of the inner surface of the beamline is presented on the top left part of the figure. The beamline is surrounded by seven superconducting solenoids (red) cooled down with liquid helium. The beam tubes 2 – 5, which are surrounded by the solenoids M2 – M5 are operating as a clod trap. Shortly before each tritium run the gold coated surface is prepared with argon frost layer (light blue) to increase the surface of the cold trap, as shown in the sketch on the lower part pf the figure.

Due to their positive (or negative) charge, the ionized molecules generated in the gaseous tritium source are guided towards the detector. As ions cannot be pumped out by the DPS or the CPS the ions have to be prevented from reaching the SDS. This task is performed by two ring electrodes in the STS elements, located in the DPS beam tube 5 and pump port 5. To prevent an accumulation of ions due to trapping between the ring electrodes and the gas pressure at the gaseous tritium source, an ensemble of dipole electrodes in DPS beam tube elements 1 – 4 has to remove the ions. The generated electric field there is orthogonal to the magnetic field direction, resulting in an $\vec{E} \times \vec{B}$ force, which is orthogonal to the magnetic and electric field direction. The resulting force drifts the ions out of the magnetic flux tube were they collide with the stainless steel surface of the beamline to recombine. Afterwards, the neutralized molecules can be pumped out, as previously explained. Since the efficiency of charge removal depends on the charge-to-mass ratio, it is of great importance to measure the number densities and the different species of ions. Therefore, a diagnostic unit, the Fourier transform-ion cyclotron resonance (FT-ICR) device, is located in beam tube element 5 of the DPS. The commissioning of the transport section is outlined in chapter 4. For more detailed informations about technical setup and latest results of the DPS and the CPS see [Ang05, Kos12, Jan15, Hac15, Gla15, Sac15, Roe16, Sch17, Fri17].

3.2.5 Spectrometer section

One of the most challenging parts of the KATRIN experiment is to achieve high-resolution spectroscopy of the electrons close to the shape of the β-spectrum. To this end, two electrotsatic spectromteters are used as high-pass filters based on the MAC-E filter technology, oulined in section 3.1 [Ang05]. Since background in the spectrometers is of major concern to reach the aspired neutrino mass sensitivity, the β-decay induced background rate there has to be kept sufficiently low. This requires that the spectrometers are operated at very stringent ultra-high vacuum (UHV) conditions of about 10^{-11} mbar. This is of key importance to reduce the scattering probability of signal electrons with molecules of residual gas in the SDS.

Pre-spectrometer

The 3.4-m long vessel of the pre-spectrometer (PS) is placed between two superconducting solenoids, pre-spectrometer solenoid 1 (PS1) and pre-spectrometer solenoid 2 (PS2). Both are operated at a nominal value of 4.5 T, resulting in minimal magnetic field of the PS at its center equivalent to an energy resolution of 70 eV at 18.6 keV [Ang05].

Low-energy electrons have a very large cross section for scattering processes with residual gas molecules, therefore the pre-spectrometer acting as a pre filter is very important. When operated at 18.3 keV, it will minimize the signal electron flux into the main spectrometer by seven orders of magnitude. If the PS would be operated at even higher potentials, there is a non-negligible risk that the beta electrons near the endpoint will be influenced by the pre-spectrometer, for instance through non-optimized transmission conditions such as early retardation. When the PS is operated at high potential, this results in a strong Penning trap between the pre- and main spectrometer. Latest results indicate however that the Penning trap has no significant impact on the background in the MS due to excellent UHV conditions in the SDS. For lower pressure, sophisticated measures (wipers) have to be taken into action to mitigate background from this trap [Pra12].

The pre-spectromter was the first component of the KATRIN beamline which was manufactured and commissioned [Hab09, Fra10, Pra11, Mer12, Wan13, Goe14]. Between 2006 and 2011, a large number of sophisticated investigations of electron transport and background processes in a MAC-E high-pass filter were performed. The design of the main

spectrometer was significantly influenced by these investigations. In 2016, the full integration of the system into the KATRIN beamline was achieved successfully. This thesis will provide first results of the magnetic flux tube alignment between the pre-spectrometer and the FPD.

Main spectrometer

With a diameter of 10.0 m and a length of 23.3 m, the main spectrometer has pushed the technical feasibility of UHV vessels to the limit, and it is thus the final step in up-sizing the MAC-E filter spectrometer technology. It is located between two superconducting solenoids, the PS2 magnet and the 6-T pinch magnet. The analyzing plane inside the main spectrometer is located at a minimum magnetic field of typically 3.0 G (~ 0.3 mT). According to equation 3.6, this is equivalent to an energy resolution (or better filter width) of $\Delta E = 0.93$ eV at 18.6 keV. A low field coil system (LFCS), which consists of 15 normal-conductive coils which surround the main spectrometer in an axially symmetric fashion, is required to fine-shape the magnetic flux tube. Additionally, an earth magnetic field compensation system (EMCS) consisting of 16 vertical and 10 horizontal cosine-coils required to compensate the earth magnetic field is implemented [Glu13]. During a standard tritium run, the spectrometer is operated at a high negative potential. A two-layer wire electrode system next to the inner surface of the spectrometer vessel is used to fine-shape this electric potential. In addition to the dominant magnetic shielding, this electrode system creates an electrostatic shield for low-energy electrons which originate from the inner surface of the vessel [Hug08, Val09, Zac09, Hug10, Val10, Lei14]. To scan the shape of the β-electron energy spectrum, the retarding potential is varied in an interval between 50 eV below the endpoint and 5 eV above the endpoint region of the β-spectrum at 18.6 keV [Kle14].

In 2013, the first commissioning and measurement campaign (SDS-I) of the main spectrometer in combination with the FPD system was successfully performed [Sch14, Lei14, Gro15]. A second measurement campaign (SDS-II) was performed in 2014 and 2015 with the focus on hardware improvements and more in-depth to investigations of the complex background characeristics at the MS [Har15, Lin15, Erh16, Kra16, Mue16]. The observed background rate at present is about fifty times higher than the design value [Har15]. Despite this high background, it is possible to reach a neutrino mass sensitivity of 240 meV [Fra17]. This sensitivity can be achieved by an optimized measurement time distribution, and a higher magnetic field in the analyzing plane to reduce the size of the flux tube (and background processes) there, taking into account that this results in a reduction of the energy resolution. The statistics and the measurement time distribution are explained in section 3.3.1.

3.2.6 Detector section

The focal plane detector (FPD) section forms the counterpart to the rear section, defining the downstream end of the KATRIN beamline. Signal electrons, which have passed the retarding potential of the main spectrometer, are guided by the magnetic flux tube through the FPD section. Two superconducting solenoids, a pinch magnet at the exit of the main spectrometer, and a 3.6-T strong detector magnet, together create the magnetic guiding field as shown in figure 3.7 [Sch14]. A silicon PIN-diode array with high efficiency ($\epsilon_{\mathrm{det}} \geq 90\,\%$) and a nearly background-free detector environment allow to count signal electrons [Ang05]. The entire monolithic silicon wafer has a diameter of 12.5 cm, while the sensitive area of this wafer has a diameter of 9.0 cm and is segmented into 148 pixels of equal area [Sch14]. Each pixel is separated by 50 µm thick boundaries, resulting in a specified resistance between pixels of 1 GΩ [Sch14]. The magnetic field at the position

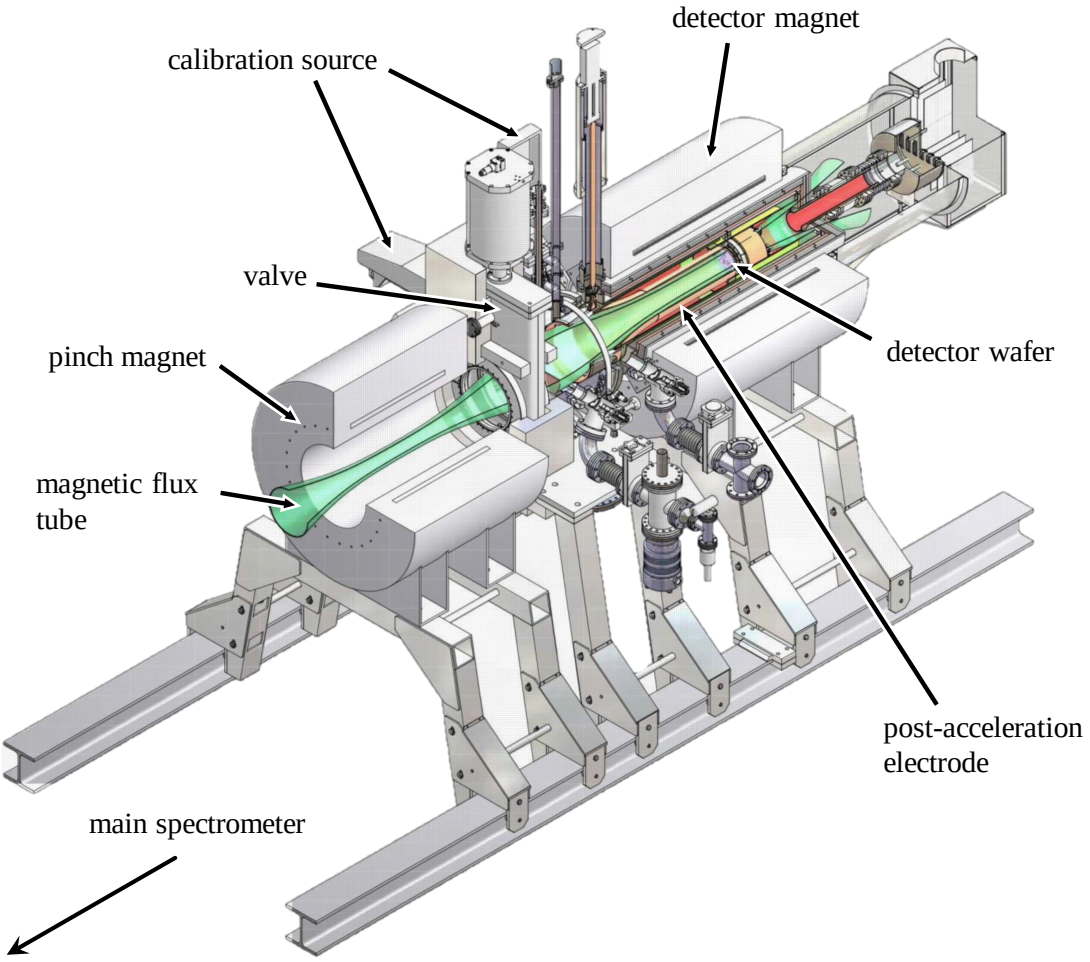

Figure 3.7: The focal plane detector section. The magnetic flux tube (green) is generated by the pinch and detector magnet and is guiding the signal electrons, which have passed the main spectrometer, to the detector wafer. To calibrate the detector system two calibration sources are mounted downstream of a valve, which is used to separate the detector from the main spectrometer for such a measurement. A much better signal to background ratio is expected for higher electron energies, therefore the signal electrons are accelerated by the post-acceleration electrode.

of the wafer is about 3.3 T, since the wafer is displaced about 140 mm in downstream direction with respect to the coil center of the detector magnet [Har15]. This field in combination with the sensitive area of the wafer results in a detectable 210 Tcm^2 magnetic flux tube. Since the 191 Tcm^2 magnetic flux tube is used for the neutrino mass analysis, the remaining outer rim of the 210 Tcm^2 magnetic flux tube can be used to investigate background processes in the outer parts of the flux tube. The spatially resolved mapping of the 210 Tcm^2 magnetic flux tube is feasible due to the identical area (44.1 mm) of each pixel [Sch14]. More information about the magnetic flux tube is presented in section 3.2.7. In combination with the good time and energy resolution it is possible to map important parameters such as the homogeneity of the column density, or the plasma potential of the gaseous tritium source. To perform independent detector calibrations, two sources, an ^{241}Am source used as a γ emitter, as well as a photo-electron source, can be placed in front of the FPD. Upstream of the detector wafer a post-acceleration electrode shifts signal electrons to higher energies by > 10 keV. In this higher energy regime, a more favorable intrinsic background rate of the FPD is provided. Additionally, signal electrons reach an energy regime where the effect of back scattering at the detector wafer and noise

is reduced. The natural environment radiation at the wafer is reduced by a cylindrical lead-copper radiation shield, which surround all sensitive parts. This complemented by an active veto system to determine cosmic ray-induced background events. The radial segmentation of the wafer enables to investigate the radial pattern of background, as well as to determine different background sources in the spectrometer volume.

The commissioning of the detector system in combination with the main spectrometer was implemented during the measurement campaigns SDS-I, SDS-II, SDS-IIA and SDS-IIB, resulting in a detailed understandings of detector systematics, the intrinsic FPD background rate, radon-induced background in the main spectrometer, and the characterization of non radon-induced background, from Rydberg states, as outlined in [Sch14, Har15, Mue16, Fra17]. Since mid-2017 the FPD system has reached full operational readiness and is ready for the neutrino mass measurement.

3.2.7 Magnetic flux tube

Due to the radially-symmetrical geometry of the source tube and its surrounding solenoids, the generated guiding field for β-electrons can be characterized best via the value of the magnetic flux:

$$\phi = \int_A \vec{B} \cdot \mathrm{d}\vec{A}, \tag{3.8}$$

which is a conserved quantity. Since this magnetic flux is constant over the entire beamline, it can be visualized as tube with a magnetic field-dependent radius. Accordingly, a reduction of the magnetic field $|\vec{B}|$ increases the radius of the flux tube cross section $|\vec{A}|$. At nominal magnetic field settings, the wafer of the FPD is located in a magnetic field of 3.3 T. Accordingly, the magnetic flux tube of 191 Tcm^2 projects an image of the source on the detector with radius of ~ 4.3 cm. Using the magnetic field of the source $B_\mathrm{S} = 3.6$ Tcm^2, the radius of the flux tube decreases to ~ 4.1 cm. This magnetic flux tube carries the relevant rate of signal electrons to be used in the neutrino mass analysis [Ang05, Dre13]. Additionally, the radius of the magnetic flux tube in the source part is less than the size of the source tube $r_\mathrm{S} = 4.5$ cm, to suppress the detection of β-electrons which were influenced by plasma related surface effects, or by small angle scattering processes with source tube surfaces. Moreover, electrons originating from the beamline surface can stem from radioactivity, cosmic muons or field emission. Due to their energies they are not able to reach this inner magnetic flux tube as the Lorentz force bends these electrons back to their origin. Due to the radially homogeneous distribution of source density, β-electrons are also generated in the outer ring shaped area encompassing the inner 191 Tcm^2. With a source tube radius of 4.5 cm and a magnetic field of 3.6 T the biggest electron-guiding magnetic flux tube has the size of about 230 Tcm^2, according to equation 3.8. The outer shape of the sensitive wafer pixel pattern has a radius of 4.5 cm at a magnetic field of 3.3 T, resulting in a detectable magnetic flux tube size of 210 Tcm^2, as outlined above. The ring-shaped structure which is formed by the 210 Tcm^2 section around the 191 Tcm^2 magnetic flux tube, is thus not used for the neutrino mass analysis, creating a buffer zone to account for small misalignments between beamline and superconducting solenoids, see figure 3.8. The effect of a potential collision of electrons traveling in the inner magnetic flux tube and the beamline is presented in section 3.3.2.3. Additionally, this ring shaped magnetic flux tube is used by the FBM to monitor the source activity. The outermost ring shaped structure between the 230 Tcm^2 and the 210 Tcm^2 magnetic flux tube is of no concern for KATRIN.

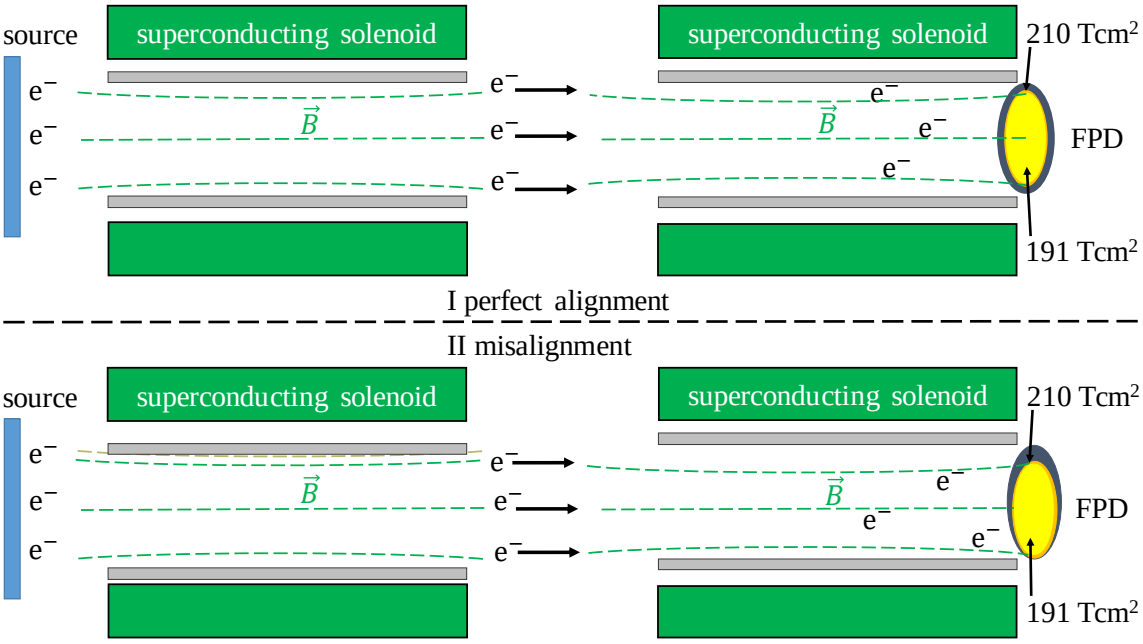

Figure 3.8: Magnetic flux tube alignment. The upper part of the figure shows a perfect aligned beamline and superconducting solenoid system with a centered detector. The 210 Tcm^2 magnetic flux tube forms an ring-shaped image around the 191 Tcm^2 magnetic flux tube. In the lower part of the figure a misalignment between the beam tube and the source solenoid is demonstrated. It is shown that the misalignment results in a shift of the mapped image on the detector. The outer shape of the 210 Tcm^2 magnetic flux tube can be used as a buffer area, in the case to compensate such an misalignment.

3.3 Neutrino mass sensitivity

The aspired neutrino mass sensitivity, as defined in the technical design report, represents an enormous challenge in many areas [Ang05]. In the scenario of a vanishing neutrino mass the sensitivity on the neutrino mass can be understood as the total uncertainty on $m^2_{\bar{\nu}_e}$, which is given by

$$\sigma_{\mathrm{tot}}(m^2_{\bar{\nu}_e}) = \sqrt{\left(\sigma_{\mathrm{stat}}(m^2_{\bar{\nu}_e})\right)^2 + \left(\sigma_{\mathrm{sys}}(m^2_{\bar{\nu}_e})\right)^2}, \tag{3.9}$$

i.e. the quadratically combined statistic $\sigma_{\mathrm{stat}}(m^2_{\bar{\nu}_e})$ and systematic uncertainties $\sigma_{\mathrm{sys}}(m^2_{\bar{\nu}_e})$. The latter includes contributions from a variety of experimental parameters, and by theoretical uncertainties in the description of the spectrum, as explained in section 3.3.2. At first, section 3.3.1 will discusses statistical uncertainties with respect to measurement intervals and background rates.

3.3.1 Statistic performance

Using the retarding potential to scan the endpoint region of the β-spectrum, the MAC-E filter measures an integral spectrum since all electrons with kinetic energies larger than the retarding potential are counted by the detector. Consequently, the expected count rate R_{ex} depends on the assumption of a constant background rate R_{bg}, the non-fluctuating retarding potential U_{i}, and the two unknowns, the endpoint of the β-spectrum E_0 and the squared neutrino mass $m^2_{\bar{\nu}_e}$. The expected count rate for a Poisson-distributed background rate is given by:

$$R_{\mathrm{ex}}(U_{\mathrm{i}}, C, R_{\mathrm{bg}}, E_0, m^2_{\bar{\nu}_e}) = R_{\mathrm{sign}}(U_{\mathrm{i}}, C, E_0, m^2_{\bar{\nu}_e}) + R_{\mathrm{bg}}. \tag{3.10}$$

The signal count rate R_{sign} depends on the number of tritium nuclei in the source:

$$N_{\mathrm{T}} = A_{\mathrm{S}} \cdot \rho \mathrm{d} \cdot 2 \cdot \epsilon_{\mathrm{T}}, \tag{3.11}$$

a proportionality constant C, the detector efficiency ϵ_{det} and the response function of the MAC-E filter:

$$R_{\mathrm{sign}}(U_{\mathrm{i}}, C, E_0, m^2_{\bar{\nu}_{\mathrm{e}}}) = C \cdot N_{\mathrm{T}} \cdot \epsilon_{\mathrm{det}} \cdot \frac{\Omega}{4\pi} \int_{qU_{\mathrm{i}}}^{E_0} \frac{\mathrm{d}^2 N}{\mathrm{d}E \mathrm{d}t}(E_0, m^2_{\bar{\nu}_{\mathrm{e}}}) \cdot R_{\mathrm{sign}}(E_0, qU_{\mathrm{i}}) \mathrm{d}E. \tag{3.12}$$

In the final neutrino mass analysis the free parameters C, R_{bg}, E_0 and $m^2_{\bar{\nu}_{\mathrm{e}}}$ have to be varied such that:

$$\chi^2(C, R_{\mathrm{bg}}, E_0, m^2_{\bar{\nu}_{\mathrm{e}}}) = \sum_i \left(\frac{R_{\mathrm{m}}(U_{\mathrm{i}}) - R_{\mathrm{ex}}(U_{\mathrm{i}}, C, R_{\mathrm{bg}}, E_0, m^2_{\bar{\nu}_{\mathrm{e}}})}{\frac{1}{t(U_{\mathrm{i}})} \cdot \sigma_{\mathrm{e}}(U_{\mathrm{i}}, C, R_{\mathrm{bg}}, E_0, m^2_{\bar{\nu}_{\mathrm{e}}})} \right), \tag{3.13}$$

is minimized. The statistical uncertainty:

$$\sigma_{\mathrm{e}}(U_{\mathrm{i}}) = \sqrt{t(U_{\mathrm{i}}) \cdot R_{\mathrm{e}}(U_{\mathrm{i}}, C, R_{\mathrm{bg}}, E_0, m^2_{\bar{\nu}_{\mathrm{e}}})}, \tag{3.14}$$

of each retarding potential then depends on the measurement time distribution and corresponds to the expected statistical uncertainty. Here, the measured time $t(U_{\mathrm{i}})$ is defined as the time spend at the specific retarding potential U_{i}. Previously, the measurement time was optimized based on the following parameters:

- **amplitude parameter**: The amplitude of the spectrum can be varied by the parameter C. The best handle on this parameter is achieved, when the low-energy tail of the β-spectrum is investigated over a longer measurement period.
- **background rate**: A total of six different retarding potentials above the endpoint E_0 of the β-spectrum allows to determine the background rate and judge that it is constant.
- **neutrino mass**: Since the best sensitivity on the neutrino mass is in a region of several eV below the endpoint, in the case that a background rate of 10 mcps is assumed, the largest fraction of measurement time will be focused on this region combined with small potential bin widths.
- **correlation**: In the spectrum region 14 eV below the endpoint, the correlation between the amplitude parameter and the endpoint energy can be determined most precisely. Therefore the second largest measurement time fraction will be located here.

A larger measurement interval slightly improves statistical uncertainties. Correspondingly, the systematic uncertainties will increase since processes involving energy losses rise significantly in intervals of a few tens of eV below E_0. Hence, there a trade-off between increasing statistics and minimizing systematics. With an optimized measurement time distribution for an expected background rate of 10 mcps, the statistical uncertainty is reduced to $\sigma_{\mathrm{stat}}(m^2_{\bar{\nu}_{\mathrm{e}}}) = 18 \times 10^{-3}\,\mathrm{eV}^2$ [Ang05].

Table 3.1: Systematic effects on the neutrino mass analysis. The table includes all known systematic effect which are highly important for the neutrino mass analysis. As it is shown, the largest proportion of systematics is origined by the source. The table is adoped from [Ang05].

source	projected accuracy	systematic shift $\sigma_{\mathrm{sys}}(m^2_{\overline{\nu}_e})$ $(10^{-3}\,\mathrm{eV}^2)$
final states	$f < 1.01$	< 6
T^--ion concentration	$n(T^-)/\ n(T_2) < 2 \times 10^{-8}$	< 0.1
energy loss function		< 6
source activity	$\Delta A_S/A_S < 2 \times 10^{-3}$	$< \frac{\sqrt{5} \cdot 5 \cdot 6}{10}$
source potential variations	$< 10\,\mathrm{meV}$	< 0.2
source magnetic field variation	$\Delta B_S/B_S < 2 \times 10^{-3}$	< 2
elastic scattering		< 5
background slope	$< 0.5\,\mathrm{mcps/keV}$	< 1.2
HV variations	$\Delta\mathrm{HV/HV} < 3 \times 10^{-6}$	< 5

3.3.2 Relevant systematic effects in the source and transport section (STS)

A large number of systematic uncertainties which have to be considered for the neutrino mass analysis are outlined in the KATRIN design report [Ang05]. An overview of sources of systematic uncertainties and their projected accuracy as well as corresponding systematic shifts for the ν-mass are outlined in table 3.1. Taken together these systematic uncertainties result in a total systematic uncertainty of:

$$\sigma_{\mathrm{sys,tot}} = \sqrt{\sum \sigma^2_{\mathrm{sys}}} \approx 0.01\,\mathrm{eV}^2. \tag{3.15}$$

Accordingly, all unaccounted-for systematic effects have to be limited to an overall uncertainty budget of:

$$\sigma_{\mathrm{sys,tot}} = \sqrt{\sum \sigma^2_{\mathrm{sys}}} \approx 0.017\,\mathrm{eV}^2. \tag{3.16}$$

Several parameters such as the source temperature have a direct impact on the source activity. Since the investigation of the source tube temperature stability and homogeneity was a major part of this thesis, the source activity and its impact are explained in the subsequent section.

3.3.2.1 Source stability

According to the design report a single neutrino mass measurement interval has the duration of one hour [Ang05]. During this time span the source activity has to be stabilized on the 0.1 % level. Several parameters can affect the source activity:

- **tritium gas purity:** The tritium gas contains trace amounts of other gases, mainly other hydrogen isotopologues. The gas composition is monitored continuously by the LARA system before injection into the source tube [Sch11, Fis11, Sch12, Sch13a, Sch13c, Sch13b, Fis14, Sch15]. To achieve the required source activity with the defined column density of $\rho d = 5 \times 10^{17}\,\mathrm{molecules/cm}^2$, a purity level of 95 % has to be reached with relative stability of 0.1 % [Ang05]. These requirements were met by previous R&D work simulating the KATRIN conditions [Fis11, Sch13a].
- **inlet pressure:** Since the column density has to be stabilized on a 0.1 %/h level, a comparable stability level is required for the inlet pressure. Again, this benchmark has been met in [Pri15].

- **pumping performance:** The pumping performance has an influence on the column density similar to the inlet pressure. Therefore, it has to be stabilized on a 0.1 %/h level. In the case of a constant gas load on the TMP type in use, the MAG W2800[2], the pumping performance is better than 0.1 %/h. Possible aging effects and resulting influences on the performance due to contact with tritium were be observed [Pri13].
- **source tube temperature:** The temperature stability and the homogeneity of the source tube influence the source activity as well, hence they also have to be stabilized at the 0.1 %/h level. Since the temperature is responsible for several other systematic effects, it is discussed in detail below.

3.3.2.2 Temperature stability and homogeneity of the WGTS beam tube

To met the necessary statistic budget of the experiment, the WGTS has to provide a source activity of about 1.7×10^{11} Bq, while stabilizing the activity on the 0.1 % level. Several parameters affecting the activity have to be stabilized on the same level as explained previously. One of the most critical parameters therein is the temperature of the source. A temperature of 30 K was chosen to minimize thermal Doppler-broadening due to the molecular motion. This leads to a specified temperature stability of $\Delta T/T = 1 \times 10^{-3}$/h and a homogeneity level of 30 mK . To achieve these specifications, the source tube is cooled by a two phase-neon cooling system, see figure 4.3. An outer helium cooling flow, which is operating at ~ 30 K, is used to cool the inner two phase-neon cooling cycle. The helium cycle is not suitedale for direct cooling, since its temperature fluctuations (± 1 K) are two orders of magnitude larger than the required temperature stability [Mar17]. The benefits of using a thermosyphon principle for two phase neon guarantees an exceptionally high degree of temperature stability, since an external temperature transfer shifts the ratio between the gaseous and the liquid phase, without changing the temperature. The commissioning of the WGTS cryostat and the first temperature stability and homogeneity results are presented in section 4.1.

3.3.2.3 Alignment of the magnetic flux tube

The knowledge about the alignment of the magnetic flux tube inside the beamline is of major importance, since collisions and the resulting scattering processes of signal electrons can resulting significant bias of the measurement result [Sim89, Him89, Sur91]. The effect of such an undetected collision was demonstrated in the eighties and nighties of the 20th century by two different experiments based on a solid detector and an external source. These measured a threshold anomaly due to scatted signal electrons between source and the detector. Since the collision remained undetected, it was published by assuming that the electron neutrino has two large mass components [Sim89, Him89, Sur91], a very light neutrino with a mass of 40 eV and a heavy neutrino with a mass of (16.9 ± 0.4) keV. New evidence for this heavy (sterile) neutrino with mixing probability given by $\sin^2(\theta) = 0.0084 \pm 0.0006 \pm 0.0005$ was published 1991 [Him91]. After using a virtually loss-free method for signal electron transport, the origin of the 17 keV neutrino mass signal was determined as an artifact caused by electrons scattering in a restricted geometry [Abe93, Him93]. Conclusively, new experiments rule out a 17 keV neutrino, demonstrating that the knowledge about the magnetic flux tube alignment is of paramount importance in view that an undiscovered collision, or even the slightest touch with the beamline, could cause a systematic effect for the neutrino mass result. If this systematic effect is not taken into account in the analysis chain it could lead to non-physical neutrino mass signals.

[2]Leybold GmbH, Bonner Strasse 498, 50968 Cologne, Germany

3.3.2.4 Consequences for the forward beam monitor (FBM)

Two monitoring systems are used during a regular runs to determine the WGTS source activity to monitor fluctuations of the activity on the per mille level. To this end, a beta-induced X-ray spectrometer (BIXS) is located at the rear wall chamber [Roe15, Bor17]. It consist of two X-ray detectors (silicon drift detectors SDD) to monitor the X-ray radiation caused by the $\sim 10^{11}$ β-electrons per second which implying on the rear wall. The feasibility of reaching a 0.1 % level for monitoring under comparable conditions could successfully be demonstrated [Bab12, Roe15, Bor17]. The second monitoring system is based on a silicon radiation detector, the so-called forward beam monitor (FBM). It is designed to measure the source activity in the downstream direction between the WGTS and the spectrometer. Therefore, it is located at the CPS pump port 2 [Ell17].

This two-fold method is important, since an asymmetric column density could lead to significant differences between the source activity measurements on the upstream and on the downstream side. Since signal electrons in downstream direction are used for the neutrino mass analysis, the source stability in this direction is highly important. The FBM is used to detect β-electrons directly in the flux tube. In order to prevent a shadowing of the 191 Tcm^2 magnetic flux tube, which guides β-electrons, it probes only the outermost rim of the 210 Tcm^2 magnetic flux tube. This part of the flux tube is not used for the analysis, as discussed in section 3.2.7. During a standard tritium run, the FBM is placed 61 – 67 mm away from the beam axis. Since the FBM has a circular active area of 1.3 mm, slightest collisions between the 210 Tcm^2 magnetic flux tube and the beamline could cause a shadow on the FBM. Consequently, a monitoring of the source activity in the downstream direction towards the main spectrometer would be impossible. Collisions between the magnetic flux tube and the beamline have to be identified and eliminated if possible.

3.4 Objectives of this work

To reach a neutrino mass sensitivity of 200 meV, KATRIN has to reach the required statistics and systematic error budget. One main objective of this thesis is thus to determine the transmission and the alignment of the 191 Tcm^2 magnetic flux tube, which guides signal electrons to the FPD. This information is important to verify that signal electrons can be guided collision-free. The information about constrictions and potential collisions between the magnetic flux tube and the beamline surface is vital to constrain systematics which could strongly influence the neutrino mass result, as discussed previously 3.3.2.3.

To minimize source-related systematic effects, the β-activity has to be stabilized on the 0.1 % level. This stability is monitored by the FBM, which counts β-electrons at the outermost rim of the 210 Tcm^2 magnetic flux tube. Hence, the transmission of the 210 Tcm^2 magnetic flux tube between source and the FBM can be investigated in addition to monitoring the source stability in downstream direction. Different parameters influences the source stability. The temperature of the gaseous tritium source is one of the key parameters therein. Thus, a key objective of this thesis in hand is to determine if the required temperature stability can be achieved.

CHAPTER 4

Commissioning and characterization of the beamline sections

A milestone in the extensive KATRIN assembly work was achieved in summer 2016, when all major components were combined to one global KATRIN beamline. Before this, the commissioning of each single STS component was necessary, before global beamline commissioning could be initiated. In this chapter the commissioning of the STS components, the WGTS, DPS and CPS is discussed in detail.

The first section 4.1 gives an overview the general commissioning of the WGTS cyostat. In section 4.1.1 the cryogenic performance of the unit is described with specific focus on the two-phase neon cooling system of the source tube, incorporating the results on the temperature stability and homogeneity. The acceptance tests of the superconducting solenoid system with respect to the required magnetic fields and their stability are discussed in section 4.1.2. The alignment between the source tube and the superconducting solenoids, which is of importance for the flux tube positioning, was measured mechanically, which is described in section 4.1.3.

The commissioning of the DPS here is discussed in section 4.2. The focus is on the commissioning of the superconducting solenoid system with its key feature of making use of loss-free liquid helium storage, as presented in section 4.2.1. In addition, the acceptance tests of the five solenoids with respect to magnetic field stability are outlined. General mechanical alignment measurements are presented in section 4.2.2. This is concluded by analyzing magnetic stray fields, as presented in section 4.2.3, completing the knowledge of the superconducting coil alignment.

The focus in the CPS commissioning detailed in section 4.3 was on quantifying the cooling performance of the cryostat, especially on the beam tube cooling of the cryogenic trap. The superconducting solenoid commissioning with emphasis on the magnetic field stability, is discussed in section 4.3.2. Finally, section 4.3.3 presents the alignment of the superconducting solenoids relative to the beamline.

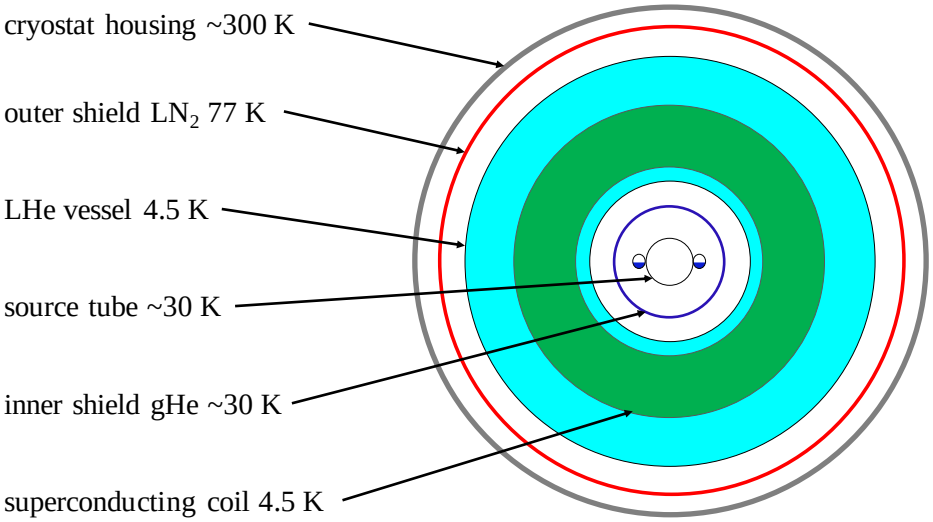

Figure 4.1: Setup of the WGTS cryostat. The shown sketch is based on a technical drawing. A special feature of this cryostat is the 30 K cold source tube, cooled by two cooling pipes located on the outer surface of the source tube and half filled with liquid and gaseous neon. The superconducting coil (green) is submerged in LHe (light blue). The inner shield (dark blue) prevents temperature exchange between the LHe chamber and the source tube. An outer shield (red) cooled down with LN_2 minimizes the heat load from the cryostat housing on the LHe chamber. The transparent areas between the different components represent the insulation vacuum chamber. To minimize the heat exchange between different components via radiation, all components are wrapped in super insulation foil.

4.1 Commissioning and performance of the WGTS cryostat

After the assembly of the WGTS cryostat by *Research Instruments GmbH* (RI)[1] was concluded, it was delivered to KIT in autumn 2015. The main task of the WGTS cryostat is to provide a 30 K cold source tube to minimize the Doppler broadening of the β-electrons [Ang05, Bab12]. The major challenge therein is to stabilize it at a level of $< 0.1\,\%$ [Ang05, Bab12]. In section 4.1.1 the underlying source tube cooling concept is presented as well as the temperature measurement system including results of this first commissioning.

The other key task of the WGTS cryostat is to create a magnetic field to guide β-electrons from their point of origin to the transport section. The acceptance test of the superconducting solenoid system is presented in section 4.1.2. The magnetic guiding field has to be aligned in a collision-free manner within the WGTS beamline. The corresponding alignment measurements between the solenoids and beamline parts is presented in section 4.1.3.

4.1.1 Performance of the source tube cooling

The LHe system with its superconducting coils and the inner shield of the WGTS cryostat are actively cooled down with gaseous helium (see figure 4.1). The helium temperature can be varied in order to adjust the temperature gradient and the cooling velocity. Due to the active cooling of surrounding components, as shown in figure 4.1, the source tube is passively cooled to 40 K by thermal radiation already (see figure 4.2). The cooling process of a cryostat is a critical operational phase since strong forces can result from the thermal contraction. A general form is used to describe the thermal contraction:

$$\frac{L_T - L_{293\,\mathrm{K}}}{L_{293\,\mathrm{K}}} = (a + b \cdot T + c \cdot T^2 + d \cdot T^3 + e \cdot T^4) \cdot 10^{-5}. \tag{4.1}$$

[1] Friedrich-Ebert-Strasse 1, 51429 Bergisch Gladbach, Germany

The following parameters are published for stainless steal (304 SS) by the National Institute of Standards and Technology (NIST) [Mar02]:

$$\begin{aligned} a &= -2.9546 \times 10^{+2}, \\ b &= -4.0518 \times 10^{-1}, \\ c &= +9.4014 \times 10^{-3}, \\ d &= -2.1098 \times 10^{-5}, \\ e &= +1.8780 \times 10^{-8}. \end{aligned} \tag{4.2}$$

These parameters apply for a temperature range from 4 K to 300 K [Mar02]. The beamline of the WGTS cryostat consist of 316LN, the bellows of 316L and the remaining cryostat of 316 stainless steel. The thermal contraction for these steels can be described to first order with equation given in 4.1 and the parameters 4.2. With respect to the 16-m long beamline of the WGTS cryostat a maximum thermal contraction of about 50 mm has to be taken in account. According to 4.1, the major thermal contraction takes place between 100 K and 300 K. Below 100 K the thermal contraction and the resulting movements are almost negligible. Hence, the most critical phase of a cool down is in the range between 300 K and 100 K. It is common hence to investigate the condition of the cryostat via a leak test at 100 K (see figure 4.2). After all actively cooled components had reached their operational temperatures, the passively cooled source tube remained at a temperature of ~ 40 K. To reach the required temperature regime of about 30 K the active cooling via two-phase neon cooling had to be turned on (see section 4.1.1.1).

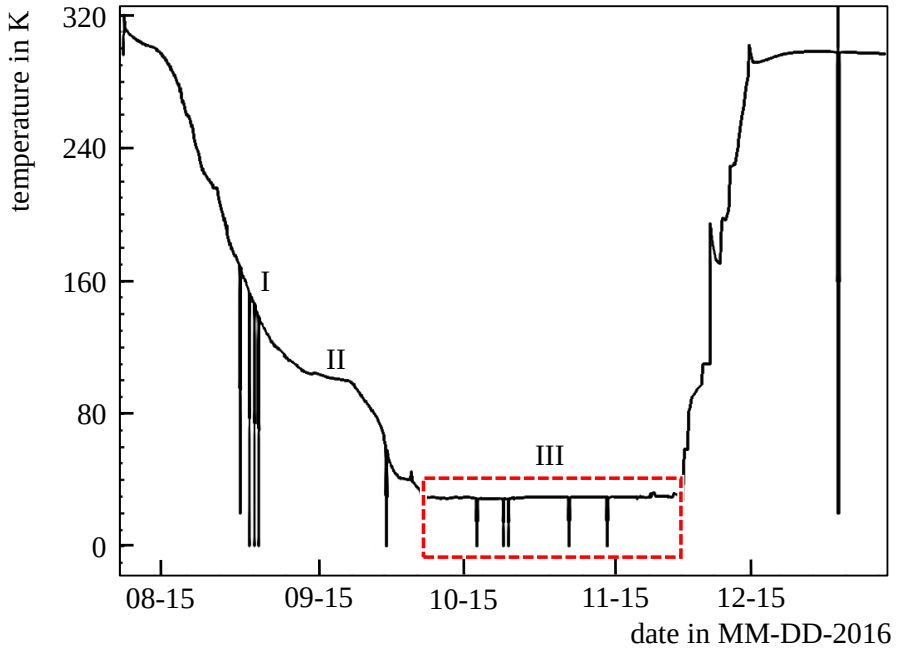

Figure 4.2: Temperature course of the WGTS source tube. The first cool-down of the WGTS cryostat started in August 2016. Shown is the source tube temperature curve which starts at room temperature with a linear drop of the temperature during the first 30 days. Before a temperature of 100 K was reached, sensor tests were performed, resulting in a quick drop of the sensor signal (I). During the following two weeks, a detailed leak test of all components was successfully performed at 100 K (II). Subsequently, the source tube was cooled further by radiation from the inner shield (see figure 4.1). The two-phase neon cooling system was used to cool the source tube from 40 K to 30 K and to stabilize the temperature, highlighted as a red dashed frame (III). The figure is adapted from [Mar17].

The task of providing reliable precision temperature measurements along the beamline is realized by Pt500[2] temperature sensors. However, the magnetic fields during normal operation will cause a temperature shift. Thus, a sophisticated calibration system is installed next to each Pt500 (see section 4.1.1.2) to handle this effect. The results of the temperature measurements are presented in sections 4.1.1.3 and 4.1.1.4.

4.1.1.1 Two-phase neon cooling system

The source tube cooling by gaseous helium used in the cooling of the inner radiation shield of the cryostat is not viable since temperature fluctuations in this cryofluid are of the order of ±1.0 K. To reach the specified temperature stability of 30 mK, a dedicated cooling concept based on a closed two phase system was implemented, brazed to the source tube (see figure 4.3) [Gro08, Gro09, Gro11, Bab12, Gro13]. The temperature of such a system is given by the vapor pressure of the chosen liquid. Neon was identified to be best suited for the temperature range between 28 K and 32 K.

The two phase neon cooling cycle consists of a neon condenser which is cooled by gaseous helium to $\sim (25 \pm 1)$ K and four electric heaters located in the two phase tubes. Due to the heat load on the source tube, liquid neon evaporates and is returned to the condenser (see figure 4.3). After the evaporated neon is liquefied again in the condenser, it drips back into the cooling tubes at the source tube. A huge buffer mass of lead (3.7 kg) inside the condenser minimizes influences of the helium cooling cycle on the two phase neon cooling system, smoothing out temperature fluctuations [Gro09]. To minimize remaining fluctuations in the two-phase neon cooling system, a system of four electrical heaters, each with a maximal power of 2 W, is used. A decrease of temperature is compensated by an increase of the heater power and vice versa. Thus, the heater power is linearly anti-correlated to the source temperature with a correlation coefficient of $\rho_r = -0.66$ [Mar17]. More informations about the relevant cycle are published in [Gro09, Gro11, Gro13, Mar17].

The average temperature of the system is regulated via the vapor pressure. In order to detect local temperature fluctuations and distortions of homogeneity, a total of 24 Pt500 sensors is mounted onto the outside of the source tube (see figure 4.4). The temperature measurement of these sensors is influenced by the magnetic field of the solenoids. Therefore each sensor is complemented by a vapor pressure sensor which enables an in-situ calibration. The principle is presented in the following section.

[2] Platinum resistors with a nominal resistance of 500 Ω at 0°C

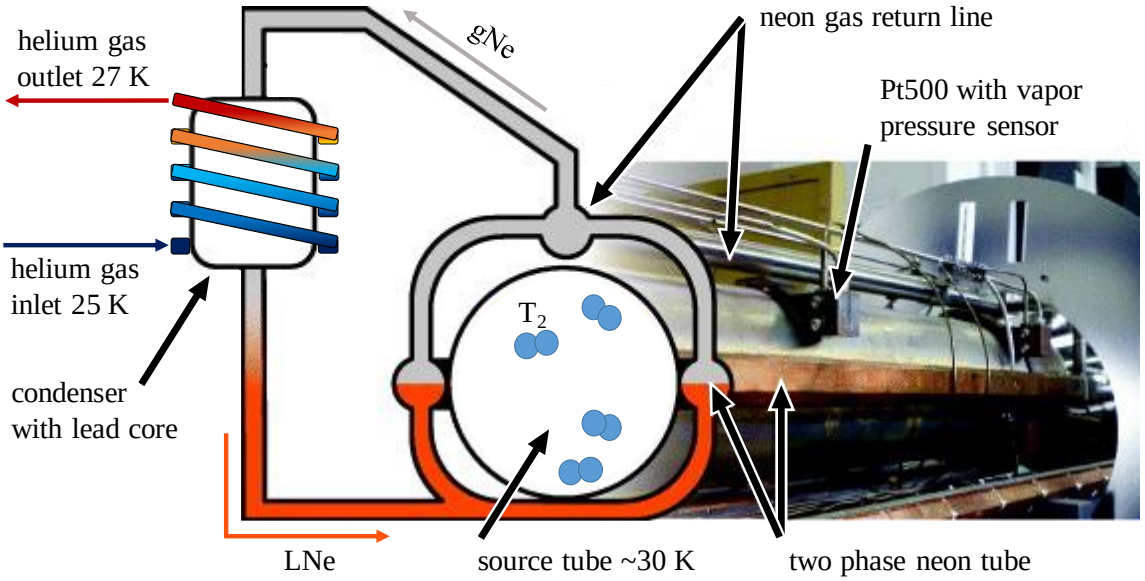

Figure 4.3: The source tube cooling system of the WGTS cryostat. The figure shows a picture of the WGTS source tube during manufacturing. A sketch of the two-phase neon cooling system is attached to the picture. The evaporated neon of the two-phase cooling tubes at both sides of the source tube flows to the condenser, where it is liquified. Afterwards the liquid neon is returned to the cooling tubes. The neon cycle is closed allowing to control the temperature via the vapor pressure. Various Pt500 sensors are mounted along the source tube to measure the temperature stability and homogeneity. Since their measurement depends on the magnetic field, a vapor pressure sensor is mounted next to each Pt500 for in-situ calibration [Gro11]. The figure is adapted from [Fis14].

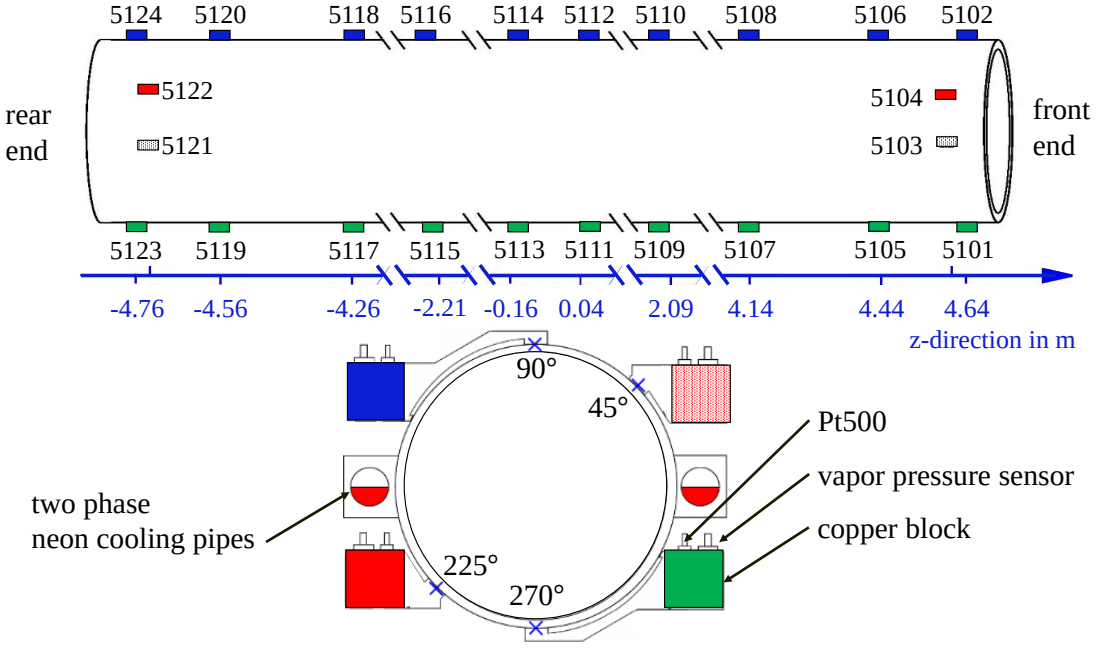

Figure 4.4: Positioning of the temperature sensors along the source tube. To measure the temperature, a total of 20 Pt500 sensors are thermally connected to the top (blue) and bottom parts (green) of the source tube. Additionally, four sensors are mounted at the side (light red / red) of the source tube near the front and rear end. The bottom figure shows the two-phase neon cooling pipes on both sides of the source tube in beam direction, as well as the colored copper blocks, each including one Pt500 and one vapor pressure sensor. The figure is adapted from [Hoe12].

4.1.1.2 Temperature measurement and calibration system

The continuous temperature measurement at the source tube is realized by an ensemble of 24 resistance sensors Pt500, shown in figure 4.4. The temperature measurements of these sensors is influenced by external magnetic fields, resulting in an offset which depends on the strength of the magnetic field, see figure 4.5. In case of a constant magnetic field, this offset is also constant. Hence, a calibration of each Pt500 sensor in a constant magnetic field environment is sufficient to enable absolute temperature measurements. To this end, each temperature resistance sensor is complemented by a vapor pressure sensor. Both sensors are thermally connected with a copper block, see figure 4.4.

A vapor pressure sensor consists of a small cylinder, which can be filled with gaseous neon. The neon infill condenses, forming a two-phase equilibrium in the cylinder. The pressure corresponds to a specific temperature, detailed by the vapor pressure curve, which is used as absolute temperature value for the corresponding Pt500 sensors. The pressure readings there are independent of the magnetic field (see figure 4.5). The filling process of the cylinder introduces small amounts of heat onto the source tube. A 30 minutes waiting period is thus required to equilibrate temperatures before the onset of temperature measurements with the vapor pressure sensors (see figure 4.6). After the calibration process the neon is removed from the cylinder.

This calibration system enables an absolute temperature measurement during magnet operation. Thus it is possible to monitor temperature stability and homogeneity during the later neutrino mass measurements. The first results of the temperature stability and homogeneity are described in the following sections. Detailed information about the calibration system with focus on the read-out electronics are published in [Gro09, Gro11, Gro13, Mar17].

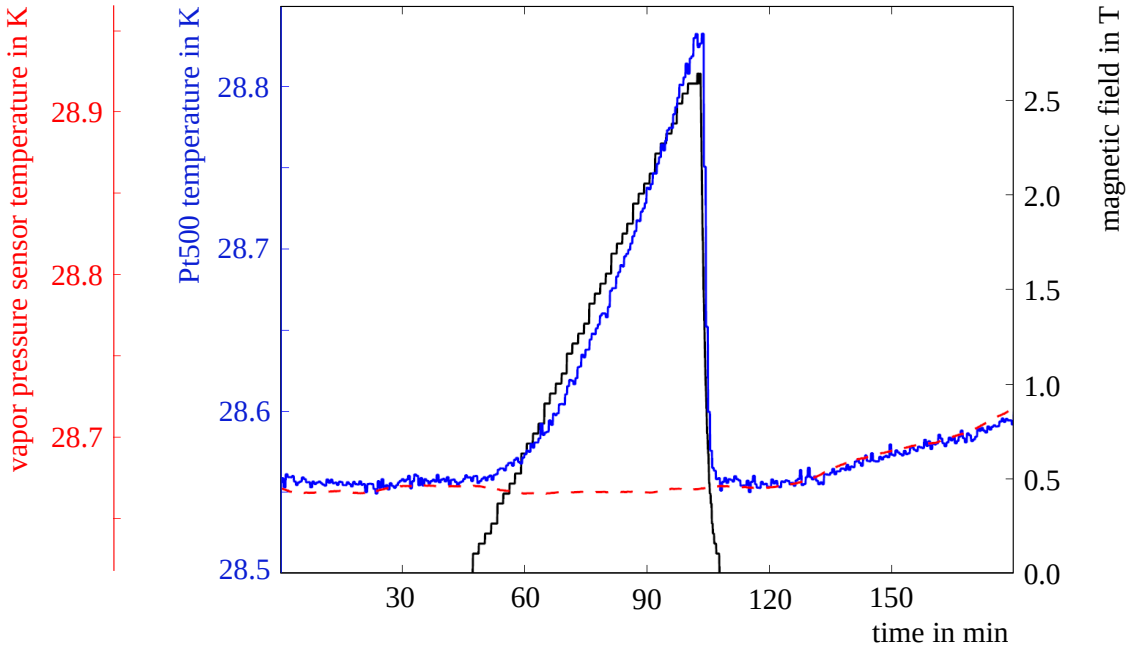

Figure 4.5: The influence of the magnetic field on the temperature-dependent resistance measurement. Shown is the influence of the magnetic field (black) on the temperature-dependent resistance measurement (blue). The temperature data of a vapor pressur sensor (red) demonstrates the magnetic field-independent temperature measurement of the calibration method. The figure is adapted from [Mar17].

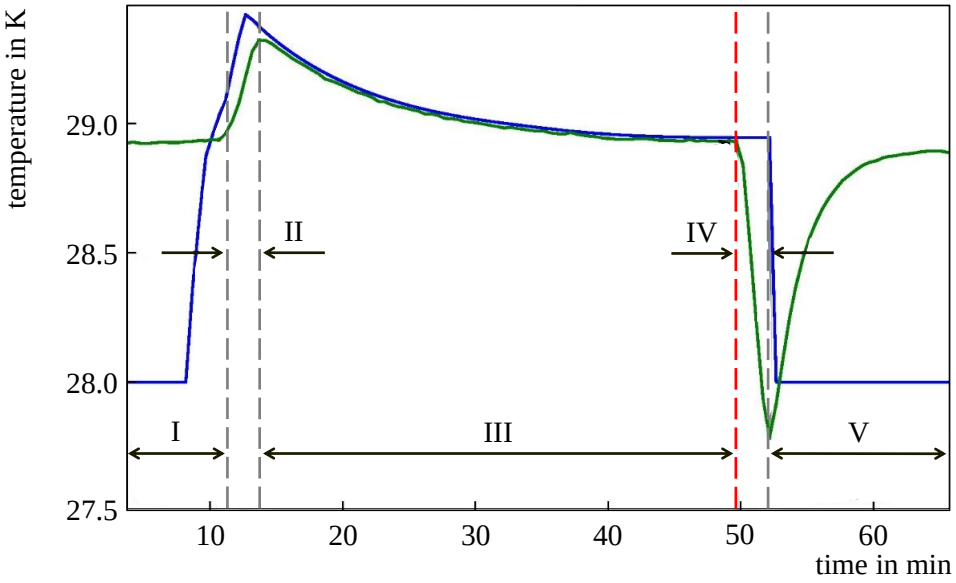

Figure 4.6: The calibration process of a Pt500 sensor by making use of the vapor pressure sensors. The figure shows the temperature measurement of the Pt500 (green) and the vapor pressure sensor (blue). By filling the vapor pressure sensor (I) with neon gas the measured Pt500 temperature (green) was nearly constant. Once the neon gas started to condensate (II), the temperature increased locally at the position of the two sensors and their holding structure. The thermalization is finished about 30 minutes after the end of the filling process (III). Afterwards the calibration of the Pt500 by using the vapor pressure sensor can be implemented, highlighted as a red dashed line. The vapor pressure sensor was emptied afterwards (IV) introducing a sharp drop in temperature. The procedure is finished once the thermalization is reached (V). The figure is adapted from [Mar17].

4.1.1.3 Temperature stability

One key objective of the WGTS commissioning was to quantify the temperature stability of the 10-m long source tube. The implemented cooling system has yielded a peak-to-peak temperature stability of $(10.10 \pm 8.27)\,\mathrm{mK/h}$ over a time span of 48 h (see figure 4.7). After the parameter settings of the two-phase neon cooling system were improved, an extended measurement interval of 16 d showed a worst-case stability value of 19 mK/h with an average temperature stability of $(3.28 \pm 1.68)\,\mathrm{mK/h}$, which is one order of magnitude better than the specified value of (30 mK/h) [Ang05, Mar17]. The uncertainty is given as standard deviation over an 1 h interval.

For later long-term operation it is important to verify that the two-phase neon cooling system has a homogeneous effect on the source tube. To investigate this, two sensors one on each end were used to identify the temperature correlation during a temperature change. As shown in figure 4.8, the correlation coefficient $\rho_\mathrm{r} = 0.9999$ demonstrates an almost perfect linear correlation of local temperatures along the source tube [Mar17]. From this it can be concluded that the source tube reacts on temperature changes by the two-phase neon cooling system in a homogeneous way with respect to the overall 10-m long dimension. Additionally, there is irrefutable evidence that the copper block provides excellent thermal coupling between the sensors and the source tube similar for all sensors (see figure 4.4).

The above results are in perfect agreement with the KATRIN specifications [Ang05].

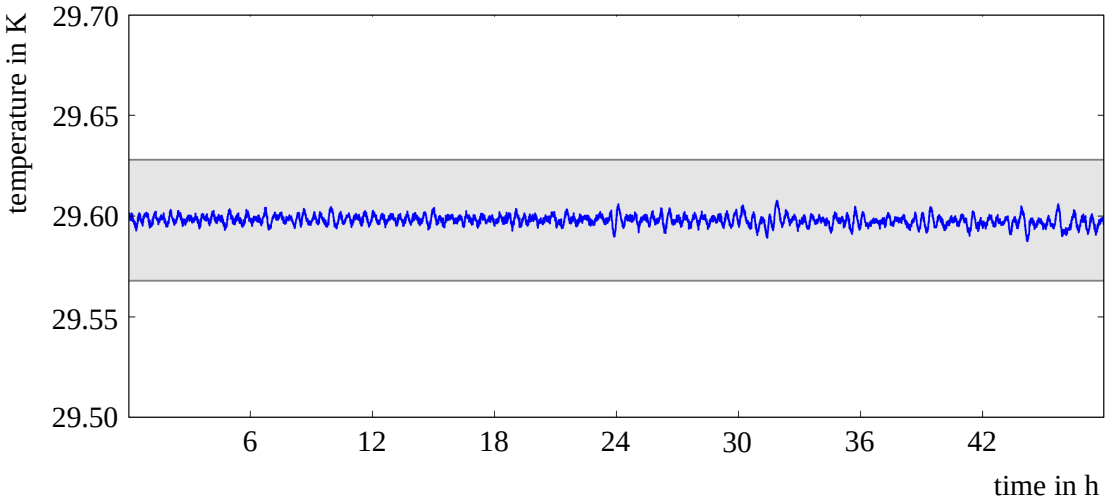

Figure 4.7: Temperature stability of the 10-m long source tube. Shown is the temperature of the source tube during 48 hours. Highlighted in grey is the specified stability of ±30 mK/h [Ang05]. The measured temperature is highlighted in blue. The peak-to-peak stability during the entire measurement time of 48 h between November 12 and 13, was ±10.1 mK.

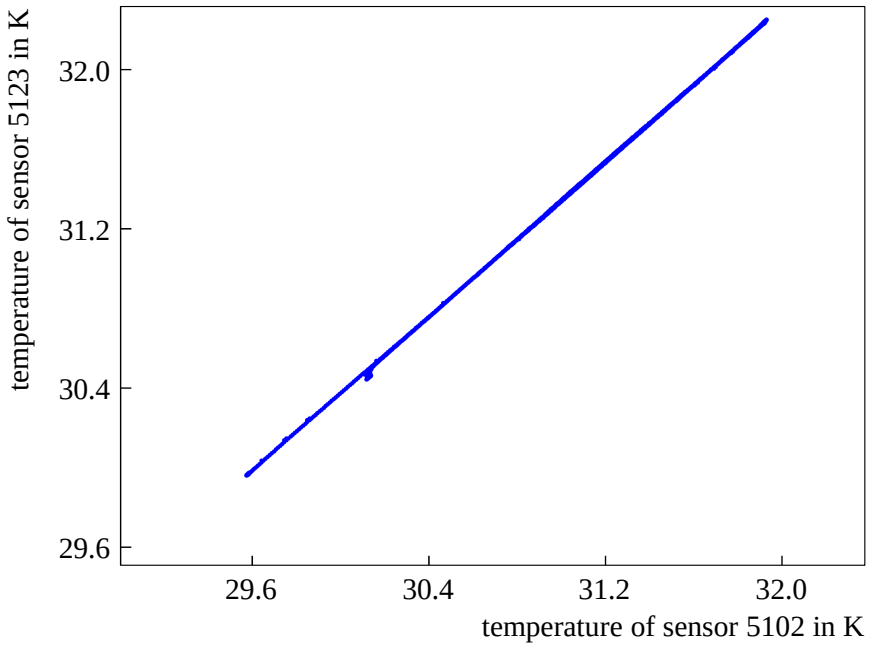

Figure 4.8: Correlation of two temperature sensors. The figure demonstrates the correlation between the temperature of the two sensors 5102 and 5123 which are located on opposite sides of the source tube (see figure 4.4). The measurement period was between November 24 and November 25 2016 with a total measurement time of 24 h. A high rate of data points (5760) and the high correlation of $\rho_r = 0.9999$ results in a nearly perfect line. The figure is adapted from [Mar17].

4.1.1.4 Temperature homogeneity

The second key objective of the WGTS commissioning was to scrutinize the temperature homogeneity of the 10-m long source tube. Due to the strong correlation between the Pt500 sensors, as verified in the last section, time-dependent local fluctuations can be excluded. Therefore, only global inhomogeneities which are constant in time, can remain along the source tube.

The maximum deviation of the temperature in comparison to the center of the source tube was detected on the rear side with (570.7 ± 16.2) mK. The deviation at the front side in comparison to the center is only (64.1 ± 15.9) mK, as given in figure 4.9. The observed inhomogeneity in temperature is more than one order of magnitude higher than specified. Despite not meeting the requirements, the resulting systematic uncertainties on the neutrino mass measurement can be minimized by including this result into the WGTS gas density model [Kuc16].

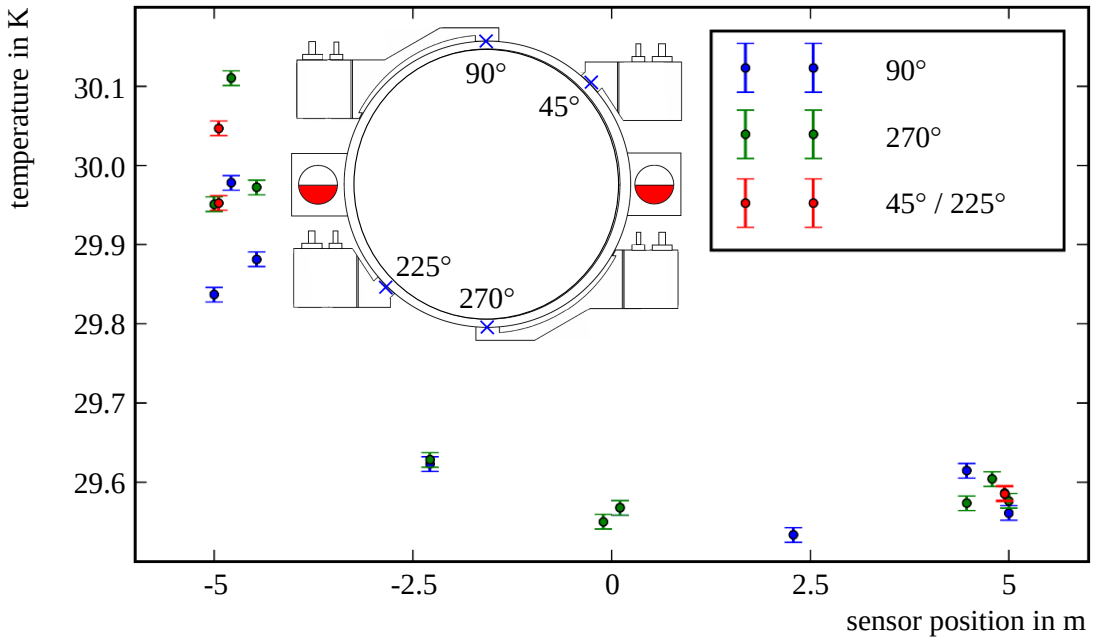

Figure 4.9: Temperature homogeneity of the 10-m long source tube. Shown are the absolute temperatures along the source tube. The average temperature was measured over one hour on November 28 2016. The blue dots represent the sensors on top (90°) and green dots indicate sensors on the bottom (270°) of the source tube. The four red dots show the measurement points at the side of the source tube. The detailed sensor positions can be found in figure 4.4.

4.1.2 Acceptance test of the superconducting solenoids

The superconducting coils of the WGTS were previously tested in single and double coil configurations at the Alternative Energies and Atomic Energy Commission (CEA) in Sacley, France. The first test of the final WGTS solenoid configuration could only be performed after the cryostat was fully assembled and the system was connected to the cryogenic infrastructure. The solenoids were successfully tested up to 100 % of their nominal field (appendix C: FL1), of 5.6 T at the front side, and 3.6 T at the center and the rear side (see figure 3.3). Monitoring of the coil currents demonstrated a magnetic field stability of ±0.02 %/30 d, which is in perfect agreement with the specified stability of ±0.03 %/30 d [Gil17]. During the First Light measurement campaign, which is detailed in chapter 5, the solenoids were operated at 20 % of their nominal field. All solenoids of the WGTS are equipped with one dimensional hall sensors to measure the magnetic field. The magnetic field during the First Light measurement campaign is displayed in figure 4.10, demonstrating that even at reduced magnetic field the coil performance is completely comparable with the field stability for nominal operation. Hence the reduced magnetic field has no influence on the measurement results of First Light.

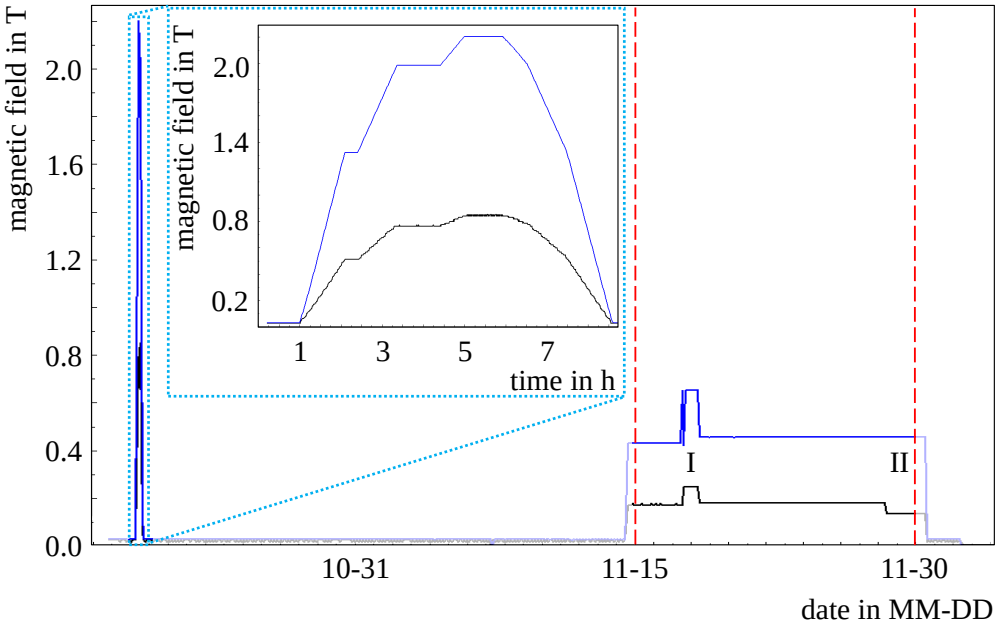

Figure 4.10: Performance of the superconducting solenoids of the WGTS. Shown are the measured magnetic fields of the WGTS solenoids M2 and M6. Due to the position of the one dimensional hall sensors, stray fields are measured, and not absolute magnetic fields. The solenoids are operated in driven mode, which means that the coil current provided by the supply units is permanently monitored and controlled. The blue line shows the hall probe which is located at solenoid M6. The black line shows the hall probe which is located at solenoid M2. The first peak, which is highlighted with the blue dashed box shows the successful acceptance test by reaching 100 % magnetic field. As shown, the energizing of the solenoids was realized in three steps via a reduction of the ramping rate at higher fields to minimize the risk of a quench. The highlighted part between the red dashed lines is the magnet operation (20 %) during the First Light measurement campaign. There, the solenoids were ramped up to 30 % of the nominal field for one day (I). At the end of the campaign, the solenoids M2 and M3 were ramped down to 15 % (II) to create a magnetic bottleneck.

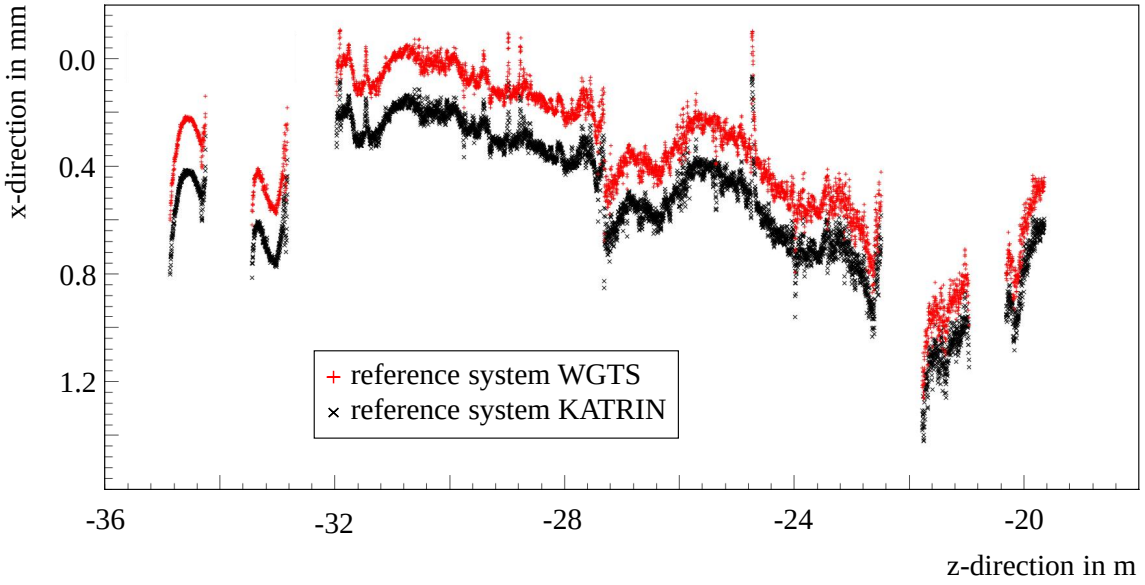

Figure 4.11: Alignment measurement of the WGTS beamline in x-direction. Shown are the alignment results of the complete WGTS beamline. The red data points are in reference to the WGTS flange for x-direction. The interruptions are caused by the pump ports. With respect to the global KATRIN coordinate system, the alignment data had to be corrected by the WGTS cryostat alignment. The figure is adapted from [Def17].

4.1.3 Mechanical measurement of the actual dimensions

The three central superconducting solenoids of the WGTS (M1 – M3) form a coil chain covering the entire source tube, see figure 3.3. A perfect coaxial alignment between the three solenoids and the source tube is important since it prevents collisions between the flux tube and the beamline. For this reason, a maximum misalignment of 1 mm was specified. The design of the holding structure between the source tube and the solenoids does not enable a misalignment of more than 1 mm. Thus, the magnets and the source tube can be considered as one single unit. Accordingly, it suffices to merge the alignment of this unit with respect to the global KATRIN coordinate system.

After the cryostat assembly was finished, a laser tracker measurement of the complete WGTS beamline was performed, see figures 4.11 and 4.12, by a so-called “pig” probe. It consist of a cylinder which contains a ball with a mirror. This probe was connected to a string and pulled through the entire beamline by hand, resulting in variations of speed of the movement. This effect can be seen in the measurement data as spikes. The pumping chambers were not covered to avoid the probe dropping into the pump ports. Consequently, no alignment data are available in the region of the pumping chambers. The reference system of these measurements was the WGTS cryostat. To transform these beamline alignment data into the global KATRIN coordinate system, the WGTS cryostat alignment was measured additionally with a laser tracker, using the KATRIN coordinate system as reference system. Over the entire length a maximum alignment deviation of less than 3 mm was determined, resulting in a maximum source tube deviation of about 2 mm (see figure 4.11 and 4.12). Since the holding structure between the WGTS beamline and the covering superconducting solenoids allow a maximum deviation in alignment of < 1 mm, this value has to be taken as level of uncertainty for the solenoid position. All data were taken for warm coil conditions. For a detailed modeling of the WGTS field and the resulting flux tube alignment, the thermal contraction of the coils has to be taken into account. By implementing the corrected alignment data into the KATRIN model, more

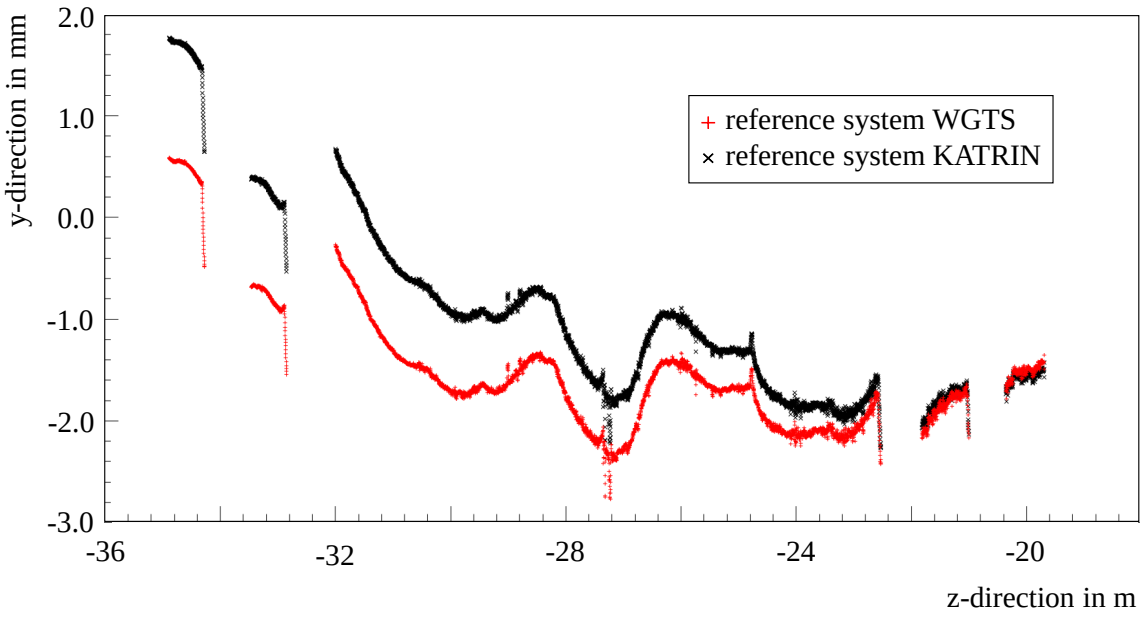

Figure 4.12: Alignment measurement of the WGTS beamline in y-direction. Shown are the alignment results of the complete WGTS beamline. The red data points are in reference to the WGTS flange for y-direction. The interruptions are caused by the pump ports. With respect to the global KATRIN coordinate system, the alignment data had to be corrected by the WGTS cryostat alignment. The figure is adapted from [Def17].

realistic magnetic flux tube alignment simulations can be performed. These simulations are discussed in detail in chapter 6.

4.2 Commissioning of the differential pumping section (DPS)

The DPS unit, located adjacent to the WGTS cryostat, fulfils three main tasks, by guiding β-electrons adiabatically and collision-free to the CPS, by reducing the tritium gas flow by more than five orders of magnitude, and by reducing and blocking the tritium ions [Ang05, Rei09, Win11, Kos12, Luk12, Jan15, Hac15].

The assembly of the DPS beamline was finished in summer 2016. It consists of five single beam tubes, which are connected via four pump ports to the omega-shaped DPS beamline (see figure 3.4). Each beam tube is mounted inside the warm bore of the superconducting solenoids. Attached to the lower part of each pump port is a valve followed by a high capacity TMP MAG W2800, (see figure 3.4). The TMPs were operated without magnetic fields already and have achieved a pressure less than 10^{-8} mbar inside the DPS beamline. This pressure regime was perfectly suited for the First Light measurements.

The superconducting solenoid system of the DPS was commissioned in 2015 and 2016. The results of these commissioning measurements are presented below, both in terms of the absolute magnetic field as well as magnetic field stability. Additionally, the coil alignment inside each solenoid with respect to the housing was determined and discussed in section 4.2.3.

4.2.1 Cryo performance and magnetic field tests of the recondensor magnets

Over the entire KATRIN operational time of at least five years, including service and repairs [Ang05], a stable operation behavior of the magnets has to be guaranteed. A single superconducting coil of the magnets in use is surrounded by LHe of temperature of 4.15 K at a nominal pressure of 1013.25 mbar to ensure superconductivity [Zha11]. To store the LHe in a loss-free manner, a so-called recondensor cryostat[3] using a pulse tube cryocooler[4] [Wan97] is used as optimum solution.

4.2.1.1 Design of the recondensor magnets

The cryostat consists of a 4.8 mm thick stainless steel housing, an insulation vacuum chamber, a LHe chamber which contains the coil, and several thermal shields (see figure 4.13). The thermal shields and the insulation vacuum are targeted with the reduction of the heat load onto the LHe chamber. Furthermore, all cryogenic parts inside the insulation vacuum chamber are covered with superinsulation foil to reduce thermal heat loads further. Despite this a remaining heat load on the LHe chamber, which is assumed to be 1.00 W (appendix C: DR1 and DR2), causes evaporation of LHe.

This heat load is compensated by a cold head of corresponding a cooling power of 1.35 W at 4.15 K (appendix C: DR1 and DR2). The cold head cools a recondensor unit, which is located on the upper side of the LHe chamber directly above the coil (compare figure 4.13). The evaporated helium starts to condense at this unit and thus rejoins liquid in the LHe chamber. The recondensor unit has several blind holes on the inner side facing the coil and is completely gold coated. The 4.2-K cold gold surface has an impact on the helium condensation since it causes droplet condensation. Inside the blind holes, the droplets start to grow and get pulled out by gravity. The back flow of droplets into the LHe chamber ensures that the LHe volume is stored without losses.

Since the cooling capacity is larger than the remaining heat load on the LHe chamber, a lower pressure in comparison to the surrounding atmosphere can be generated. To prevent penetration of atmospheric gases into the LHe chamber, a heater is located on top of the recondensor unit. The heater power is used to control the pressure inside the LHe chamber, which is continuously being monitored and controlled by a pressure sensor.

4.2.1.2 Cooling procedure

The cooling procedure protocol of the manufacturer CMI suggests to cool the solenoid initially with liquid nitrogen (LN_2) and blow it out with gaseous helium on the following day. With this pre-cooling method more than 90 % of the thermal energy can be removed (see figure 4.14). The cold head is started afterwards to cool the system even further. One day later the solenoid can be filled with LHe. This process requires a LHe consumption of about 250 ℓ.

The cooling procedure was improved by extending the cooling phase of the cold head to a period of four days. A reduction of more than two thirds of LHe consumption was achieved (see figure 4.14). The required LHe consumption now is about 80 ℓ only, while the LHe chamber has a capacity of 60 ℓ. Hence, only 20 ℓ of LHe are required to reach the operational temperature of the system[5].

[3] Cryomagnetics, Inc., 1006 Alvin Weinberg Drive, Oak Ridge, Tennessee 37830, USA

[4] Cryomech, Inc., 113 Falso Drive, Syracuse, New York 13211, USA

[5] Oliver Hartwig, Cryogenic Commissioning of the DPS-Magnets and Improvement of the Helium Consumption, Bachelor Thesis, Karlsruhe Institute of Technology, 2015

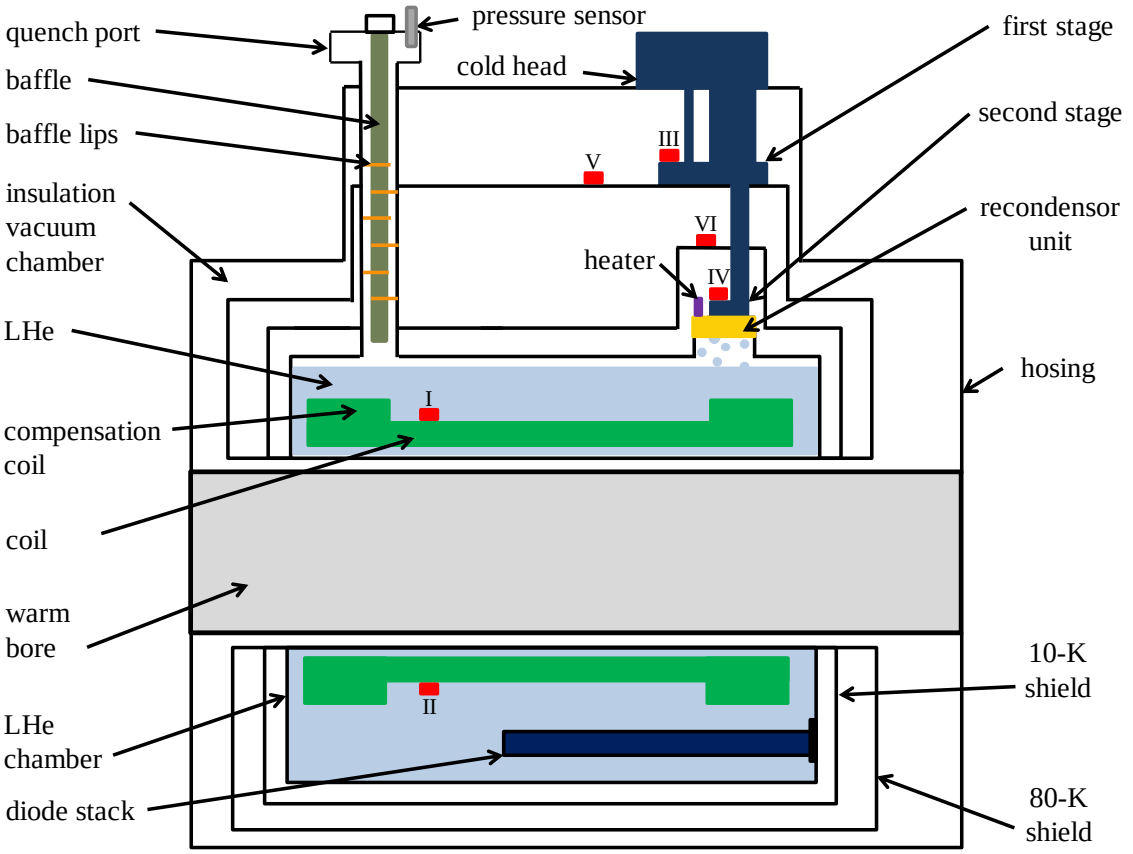

Figure 4.13: Sketch of a recondensor solenoid setup. This sketch is based on a technical drawing by CMI. A special feature of this recondensor solenoid is the huge warm bore (grey) with a diameter of 254 mm which is required to house of the beam tube. The superconducting coil (green) is surrounded by LHe (light blue). A system of six (I – VI) temperature sensors (red) is used to monitor system performance during operation. The cold head (dark blue) has two stages, which cool the thermal radiation shields, and, more importantly, the recondensor unit. A pressure sensor is used to monitor the pressure inside the LHe continuously. Due to the cooling power of the cold head and the recondensing of helium, a lower pressure than the surrounding atmospheric pressure can be reached. To prevent penetration of atmospheric gases due to diffusion or leakage into the LHe chamber, a heater on top of the recondensor unit counteracts against the cooling power, ensuring a permanent positive over-pressure in the system.

The LHe consumption can be reduced even further by a further extended time interval of cold head cooling. During cooling of the LHe chamber, it is permanently connected to a gaseous helium supply. This guarantees a permanent over pressure in the system during the cool-down to prevent penetration of atmospheric gases into the system. It was observed that the recondensor unit starts condensing the gaseous helium on the sixth day of cold head cooling. This new filling concept is currently under investigation and first parts of the required helium gas supply have already been assembled. The most important advantage is the capability of refilling the system during neutrino mass measurements without interruption and time-consuming hardware modifications.

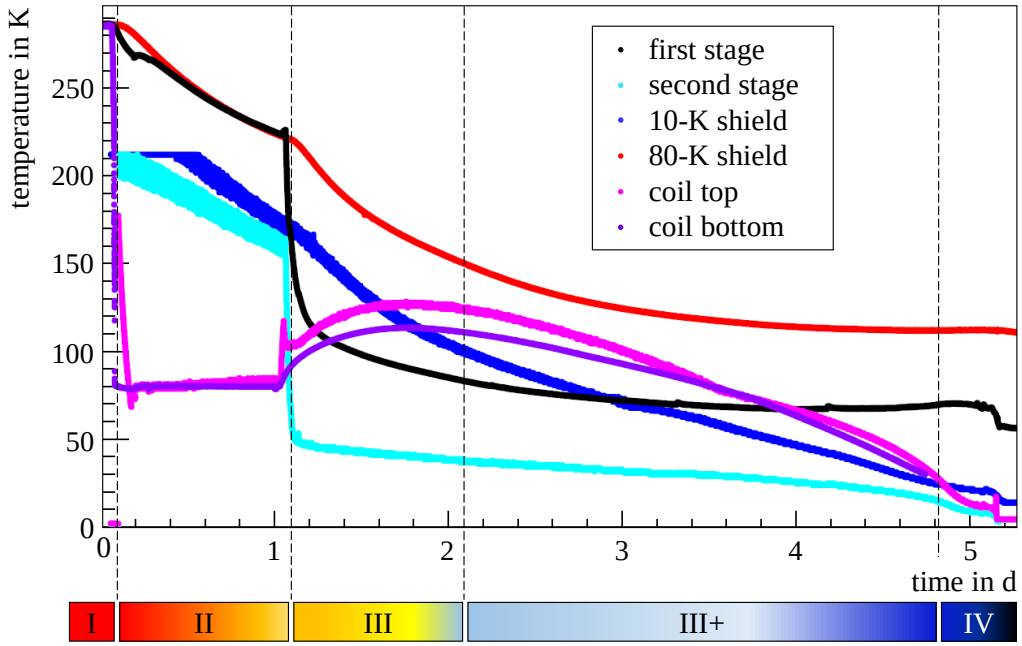

Figure 4.14: Temperature course of the DPS recondensor solenoids. The first phase (I) of the cool-down is the evacuation of the insulation vacuum chamber. If a pressure $< 10^{-5}$ mbar is reached, phase two (II) starts by cooling and filling the LHe chamber with LN_2. After one day, the LHe chamber is purged with gaseous helium. Afterwards the cold head is started, going over to phase three (III). The instruction manual of the supplier CMI suggests a beginning of the LHe filling after one day, which requires a high amount of LHe due to the remaining thermal energy in the system. The phase three plus (III+) extends phase three by up to four days. The cooling power of the cold heat is sufficient to nearly reach LHe temperatures during this time. The LHe filling is the last phase (IV) of the cool-down before the solenoid has reached operational readiness.

4.2.1.3 Magnetic field tests

All solenoids were tested up to 5.5 T as was specified in the design as maximum reachable magnetic field, which is 10 % above the KATRIN requirements of 5.0 T (see figure 4.15). Additionally, it could be demonstrated that all solenoids can simultaneously reach 5.5 T without quench. To verify the required stability of the magnetic field ($\leq 0.2\,\%/30\,\mathrm{d}$), the magnetic field of the DPS solenoids was determined with the help of a nuclear-magnetic resonance (NMR) probe over several hours, demonstrating a stability of $\leq 0.085\,\%/30\,\mathrm{d}$, which is one order better than required [Gil17].

4.2.2 Mechanical measurement of the actual dimensions

The setup of the DPS consists of a support structure on which the superconducting solenoids are placed. The beam tubes are located inside the warm bore of the solenoids and connected to the entire DPS beamline via pump ports (see figure 3.4). The modular setup of the DPS superconducting solenoids enables individual positioning of each magnet on the support structure. The horizontal directions (x- and z-direction) are aligned with adjusting screws (see figure 3.4), while packing plates are used to adjust the height.

Since each coil is placed inside its cryostat, it was assumed that the coil is perfectly aligned to the warm bore. This is possible because the specifications allow a maximum deviation between the coil axis and the axis of the warm bore of 1 mm. Hence, the warm bore was used as reference system for the superconducting coil (see figure 4.13). The outcome is that the cryostat position differs by less than 1 mm from the design position and hence the coil position. In order to guarantee a collision-free guidance of the magnetic flux tube in the

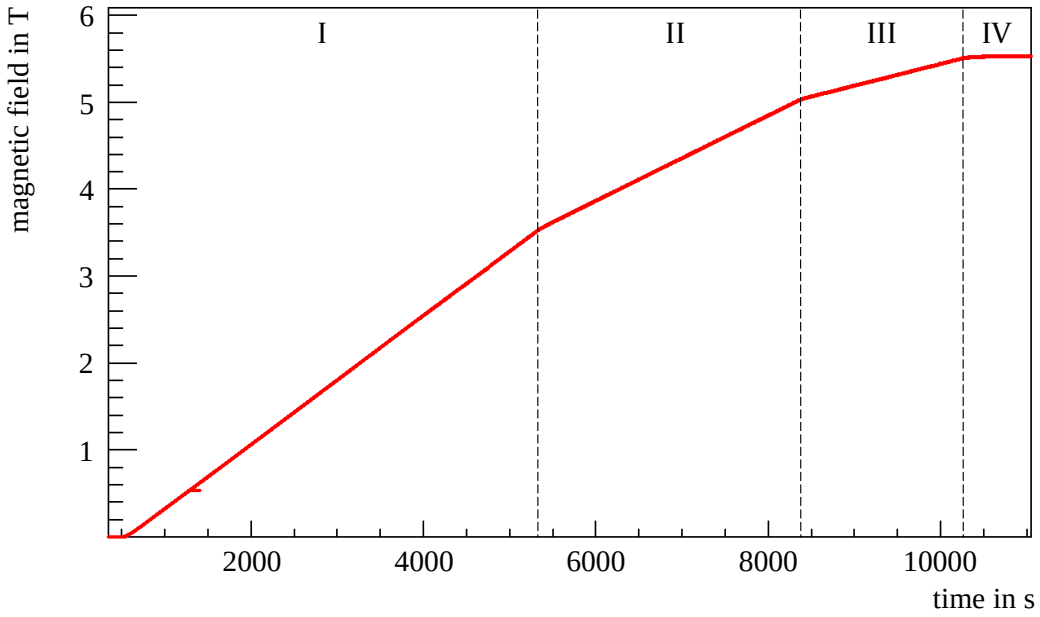

Figure 4.15: Magnetic field ramping of a DPS solenoid. Shown are three different ramping rates of a DPS superconducting solenoid. The first phase (I) is based on a ramping rate of 10.5 mA/s until 50.0 A are reached, followed by the second phase (II) with a ramping rate of 7.0 mA/s. The third phase (III) starts at 71.164 A with a rate of 3.5 mA/s. Finally, the required magnetic field is reached at the beginning of phase (IV). The shown magnetic field was measured with a three axial hall probe.

beamline of the DPS, the beam tubes have been aligned coaxially to the warm bore with sub-mm accuracy. The central solenoid M3 is tilted upwards by 0.4° on the downstream side with respect to its design position (see figure 3.4). This tilt was necessary to prevent collisions inside the CPS beamline due to a misalignment of the CPS solenoids, as discussed in detail in section 4.3.3.

As a result of vibrations during the shipping and installation, and thermal contractions in the process of reaching the cryogenic operation temperatures or magnetic forces during magnetic field operation, a variety of factors can induce a relocation of the coil. This can cause misalignments between the beamline and the coil position and hence misalignments between the magnetic flux tube and the beamline. These effects were investigated by detailed magnetic stray field measurements, providing more precise alignment data of the coil position as outlined in the following.

4.2.3 Position measurements of the superconducting coils

Each coil position was determined during the manufacturing process by mechanical and optical measurements of the supplier. Directly after each solenoid was manufactured, the coil position was measured again using the magnetic field to verify that the deviation between the coil axis and the warm bore axis is less than 1 mm in radial direction. This measurement had to be repeated after the solenoids arrived at KIT, since the shipping could have caused a relocation of the coil inside the cryostat. For both magnetic field measurements the same measurement setup and the same set of hall sensors as well as the same monitoring system were used. A one dimensional hall probe was rotated around the axis of the warm bore on both sides of the warm bore with a radial distance of 38 mm to measure the angle-dependent magnetic stray field (see figure 4.16). In radial direction the magnetic field was measured by rotating the hall probe step wise in 15° steps . The largest radial displacement of coils is less than 1 mm, and no deviations between the results before

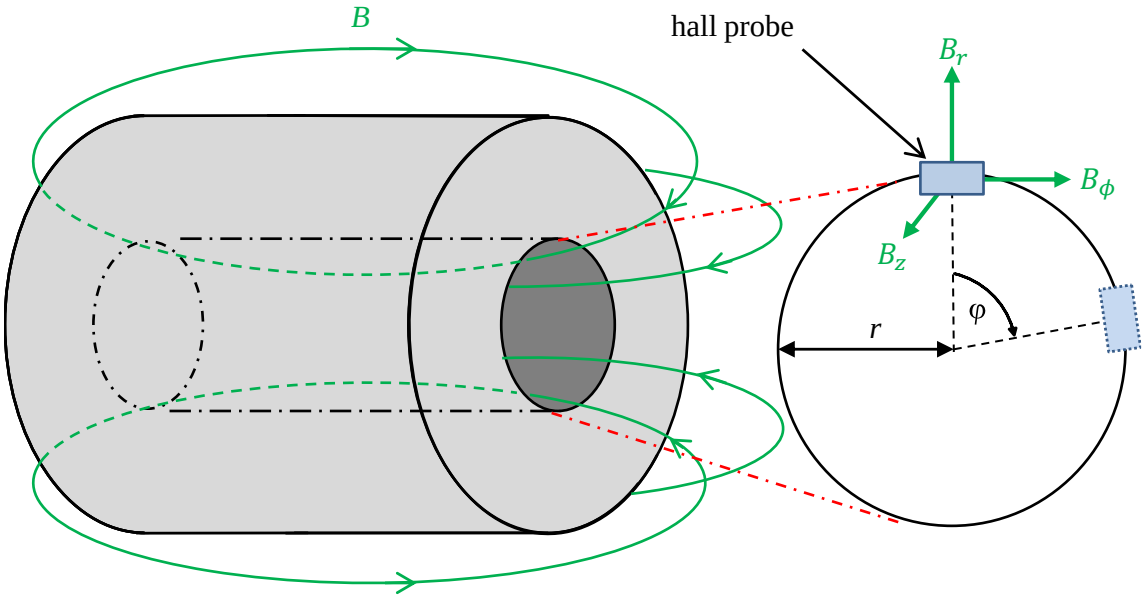

Figure 4.16: Magnetic stray field measurement principle to determine the coil alignment. Shown in grey on the left side is the cryostat. A hall probe is rotated on both ends of the coil while measuring the magnetic field.

and after shipping were found. Thus, the coil position in the cryostat complies with specifications. A deviation of the coil position in axial direction was determined to be $> 1\,\text{mm}$. This result is caused by the measurement principle, since only the magnetic field in radial direction was determined, resulting in a large non-quantifiable uncertainty. A detailed description of the measurement principle and the coil alignment results are presented in [Hac15]. Additionally, a comparison of position measurements during assembly of each solenoid with the later position investigations based on by measuring the magnetic field show deviations in the sub-mm range. This is clear indication that the coil position is not influenced by its operating temperature of 4 K in comparison to the previous mechanical measurements at CMI.

A final measurement was performed using a three axial hall probe with a modified setup to measure the angle-dependent magnetic stray field [Gla15] (see figure 4.16). It could be demonstrated that the radial shift of the superconducting coils in x-direction is $< 1\,\text{mm}$. However, the central solenoid M3 shows a coil shift in y-direction of about $-1.4\,\text{mm}$ [Gla15]. In contradiction to the previous results, the coil alignment in beam direction could be determined resulting in a position accurancy $< 0.5\,\text{mm}$ [Gla15]. By measuring the entire magnetic field, the results obtained are more precise than results of previously presented measurements. For this reason, the alignment results obtained in this final measurement of the superconducting coils were implemented into the geometry package of Kassiopeia [Gla15, Sac15].

Since the superconducting solenoids of the DPS are arranged in an omega shaped design, the coils are exposed to considerable remaining forces during global magnetic field operation of KATRIN (see figure 4.17). A remaining force acting upon a coil potentially can shift its position. To determine the influence of this effect on the coil position, the strongest magnetic forces to occur in the DPS were investigated. In this case only two neighboring solenoids were operated with the magnetic field of 5.5 T, resulting in a maximum force of 33 kN, and a torque of 2 kNm. The maximum dislocation of the coil determined was $(0.8 \pm 0.1)\,\text{mm}$. This is an excellent result, since the investigated forces are one order of magnitude larger than the forces during nominal KATRIN magnetic field operation for

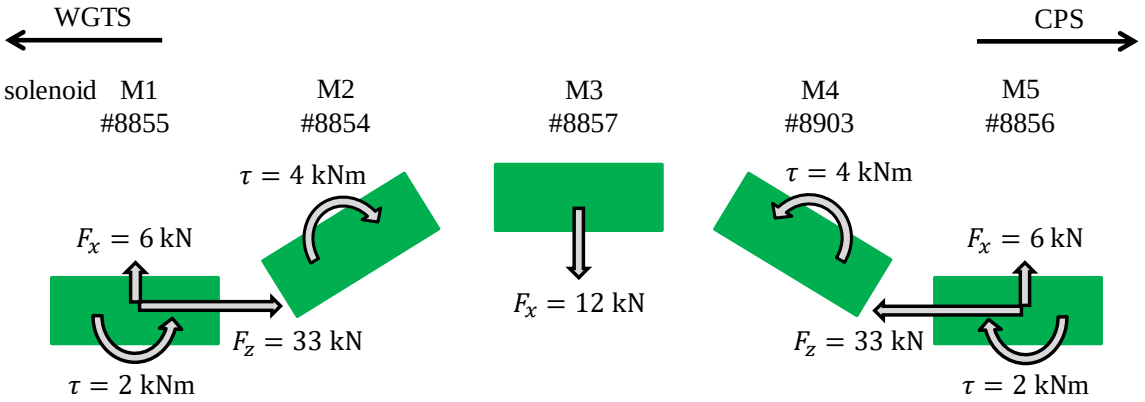

Figure 4.17: Magnetic forces on the DPS coils. Shown are the forces on the coils during stand-alone magnetic field operation mode of the DPS. During a global KATRIN magnetic field operation, the magnetic forces in z-direction on solenoids M1 and M5 are almost compensated by the forces of the neighboring solenoids M5 of the WGTS and the M1 of the CPS.

neutrino mass runs. For more information see [Gla15].

The alignment measurements presented in this section provide the following results:

- Coil position are not influenced by the operational temperature of 4 K.
- Vibrations or shocks during the shipping and installation have had no influence on coil positions.
- Even the strongest magnetic forces which can occur in the DPS only influence the coil position on a sub-mm range. As a result, this effect can be neglected effect for standard operation.

These alignment results provide a detailed model of the superconducting solenoids which can be used to create a simulation model in the next step.

4.3 Commissioning and performance of the cryogenic pumping section (CPS) cryostat

The main task of the final STS component, the cryogenic pumping section (CPS) is to reduce the tritium gas flow between the DPS and the pre-spectrometer by a further factor of $\sim 10^7$ while simultaneously guiding β-decay electrons to the spectrometer section [Ang05]. The required gas flow reduction factor is achieved by implementing a 3-K cold argon-frost layer to trap the remaining tritium by cryosorption. In section 4.3.1 results of the beam tube cooling are presented. The acceptance tests of the superconducting solenoids follow in section 4.3.2. Finally, the measured coil positions and their influence on the magnetic flux tube alignment is presented in section 4.3.3.

4.3.1 Beam tube cooling of the CPS

Argon was identified as ideal adsorbent to cover the cryo-surface of a cold beamline since it is chemically inert and features a high binding energy of at least F = 1200 J/mole with tritium [Luo08, Sch17]. The argon frost has to be prepared at a temperature of 6 K. At this temperature argon crystallizes in a very porous structure with porousity of 15 % [Nep05]. The density at ~ 6 K is $\rho \approx 1.77\,\mathrm{g/cm^3}$ [Dob56, Pet66, Kaz08, Eic08, Jan15]. The increased surface leads to a high amount of tritium which can be trapped. Due to the increase of the mean sojourn time in case of a decreasing temperature, a system of beam

tubes is operated at a temperature of 3 K, with a maximum overall temperature gradient of 0.5 K in beam direction, and of 0.2 K in radial direction (appendix C: DR3).

To prepare a pure argon frost layer, the remaining molecules such as water on the inner beamline surface have to be removed. Therefore the beamline has to be baked out in advance. The two beam tube sections at the front end, which include getter pumps, have to be baked out at 620 K to activate the getter material (see figure 3.6). The remaining beam tube sections, including the pump port 1 and the cold gate valve, should be heated up to 500 K (appendix C: DR3). Since the foreseen getter pumps have now been removed from the design, the reference is bake out the entire beamline, including pump ports and cold gate valve at 500 K to remove remaining water on the beam tube surface.

The cooling of the system started with the bake-out at reduced baking temperature of 400 K prior to first cool down. This challenge could be achieved. The directly following cool-down process afterwards reached operational temperatures of beam tube elements 2 – 5 after a period of 40 days (see figure 4.18). The preparation of the argon frost layer could not performed during this commissioning, since parts of the required argon injection system were still under construction at that time. As shown in figure 4.18, the stringent temperature specifications could only be achieved for parts of the beam tube. However, in-depth simulations showed that the measured temperature profile allows to reach a reduction factor of 10^7 [Sch17, Fri17].

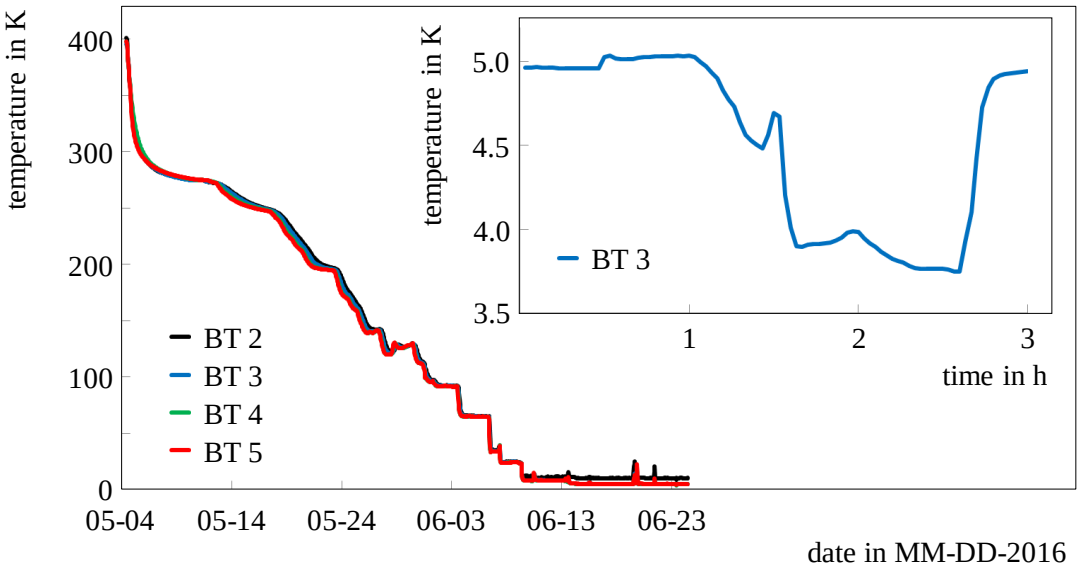

Figure 4.18: Temperature course of the CPS beam tubes. The cool-down of the CPS cryostat started after beam tubes were baked out with temperatures of up to 400 K. It took more than four weeks before the beam tubes reached their operational temperature. The inlet demonstrates the first cooling of the beam tube element 3 by activating the 3 K beam tube cooling system. The measurement was realized on June 23 2017 between 8:00 and 11:00 p.m. The figure is adapted from [Roe17].

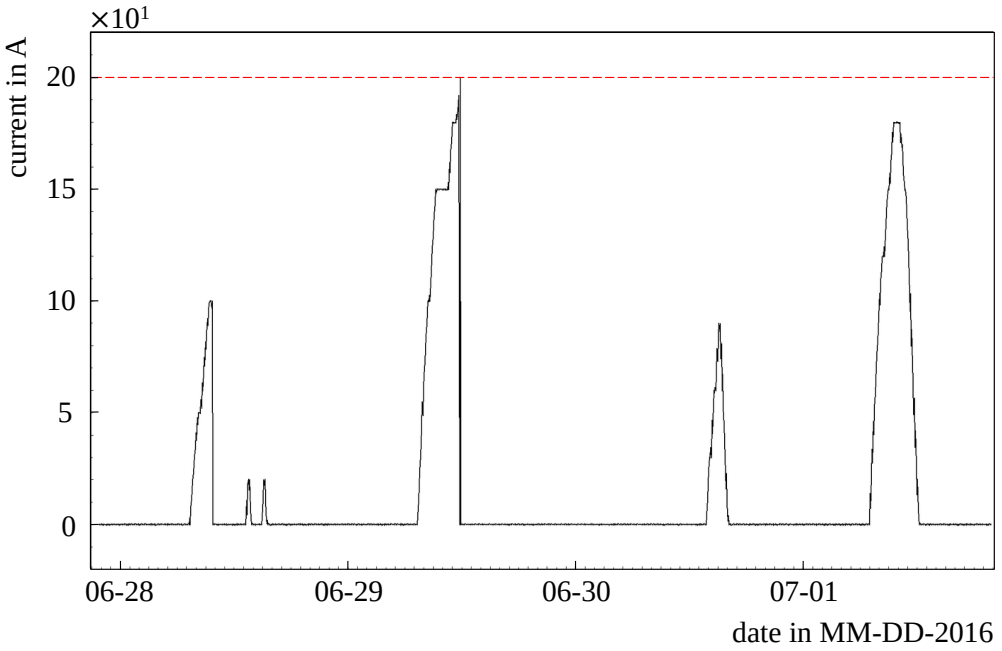

Figure 4.19: Performance of the CPS superconducting solenoids. The required current for nominal magnetic field is highlighted as a red dashed line. The first peak shows an initial test up to 50 % of nominal magnetic field, followed by two single tests up to 10 %. The third peak shows a quench occuring at 194 A with its characteristic sharp right edge. To ensure that the coils were not damaged during the quench, they were ramped up on June 30 to 50 % of the nominal magnetic field to perform further functionality and safety tests. The final peak shows that 90 % of the nominal magnetic field can be reached when the PS1 solenoid is energized.

4.3.2 Acceptance test of the superconducting solenoids

The first commissioning of the superconducting magnet system of the CPS was performed after operational temperatures were reached and the LHe vessel was filled with LHe. The CPS was tested at first as stand-alone unit. A preliminary magnetic field test up to 100 A corresponding to 50 % of the nominal magnetic field showed the expected usual behavior (see figure 4.19). However, during ramping of the solenoids up to 200 A, a quench occured at 194 A in solenoid M7 (appendix C: BW3). Additional tests suffered further quenches at 166 A and 167 A. This behavior changed after the PS1 solenoid was ramped up simultaneously so that a current of 180 A could be reached without quench. Due to the frequency of quenches it was decided to reduce the global magnetic field to a value of 70 % of the nominal magnetic field for the long-term neutrino mass measurements. Despite this, a magnetic field stability of $< 0.001\,\%/30\,\mathrm{d}$, which is more than one order of magnitude better than the specified stability of $\pm 0.03\,\%/30\,\mathrm{d}$ (appendix C: BW4) was measured by the monitoring system of the coil currents [Gil17].

4.3.3 Mechanical measurement of the actual dimensions

The CPS cyostat was designed and engineered by *ASG Superconductors*[6] in Italy. The alignment measurement between the beam tubes and the superconducting solenoids was performed during the extended assembly period by using a laser tracker. The very careful assessment of the alignment of the beam tubes with respect to the superconducting solenoids had to be performed in view of the later magnetic flux tube alignment inside the beamline. A maximum misalignment of 1 mm was specified to ensure a collision-free

[6] Corso F.M Perrone, 73r, 16152, Genoa, Italy

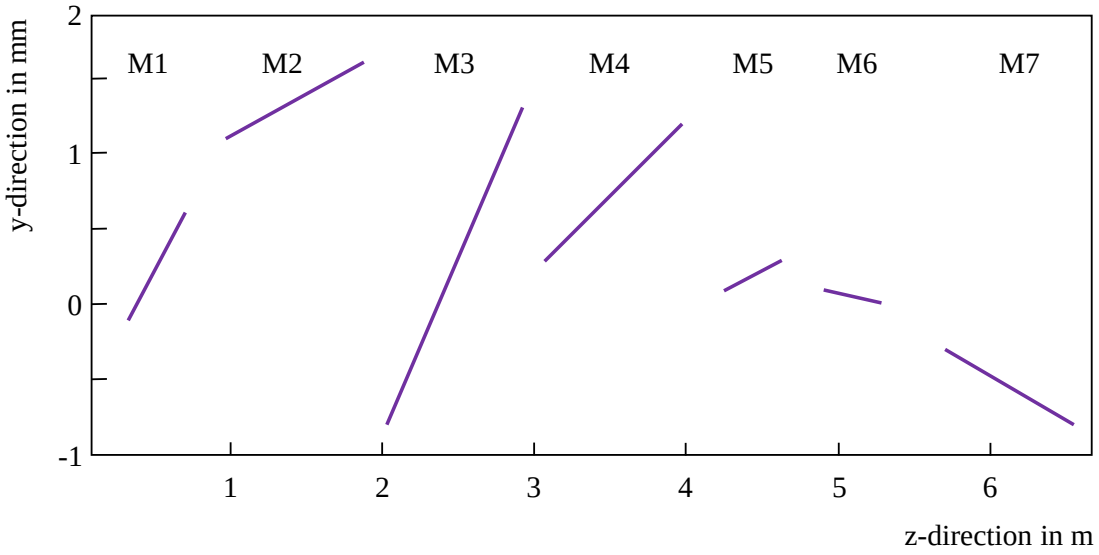

Figure 4.20: Measured position of the superconducting solenoids of the CPS. Shown is the position of the interpolated coil axes of the CPS solenoids in the y-z-plane. The solenoids M1 - M5 are tilted upwards in downstream direction. This results in an upwards shift of the magnetic flux tube which cannot be compensated by the solenoids M6 and M7 alone, which are tilted downwards in downstream direction.

magnetic flux tube guiding through the beamline (appendix C: DR3). Again the thermal contraction has to be taken into account since mechanical alignment measurements can only be performed under warm conditions. The largest deviation was determined to be $-1.1\,\mathrm{mm}$ in y-direction for solenoid M6. The measurement uncertainty is expected to be $\pm 0.25\,\mathrm{mm}$.

The measured alignment between the solenoids and the beam tubes are in good agreement and within specifications, except the alignment of coil M6. However, all coils except M6 are tilted upwards (+y-direction) in downstream direction with respect to the beam tubes. The magnetic flux tube is shift upwards (positive y-direction) on the downstream side of the CPS. The measured alignment of each CPS solenoid (M1 – M7) with respect to their design position is presented in figure 4.20. Since there are constrictions inside the beamline, this shift can cause collisions of the magnetic flux tube and need special attention.

Previous investigations reported in [Sac15, Gla15, Roe16] showed already the existence of non-negligible constrictions between the magnetic flux tube and the CPS beamline due to the tilt of the solenoids. This causes a magnetic flux tube shift at the downstream side of the CPS up to 2 mm. In combination with the DPS alignment, simulations indicate the occurrence of a vertical collision between the magnetic flux tube and the CPS beamline. In order to prevent these collisions, the DPS solenoid M3 was tilted downwards (−y-direction) by 0.4° in downstream direction to reduce the upwards shift within the CPS [Sac15, Gla15, Roe16].

4.4 Summary and outlook for the beamline modeling

In this chapter the individual commissioning of the WGTS, DPS and CPS was presented.

Two key systematic effects are caused by the WGTS source temperature. First, it results in Doppler broadening of the kinetic energy of β-electrons due to molecular motion. To

minimize this effect the source tube temperature has to be operated at a temperature of about 30 K. The commissioning of the two phase neon cooling system could demonstrate that the specified temperature regime can be reached. Second, at this temperature regime, a stabilization of the source tube temperature is paramount. The measurements revealed a temperature stability on the 0.1 % level [Ang05, Bab12] equivalent to 30 mK/h could be exceeded by one order of magnitude. In contrast to the outstanding result of the temperature stability, an inhomogeneity of about 500 mK was determined on the rear part of the source tube. Although the required temperature homogeneity was exceeded, simulations could confirm that its influence on the neutrino mass measurement can be neglected if the inhomogeneity accounted for the analysis of the source activity. This is possible due to the excitingly pefect level of temperature stability [Kuc16].

The required systematics can only be achieved if the 191 Tcm^2 flux tube guiding β-electrons is aligned collision-free inside the beamline. To prevent collisions, a maximum deviation of 1 mm between the beam tube and the corresponding solenoid was specified in the design. The observed alignment of the entire STS elements is in good agreement with specifications. However, the tilts of the CPS coils cause a shift of the magnetic flux tube which results in collisions. To compensate and counteract this shift, the solenoid M3 of the DPS was tilted in the opposite direction. The alignment obtained by this indicates a collision-free flux tube guiding of the 191 Tcm^2 flux tube. To prove this, all geometry and alignment data were implemented into the overall KATRIN simulation model. The shape and extension of the flux tube inside the beamline can then be calculated with the custom-made software package Kassiopeia. The Kassiopeia software and corresponding calculations of the alignment of individual STS components are discussed in chapter 6. Finally, the required magnetic field stability could be demonstrated, which is important for the magnetic flux tube alignment with respect to the extended KATRIN measurement duration of 60 days a single run.

CHAPTER 5

First Light measurement campaign

The KATRIN experiment has reached a distinct milestone on October 14, 2016, when electrons were first successfully guided through the complete system. This event, the so-called "First Light", was based on low-energy electrons generated at the upstream end of the 70-meter long beamline being detected and counted by the FPD. A comprehensive measurement campaign followed until December 2016, involving detailed alignment measurements as well as commissioning of an ensemble of beamline instrumentation units used for ion-blocking and -removal.

This chapter gives an in-depth overview of the objectives of the First Light measurement campaign, with a main focus set on alignment measurements and analyses, starting with the underlying objectives of the measurements in section 5.1. Since the final setup of KATRIN was not operational at this point in time, minor changes had to be implemented to enable these measurements. In section 5.2, the experimental setup is explained in detail. A detailed overview of the measurement principles and the methods to analyze the data with respect to alignment measurements is outlined in section 5.3.

5.1 Objectives of the First Light measurement campaign

As outlined above, after the final KATRIN main components were delivered in 2015 to KIT, each component was integrated with sub-millimeter accuracy into the beamline. The positions of each component and superconducting coil was measured mechanically during the extended assembly work by the supplier to comply with the required maximal position deviations. Chapter 4 gives a detailed overview of the on-site works to verify coil positions with respect to the beam tube elements.

All measured coil positions and geometry data were then included into the simulation software package Kassiopeia [Fur17] to perform first flux tube alignment simulations of the DPS [Hac15, Gla15, Sac15], the CPS [Jan15, Roe16] and the adjacent SDS part of KATRIN [Sch14, Har15, Mue16, Erh16]. These simulations already identified specific narrow spots between the 191 Tcm^2 flux tube and the STS beamline. Consequently, it is of major importance for the neutrino mass measurement to investigate alignment and transmission of the magnetic flux tube throughout the beamline experimentally and compare results to the simulations. This is the key objective of the First Light measurement campaign and the main objective of the thesis in hand.

During the First Light measurement campaign, an ion source allowed to investigate the extensive DPS beamline instrumentation used to block and remove ions. Furthermore, at this time the pre-spectrometer was first attached to the main spectrometer. This allowed more in-depth background investigations with the nominal SDS setup. For detailed

information about the ion investigation see [Kle18]. The objectives of the First Light measurement campaign relied on the properties of the electron and ion source in use.

5.2 First Light setup

The hardware configuration of the KATRIN beamline during the First Light measurement in the time period between October and December 2016, is special as all superconducting solenoids were situated at their foreseen places, generating a magnetic flux tube inside the fully constructed and evacuated beamline. To characterize alignment accuracies and transmission properties of the flux tube, a commissioning (phase III) of the system with non-radioactive sources was scheduled, making use artificial electron and ion sources.

However, the construction of the DPS beamline instrumentation was not completed during First Light. This system consists of three dipole electrodes, located in the beam tube elements 2 – 4, and two ring electrodes in beam tube 5 and pump port 5. Hence, the following beamline instruments were missing: the dipole electrode in beam tube 1 and the FT-ICR module in beam tube 5. A figure of the DPS beamline instrumentation is presented in the appendix A.

Of specific interest for these measurements was the rear end of the beamline, which is formed by the RW chamber, including the RW used as a photo-electron source. For the measurements, minor changes had to be performed as the regular UV-irradiation system was not available. Also, the assembly of the rear section EGUN was not completed at that time. Therefore, another readily available electron source had to be installed. To achieve all objectives, an ion source was needed as well, if possible with the opportunity to generate deuterium ions, since they are closest to the later tritium operating. Since the RW chamber has just one port in beam direction, for the EGUN, a combined source for generation of electrons as well as of deuterium ions had to be identified. The pre-existing ELectron Impact IOn source To Test the DPS (ELIOTT) was found to be the optimum solution, since it can be used as both an effective electron source as well as an ion source [Luk11, Win11, Sac15]. Additionally, it offers the opportunity to generate different ion species. It was attached to the central beamline flange of the RW chamber. The working principle of both electron sources is discussed in the following.

The rear wall irradiation

As described in section 3.2.2. the task of the RW is to generate a wide beam of low-energy electrons to obtain quasi-neutrality of the plasma inside the WGTS. During First Light it was used to fully illuminate the magnetic flux tube with low-energy electrons. Electrons at the gold coated RW surface are created via photo-effect by irradiating the RW surface with UV-light. The following requirements had to be fulfilled by the light source:

- Suitable for use in magnetic fields of the order of 300 mT
- Absence of illumination hot spots, corresponding to a homogeneous irradiation of the RW
- Deliverable rate of electrons per pixel of the FPD of the order of 10^2 up to 10^3 electrons/s

A so-called *mini-z*[1] system was identified as ideal easily-to-implement UV light source, which fulfills the first two requirements. The maximal measured electron rate during previous tests at the monitor spectromter was > 70 kcps over an area of 24 mm^2 , which corresponds to $\sim 2 \cdot 10^8$ cps/pixel (appendix C: BW1) at the FPD. The dead-time free

[1] RBD Instruments, Inc., 2437 NE Twin Knolls Dr., Suite 2 Bend, Oregon 97701, USA

maximum rate of operation at the FPD, with absence of due to pile-up effects, was exceeded [Sch14]. A light tube with two elbows was the identified to reduce the rate of an optimum of $\sim 400 - 600\,\mathrm{cps/pixel}$ (appendix C: FL2) at the FPD. Figure 5.1 shows a sketch of the setup, for more information see [Bab14, Sch16, Wec17].

The installed RW sample (ID number: 3-SS-ep-6)[2] was selected by K. schönung after comprehensive investigations [Sch16]. The local work function fluctuations over the whole RW was measured to be $\overline{\sigma}_{\mathrm{RMS,surface}} \sim 50\,\mathrm{mV}$, slightly above the specification demands of $\overline{\sigma}_{\mathrm{RMS,surface}} = 20\,\mathrm{mV}$. The time stability of the work function was measured to be $\leq 19\,\mathrm{mV}$ over three weeks [Sch16]. Since the specifications were not met, and additional scratches on the surface were detected, this sample will not be used for the neutrino mass measurement. However, this sample was perfectly adequate for use as a wide electron source, as this does not require an electron energy precision (or more specific work function homogeneity) in the sub-eV region. Hence, it is perfectly suitable for the commissioning tests [Sch16] described below.

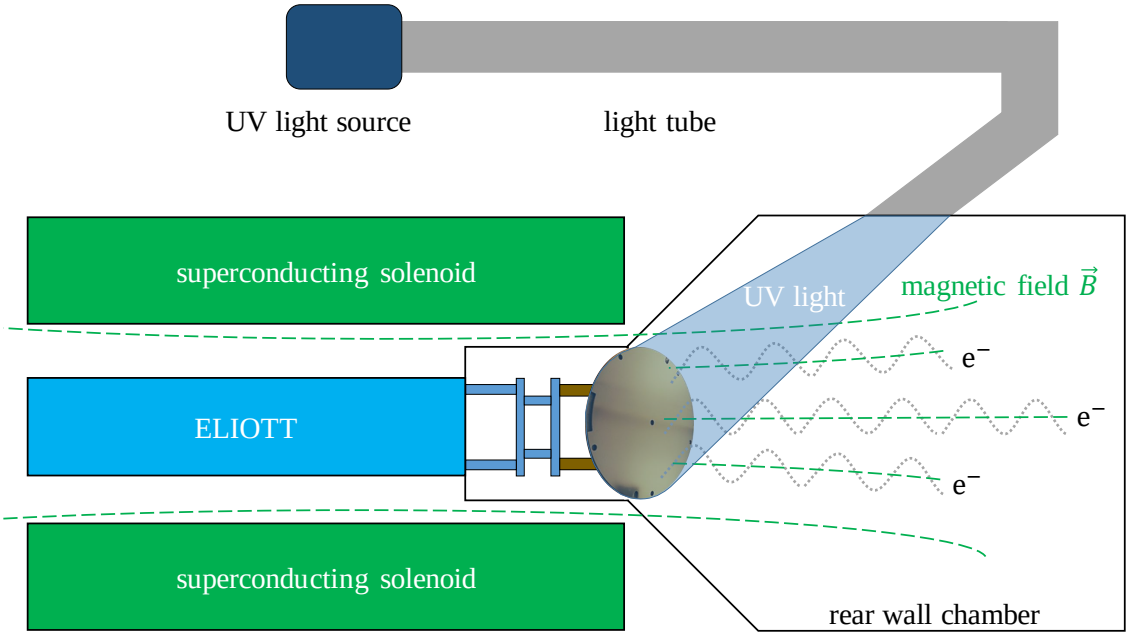

Figure 5.1: Principle to generate electrons at the Rear Wall. Shown is the sketch of the RW irradiation setup. UV light (light blue) from an emitter is guided trough an evacuated light tube and is focused on the gold-coated RW. A holding structure consisting partly of insulators (brown) enables to elevate the RW. The ELIOTT system is connected windowless to the chamber. Charged particles which are produced with ELIOTT can thus cross the central hole in the RW to generate a pencil beam of electrons or ions.

[2]Private communication K. Schoenung

The ELIOTT electron pencil beam

The ELIOTT ion source allows to produce either an ion beam or an electron beam without time-consuming hardware modifications. It was originally designed to serve as wide beam ion source covering the entire a magnetic flux tube with an area of 10.2 cm^2. The entire setup was installed inside the warm bore of the RS solenoid, which generates the magnetic guiding field downstream of the WGTS. A UV light source (Hamamatsu L10366) is used to irradiate a window, coated on one side with 5-nm thick backing layer of titanium, and a 15-nm thick gold layer. As UV light penetrates the thin gold layer, electrons are generated thus via the photo effect. By connecting the window to a negative potential and the neighboring electrode to a positive potential, electrons are accelerated and follow the magnetic field lines into a cylindrical mesh electrode. All electrodes are located inside an enclosing vacuum chamber, which is filled with the target gas be ionized by the electrons. An extraction electrode at negative potential retards electrons but accelerates positive ions, resulting in a positive ion beam, as illustrated in figure 5.2. The emitted rate of ions depends on the energy of the impinging electrons, the type of target gas and the pressure. For more informations on ELIOTT see [Luk11, Win11, Sac15]. To produce an electron beam, the target gas pressure inside ELIOTT has to be reduced ($< 10^{-5}$ mbar) to prevent ionization in the volume of the mesh electrode. The window is used as wide electron source. It is connected to a slightly lower negative potential than the RW, while all other electrodes are set to zero potential. The ion or electron pencil beam is finally released through a hole of 5-mm diameter inside the RW, which can only be passed by charged particles, at the center of the magnetic flux tube. In the following this electron pencil beam is named “pencil beam”.

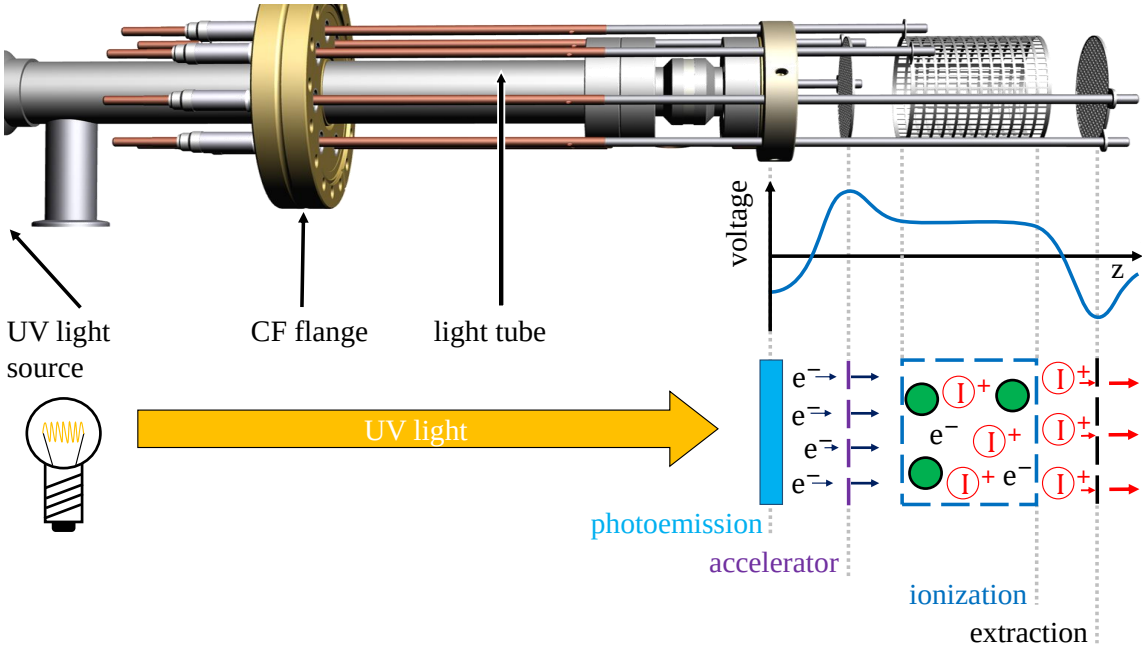

Figure 5.2: Ion production principle of the electron impact ion source ELIOTT. Shown on top is the CAD drawing of ELIOTT. The UV light is guided trough an evacuated pipe to a gold coated magnesium fluoride (MgF_2) window. There electrons are produced by the photo-effect. The following electrode is connected to a positive potential of up to +150 V and used as an accelerator [Luk12]. The target molecules ($p > 10^{-3}$ mbar) are ionized inside the cylindrical electrode. Accelerated by the extractor electrode, the ions can finally leave the ion source. Conversely, electrons are retarded and contained by the negative potential of the extractor electrode.

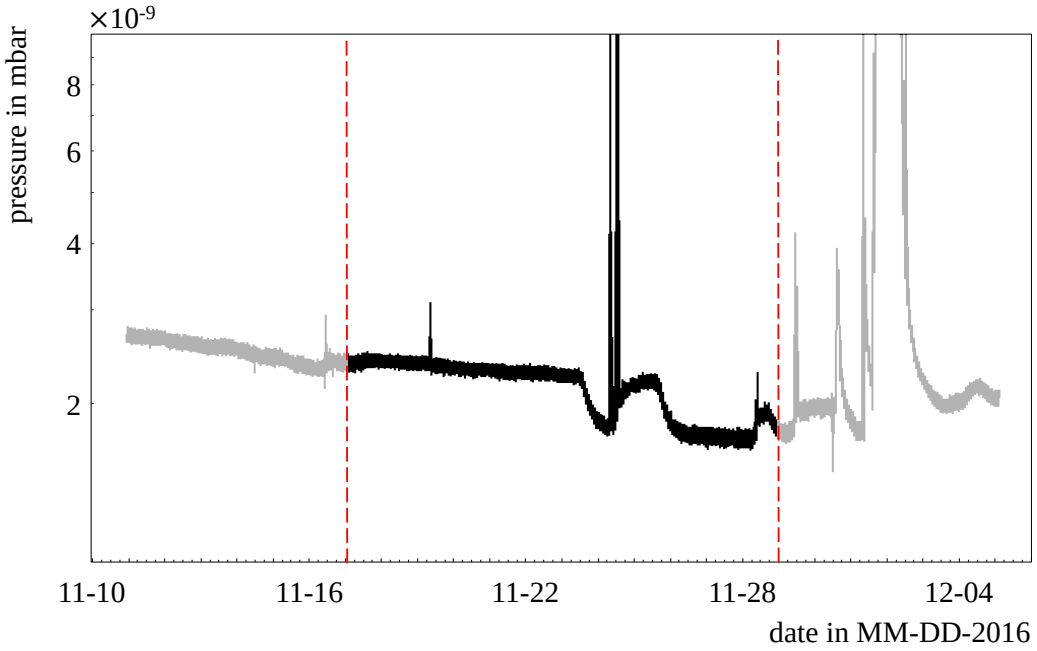

Figure 5.3: The vacuum performance in the main spectrometer. During the First Light measurement campaign lasting from November ten and December five, highlighted as the First Light time period. The pressure gauge (KATRIN number: 432-RPI-3-3110) is located at pump port three. In the unbaked spectrometer water is the dominant molecule. To receive the real pressure value, the gas correction factor for water (leybold extractor gauge manufacturer handbook ~ 1.0), the magnetic stray field (~ 1.05)[1] and the N_2 calibration factor (~ 1.16)[1] have to be considered. As a result, the measured pressure has to be multiplied by an overall correction factor of 1.218. The brief and abrupt pressure increases are caused by sensor failures.

Vacuum and magnetic field performance

During measurements, the STS beamline was evacuated by two turbo molecular pumps attached to the WGTS and the DPS, respectively, creating a pressure regime of $< 10^{-8}$ mbar. In addition, the 3 to 5-K-cold CPS beamline was acting as cold trap, reducing the gas flow into the SDS part of KATRIN by more than one order of magnitude. Since no gas was injected into the WGTS, the required reduction factor of the CPS, as outlined in section 3.2.4, had not relevance. Therefore, the operational temperature of the beam tubes had not be attained and no argon frost layer was prepared. The pressure in the main spectrometer pump port 3 was measured to be $< 10^{-8}$ mbar. In figure 5.3 the vacuum performance over the course of the First Light measurement campaign is shown.

A detailed investigation of the flux tube alignment can only succeed if the specified magnetic field stability can be maintained. Previous tests during the commissioning of all superconducting solenoids verified the specifications (chapter 4). Shortly before the start of the First Light measurement campaign, issues in the ramp-up of DPS solenoid M1 were observed (appendix C: DP1). It results from an abnormal fast increase of the pressure inside the LHe chamber during the ramp-up. To minimize the risk of a quench, the maximum allowed magnetic field was reduced to 30 % of the nominal value for this measurement campaign. Dedicated simulations which are outlined in section 6.1.3, were carried out to study the influence of a reduced magnetic field on the alignment measurements. After the start of the measurements, a drift of the magnetic field of the rear section magnet was detected. Corresponding magnetic field stability measurements with an NMR probe showed a significant decrease of the magnetic flux density. Within four days, the magnetic flux density continuously decreased from 0.799 T down to 0.780 T, resulting in a decline of

[1] Private communication J. Wolf

about $\partial B/\partial t = 5.03^{-3}\,T/d$. The loss of magnetic flux density was equivalent to $\sim 0.5\,\%$ in one day (appendix C: FL6). However, the magnetic field decay has no impact on the alignment measurements since the decay rate is two low for a short measurement period of 14 days. Since the electron pencil beam was used for the alignment measurements in the STS, the effect of the decreasing field of the RS solenoid results in a more focused electron beam, which has no impact on the alignment results, or on the SDS alignment measurements.

5.3 The alignment measurement

The main objective of the alignment measurements was to verify that the $191\,Tcm^2$ magnetic flux tube can indeed be guided collision-free through the entire KATRIN beamline. The second objective was to determine if also the larger $210\,Tcm^2$ magnetic flux can be guided collision-free between source and the FBM, since the FBM monitors the source activity in this outer region of the flux tube. The third objective was to determine the alignment of individual beamline components with respect to the FPD.

Previous measurements during SDS-II revealed that a $210\,Tcm^2$ magnetic flux tube can be guided collision-free through the SDS half of KATRIN [Har15]. Hence, only the alignment of the pre- and the main spectrometer with respect to the detector has to be investigated. Previous investigations found an asymmetric magnetic field configuration to be the ideal configuration to study the alignment of the spectrometers with respect to the FPD [Sch14, Har15]. For this type of measurement, the magnet on the upstream side of the spectrometer needs to be deenergized and the air coil system needs to be adjusted. An asymmetric magnetic field configuration in the spectrometer guides low-energy electrons produced by electron field emission [Fow28] from the wire combs of the spectrometer inner electrode system to the detector. In this way, the ring-shaped comb structure is projected on to the detector [Sch14]. Comparing the center of the mapped rings with the wafer center provides the alignment between the spectrometer electrodes and flux tube and the FPD. To identify the best suitable magnetic field setting for the alignment measurement of pre- and main spectrometer, extensive tracking simulations have to be carried out. The simulations and their results are then presented in section 6.3.2. The First Light alignment measurements of SDS and their results are presented in section 7.3 and compared to the simulation results.

For the STS alignment measurement, the magnetic bottleneck method is used since it provides the information about the largest collision-free magnetic flux tube as well as

Table 5.1: Expected radii of the image of the bottlenecks on the FPD for different magnetic flux tubes. The table shows the radii of two different magnetic flux tubes at different locations along the beamline. The size of the mapped bottleneck image at the FPD provides the information about the collision-free flux tube size. Highly important is the fact that the magnetic flux tube at the bottleneck part (15 %) defines the two flux tube volumes of interest. Due to the higher magnetic field ratio of the FPD solenoids (20 %), the magnetic flux tube is compressed according to equation 3.8. The magnetic field at the center of the FPD was calculated with Kassiopeia to be 0.665 T at 20 % of the nominal field.

section	magnetic flux tube radius in mm	
	$210\,Tcm^2$ equivalent	$191\,Tcm^2$ equivalent
FPD	38.8	37.0
WGTS	43.1	41.1
DPS	36.6	34.9
CPS	34.6	33.0

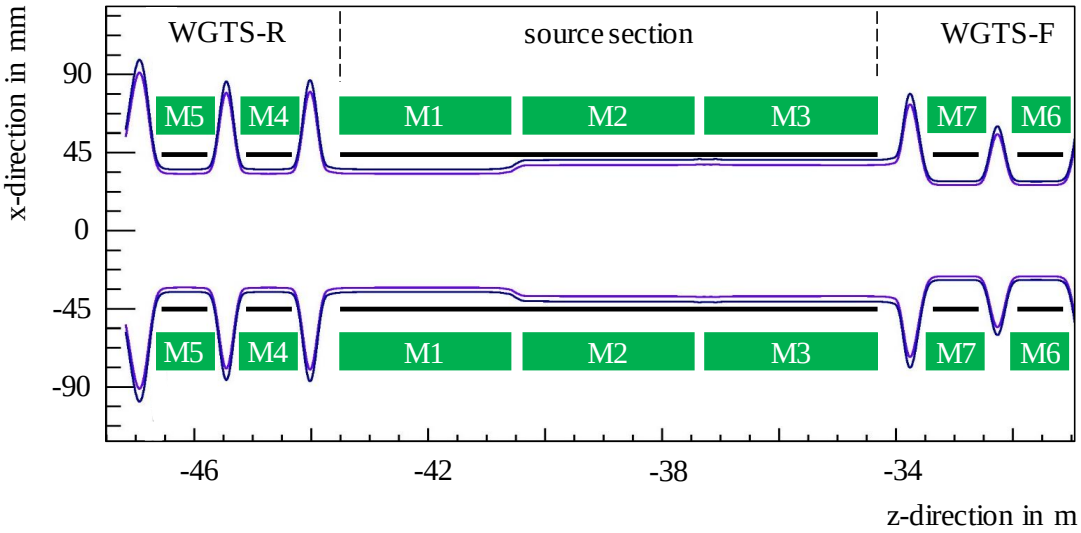

Figure 5.4: Principle of the magnetic bottleneck. All solenoids are operated at 20 % of the nominal field, except the two WGTS solenoids M2 and M3, which are operated at 15 % (0.54 T) of nominal value. The width of the flux tube at this position is extended to creates a magnetic bottleneck. The left end of the bottleneck is less pronounced than the right end, since the 20 % field of the WGTS-R and M1 is 0.72 T and the WGTS-F field is at 1.12 T. The inner surface of the beamline is highlighted as a black line.

the alignment between the investigated section and the FPD. The magnetic bottleneck method is based on the magnetic flux tube conservation according to equation 3.8. To this end, the magnetic field of the solenoids in the section to be investigated is slightly decreased, as demonstrated for the WGTS solenoids M2 and M3 in figure 5.4. As a result, the magnetic flux tube in this section expands and its outer parts will eventually collide with the beam tube, defining the shape of the bottleneck. If the shape of the bottleneck is investigated by making use of the wide beam source or the pencil beam, an image is mapped onto the FPD. The image size mapped in combination with the magnetic field at the FPD then provides the maximum size of the flux tube which can be guided through the section investigated (see table 5.1). The center of the mapped image can be comprised to the center of the wafer provide alignment information.

Since the global magnetic field had to be reduced to 20 % of the nominal value due to the issues with the first DPS solenoid M1, the value magnetic flux reduces by the same factor. With the outlined bottleneck method the flux tube volume is investigated, however, which is independent of the global magnetic field settings. Hence the reduced magnetic flux value is of no concern, and the original magnetic flux values of 191 Tcm^2 and 210 Tcm^2 will be used in the following but with the extra title “equivalent”.

Due to the reduced global magnetic field during First Light, simulations have to be used to investigate whether the alignment data at reduced field is comparable to alignment data at nominal field. The simulations also provide position information for collisions and constrictions of the magnetic flux tube. These then are used to analyze the measurement data. Finally, the simulations are used to find out which electron source is best suited to map a bottleneck image onto the wafer.

CHAPTER 6

Modeling of the KATRIN beam line

The focus of this chapter is to determine the magnetic flux tube alignment of the KATRIN Kassiopeia model, including its detailed transmission characteristics. The data obtained via simulations is used to interpret the corresponding results of the alignment measurements. Therefore it is necessary to investigate and precisely localize the points or area of collision or of close encounters between the magnetic flux tube and the beamline. This information is of vital importance for subsequent measurements at nominal magnetic field settings will provide only integrated transmission probabilities over the global beamline as mapped image on the FPD. The collision location along the z-axis of the beamline cannot be inferred from these data. Simulated collision points and their positions have to be verified by measurements, but at nominal magnetic field setting this is difficult. To localize the collision points along the beamline, a different magnetic field setting is used to investigate the beamline section-wise.

The magnetic bottleneck is based on an expansion of the magnetic flux tube in the section to be investigated by reducing the magnetic field in this section, while leaving all other magnets on their initial field. The creation of such a magnetic bottleneck has to be verified by the simulations. The detector wafer delivers data of a measurement only as mapped image. A major aspect of this work is to identify the best electron source to map these bottlenecks along the z-axis as well as in azimuth. Therefore, first a wide beam to fully illuminate the magnetic flux tube with electrons and identify a bottleneck was simulated, and later a pencil beam, which was used to scan the magnetic flux tube. Since the resolution of the mapped image on the detector wafer is limited by the pixel size, a comparison between both sources has to be implemented to identify the best measurement technique. The two measurement techniques for the bottleneck method in the STS part, and the asymmetric magnetic field setting for the SDS were simulated and evaluated in this thesis for the subsequent First Light alignment measurements.

This chapter will initially outline the framework of Kassiopeia in section 6.1, and introduce its implementation for the KATRIN geometry as well as the global magnet configuration. In addition, first investigations for different magnetic field settings and their influence on the flux tube alignment as well as collision points are outlined there. Afterwards, simulation results presented which describe the influence of magnetic dipole fields at the WGTS on shifts of the pencil beam in section 6.2. The scanning both electron beams is then used in section 6.3 to map magnetic bottlenecks in the STS part. This then gives key insights to alignment and transmission of the STS beamline. Additionally, the alignment of the SDS part is simulated and outlined in section 6.3.2.

6.1 Kassiopeia – A versatile particle tracking simulation tool

The Kassiopeia particle tracking framework was developed by the KATRIN collaboration with the key objective to provide a tool to propagate electrons or ions through the complex fields and geometries of setups such as KATRIN [Fur17]. In this regard, not only particle trajectories have to be calculated, but also electromagnetic fields via KEMfield which influence the particle tracks. Each of these tasks could, in principle be performed separately by existing tools, such as GEANT4 [Ago03] for particle tracking, and COMSOL[1] for electromagnetic field calculations. The simulation toolkit Kassiopeia outperforms a fusion of both codes. It is based on C++ object-orientated code and XML to define geometries and field configurations. Based on the fast and accurate computation of three-dimensional and axially symmetric static electromagnetic fields, it is possible to evaluate the sensitivity of the entire experiment via the simulation of interactions between tracked particles and the residual gas molecules as well. This even includes interactions with stainless steel surfaces for an detailed investigations of background processes.

For axisymmetric coils, the zonal harmonic expansion method is used to calculate magnetic fields [Gar51, Glu11]. This method is up to a factor 10^3 faster than the elliptic integral method, and is especially appropriate for trajectory calculations of charged particles with high accuracy [Glu11]. In case of non-axisymmetric coils, such as the WGTS dipole magnets with their transverse dipole fields, a directly integrating Biot-Savart formula is computed [Glu11]. Hence, Kassiopeia is a powerful and fast simulation tool kit to study the motion of charged particles trough the entire KATRIN beamline. These advantages, make it perfectly suited to investigate the magnetic flux tube alignment of the system. To do so, the complex geometries of the superconducting (s.c.) solenoids or the dipole magnets have to be implemented first, which is detailed in the following.

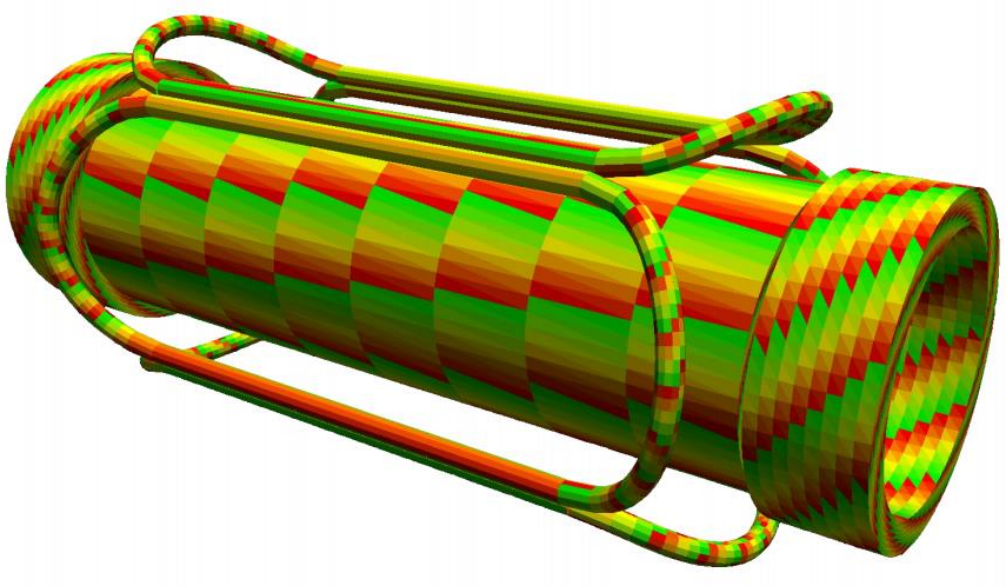

Figure 6.1: Kassiopeia model of the WGTS superconducting magnet M5. The superconducting main coil is surrounded on both ends by two superconducting correction coils. Located around this coil system are two superconducting dipole systems. The figure visualizes the discretized geometry mesh used in Kassiopei. The figure is adopted from [Def17].

[1]Comsol Multiphysics GmbH, Robert-Gernhardt-Platz 1, 37073 Göttingen, Germany (https://www.comsol.de/)

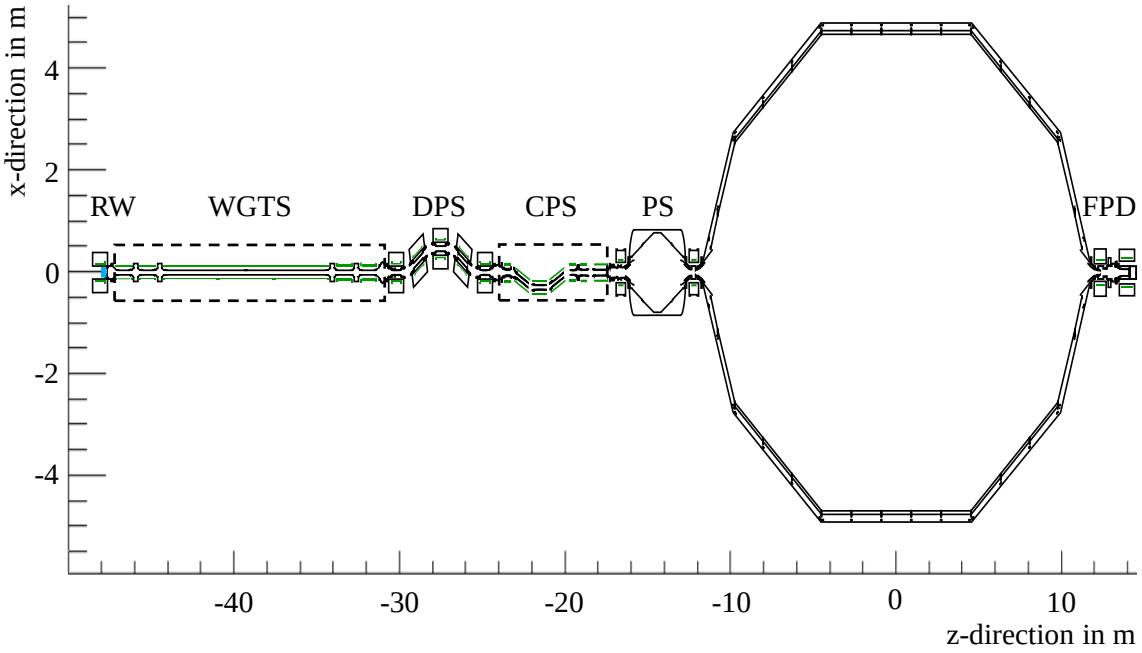

Figure 6.2: The First Light KATRIN Kassiopeia model. Black lines shows the implemented beamline components in the x-z-plane during First Light. The WGTS and CPS cryostats are highlighted with dashed lines. Individual superconducting solenoids are drawn in green. On the downstream side, the beamline ends with the detector wafer (FPD), and at the opposite side patricide trajectories start with the RW drawn in light blue.

6.1.1 Implementation of the global KATRIN beamline

The Kassiopeia model make use of a global coordinate system where individual components such as the WGTS or the main spectrometer are placed. The geometries of each components are defined in a local coordinate system. Each component is composed of basic and complex shapes. The whole setup can be put together by placing components in the global coordinate system.

To define geometries in Kassiopeia, all required information is implemented in XML-files. To build the entire beamline, templates for basic and complex shapes are provided. For instance, a tube with defined radius and length can be created from a basis shape template for a rotated polyline surface. To create a tube, the information about its radius and initial and final z-positions are required. Connecting these two points to a line and rotating it around the z-axis creates a cylinder geometry. To create more complex shapes, such as pump ports, multiple surfaces are put into one space and aligned via separate translation and rotation.

Figure 6.1 exemplifies the Kassiopeia model of the WGTS coil M5, which consists of three cylinders. The largest cylinder is the main coil. Two small cylinders, the correction coils surrounding both ends of the main coil, plus a vertical and a horizontal pair of superconducting dipole magnets are also implemented. The dipole magnets most vividly illustrate the convenient creation of a complex geometry in Kassiopeia.

The actual position of the individual sections with respect to each other was obtained by using advanced measuring equipment such as Laser Tracker[2] and FaroArm[3]. A realistic geometry of each section is based on the "as-built" computer aided design (CAD) drawings. The position of critical parts of the geometry such as the beamline or the coil position

[2] Accuracy up to 0.015 mm (http://www.faro.com)
[3] Single point repeatability from 0.024 mm to 0.064 mm (http://www.faro.com)

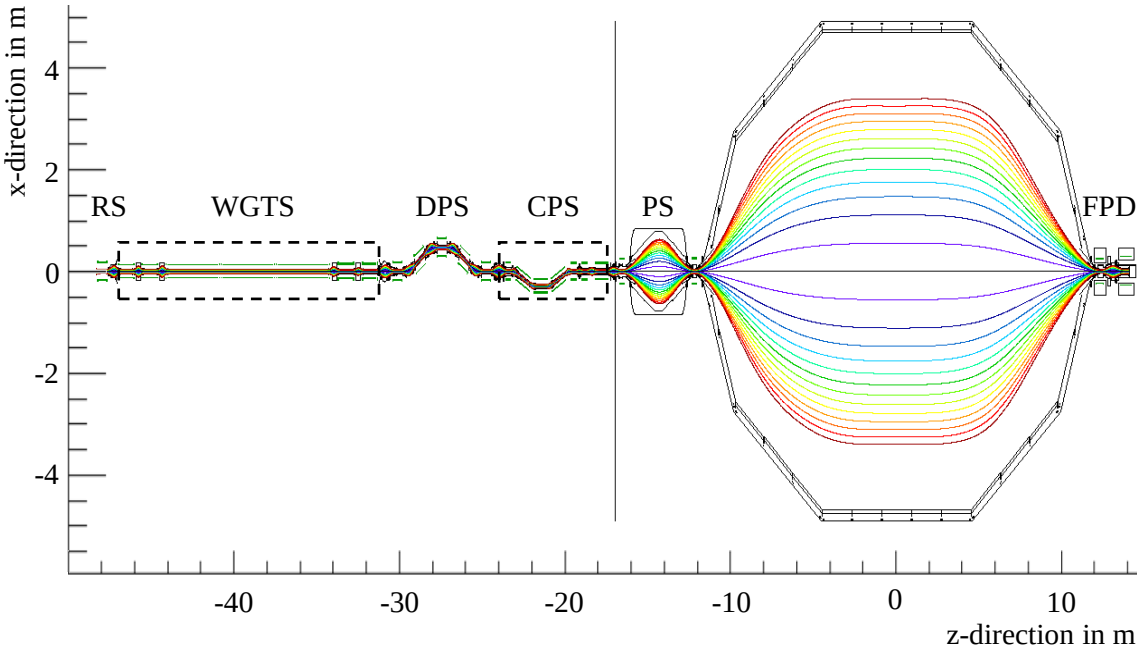

Figure 6.3: Simulation of the global magnetic flux tube. All magnets are operated at 20% of the nominal field. The simulated magnetic flux tube corresponds to the 191 Tcm^2 equivalent. Hence the flux tube volume is the identical.

were investigated in more detail (see chapter 4). Different effects can influence the coil position. To achieve a realistic model of the global magnet configuration, these effects and their implementation are outlined in the following.

6.1.2 Global magnet configuration

A large set of position measurements was obtained during assembly of the cryostats to obtain position and orientation of single coil to verify the stringent specifications, as detailed in chapter 4. To improve the magnet model even further, more precise position data of single coils inside the cryostats is required. In addition, the following effects have to be taken into account to obtain coil positions during magnetic field operation:

- The low temperatures (4 K) to ensure the superconductivity of the coil causes significant thermal contraction, which can lead to a relocation of the coil as well.
- The rather strong magnetic forces can also cause a displacement of a coil, in particular as some magnets in the DPS or CPS cryostats are arranged in an Ω-shaped geometry, whereby the coil experiences a torque (see figure 4.17).
- During shipping magnets can be exposed to vibrations which also could lead to a relocation.

Each coil in the Kassiopeia model is implemented via the number of windings from the as-built drawings. The required coil current to reach design values was determined in pre-acceptance by the manufacturer. Since currents can easily be adjusted and fine-tuned in Kassiopeia, it is possible to simulate different sizes of the magnetic flux tube along the beamline. For all charged particles being tracked along through the beamline, the corresponding field line can be visualized (see figure 6.3).

This model provides a realistic magnetic flux tube model. One benefit is that narrow gaps between the beamline and the magnetic flux tube can easily be identified. Another benefit is that a large number of different magnetic field settings can be investigated to obtain the best suited lay-out. In the case of First Light the main objective was to check whether

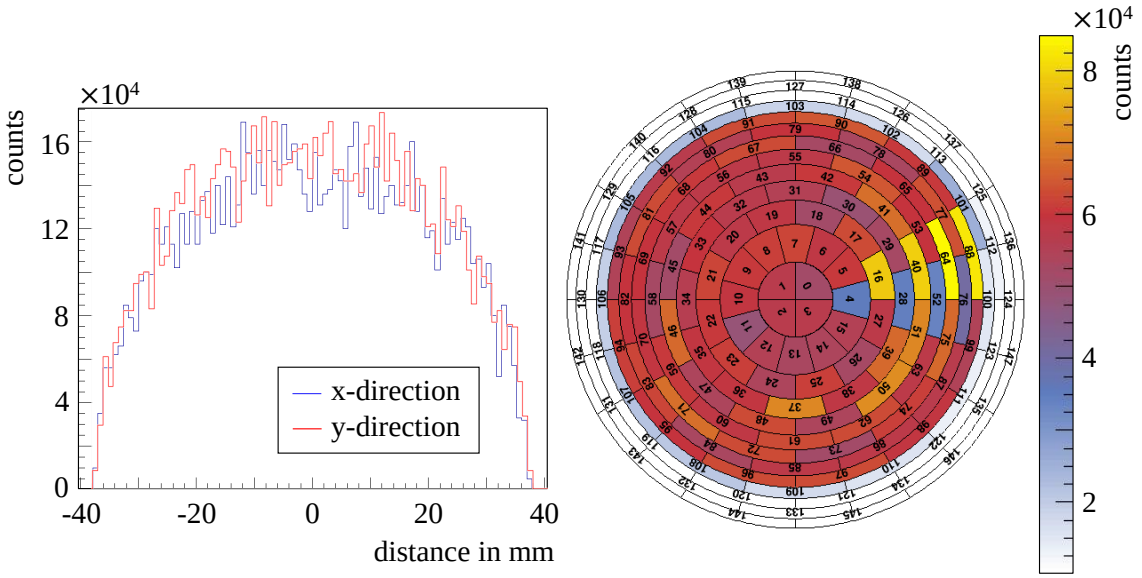

Figure 6.4: Simulation of a mapped image of a fully illuminated magnetic flux tube of the rear wall. The left figure shows the count rate of the mapped RW-image along the x- and the y- directions on the detector. On the right side the event pattern on the detector wafer shows the simulated count rate of each pixel, illustrating the mapped RW image. The simulation is created for a global magnetic field of 20 %, with the rear section solenoid operated at 15 % to map the complete RW image complete with the FPD. Using a magnetic field of 100 % and a rear section solenoid at 75 %, identical simulation results are achieved.

the alignment results obtained at a reduced magnetic field are comparable to alignments at nominal field, as presented in the following section.

6.1.3 Different magnetic field settings

The alignment simulations described here are used for later comparison with alignment measurement data obtained during the First Light campaign, presented in chapter 5. The following simulations were carried out to ensure comparability of the alignment measurement data for different magnetic field settings, resulting in two major objectives.

The first objective was to investigate the distance between the magnetic flux tube and the inner surface of the beamline. Since the flux tube alignment does not depend on the overall magnetic field and the alignment simulations of section 6.1.4 apply for all global magnetic field settings. This is proven by distance simulations at 20 % and 100 % of the nominal magnetic field. In comparison to the simulation, the reduced magnetic field has a noticeable influence on the flux tube alignment in reality, due to the decrease of the force between the coils which decreases quadratically with the magnetic field, resulting in possible coil movements due to the different magnetic forces. The resulting coil movement at maximum magnetic field was determined to lie in the sub-mm region only, as shown in section 4.2.3. This effect on the alignment measurement hence is negligible as the detection of sub-mm changes is not possible due to the FPD resolution. In addition, one has to take into account that magnetic materials, such as weldings at the beamline components, could produce a non-negligible effect at reduced magnetic field settings $< 10\,\%$, due to stray field. However, it could be verified that this effect is negligible at values of 20 % nominal.

The second objective was to prove the size of the image on the detector, which should be constant due to the conservation of the magnetic flux, according to equation 3.8. This could also be confirmed, as no variation of the image was observed (see figure 6.4). These

initial results already confirm that the global alignment measurement is independent of the magnetic field, as long as the global magnetic field is reduced by the same ratio, including the air coil system.

6.1.4 Identified constrictions

As shown above, the alignment of the magnetic flux tube remains constant for different magnetic field settings, if the global field is reduced by the same ratio. Thus, alignment results presented in this section are simulated at nominal settings.

An in-depth understanding of constrictions in each section can be obtained by calculating the distance between the 191 Tcm^2 magnetic flux tube and beamline components. The focus here is critical areas in STS, as corresponding areas into SDS part were already determined in previous investigations during the SDS-I and SDS-II campaigne mitigated by hardware updates, resulting in full transmission of the 210 Tcm^2 magnetic flux tube there [Sch14, Har15, Erh16].

In the STS components, the Ω-shaped beamline parts of DPS unit obviously and the CPS are of special interest. As shown in figures 6.5, 6.6 and 6.7, the distance between the 191 Tcm^2 magnetic flux tube and the inner surface of the beamline can shrink to < 3 mm at distinct sections of the beamline, especially in the region of the beamline instrumentation at the DPS and beam tubes 5 and 7 of the CPS. The simulated magnetic field lines in these plots correspond to the outer field lines of the 191 Tcm^2 magnetic flux tube, but apply for each 191 Tcm^2 flux tube equivalent as well.

To measure the 191 Tcm^2 flux tube, wide beam electrons can be used to detect rough collisions, since the UV-source illuminates a larger flux tube area of 195 Tcm^2. Hence, collisions manifest as reduced count rate or even as complete shadow at some pixels of the FPD. However, this projection includes no information about the z-position of collision points along the beam axis. A section-wise investigation of collision points thus is necessary with the magnetic field being lowered in one section to create a magnetic bottleneck as described in section 5.3. However, a fully illuminated flux tube is a first rough check to locate collision points in azimuth and radius and to determine the largest collision-free magnetic flux tube. Evidently, the pixel size limits the resolution of the FPD.

An electron pencil beam which can be created by the ELIOTT provides more precise information when scanned across the magnetic flux tube (see section 5.2). Since the pencil beam has a fixed position at its point of origin at the RW (see figure 5.1), it has to be steered across the magnetic flux tube by using the s.c. dipole magnets of WGTS. Based on the very good correlation between dipole currents and the pencil beam shift, the location of the magnetic bottleneck in azimuth can be measured more precisely. This provides a more accurate estimate of the size collision-free magnetic flux tube. To this end, simulations were carried out to investigate the pencil beam behavior under influence of the dipole magnets.

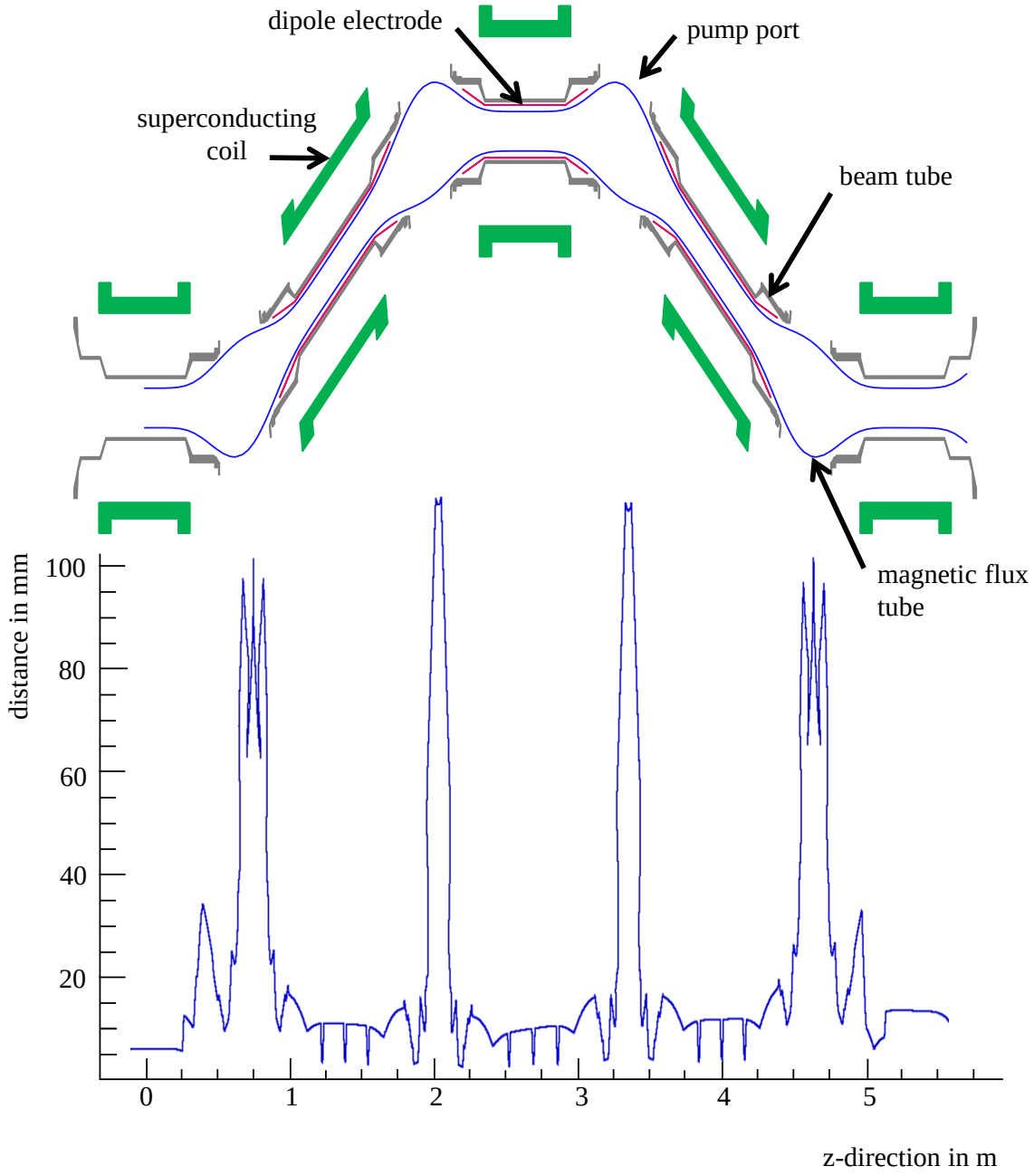

Figure 6.5: Distance between the magnetic flux tube and the DPS beamline. In the upper part of the figure the DPS beamline setup during First Light is shown, including the dipole electrodes highlighted in red and the 191 Tcm^2 flux tube equivalent in blue. The vertical scale is magnified to improve visibility of the beamline and its instrumentation. The single beam tube elements, highlighted in grey, are surrounded by the s.c. coils marked in green. The pump ports connecting the beam tube to the beamline are not displayed here (see figure 3.4). The lower part of the figure shows the distance between the nominal magnetic flux tube (191 Tcm^2) and beamline elements as function of the z-direction. The smallest distance occurs at the position of the three dipole electrodes, and in particular in azimuth at their lobules. No deviation of the distance for 20 % and 100 % of nominal field setting occurs.

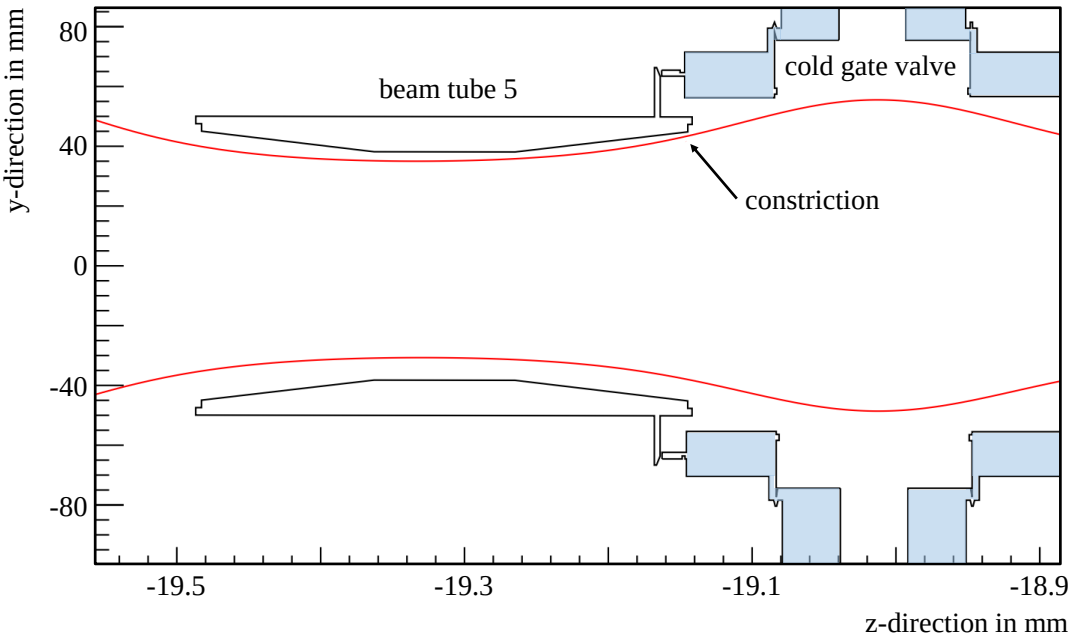

Figure 6.6: Distance between the magnetic flux tube and beam tube 5 of the CPS. Shown is the constriction between the 191 Tcm^2 flux tube equivalent in red and beam tube element 5 of the CPS (see figure 3.6). The figure is adapted from [Roe16].

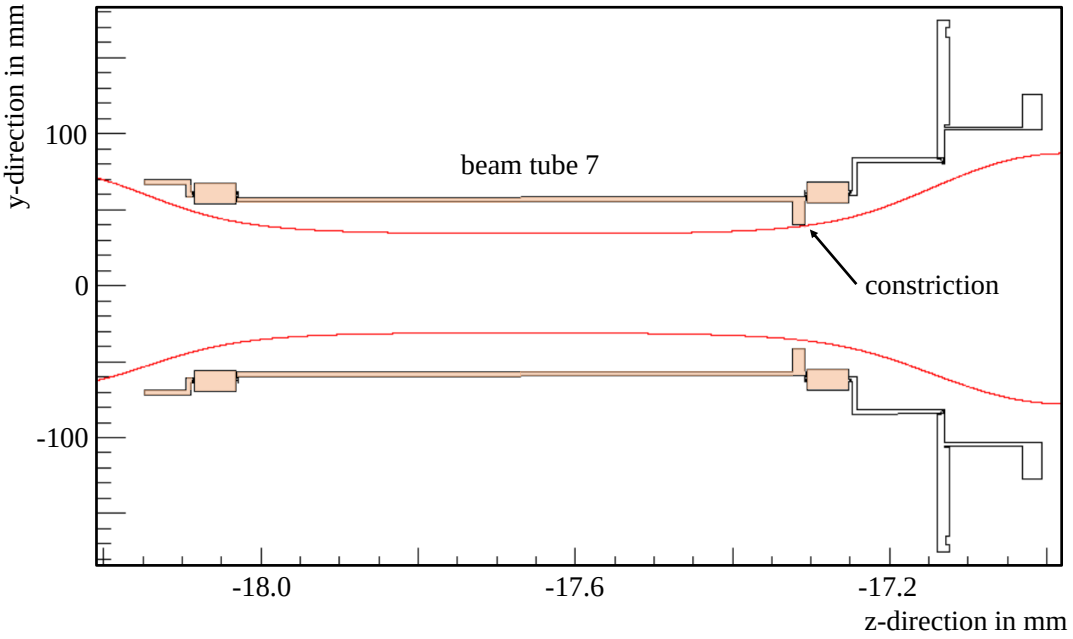

Figure 6.7: Distance between the magnetic flux tube and beam tube 7 of the CPS. Shown is the constriction between the 191 Tcm^2 flux tube equivalent in red and beam tube element 7 of the CPS highlighted in orange (see figure 3.6). The figure is adapted from [Roe16].

6.2 Simulation of the electron pencil beam

In the following the behavior of the pencil beam under the influence of the s.c. WGTS dipole magnets is investigated to quantify the correlation between shifts of the pencil beam and dipole currents. This corresponding simulation is performed at a global magnetic field setting of 20 %.

In a first step (see section 6.2.1) the pencil beam shift for horizontal and vertical directions is simulated in integer steps of the dipole current until collisions of the pencil beam with the beamline occurs. This provides the correlation values. In the second step the influence of the s.c. dipole stray field on the magnetic bottleneck is investigated (see section 6.2.2). This is motivated by the fact that a significant change of the magnetic field of the bottleneck would affect the alignment results obtained by the pencil beam scan. The third step is to investigate the transmission of the global flux tube in section 6.2.3.

In contrast to the real test-setup, simulated electrons of the pencil beam are not generated behind the RW, since the ELIOTT module was not integrated into the Kassiopeia model. Therefore, the hole inside the RW disc was used as point of origin (see figure 5.1).

6.2.1 Deflection of the electron pencil beam by using magnetic dipoles

To investigate a bottleneck in the WGTS, created by the solenoids M2 and M3 (see figure 5.4), the dipole magnets on the rear side of the WGTS have to be used (see figure 3.3). As the setup of the dipole magnets on the rear side and on the front side are identical, the following results apply to both.

To obtain correlation values, the current is varied in 2 A current steps in x- and y-direction. The behavior of the pencil beam under influence of the horizontal dipole magnets is illustrated in figure 6.8. The simulation evidently provides the exact location of the pencil beam on the detector wafer. Hence, the distance to the wafer center is known accurately. The results for horizontal and vertical pencil beam shifts is combined in figure 6.9.

The observed shifts of pencil beam is influenced by systematic effects (see section 7.2.2), which depends on the shift direction and on the positive or negative orientation of x- and y-direction. To obtain simulation results, which are comparable with the experimental results, the shift of the pencil beam was investigated separately for all four orientations. Thus, four different linear correlations between dipole current (I) and shift (S), with respect to the wafer center are required:

$$S(I_{+\mathrm{x}}) = (+2.06 \pm 0.02)\,\frac{\mathrm{mm}}{\mathrm{A}} \cdot I_{+} + (0.16 \pm 0.26)\,\mathrm{mm}, \tag{6.1}$$

$$S(I_{-\mathrm{x}}) = (-2.04 \pm 0.02)\,\frac{\mathrm{mm}}{\mathrm{A}} \cdot I_{-} + (0.54 \pm 0.21)\,\mathrm{mm}, \tag{6.2}$$

$$S(I_{+\mathrm{y}}) = (+2.10 \pm 0.02)\,\frac{\mathrm{mm}}{\mathrm{A}} \cdot I_{-} - (3.33 \pm 0.25)\,\mathrm{mm}, \tag{6.3}$$

$$S(I_{-\mathrm{y}}) = (-2.12 \pm 0.03)\,\frac{\mathrm{mm}}{\mathrm{A}} \cdot I_{+} + (3.51 \pm 0.32)\,\mathrm{mm}. \tag{6.4}$$

These linear equations include all necessary alignment information between RW and the FPD. The average of the x-axis interceptions of equation 6.1 and 6.2 is $\mathrm{x} = (-0.15 \pm 0.24)\,\mathrm{mm}$, caused by the horizontal misalignment between the RW and the FPD. The vertical misalignment between the RW and the FPD corresponds to the average of the y-axis interception of equation 6.4 and 6.3, it is $\mathrm{y} = (+3.42 \pm 0.29)\,\mathrm{mm}$. Equivalent to three x- and y-axis interceptions, a current of $I_{\mathrm{x}} = +0.07\,\mathrm{A}$ and of $I_{\mathrm{y}} = +1.63\,\mathrm{A}$ is required to center the electron pencil beam onto the wafer.

The pencil beam can then be centered by adjustius dipole currents so that all four “bulls eye” pixels of the FPD center yield nearly the same count rate. The tolerable deviation of

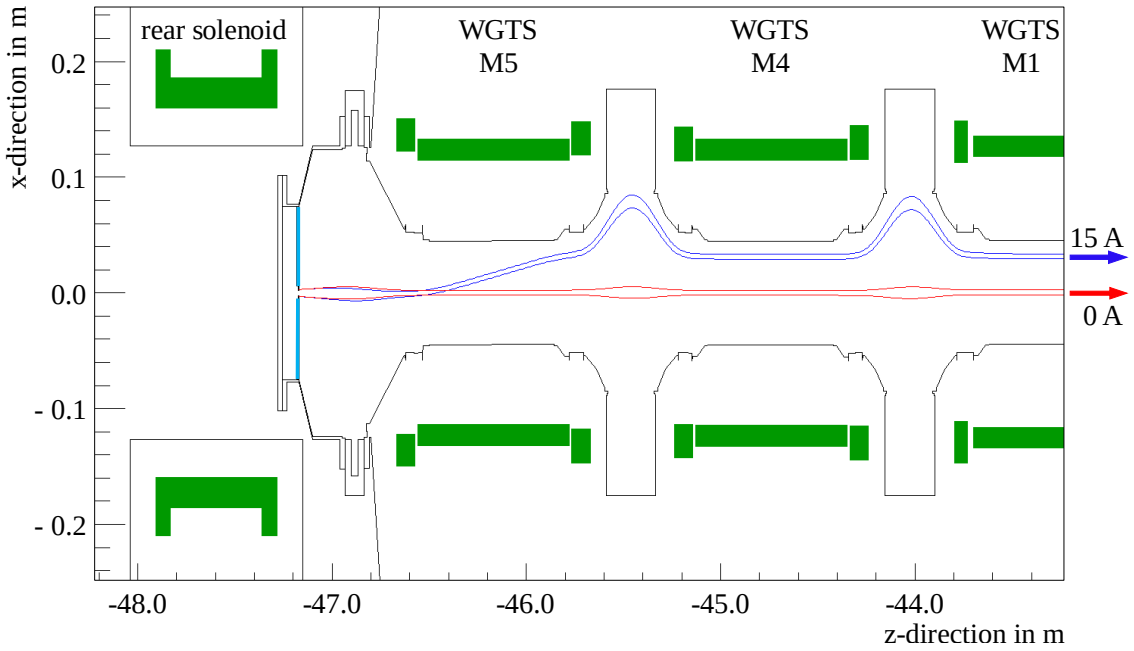

Figure 6.8: Simulated shift of the electron pencil beam. Shown is the rear part of the WGTS with its magnetic coils M4 and M5 displayed in green, as well as the solenoid of the rear section in the x-z-plane. The dipole magnets on this side are located around the solenoid M5 (see figure 6.1). A 2.5-mm radius hole in the center of the RW disc, highlighted in light blue, is the point of origin of the electron pencil beam. The simulation was performed at global magnetic fields of 20 %. To visualize the shift due to the dipole magnets, the non-shifted beam in red and the horizontally shifted beam with a dipole current of $I_x = 15\,A$ in blue are compared. Figure is adapted from [Def17].

the observed count rate on these 4 detector pixels is about 10 %. Since the radius of the electron pencil beam is $r_{pb} = 1.8\,mm$, a correction in horizontal direction is not necessary. The vertical correction current was found to be $\Delta y = 1.6\,A$. Both results are in excellent agreement with the axis interception results from the linear equations, since the deviation of the results is $< 0.1\,mm$. Hence, both techniques can be used to determine the alignment between the the RW an the FPD with high precision.

The pencil beam shift investigations are for a magnetic field of 20 % nominal. If the global field is increased to reach nominal values, the field of the dipoles has to be increased as well to maintain a constant pencil beam shift. Hence, correlation values between the global magnetic field and the required dipole current for constant pencil beam shift needs to be investigated as well. The required current for a constant pencil beam shift of 2 mm and 4 mm was quantified for several global field settings, as demonstrated in figure 6.10. The figure underlines the linear dependency between the slope of the functions ($S(I_{+x})$, $S(I_{+x})$ and $S(I_{+y})$, $S(I_{+y})$) and the global magnetic field. Consequently, the required current to maintain a constant shift does scale with the global magnetic field setting (see figure 6.10). To align the electron pencil beam on the "bulls eye" of the wafer, a current of 1.6 A has to be used at magnetic field setting of 20 %, while at full field (100 %) a stronger current of 8.0 A is required, demonstrating the linear correlation as shown in figure 6.10.

The key result here is that the position of the pencil beam on the wafer can be determined with more precision from a measurement based on using dipole currents in combination with the set of linear equations: 6.1 – 6.4, making alignment essentially independent of the wafer resolution. This method to determine the hit position of the pencil beam on the wafer is named "Collision point identification" (CPI). This method will be used in the following to determine the collision points between the magnetic flux tube and the

beamline to obtain a cencise flux tube alignment.

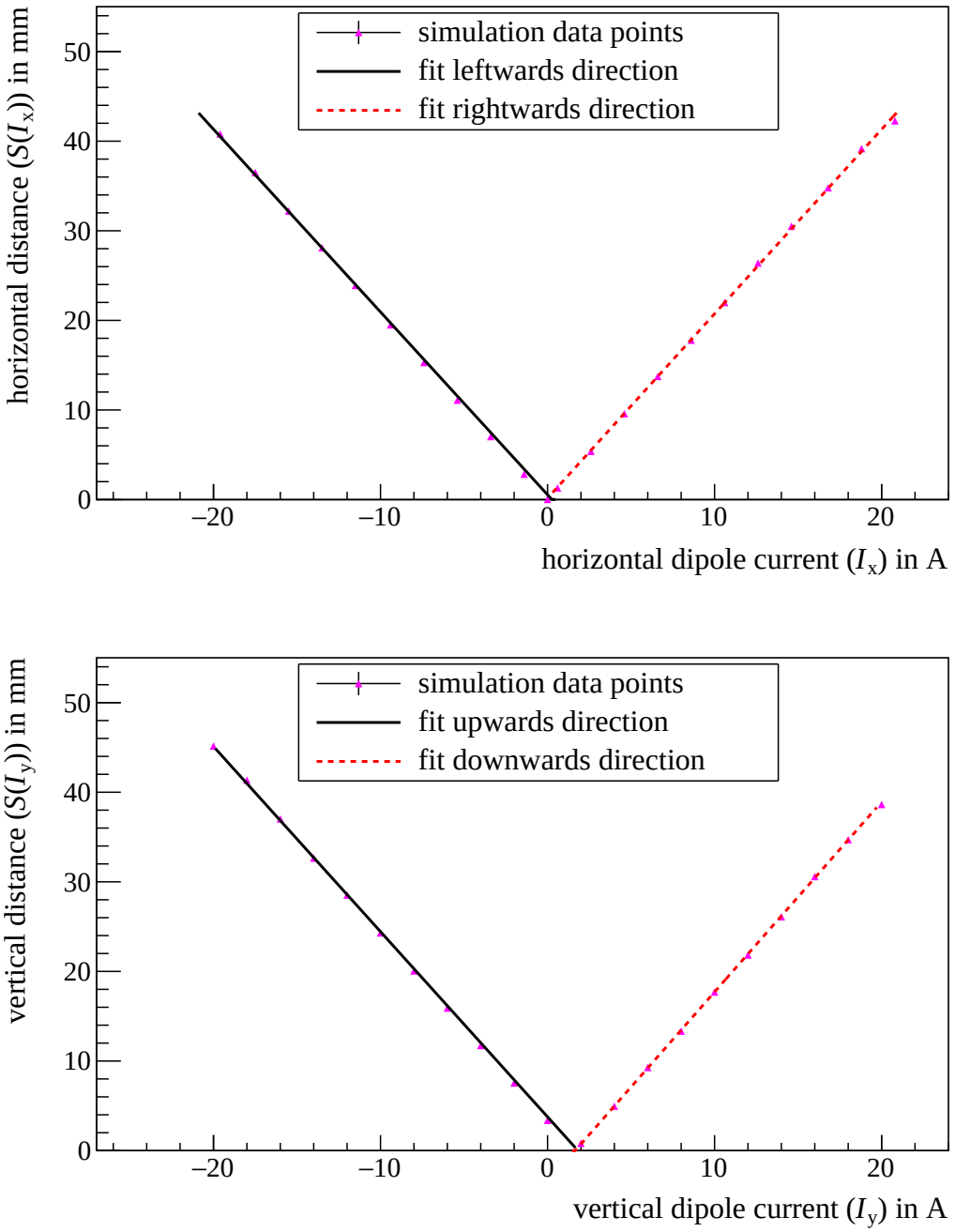

Figure 6.9: Simulation of the magnetic flux tube scan with the electron pencil beam in horizontal and vertical directions. Shown are the linear correlations between the currents (I) of the s.c. dipole magnets on the upstream side of the WGTS and the corresponding shift of the electron pencil beam on the detector wafer. In the upper figure, the shift caused by the horizontal dipole coils is visualized, and in the lower figure the shift caused by the vertical dipole coils is displayed. The outermost measurement point of each direction shows a distinct decrease of counts which indicates collision with the beamline.

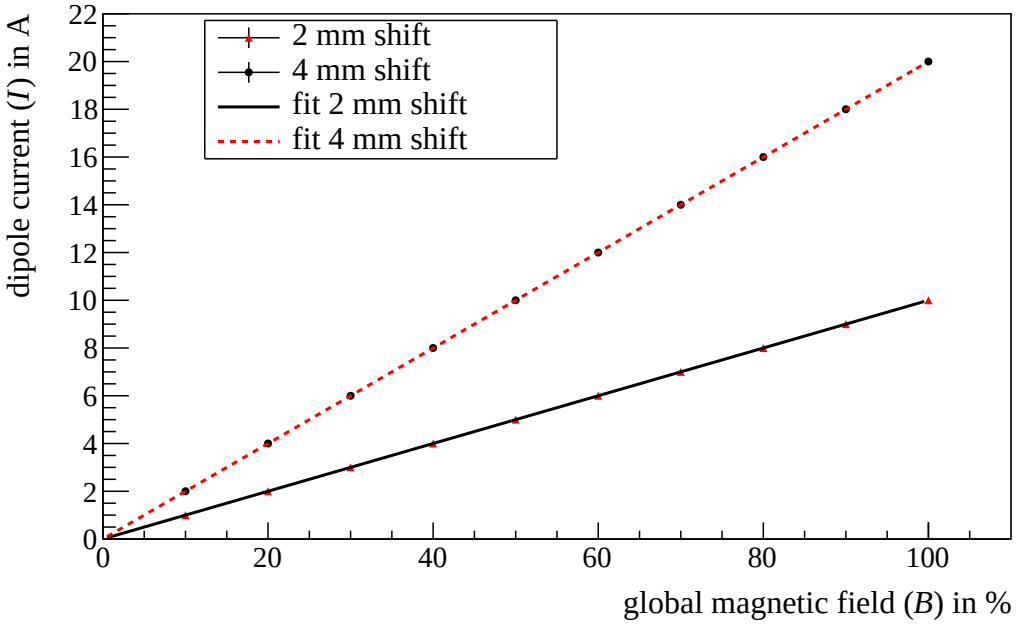

Figure 6.10: Required dipole currents for identical electron beam shifts at the FPD for different magnetic fields. Here the required dipole current to shift the electron pencil beam by a constant distance (2 mm and 4 mm) is displayed for different global magnetic fields. There is a very good linear correlation between dipole current and magnetic field.

6.2.2 Influence of the magnetic dipole stray field on the magnetic flux tube

As mentioned above, the required dipole currents scale linearly with the global magnetic field. To investigate the alignment section-wise in STS, a variety of magnetic bottlenecks is created by reducing the magnetic field inside the section to be examined, as presented in section 5.3. Since a WGTS bottleneck would be located next to the magnetic dipoles (see figure 5.4), the influence of the dipole stray field needs to be investigated. The reduced magnetic field in the region of the bottleneck could also be influenced by the stray field of the dipoles, causing further unknown uncertainties to the alignment results. Simulations for a maximum dipole currents of 20 A (15 % nominal field) have shown, however, that the influence of the dipole stray field on the bottleneck at M2 and M3 is negligible, changing the total magnetic field by $< 0.01\,\%$. The same change of the field was determined for the nominal magnetic field. Additionally, the collision-free size of the flux tube of the WGTS beamline, which was determined from the collision currents in combination with the linear equations (6.1 – 6.4), was in good agreement with the fully illuminated magnetic flux tube. This demonstrates the negligible influence of the dipole stray fields. Also, a comparison between the parameters of the linear equations for a global magnetic field setting of 20 %, with a configuration of a bottleneck of 15 % at the WGTS showed no variation of the linear equation parameters. Hence, the influence of the magnetic dipole stray fields on bottlenecks and vice versa plays no role in alignment measurements. Therefore, the CPI method can be used to examine the size and shape of the magnetic bottleneck by scanning for collision points between the magnetic flux tube and the beamline.

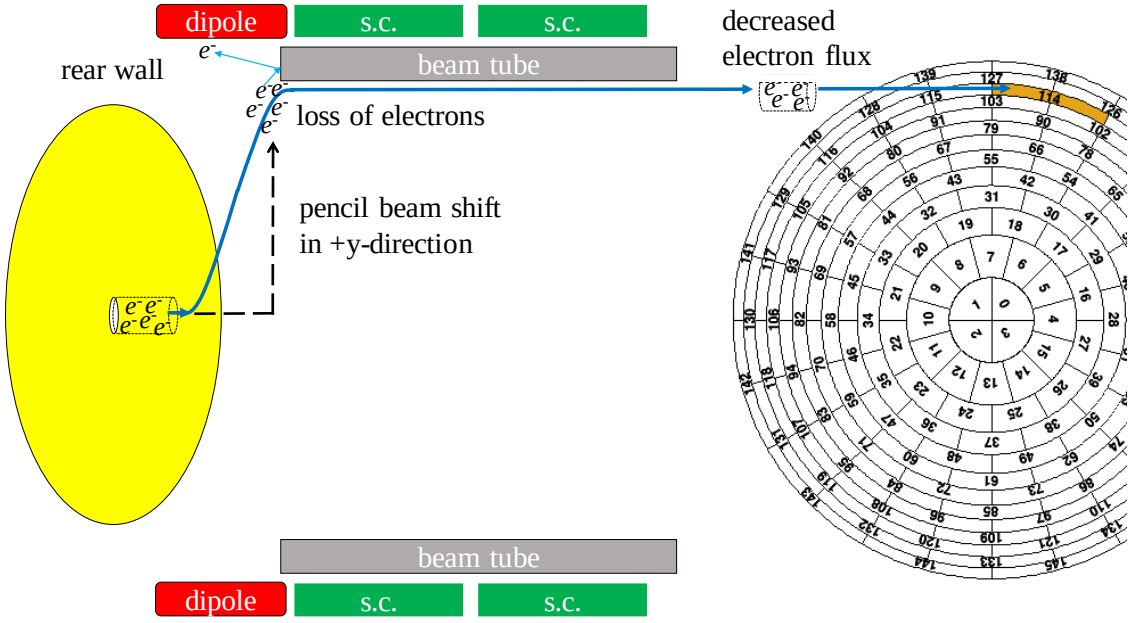

Figure 6.11: Shift the pencil beam upwards until it collides with a beam tube. The sketch shows the vertical shift of the pencil beam in +y-direction. It demonstrates that some electrons of the pencil beam collide with the surface of a beam tube. This causes a decrease of the electrons counted at the detector. The detector wafer on the right side displays the final illuminated pixel, any further shift would block electrons there. Hence the collision point between the magnetic flux tube and the beamline is determined. Its value can be linked to the adjusted dipole currents for the required corresponding pencil beam shift.

6.2.3 Collision points between the magnetic flux tube and the beam line

A step-wise pencil beam scan across the x-y-plane allows to identify four collision points (see figure 6.11). These correspond to the outermost measurement points in each direction where the count rate just starts to drop (see figure 6.9). A collision point projects the shape of the largest collision-free magnetic flux tube on the wafer. Since these points show a count decrease between $10 - 75\,\%$, they can easily be used for a first order analysis of the size of the collision-free flux tube. By using the CPI method in combination with the collision currents of these four points, the four corresponding image points on the wafer can be calculated, representing the shape of the largest collision-free flux tube. This comparison results in a maximum collision-free flux tube with a radius of $\sim 42\,\mathrm{mm}$ at the surface of the detector. As all solenoids are operated at $20\,\%$ of nominal field, this diameter corresponds to a $183\,\mathrm{Tcm}^2$ magnetic flux tube equivalent according to equation 3.8.

Since the count rate decrease occur over a broad range ($10 - 75\,\%$), the results obtained for the collision-free size of the flux tube has to be verified. Therefore, the wide beam source (see section 5.2) is used to corroborate the above result. The wide beam projects a mapped image with sharp edge in the simulation, which provides the exact point of impact of electrons onto the FPD. An image radius of $\sim 43.5\,\mathrm{mm}$ on the wafer was determined in this ansatz, which corresponds to a $\sim 195\,\mathrm{Tcm}^2$ magnetic flux tube equivalent. Consequently, the broad range of count rate decrease ($10 - 75\,\%$) strongly influences the determined collision-free flux tube size using the CPI method. To achieve a more accurate result, a count rate decrease down to values of $10 - 20\,\%$ is aimed for in the following investigations to localize bottlenecks with the pencil beam. This count rate decrease was simultaneously used for the pencil beam measurement during First Light.

The results for simulated images on the FPD point to a reduced size of the transported magnetic flux tube, less than the benchmark of 210 Tcm^2 magnetic flux tube which should reach the FPD undisturbed, as described in section 3.2.7. Additional simulations revealed the WGTS-R section to be the origin of the reduced flux tube size, giving a collision-free flux tube of 195 Tcm^2 for the entire beamline between the RW and the FPD, which is slightly larger than the 191 Tcm^2 nominal value, which is the most relevant setting for the neutrino mass analysis (see section 3.2.7).

The collisions occuring the 210 Tcm^2 magnetic flux tube cannot be investigated with nominal field settings. In the following, the magnetic bottleneck method is used to investigate the alignment section-wise.

6.3 Simulation of the magnetic flux tube alignment

In this chapter two different magnetic field settings are used to simulate the alignment of individual KATRIN components, the magnetic bottleneck and the asymmetric field setting, to determine the largest collision-free magnetic flux tube of each section. As previous measurements showed that the SDS part transmits a 210 Tcm^2 magnetic flux tube in a collision-free way, asymmetric field settings are only used to investigate the alignment of the pre- and the main spectrometer to the FPD.

6.3.1 Investigations with the magnetic bottleneck method

Based on the following reasons, a magnetic bottleneck reduction factor of one quarter was identified as the optimum for the investigations:

- The full flux tube of the WGTS (230 Tcm^2) is defined diameter of 90 mm of the source tube at nominal field of 3.6 T. During normal field settings the FPD cannot map this entire flux tube, since it has a diameter of about 47 mm, while only the sensitive area of the wafer has a diameter of 45 mm. A bottleneck in the WGTS would thus lead to a reduction of the image size to a value of 40.6 mm. Hence, the bottleneck image can be mapped completely.
- The remaining distance between the 230 Tcm^2 flux tube image and the edge of the detector wafer is about 4 mm. This distance is large enough to compensate a possible misalignment between the mapped image and the wafer.
- On condition that the 230 Tcm^2 flux tube of the WGTS is mapped onto the FPD this gives a clear evidence that the collision happens in the source tube.
- Additionally, the magnetic flux tube of 210 (191) Tcm^2 yields an image diameter at the FPD image of 39.0 (37.2) mm which allows the image to be distinguished despite the finite pixel size.
- Another important aspect is that the magnetic flux tube is compressed after the bottleneck due to the higher fields of the remaining solenoids. Further collisions making the images useless for an alignment analysis are thus prevented.

The image size of a magnetic bottleneck on the detector for different flux tube sizes is outlined in table 6.1.

Table 6.1: Radius of different magnetic flux tubes at the detector. With a magnetic field of 20 % at the detector and 15 % in the bottleneck section, different transported flux tube sizes can be detected. As the field is reduced, the magnetic flux tube value is reduced, accordingly, but the investigated volume remains constant, so that the detectable radius at the FPD can be associated to a magnetic flux tube at nominal field settings. The required magnetic fields in each section correspond to design values, the computed values are provided by Kassiopeia.

flux tube in Tcm^2	image radius in mm	
	Kassiopeia	**design**
230	40.6	40.7
210	39.0	38.8
195	37.4	37.2
191	37.2	37.0

6.3.1.1 Implementation of the magnetic bottleneck method

Since β-electrons are guided from the source to the detector it is useful to start bottleneck searches at the rear end of the STS beamline.

To this end the first part to be investigated is the WGTS-R, which is located between the rear section and the rear end of the 10-m long WGTS source tube (see figure 3.3). Corresponding simulations of a scan of the magnetic flux tube with the pencil beam already revealed that this part limits the usable flux tube size, resulting in transmission of a smaller $195\,\mathrm{Tcm}^2$ flux tube (see section 6.2.3). This value of major importance as it defines the area, when RW electron are guided to the source to control the source plasma during the neutrino mass measurements (see section 3.2.3). Due to this fact, a more detailed investigation via the magnetic bottleneck has not been implemented.

The next part of STS part is the 10-m long source tube, which is surrounded by the WGTS solenoids M1, M2 and M3 as shown in figure 3.3. The circuit of the two solenoids M2 and M3 is connected as a group, as well as the triplet M1, M4 and M5. Solenoids M4 and M5 are surrounding the WGTS-R (see figure 3.3) giving the above quoted $195\,\mathrm{Tcm}^2$ flux tube equivalent. Creating a magnetic bottleneck with these two groups is useless, since the magnetic flux tube would be reduced at the beginning. Hence the bottleneck in the source part can only created via WGTS solenoids M2 and M3.

The final part of the WGTS cryostat in downstream direction is the WGTS-F section which is surrounded by solenoids M6 and M7 (see figure 3.3). These coils are designed to operate at a higher nominal magnetic field of 5.6 T, which compresses the magnetic flux tube from the source part (3.6 T). The WGTS-F mechanical beam tube diameter is identical to the source tube (90 mm). This is the reason that no collisions or small distance areas occur between magnetic flux tube and beamline in corresponding simulations.

In the DPS and CPS to be investigated below, close encounters of the $191\,\mathrm{Tcm}^2$ flux tube and the inner surface of the beamline or beamline instrumentation were observed (see section 6.1.4).

6.3.1.2 Alignment results of the simulated magnetic bottlenecks in STS

In the following the alignment results based on the bottleneck method via shifting of a pencil beam by dipole magnets are presented (see section 6.2.1). These simulations closely follow the experimental approach reported above. Finally, the wide beam experimental results are simulated providing a full mapped image at the FPD which is used to verify the CPI results. In doing so, electrons are tracked in Kassiopeia, through the entire beamline

providing additional the information about the alignment between each investigated section and the FPD.

At first simulation targeted at investigating the largest collision-free flux tube are presented, and later the results with respect to the alignment of each section relative to the FPD.

Determination of the collision-free flux tube in STS

The four image points discussed in section 6.2.3 are used to obtain the largest collision-free flux tube via calculating the mean for each direction:

$$\overline{\mathrm{x}} = \frac{|S(I_{+\mathrm{x}})| + |S(I_{-\mathrm{x}})|}{2}, \tag{6.5}$$

$$\overline{\mathrm{y}} = \frac{|S(I_{+\mathrm{y}})| + |S(I_{-\mathrm{y}})|}{2}. \tag{6.6}$$

The smallest mean value defines the radius of the mapped image of the collision-free flux tube (see table 6.1).

WGTS and DPS1-F

The simulation results for the pencil beam scan of the WGTS bottleneck is outlined in table 6.2. The minimal radius is ~ 41 mm (see table 6.2), which corresponds to a $230\,\mathrm{Tcm}^2$ collision-free flux tube (see table 6.1). To demonstrate the onset of bottleneck formation, a flux tube equivalent $> 230\,\mathrm{Tcm}^2$ is illuminated with electrons, starting at the RW. The result of this extended wide beam is displayed in figure 6.12. At the beginning of bottleneck impact, electrons located in the flux tube part $> 230\,\mathrm{Tcm}^2$ collide with the beamline. Figure 6.12 shows the mapped image, the size of which corresponds to the remaining $230\,\mathrm{Tcm}^2$ flux tube defined by the source tube, as explained in section 3.2.7. Here, the bottleneck was extended by solenoids M6 and M7 (see figure 3.3). The flux tube results are still identical, as expected due to the stronger field of this section.

A collision-free $230\,\mathrm{Tcm}^2$ flux tube transmission inside the source tube and the WGTS-F is an important result as it is larger by a safe margin then the two reference magnetic flux tube sizes ($191\,\mathrm{Tcm}^2$ and $210\,\mathrm{Tcm}^2$) of KATRIN.

Table 6.2: Simulated collision currents for the WGTS. The current of the collision point of each direction for the WGTS bottleneck M2 and M3 generated by 15 % of the nominal magnetic field . By extending the bottleneck at WGTS magnet M6 and M7 no change could be determined. The displacement is related to the wafer center. The mean radius per axis is given by $\overline{\mathrm{x}}$ and $\overline{\mathrm{y}}$ (eqs. 6.5 and 6.6).

direction	dipole current (I) in A	displacement ($S(I)$) in mm
+x	+19.6	$+40.54 \pm 0.11$
−x	−20.4	-42.16 ± 0.55
$\overline{\mathrm{x}}$	20.0	41.35 ± 0.33
+y	−20.0	$+45.33 \pm 0.76$
−y	+20.0	-38.89 ± 0.89
$\overline{\mathrm{y}}$	20.0	42.11 ± 0.83

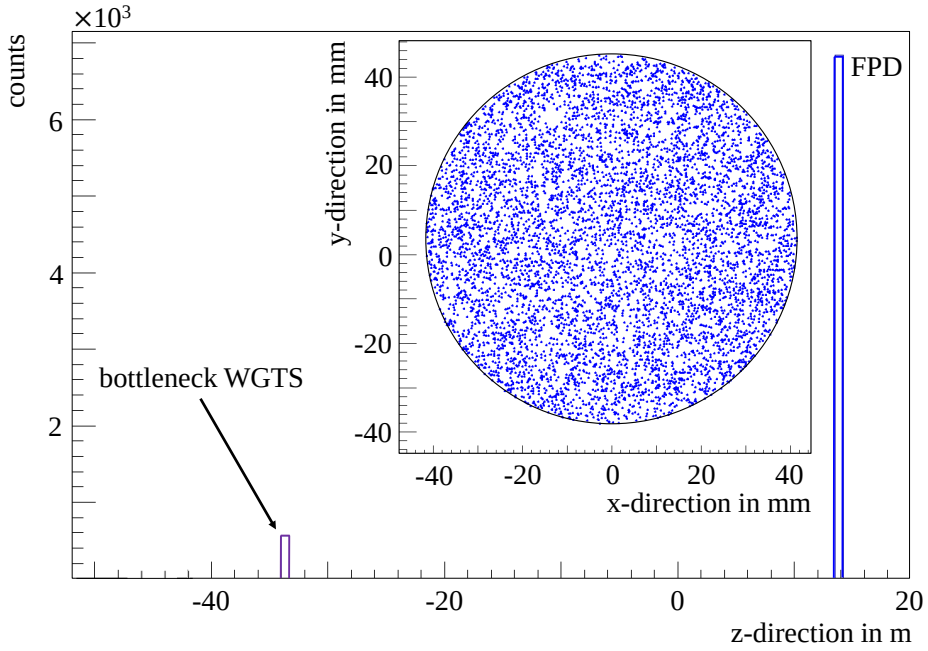

Figure 6.12: Collision counts at the bottleneck in the WGTS. While the global magnetic field was reduced to 20 %, solenoids M2 and M3 were set to 15 % to create a bottleneck in the WGTS. An extended wide beam source at the RW is simulated, which fills a magnetic flux tube of $> 230\,\mathrm{Tcm}^2$. The maximum magnetic flux tube which fits into the source tube, due to the design geometry is $230\,\mathrm{Tcm}^2$. The mapped circular image (black circle filled with blue dots) at the FPD has a radius of $\sim 41\,\mathrm{mm}$, corresponding to this $230\,\mathrm{Tcm}^2$ flux tube. Hence electrons of the extended wide beam which located in the area $> 230\,\mathrm{Tcm}^2$ collide with beamline elements at the beginning of the induced WGTS bottleneck at z-position $-34\,\mathrm{m}$. The detected counts are highlighted in blue at z-position 13.7 m. When expanding the bottleneck along the z-axis by M6 and M7, no further collisions occur.

DPS

Now the bottleneck is moved to the solenoids of DPS and investigated via scanning of the pencil beam. The results are outlined in table 6.2. The minimal image radius is $\sim 38.3\,\mathrm{mm}$ (see table 6.3). Hence the $191\,\mathrm{Tcm}^2$ magnetic flux tube is guided collision-free, but not the $210\,\mathrm{Tcm}^2$ flux tube (see table 6.1).

The reduction of the flux tube radius is caused by collisions in horizontal and vertical direction. However, it is important to guide the $210\,\mathrm{Tcm}^2$ flux tube in a collision-free manner trough the DPS beamline, as the FBM located at pump port 2 of the CPS has to monitor the source activity in the outermost horizontal part of $210\,\mathrm{Tcm}^2$ flux tube (see section 3.3.2.4). While the nominal magnetic field for the DPS is 5 T the successful test of the DPS solenoids up to 5.5 T, allows to operate these magnets at slightly higher magnetic fields to compress the magnetic flux tube and mitigate horizontal collisions.

A corresponding simulation with a magnetic bottleneck with 17.5 % of the nominal field was performed in addition. In the case, collisions in DPS completely vanquish, resulting in a collision-free guiding of a $230\,\mathrm{Tcm}^2$ flux tube (see table 6.3). This allows to conclude that collisions in the DPS disappear when its magnetic field is increased by $\sim 16\,\%$ relative to the global field settings.

The results of the CPI method for the two bottlenecks (15 % and 17.5 %) was verified by making use of the extensive wide beam, as shown in figure 6.13. The extended wide beam simulation show in addition that a small fraction of electrons still collide inside the DPS beamline, however (see figure 6.13).

Table 6.3: Simulated collision currents for the DPS. The dipole currents for the onset of collisions for two DPS settings (15.0 %, 17.5 %). Displacement value in the last two columns relate to the wafer center. The mean radius per axis is given by $\bar{x}$ and $\bar{y}$ (eqs. 6.5 and 6.6).

	dipole current (I) in A		displacement ($S(I)$) in mm	
direction	15.0 %	17.5 %	15.0 %	17.5 %
+x	+18.4	+20.4	$+38.06 \pm 0.58$	$+42.18 \pm 0.81$
−x	−18.6	−19.6	-38.48 ± 0.05	-40.52 ± 0.54
$\bar{x}$	18.5	20.0	38.27 ± 0.32	41.35 ± 0.68
+y	−19.0	−20.0	$+43.23 \pm 0.29$	$+45.33 \pm 0.05$
−y	+19.0	+20.0	-36.77 ± 1.18	-38.89 ± 0.73
$\bar{y}$	19.0	20.0	40.00 ± 0.74	42.11 ± 0.39

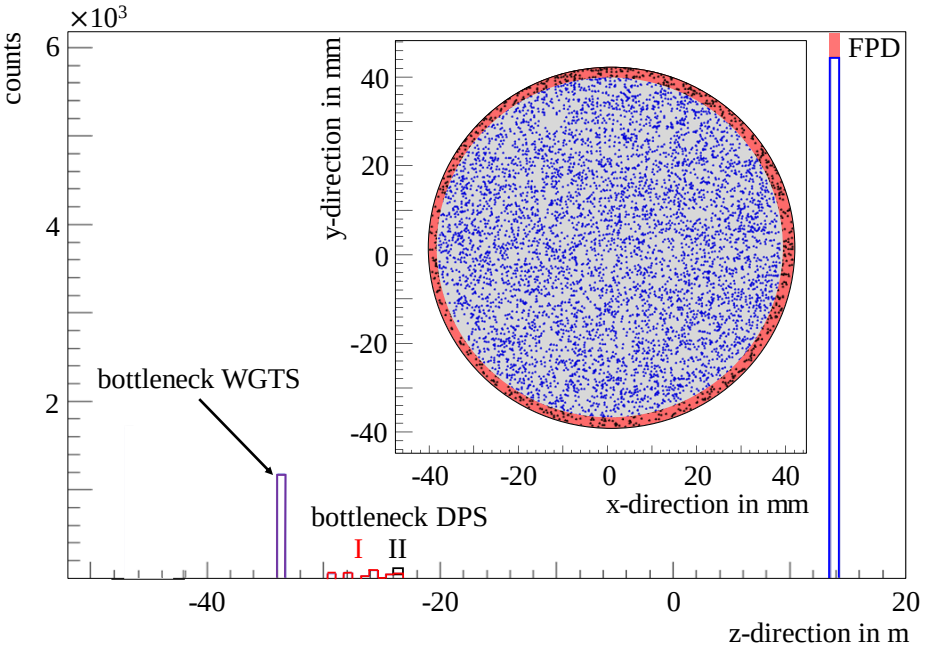

Figure 6.13: Collision counts along the STS beamline by applying a bottleneck in the WGTS and the DPS. The figure shows the collision in x-y-axis (inlet) and along the z-axis for the extended wide beam along the STS beamline. A magnetic bottleneck with a field of 15 % was implemented inside WGTS and DPS, labeled with I. Afterwards the DPS bottleneck was set to 17.5 % of the nominal field , labeled with II. Main collisions occur in both settings at the beginning of the WGTS bottleneck, near the upstream end of solenoid M2 (see figure 6.12). The 230 Tcm^2 flux tube is reduced in the bottleneck of the DPS for setting I. The collision rate along the DPS beamline (z-position: $-30\,\mathrm{m} \rightarrow -24\,\mathrm{m}$) is highlighted in red for setting I. The mapped circular image at the FPD for setting I is highlighted in blue. The detected counts at the FPD are shown in blue at z-position 13.7 m. When using the magnetic field setting II, the collisions at the DPS almost disappeared, and the red collision counts disappear. Only a small collision rate is left, highlighted in black at z-position $-24\,\mathrm{m}$. Due to the reduced collisions, the mapped image at the FPD has obtained the red ring-shaped area, and the counts at the detector increase due the red highlighted fraction (z-position 13.7 m).

Table 6.4: Simulated collision currents for the CPS. Since the DPS limits the flux tube radius, the maximum flux tube diameter of the CPS was simulated at first by keeping the DPS on 20.0 % of the nominal field. Afterwards the DPS was set to 17.5 % to detect significant changes of the flux tube radius. The mean radius per axis is given by $\overline{\mathrm{x}}$ and $\overline{\mathrm{y}}$ (eqs. 6.5 and 6.6).

direction	dipole current (I) in A	displacement ($S(I)$) in mm
+x	+19.4	$+40.12 \pm 0.16$
−x	−19.6	-40.52 ± 0.51
$\overline{\mathrm{x}}$	19.5	40.32 ± 0.33
+y	−18.0	$+41.13 \pm 0.41$
−y	+20.0	-38.89 ± 0.10
$\overline{\mathrm{y}}$	19.0	40.01 ± 0.25

CPS

Simulations of the DPS bottleneck showed a reduced size of magnetic flux tube for nominal magnetic field settings. This can be avoided by setting all DPS coils to a value of 17.5 %. This allows to investigate the CPS elements with no influence from the DPS collisions.

The results of the pencil beam scan of the CPS bottleneck is outlined in table 6.4. A minimal radius of $\sim 40\,\mathrm{mm}$ (see table 6.2) is determined. Hence, the $210\,\mathrm{Tcm}^2$ flux tube can be guided collision-free through the CPS beamline (see table 6.1). Since the pencil beam results of the CPS bottleneck (see table 6.4) are nearly identical in comparison to the previous results of the DPS bottleneck at 17.5 % (see table 6.3), this fact shows that the combination of DPS and CPS limits the collision-free flux tube size. This is verified by corresponding wide beam investigations, as shown in figure 6.13. A small number of additional collisions in the CPS occurs, due its small number, they are not visible in the image.

The final result is that the $210\,\mathrm{Tcm}^2$ flux tube can be guided collision-free through the STS beamline, in condition that the DPS solenoids are operated at a slightly higher field as designed. Since the $210\,\mathrm{Tcm}^2$ flux tube can be guided collision-free through the STS, the required full transmission can be realized.

Alignment between the STS components and the FPD

The alignment between an investigated beamline section and the FPD is given by the offset between the image center in comparison to the wafer center. The four image points are used to calculate the image center. The offset is then given by half the difference:

$$\mathrm{x} = \frac{S(I_{+\mathrm{x}}) + S(I_{-\mathrm{x}})}{2}, \tag{6.7}$$

$$\mathrm{y} = \frac{S(I_{+\mathrm{y}}) + S(I_{-\mathrm{y}})}{2}. \tag{6.8}$$

The results for different magnetic bottlenecks are summarized in table 6.5. The misalignment in x-direction between individual STS components and the FPD is not significant since the offset is typically $< 1\,\mathrm{mm}$. The misalignment in y-direction between individual STS components and the FPD is significant, however, with offsets typically $> 1\,\mathrm{mm}$. Especially the WGTS and the CPS components show an offset of $> 3\,\mathrm{mm}$.

With respect to achieved full transmission of the $210\,\mathrm{Tcm}^2$ flux tube in the beam line, the CPS is the final component to influence the mapped source image due to collisions. Hence the mapped image of the CPS provides the alignment between the source image

Table 6.5: Simulated alignment of the individual STS components to the FPD. The presented alignment results of individual STS components are with respect to the wafer center. Since collisions of the 210 Tcm^2 magnetic flux tube have been determined in DPS, the bottleneck simulation of DPS was repeated with 17.5 % of the nominal field. Alignment results of this setting are presented as well.

section	bottleneck	axis	displacement in mm
WGTS	15.0 %	x	-0.81 ± 0.44
WGTS	15.0 %	y	$+3.22 \pm 0.86$
DPS	15.0 %	x	-0.21 ± 0.19
DPS	15.0 %	y	$+3.23 \pm 0.96$
DPS	17.5 %	x	$+0.83 \pm 0.61$
DPS	17.5 %	y	$+3.22 \pm 0.56$
CPS	15.0 %	x	-0.20 ± 0.42
CPS	15.0 %	y	$+1.12 \pm 0.18$

and the FPD. The determined alignment parameters of the CPS can then be corrected by adjusting the WGTS s.c. dipole magnets currents resulting in a source image perfectly aligned to the FPD. This final adjustment will be performed along the methods presented here in the first quarter of 2018.

6.3.2 Investigation with asymmetric magnetic field in SDS

A well-established method to investigate the alignment of the spectrometer relative to the detector is to map the inner electrode wire combs on the detector wafer (see section 5.3). Since the solenoids of the STS part are not required for the asymmetric field method in SDS, the issues related to the DPS solenoid do not influence the absolute magnetic field during the First Light measurements. Hence, asymmetric field simulations were prepared for all magnetic field settings. In this section the magnetic field settings are presented first. Thus, the results of alignment simulations between the pre- and the main spectrometer the FPD are discussed in detail.

6.3.2.1 Description of the asymmetric magnetic field method

When simulating electron field emission in Kassiopeia, the point of origin of electrons is defined as the position of the wire comb holding structures. These are located rotationally symmetric around z-positions $z_2 = 2685\,\text{mm}$ and $z_3 = 4472\,\text{mm}$ with respect to the MS center. Thus, two ring shaped electron sources are created in the main spectrometer.

To create an asymmetric field, the detector and pinch solenoids are set to 72 % of their nominal magnetic field values ($B_{\text{pinch}} = 4.32\,\text{T}$ and $B_{\text{detector}} = 2.59\,\text{T}$), while both the PS1 and PS2 solenoids are switched off (see figure 6.14). Also, all but three air coils are switched off, these are operated with inverted polarity (LFCS: AC2 $= -50\,\text{A}$, AC3 $= -40\,\text{A}$, AC4 $= -30\,\text{A}$). Additionally, the EMCS is set to 9.0 A in x-direction and 50.0 A in y-direction. All inner electrodes are set to zero potential for the simulation.

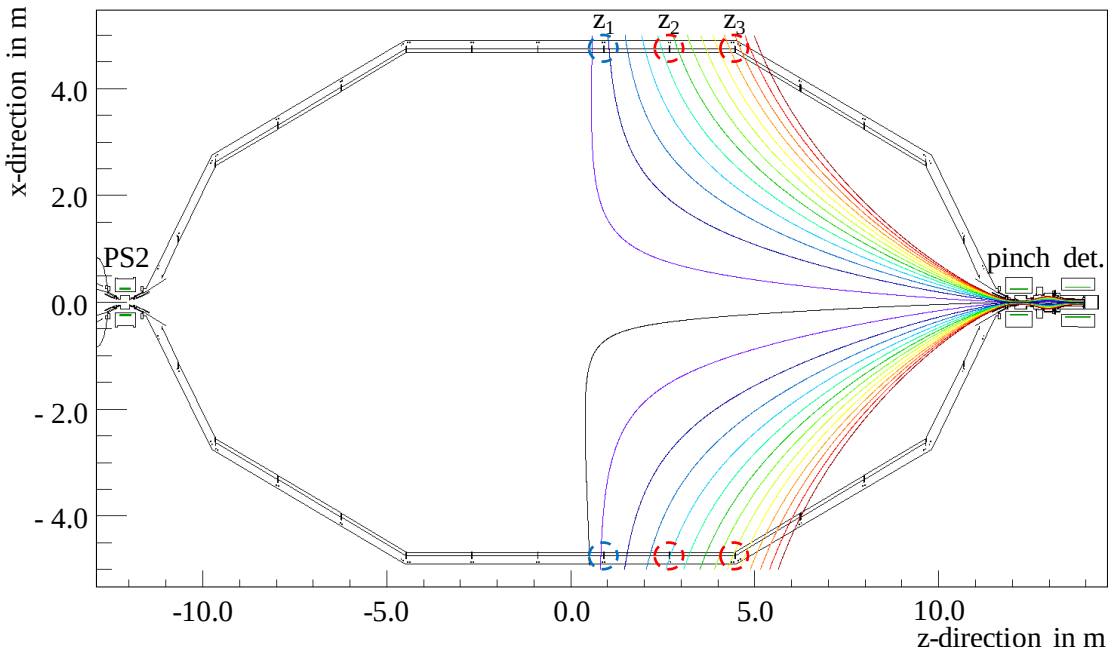

Figure 6.14: Asymmetric magnetic field method used for alignment measurements between MS and FPD. Shown is the main spectrometer vacuum chamber, filled with colored magnetic flux tubes originates from the detector rings. The red dashed circles indicate the holding structures of the inner electrode wire comb to be mapped. The structures z2 and z3 have been used for the alignment analysis, where simulated electrons are started at their point of origin. The structure z1 is not used for the simulation or the alignment measurement, since it fully illuminates the "bulls eye" of the wafer, making it useless for alignment analyses.

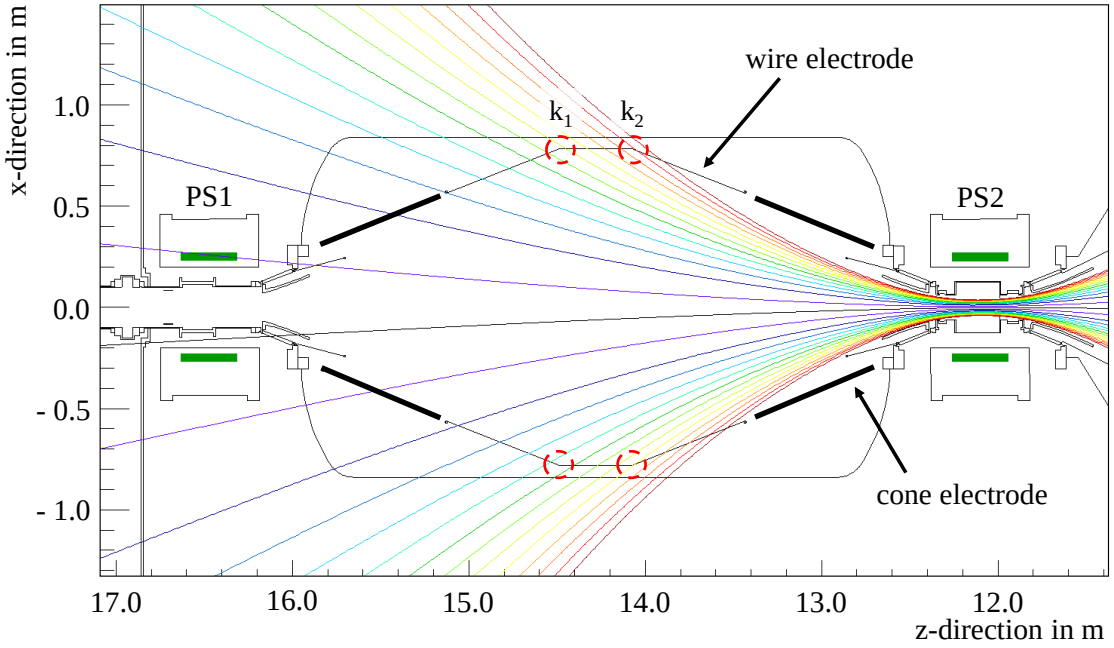

Figure 6.15: Asymmetric magnetic field method used for alignment measurements between PS and FPD. The inner electrode consists of three parts, a central wire electrode separated into two single half shells, and two solid cone electrodes. The kinks (k_1 and k_2) of the electrode system can be mapped onto the FPD by using the asymmetric magnetic field configuration, displayed here, where the PS1 solenoid is deenergized.

In the next step, the alignment between the PS and the FPD is investigated, making use of the inner wire electrode system of the pre-spectrometer. Its electrode system consists of three sets of electrodes. A quasi massless wire electrode forms the central element of the setup, and two cone electrodes, one on each side of the spectrometer (see figure 6.15). The wire electrode features two kinks, which generate the rings to be mapped onto the detector wafer. Hence, these kinks are used as point-of-origin in the simulation. The superconducting solenoid PS2 between the PS and MS is set to 3.24 T, corresponding to 72 % of the nominal field. To generate the asymmetric field inside the PS, the PS1 solenoid is kept off (see figure 6.15). The EMCS is kept on the its nominal value.

In both cases the magnetic flux tube widens up, and surface electrons are guided by the magnetic field lines onto the detector wafer. Since both spectrometers and their electrode systems have cylinder symmetry electrons produce a ring on the wafer. The results of simulations of these investigations are presented in the following.

6.3.2.2 Alignment results of the simulated asymmetric magnetic field in SDS

The investigation of the alignment of PS and MS with respect to the FPD is based on a circle fit to data and the computation of the ring center. The misalignment between the center of the main spectrometer and the detector wafer is found to be $x = -0.99\,\text{mm}$ and $y = -2.50\,\text{mm}$. For the pre-spectrometer, a corresponding misalignment of $x = -1.44\,\text{mm}$ and $y = -2.89\,\text{mm}$ is determined. In view of the diameter of the components and in view of the mechanical misalignment of the SDS construction, both simulations provide reasonable alignment results.

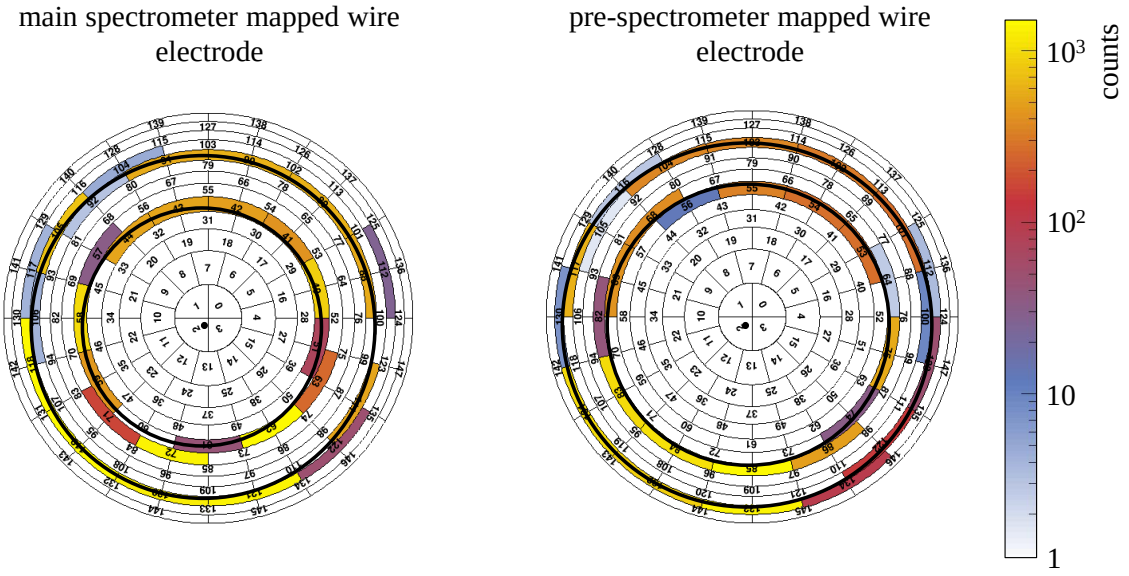

Figure 6.16: Simulation results of the asymmetric magnetic field at the PS and the MS. The determined circles and their center (dot) for each simulation are superimposed on the mapped image on the wafer. The asymmetric magnetic field simulation of the PS was performed with a larger number of electrons compared to the MS.

6.4 Conclusion

This chapter has given an in-depth overview of principles and results in the extended alignment investigation for the STS and SDS parts of the KATRIN experiment. Experimental data were verified by using the simulation software package Kassiopeia. Previous alignment measurements with the SDS part using the asymmetric magnetic field setting, showed already very good agreement between simulations and measurements [Sch14, Har15, Erh16]. The new simulations of this thesis indicate a complete transmission of the magnetic flux tube. It should be noted in this context that the pre-spectrometer was implemented for the first time into the simulation software, completing the KATRIN beamline geometry. As the electron field emission as well as secondary electron emission produce electrons at the electrode wire comb, this background source can be used to good effect as an electron source to map the structures on the detector with an asymmetric field. Since this emission is not implemented into the software package, a ring shaped electron source was implemented into Kassiopeia at this position. The maximum misalignment between the spectrometer and the detector was determined to $\sim 2.9\,\mathrm{mm}$. Due to uncertainties relative to the mechanical structures, the measurement uncertainties of the alignment are estimated to be in the order of $\sim 1.0\,\mathrm{mm}$ [Sch14].

Since the DPS solenoid M1 did not reach the required field, simulations for the first alignment measurement had to be implemented, which showed that the alignment and transmission results of STS are independent of the absolute magnetic field, as long as all solenoid currents are reduced by the same factor. The mapped image on the detector provides only an overall transmission information of the entire beamline, but not information about the location of the collisions along the beam axis. It could be demonstrated first that a magnetic flux tube of $195\,\mathrm{Tcm}^2$ can be guided without collision through KATRIN. This includes two important results: first the RW electrons which are required to control the plasma potential are guided collision-free by the foreseen $195\,\mathrm{Tcm}^2$ flux tube. Second, signal electrons can be guided collision-free from source to detector over an $195\,\mathrm{Tcm}^2$ flux tube which is larger than the required $191\,\mathrm{Tcm}^2$ flux tube. To investigate the flux tube alignment and transmission section-wise, a new method had to be implemented. By deliberate creation of a magnetic bottleneck, a reduction of the magnetic field by one quarter was found to be the best solution for a section-wise investigation. The investigation of these bottlenecks can be implemented making use of a pencil beam to scan for collision points between the magnetic flux tube and the beamline in four directions, or by full illumination of the magnetic flux tube with a wide beam. The resolution of the transmission and alignment information of a bottleneck image is limited by the pixel size of the detector wafer. More precise results can thus be achieved by scanning the shape of the bottleneck with a pencil beam, as condition that a linear correlation between the shifting dipole current and the displacement of electrons is determined previously. Therefore, count rate monitoring at the detector is key to observe measured during the movement of the pencil beam. The onset of collision is defined if the rate drops below $10 - 20\,\%$. The image of collision onset at the detector can be calculated afterwards by making use of the linear dependency in combination with the corresponding currents of the WGTS dipole magnets, the basis of the so-called CPI method.

By using the bottleneck for individual STS sections, the extensive simulations performed here have demonstrated that the linear correlation method is in good agreement with simulated collision points of a fully mapped bottleneck image on the wafer. The investigation of bottlenecks with both electron sources has revealed that it is possible to determine the maximum collision-free flux tube with an uncertainty of $\sim 1.0\,\mathrm{mm}$. The main result of the bottleneck simulation demonstrates that it is possible to guide the $191\,\mathrm{Tcm}^2$ flux tube through the entire beamline without collisions for the nominal magnetic field. A larger magnetic flux tube is limited by the DPS beamline. Finally, and most importantly, it

could be demonstrated that a slightly higher magnetic field of the DPS solenoids, relative to all other solenoids, eliminates these collisions, resulting in an collision-free guiding of the 210 Tcm^2 flux tube through the entire KATRIN beamline.

CHAPTER 7

First Light and the global magnetic flux tube alignment measurements

The key objective of the First Light measurement campaign is to characterize the global magnetic flux tube transmission and alignment of the global KATRIN beamline. By utilizing different magnetic field settings, a large ensemble of alignment investigations could be performed section-wise. Thereby, specific information on the largest possible flux tube without transmission losses can be obtained. Due to the importance of this key task, the results of this extensive analysis have been verified via a detailed Kassiopeia simulations. This model includes the design geometries of all beamline elements as well as as-built geometries of the superconducting solenoids taken from the technical drawings of the manufacturer, complemented by accurately ascertained solenoid positions. All mechanical alignment data has been implemented into Kassiopeia and verified by section-wise transmission simulations of the already commissioned individual KATRIN beamline systems. In preparation of the First Light measurements, global alignment simulations were performed which have been presented in the previous chapter 6. The model allows to test and compare different alignment measurement principles, and to identify the ones best suited for the STS and SDS beamline parts and verify them with the First Light data.

In the following section 7.1 a method to map collisions of the flux tube with the beamline to first order by using the RW as a wide beam electron source will be presented. Different techniques are detailed which allow to analyze characteristics of the resulting detector patterns and to extract information about specific collision points from the data. A more precise measurement technique is based on using an pencil beam to perform a scan of the flux tube, this is presented in section 7.2. The scan of the magnetic flux tube is carried out by shifting this pencil beam with the superconducting dipoles of WGTS. First, the correlation between the shift of the beam spot and the currents of the superconducting dipole is measured. This information is used afterwards to identify magnetic bottlenecks in the STS part of the beamline. Two independent results can be extracted from this data. This complises both the alignment between the RW and single STS components, as well as the alignment between these components and the detector. At the end of section 7.2, the alignment between the RW and the detector is analyzed and used to cross check previous results. In section 7.3 a set of alignment measurements with asymmetric magnetic fields in the SDS is presented. Here, the alignment of pre- and main spectrometer with respect to the detector is investigated. Building on these results, the STS and SDS alignment data are combined into a global magnetic flux tube alignment model in section 7.4. Section 7.5 they focuses on potential improvements of the flux tube guidance, followed by a discussion about the corresponding implications on the neutrino mass measurements in section 7.6. The chapter closes with recommendations for future alignment measurements in section

7.7.

7.1 Full illumination of the magnetic flux tube at nominal magnetic fields

The key objective of the First Light measurements is to obtain a quantitative result for a fundamental observable, the detected electron rate at the detector. A first impression about the general characteristics of the beamline transmission can be achieved by using the RW to fully illuminate the magnetic flux tube with electrons. Thus, an image of the RW is projected onto the FPD. As shown in section 6.1, this measurement was simulated with Kassiopeia to investigate the flux tube mapping of the RW onto the FPD. The simulation shows that the ideal rate and distribution of the mapped image is reached only if all superconducting solenoids are operated at nominal field, or if they are reduced by the same ratio. Due to the hardware related issues with the DPS solenoid M1, which are discussed in section 5.2, the global magnetic field during First Light had to be reduced to 20 % of its nominal value. To accelerate the electrons, the RW voltage is elevated to $U_{\mathrm{RW}} = -50\,\mathrm{V}$ (appendix C: FL2). The simulations indicate a loss-free guiding of the electrons for this specific magnetic field setting. Furthermore, previous measurements with the RW setup can be used to obtain information about the expected electron rate at the FPD (see section 5.2). These preliminary works gives a rough idea of the size of the mapped RW image, as well as on the expected electron rates.

7.1.1 Measured shadow on the detector wafer

During the first measurement campaign with all magnetic fields set to 20 % of their nominal values, about three quarter of the detector wafer was illuminated by electrons from the RW (see figure 7.1). From simulations it was expected that not all pixels are illuminated, since the size of the transmitted flux tube has a value of $195\,\mathrm{Tcm}^2$. Hence, it is expected to generate a circular image at the FPD which covers an area with a radius of 43.3 mm. In contrast to simulation results shown in figure 6.4, the measured image of the flux tube (see figure 7.1) is shifted upwards in positive y-direction, as is evident from the fact that the outer rings in the upper part of the detector are illuminated. Furthermore, it seems that the image is shifted by a small offset to the left side, in negative x-direction. The RW image is thus not aligned to the center of the wafer, which has to be investigated in the context of the superconducting dipole magnets of WGTS. This shift is investigated in greater detail with a different measurement technique at a later point to be discussed in section 7.2.4. The key result of this first measurement is the observation of a shadow visible on the bottom part of the wafer, covering approximately one quarter of the image. In the following, the origin of this shadow is investigated and discussed.

7.1.2 Investigation the origin of the shadow

A shadow on the detector wafer can have several reasons. The first conjecture is that no electrons are produced in the area of the shadow resulting from a partial UV illumination of the RW. In addition, the non functionality of several neighboring detector pixels or their read-out electronics could produce such a shadow-like effect. Finally, this can be attributed to the fact that parts of the flux tube collide with beamline elements, generating a shadow similar to the observed one. Apart from a mechanical collision blocking the electron flux, an electrostatic barrier in the range of several tens of V would have a similar effect on low energetic RW electrons. In the following this shadow producing effect is investigated in detail.

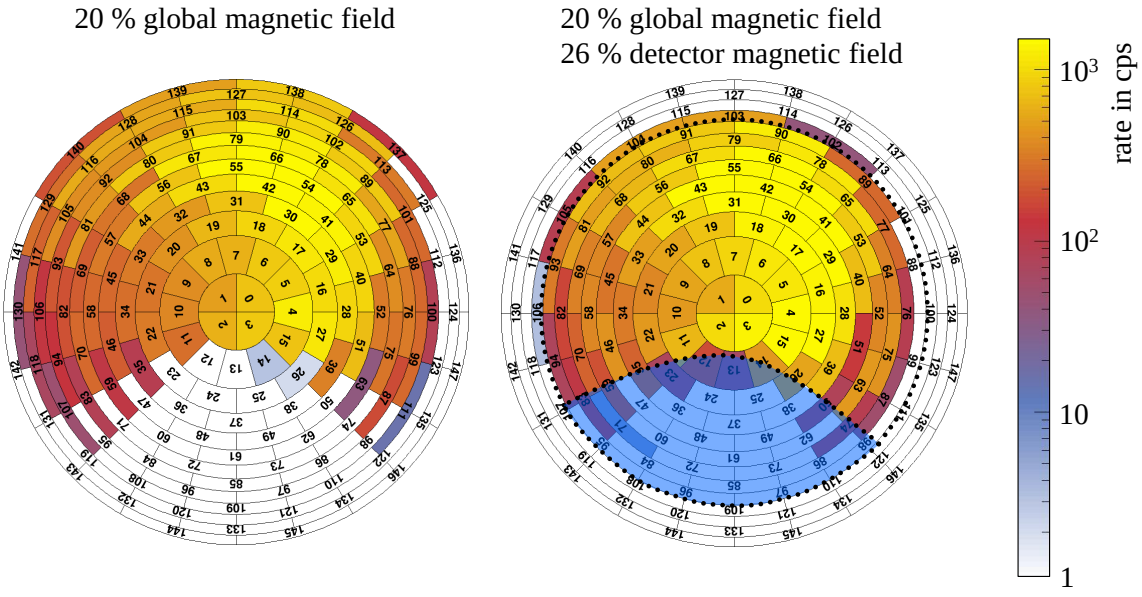

Figure 7.1: Full illumination of the magnetic flux tube. To fully illuminate the flux tube with electrons, the UV irradiation of the RW was switched on. The RW was elevated onto $U_{\mathrm{RW}} = -50\,\mathrm{V}$ to accelerate the electrons. To achieve a full transmission of the electron flux, the spectrometers are grounded, so that a rate of $\sim 5.5 \times 10^4$ cps is detected (left figure). The background events have a rate < 1 cps and are not shown. The left figure shows the detector image with all superconducting solenoids operating at 20 % of their nominal field. Consequently, the image gets compressed if the detector solenoid is ramped up to 26 % of its nominal field, shown in the right figure. Here, the shadow-affected part is highlighted in blue. The decrease of the shadow-affected area is attributed to the resolution of the detector. The black dashed circle with a radius of ~ 38 mm indicates the image size which is expected from simulations.

Rear wall not fully irradiated

In case of a not fully irradiated RW, the resulting image could be a non-circular pixel distribution on the detector wafer. If this is assumed to be the reason for the observed shadowing, it should be possible to move the mapped image of the RW on the detector by using the dipole magnets of the WGTS. In doing so one does not expect to observe a change of the counted electron rate or any major changes of the image shape. To test this the vertical dipole magnet at the upstream end of the WGTS was ramped to 11 A to move the illuminated hotspot on the detector in the upward direction. The position of the shadow, however, shows no change. This proves that the shadow is not due to an improper RW irradiation.

Detector wafer not fully illuminated

By fully deenergizing the superconducting solenoid of the rear section, with all other magnets operating at 20 % (detector solenoid at 26 %) of their nominal field, the diameter of the electron beam from the RW can be decreased to a diameter < 20 mm on the detector (appendix C: FL3), according to equation 3.8. A significant increase of the rate of ~ 30 % during the ramp down of the solenoid has been detected. Previously, it was mentioned that the shadowed area results in a decrease of the overall rate by about one third. This is the first indication that the wafer is indeed detecting the complete image when the RS solenoid is fully deenergized. The fact that the hotspot is not moved to the upper part of the wafer demonstrates that there is no major and relevant misalignment between the RW and the FPD which would otherwise have explained the shadow.

The measurement configuration with the RS solenoid at zero field has resulted in a rather narrow electron beam. This small area beam is ideally suited to scan the flux tube in x- and y-direction by shifting the spot with the magnetic dipole coils on the rear side of WGTS. An important strategy there is to shift the beam until it collides with the beamline, which is detected as a decrease of the measured electron rate. The absolute value of the horizontal current of the dipole coils of $\pm 27.2\,\mathrm{A}$ for collision to occur is constant for left and right direction. It is comparable with the current of $-27.2\,\mathrm{A}$ in upward direction. However, the current of $+10.0\,\mathrm{A}$ in downward direction diverges significantly (appendix C: FL3). Since all dipole coils are build identically, and the beamline is expected to be radially symmetric, the collision current should be the same for each direction. By combining this observation with the rate increase during the ramp down of the RS solenoid, it can be concluded that a potential misalignment between the RW and the FPD can be excluded as underlying reason for the shadow observed in figure 7.1.

Defective detector pixels

A quick functionality check of all pixels can be performed by analyzing detector-related background data. The data shows that each pixel counts an almost identical rate of background electrons. A failure of the pixels or the read-out electronic therefore can be excluded.

Collision of the flux tube along the STS or the SDS beamline

As all superconducting coils along the KATRIN beamline can be adjusted and controlled individually or groupwise, a collision point between the magnetic flux tube and the beamline can easily be localized by separately ramping up specific coils. Here, the magneto-optical characteristics, displayed in equation 3.8, are used to compress the magnetic flux tube and hence the guided electron beam in the section investigated. Consequently, in the case that the collision is located in the area of the magnetic field being ramped, the collision in the outer part of the flux tube is expected to decrease. Accordingly, the total electron rate at the detector is expected to increase. In the case of multiple collision points, the solenoids have to be ramped up sequentially. Once a solenoid is ramped up, it remains at the defined field, and the neighboring solenoid, or group of solenoids, is ramped up. As the total collision area is a sum of all single areas, the total electron rate equals the sum of the initial rate plus each single change of rate. Furthermore, it is possible to estimate the collision area in each ramped section. The different magnetic field settings during the search for collision points can be found in table 7.1, including the change of the detected event rate on the detector. A more detailed visualization of this rate change is shown in figure 7.2. To obtain an impression of the mapped image, the FPD images are attached to the rate trend histogram. An unambiguous localization of the cause for the shadow could not be performed, as all sections contain certain collision points. However, the most significant change of rate was found during ramp up of the solenoid PS2 located between pre- and main spectrometer (see table 7.1). This lends credence to the hypothesis that the shadow is generated inside the flapper valve, located in the warm bore of this solenoid. Here, a rather simple explanation for the shadow would be to correlate it to a not fully opened flapper valve. From the orientation and shape of this specific beam element (see figure 7.3), the observed shape of the shadow would be explainable. However, this presumption can be excluded since the opening mechanism of the valve guarantees it to be fully opened.

Table 7.1: Parameter settings during the strategic search for the blockade in the beamline. At the beginning all superconducting solenoids are operated at 20 % of the nominal value, except the detector solenoid with a value of 26 %. The UV light irradiation of the RW is in operation, and the RW is elevated to a value of $U_{\mathrm{RW}} = -50\,\mathrm{V}$. In the first row the operation mode noted in bold, indicates the section under investigation. In the columns below the magnetic field settings are presented as well as the measured electron rate at the detector, together with the internal run number and the corresponding internal logbook entry.

	mode of magnetic field settings				
	start	**PS2**	**CPS**	**DPS**	**WGTS**
PS1 in %	20.0	20.0	100.0	100.0	100.0
PS2 in %	20.0	40.0	40.0	40.0	40.0
CPS in %	20.0	20.0	60.0	60.0	60.0
DPS in %	20.0	20.0	20.0	30.0	30.0
WGTS in %	20.0	20.0	20.0	20.0	30.0
rate in kcps	56.1	62.0	65.9	69.7	71.6
run number	30250	30265	30590	30685	30696
ELOG, First Light, Message ID:	8	8	9	11	12

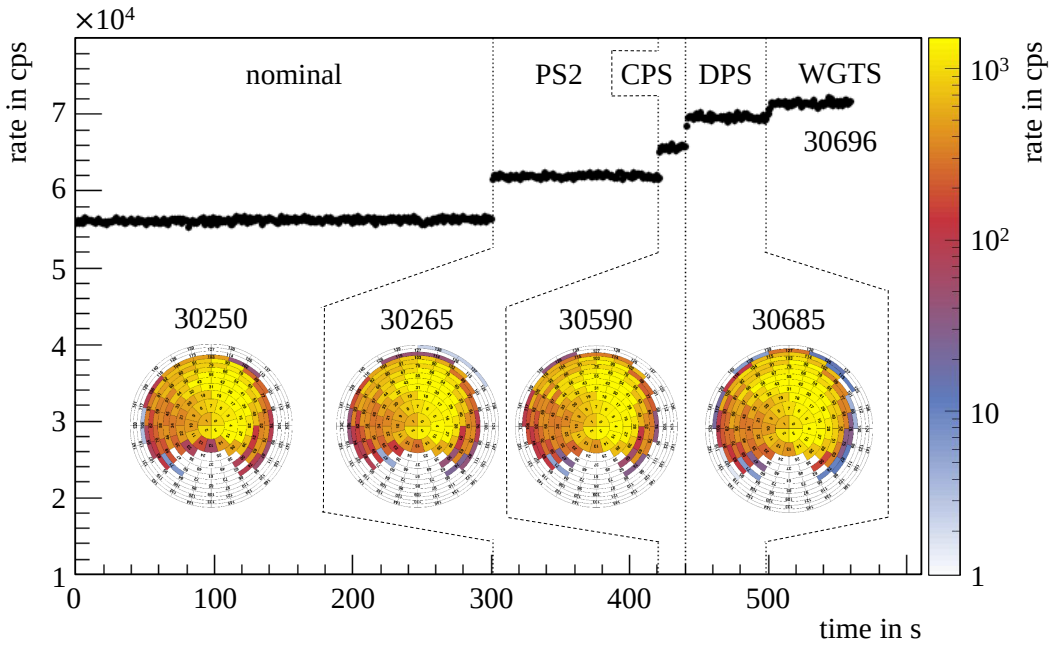

Figure 7.2: The observed electron rate during successive ramping of several superconducting solenoid systems. The time range is segmented in five parts, starting with run #30250 where all magnets are at 20 % of their nominal magnetic field. The second run #30265 shows an increase of $\sim 6\,\mathrm{kcps}$ in electron rate, as the PS2 solenoid is ramped up, resulting from pixels next to the shadowed area. By ramping up CPS and DPS (run #30590 and #30685) the rate change is about $\sim 4\,\mathrm{kcps}$. Some new pixels are hit by electrons, however only on the upper and right part of the image. Ramping up the WGTS in run #30696 is changing the electron rate only insignificantly.

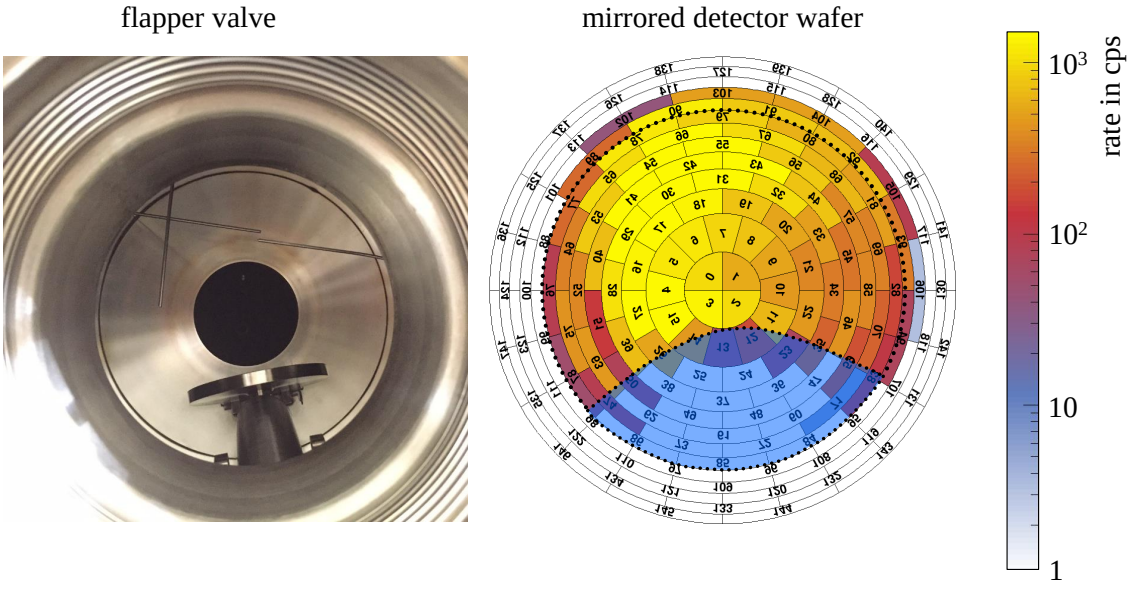

Figure 7.3: Flapper valve between PS and MS and the shadowed rear wall image on the detector wafer in downstream direction. The flapper valve is slightly tilted inside the beamline part between pre- and main spectrometer. The left picture shows the flapper valve during installation works prior to First Light measurement campaign, looking in downstream direction. The valve disc is completely open, as assumed during measurements. On the right side the event pattern on the detector wafer is mirrored to obtain an equivalent pixel view in downstream direction. A visual comparison between both figures indicates that the shadow and the flapper valve indeed feature approximately the same tilt, as the highlighted area is tilted by 7.5°, and the flapper valve is tilted by $\sim 10°$.

7.1.3 Characteristics of the identified blockade

The successive ramp up of the solenoids along the beamline described previously did not allow to definitively identify a collision point of the flux tube that could explain the observed shadow. However, there is a clear evidence for the fact, that low-energy electrons are blocked in the area of the PS2 solenoid. This blocking effect could be traced back to an electrostatic potential, which reflects low-energy electrons from the RW. To test this hypothesis, the starting energy of electrons was increased step-wise by setting the RW to a more negative potential, typically in steps of $-10\,\mathrm{V}$ every 20 seconds (appendix C: FL4). To obtain comparable results, all solenoids are operated at 20 % of their nominal field (except detector solenoid at 26 %). The corresponding change of the count rate on the FPD is shown in figure 7.4. Indeed, as expected in this scenario, the ramp up of the RW potential is causing an increase of the observed electron rate and the shadowed area decreases. Finally, at large potential offsets, the RW image is completely projected onto the FPD, resulting in a 22.8 % higher count rate, which is in good agreement with the previously estimated effect of the shadowed area. Thus, it can be concluded that the observed shadow is due to an electrostatic blockade in the region of the PS2 magnet.

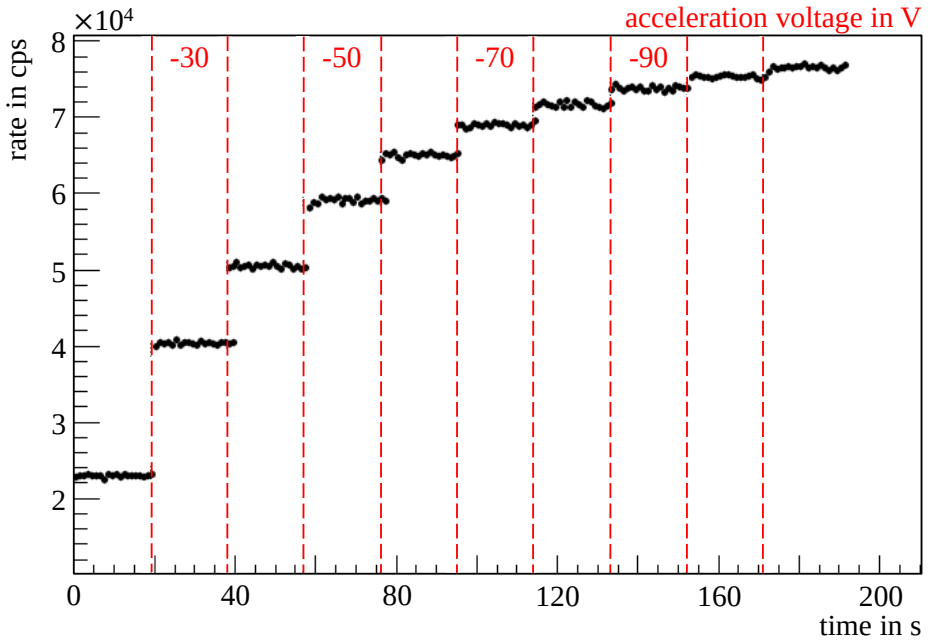

Figure 7.4: Correlation between the FPD count rate and the rear wall potential. To verify the hypothesis of an electrostatic blocking potential, the RW potential is increased in −10 V steps every 20 seconds, starting with −20 V. A higher voltage than −110 V can not be reached with the power supply in use during the measurement. The change in rate between the standard elevation potential of −50 V (59433.4 cps) and the maximum −110 V (77016.3 cps) is 22.8 % (appendix C: FL4).

7.1.4 Localization of the electrostatic blockade

To investigate whether the flapper valve inside of the PS2 magnet is indeed correlated with the origin of the shadow, the entire valve is elevated to positive potential. This is possible as the valve is electrically separated by insulators on both ends against the two spectrometers. For this investigation the RW voltage was set to −20 V. The flapper valve beamline part was connected to positive potential, starting at 0 V, and increasing every 20 seconds by a value of +10 V (appendix C: FL7). Figure 7.5 shows the change of the rate during this measurement, which resulted in a fully projected RW image onto the FPD at a potential offset of +90 V at the flapper valve. As figure 7.4 and 7.5 demonstrate, the count rate on the FPD is directly correlated with the potential between the RW and the shadow generating beamline part inside the warm bore of the PS2 magnet. It provides unambiguous evidence for an electrostatic blocking potential produced by the flapper valve components.

7.1.5 Conclusion

During the First Light measurements the RW was mapped onto the FPD wafer as a wide beam electron source. The shadow observed in the event pattern of the FPD could be traced back to a negative electrostatic potential in the regime of the PS2 magnet. More specifically, the PS-MS flapper valve causes a reflection of the low-energy electrons from the RW. This blockade can be overcome by increasing the potential of electrons at the RW. In view of the limited amount of measurement time, it could not be conclusively clarified which part of the flapper valve generates the electrostatic potential. Further investigations are required to determine the formation of the electrostatic potential.

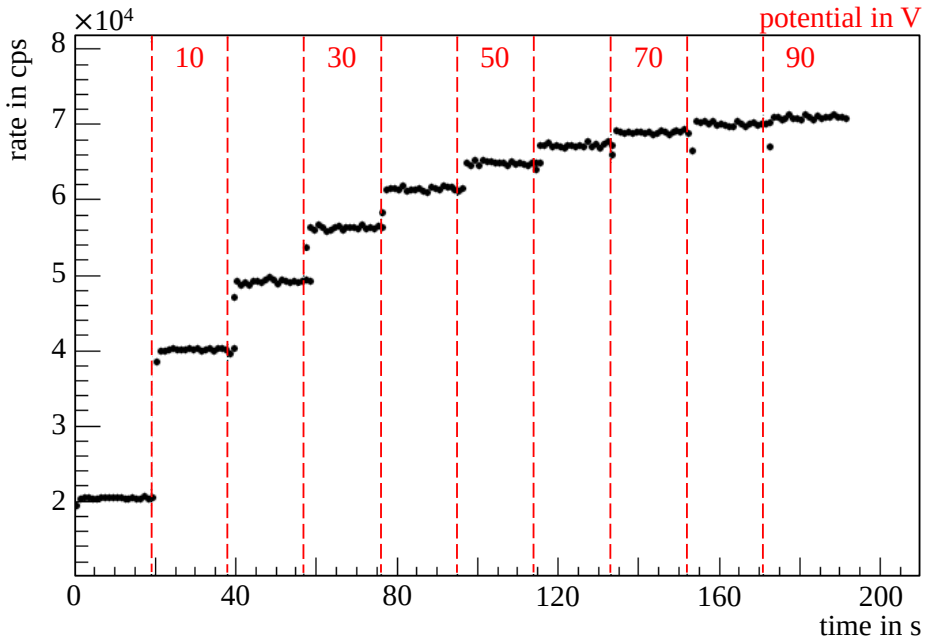

Figure 7.5: Correlation between the FPD count rate and the potential of the flapper valve beside the PS2 warm bore. The electrons start with a constant energy of −20 eV at the RW, reaching the electrostatic blocking in the regime of the flapper valve between the pre- and main spectrometer, which is connected to positive potential that is step-wise increased every 20 seconds by +10 V (appendix C: FL7).

7.2 Alignment measurements in STS

The main goal of the analyses presented below is to identify the largest collision-free size of the magnetic flux tube by characterizing the transmission of each STS beamline section. To measure the alignment and the transmission characteristics of the magnetic flux tube in each STS section, the bottleneck method is used, which was explained in the previous section 5.3. It relies on an pencil beam to scan each magnetic bottleneck by projecting it onto the wafer as a specific shape. The shape of the bottleneck image results from the collision between the magnetic flux tube and the beamline surface includes information about the alignment and transmission characteristics of the magnetic flux tube in the bottleneck section investigated.

Although the global superconducting solenoid system of the beamline was operated at a value of 20 % of their nominal magnetic field, the alignment and transmission results can be transferred 1:1 to a field layout with up to 100 % of the nominal field. This was demonstrated by simulations discussed in section 6.1.3. In all field layouts, there are two important magnetic flux tube sizes: 191 Tcm^2 and 210 Tcm^2, occupying a well-defined volume inside the global beamline, as described in section 3.3.2.3. This volume is independent of the overall magnetic field. Since only this volume is of interest and not the magnetic flux value, the results are described by the "magnetic flux equivalent" at the nominal magnetic field (see section 5.3).

7.2.1 Overview

Below measurements with the pencil beam are detailed. At first the scanning principle by shifting the pencil beam using the superconducting dipole magnets of the WGTS is verified. This is of major importance since it is used later on for analysis of the measured magnetic bottlenecks. The method used to calculate the pencil beam center is prone to be influenced by some effects, which also will be discussed in this section.

Then the investigation of magnetic bottlenecks is presented in section 7.2.3. A full area pencil beam to scan circular shaped bottlenecks had to postponed, due to limited measurement time. Consequently, only the pencil beam is used to scan magnetic bottlenecks in horizontal and vertical direction, resulting in four image shape points. The bottleneck is identified once the measured electron rate at the detector drops significantly (see section 6.2.3). The four measured points thus correspond to the collision points of the magnetic flux tube with the surface of the beamline and can be used to calculate the mapped bottleneck image, thereby providing information about transmission characteristics and alignment systematics between the bottleneck section examined and the detector.

As outlined preciously, a precise position of the pencil beam on the detector wafer can not be determined. Each measured collision point is related to a dipole current, the so-called collision current, which in combination with the linear correlation between dipole current the pencil beam shift, results in a much more precise determination of the pencil beam on the detector wafer. Accordingly, the shape of the bottleneck image can be calculated more precisely, in addition, dipole currents include information about the alignment between the bottleneck being probed section and the RW. The latter is cross referenced to the FPD in section 7.2.4.

Consequently, the alignment for each STS component is determined relative to the detector wafer. This allows to implement a cross check of the alignment of the STS components to each other, so that the measurement and analysis techniques can be verified, as presented in section 7.2.5.

7.2.2 Shifting the electron pencil beam with the dipole magnets

For measurements with the pencil beam all beamline magnets were operated at 20 % of their nominal magnetic field. At the beginning of the measurement campaign, the superconducting dipole magnets were deenergized so that the pencil beam hit the FPD at central pixel 1. The result points to a misalignment with a slight shift in the left and upward direction. For the beam shift measurements, the pencil image needs thus to be centered on the detector wafer by a dipole current of +0.6 A in horizontal (x) and +2.0 A in vertical (y) direction. Then the pencil beam is moved horizontally in x-direction, and vertically in y-direction. The correlation between pencil beam shifts and dipole currents are given in figure 7.6. The step size of 2.0 A for the displacement currents yields delivers a good efficiency with respect to the limited available measurement time and the required precision.

To calculate the exact position of the pencil beam on the segmented pixel wafer, the center-of-mass (CM) of events on the detector is calculated using Monte Carlo methods to take in account details of the wafer geometry. A series of x- and y-scans is carried out until the pencil beam collides with the STS beamline. During data-taking, a collision is defined as rate drop to $10 - 20$ % of the original rate (see section 6.2.3). In this context it has to be noted that a halo of electrons surrounds the pencil beam, being created by scattering processes and by background processes from the ELIOTT components. Unfortunately, this halo makes up more than 10 % of the total electron rate on the detector, implying that the last data points of each scan are already affected by a collision. These data points are thus not used for the linear fit analysis shown in figure 7.6.

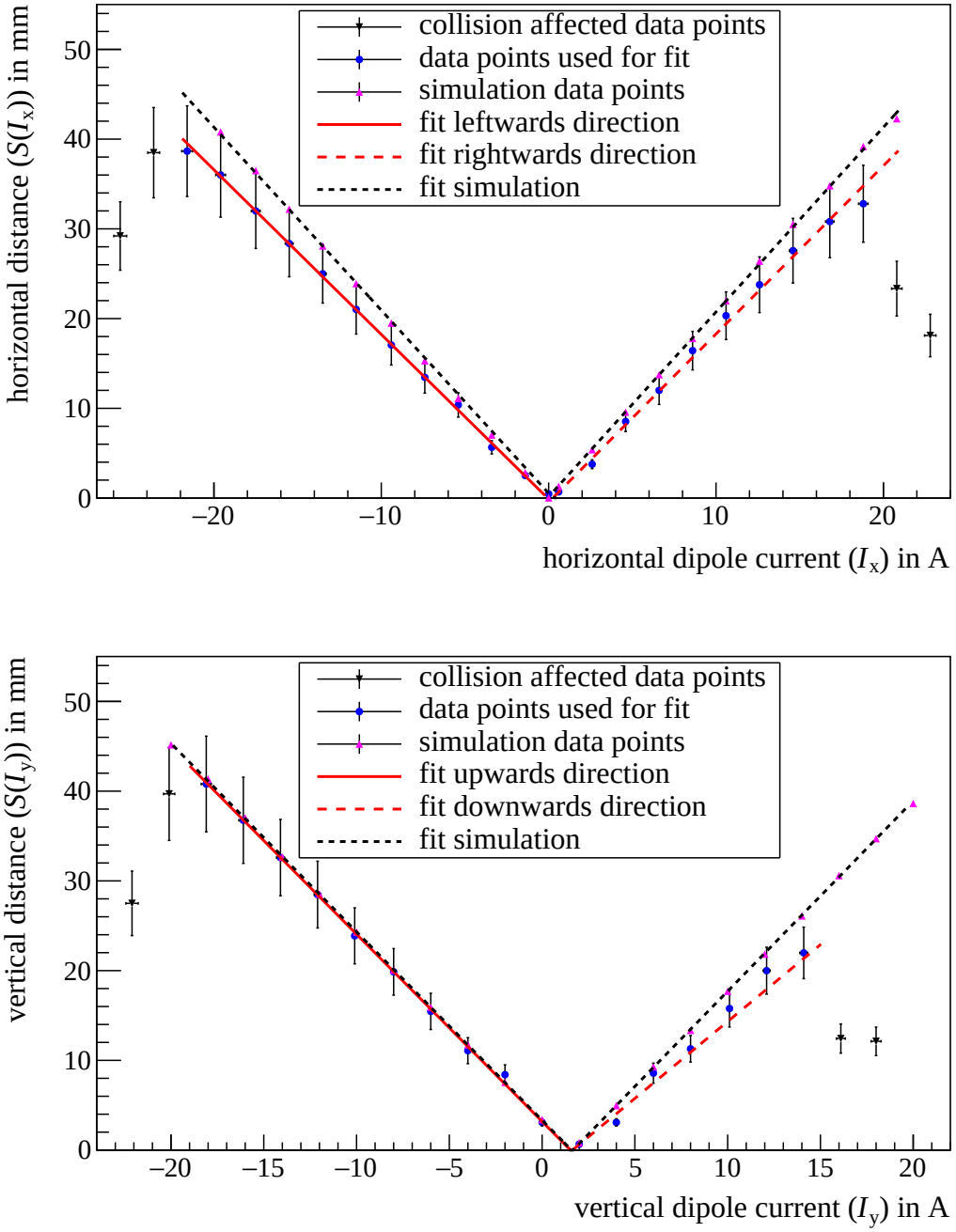

Figure 7.6: Magnetic flux tube scan with the pencil beam in horizontal and vertical direction. Displayed is the linear correlation between the current (I) of the s.c. dipole magnets at the upstream side of the WGTS and the resulting shift of the CM of the pencil beam as observed by the detector. In the upper figure the shift caused by the horizontal dipole coils is shown, the lower figure displays the shift caused by the vertical dipole coils. The final two measurement points on each side are removed from the analysis, as collisions with the beamline in combination with the surrounding beam halo yields inconclusive results. In the lower figure the effect of the electrostatic potential at the position of the flapper valve is visible which shields electrons of the pencil beam. Hence, no data above $I_+ = +14\,\mathrm{A}$ are used, these are strongly affected by the electrostatic blockade. Even at lower currents a systematic non-linearity of the correlation is found which is attributed to the shadow as well. To compare the corresponding shift to Kassiopeia simulations, the figures include simulated dipole shifts. In the upper figure the simulation and the measurement data for the horizontal direction show a distinct deviation. The same deviation is observed for the vertical direction. Measurement and simulation in the upward vertical direction are in perfect agreement.

At the time of these first measurements the shadow in the lower part of the detector had not yet been identified as being due to an electrostatic blockade, as explained in section 7.1. Consequently, the electron acceleration potential at the RW was fixed to $U_{\mathrm{RW}} = -50\,\mathrm{V}$. The ensuing electrostatic blockade could not be passed by electrons, as shown in figure 7.6. The mapped pencil beam image for each measurement point of the dipole current is presented in figure B.2 and B.3 in the appendix. Following linear correlations are identified for the four scans with the dipole coils:

$$S(I_{+\mathrm{x}}) = (+1.91 \pm 0.01)\,\frac{\mathrm{mm}}{\mathrm{A}} \cdot I_{+} - (0.52 \pm 0.03)\,\mathrm{mm}, \tag{7.1}$$

$$S(I_{-\mathrm{x}}) = (-1.85 \pm 0.01)\,\frac{\mathrm{mm}}{\mathrm{A}} \cdot I_{-} - (0.16 \pm 0.05)\,\mathrm{mm}, \tag{7.2}$$

$$S(I_{-\mathrm{y}}) = (+1.87 \pm 0.05)\,\frac{\mathrm{mm}}{\mathrm{A}} \cdot I_{+} - (3.40 \pm 0.39)\,\mathrm{mm}, \tag{7.3}$$

$$S(I_{+\mathrm{y}}) = (-2.07 \pm 0.03)\,\frac{\mathrm{mm}}{\mathrm{A}} \cdot I_{-} + (3.34 \pm 0.27)\,\mathrm{mm}. \tag{7.4}$$

The misalignment between the center of the pencil beam and the wafer center in case of deenergized dipole coils results in an offset for each direction. The value is provided by linear equations. A misalignment of $\mathrm{x} = -0.34\,\mathrm{mm}$ was determined for the horizontal direction making use of equations 7.1 and 7.2. For the vertical direction, an offset of $\mathrm{y} = +3.37\,\mathrm{mm}$ was determined using equations 7.3 and 7.4. The misalignment results between the center of the pencil beam and the wafer center are in good agreement with simulated results, as presented in section 6.2.1. The maximum deviation between the simulation and the measurement offset results is $< 0.15\,\mathrm{mm}$.

The simulations in section 6.2.1 were performed for a reduced global magnetic field of 20 % to allow direct comparison between measured and simulated data. The measured (eqs. 7.1 – 7.4) and simulated (eqs. 6.1 – 6.4) linear behavior between the dipole current and the pencil beam shift show significant deviations as visible in figure 7.6. This deviation is caused by the CM method used, in combination with the existing beam halo, which surrounds the pencil beam. Consequently, the halo generates a systematic uncertainty, which is highlighted in figure 7.6. The impact of the halo on the CM result is outlined in the following.

Systematic uncertainties due to the halo of the electron pencil beam

For a perfect pencil beam with sharp edge, its position on the segmented wafer can be calculated very precisely by using the CM method. This was verified by simulations with Kassiopeia. However, in the case of a realistic pencil beam impinging onto the FPD its surrounding halo has an impact on the calculated CM results. A first simplified analysis is used to compare measured and simulated CM values of the pencil beam: here, only the two pixels with the highest count rate during measurements are used. Hence, the halo can be neglected. Afterwards, these results are compared with the results of the previous CM method to scrutinize impact of the halo.

Kassiopeia simulation reveal that a pencil beam generates a hotspot at the detector with diameter of 3.6 mm. The radial width of the inner four pixel rings is big enough so that the pencil beam impinges onto one pixel only. In the case of 1-pixel illumination of the pencil beam is centered to the middle of the pixel. This first approximation is verified by simulations. On the other hand, when the pencil beam is located on two pixels, the geometry of the outer ring elements of $\sim 2\,\mathrm{mm}$ or less, the pencil beam center can be calculated on the basis of circular segments intersecting a circular shaped pencil beam. Hence, the fraction covered by the circular segment is directly correlated with its expected

count electron rate. An pencil beam without halo should have a count rate which is the sum the two count rates of the two adjacent illuminated pixels ($\gamma = \chi + \omega$). The distance d between the pencil beam center and the joint pixel boundary can then be calculated by using the formula for circular segments:

$$\chi/\gamma = \frac{\theta - \sin\theta}{2\pi}, \tag{7.5}$$

$$d = r \cdot \cos(\theta/2). \tag{7.6}$$

A visualization of the segmentation of a circular pencil beam is presented in figure 7.7. Although the boundary between the pixel rings is circular shaped, it was assumed for the circular segment calculation to be straight. This is applicable as its effect on the calculated distance is negligible to first order.

To investigate the difference between simulated and measured pencil beam events, the appropriate run number 31392 was used. During this measurement the pencil beam was shifted by a dipole current of +16.6 A in horizontal direction. Assuming that the real pencil beam has the same diameter as the simulated one (3.6 mm), the pencil beam center should be located on pixel 99, as displayed by far the highest counted rate (ω = 20485.8 cps). Due to the extended diameter of the pencil beam (3.6 mm) in comparison to the radial width of pixel 99 (r_{pw} = 2.29 mm), the pencil beam does not fit completely into this pixel. Hence, a part of the pencil beam area is located at the neighboring pixel, showing the second highest count rate. Here, pixel 76 is identified with the second highest count rate (χ = 8539.0 cps). By analyzing only these two pixels and neglecting pixels affected by the beam halo, a rate ratio of 0.29 was determined resulting in a distance of 0.6 mm between the pencil beam center and the joint boundary. Since the joint boundary has a radial distance to the wafer center of +34.7 mm, the total shift of the pencil beam center is x = +35.3 mm. Corresponding simulations provide a pencil beam position at 16.6 A of x = +34.9 mm, resulting in a distance of 0.2 mm between the pencil beam center and the joint boundary. The difference between simulated and calculated pencil beam positions is 0.4 mm. Hence, the simulation results are in good agreement with measurement results to first order.

Using the CM method to analyze the pencil beam center for run number 31392, a shift of x = +32.5 mm was calculated. Comparing this CM result with the circular segment result, a significant deviation of about 2.80 mm is determined in horizontal direction. A visualization of the horizontal pencil beam scan and the resulting deviation between CM and measured pencil beam result is shown in figure 7.8. A linear dependence between the size of the deviation and the shift distance of the pencil beam to the wafer center can be obtained by analyzing all data. This gap, which is generated by the halo in combination with the CM method, corresponds to the systematic uncertainty of the pencil beam center in radial direction. Hence, the systematic uncertainty in radial direction is given by the linear correlation coefficients of ~ 0.1 ($\sim 10\,\%$).

To calculate the uncertainty for the tangential direction, the pixel geometry and the specific arrangement of the pixels have to be taken in account. The pixel rings are rotated by 15° against each other. Hence, once an pencil beam is located on two pixels on neighboring rings, such as in the previous example shown in figure 7.8, systematic uncertainties for the tangential direction are limited by radial boundaries. Since these have a displacement of 15° for two neighboring pixel rings, the maximum systematic uncertainty for the tangential direction is 7.5°.

The deviation between the CM results and simulation results of the pencil beam scan can thus be resolved by taking into account the outlined uncertainties.

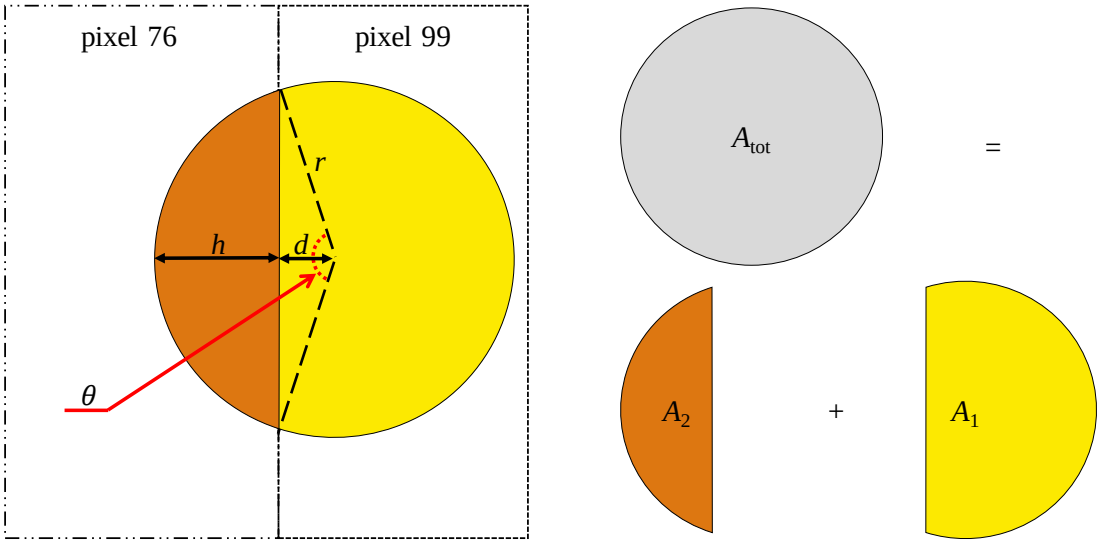

Figure 7.7: Visualization of the circular segment calculation. The figure shows the pencil beam distribution on two pixels. The total area of the pencil beam A_{tot} corresponds to the total counts of electrons γ. A fraction of these counts χ is located on a neighboring pixel (pixel 76), demonstrated as the small circular segment A_2. The distance d between the beam center and the pixel boundary can be calculated according to equation 7.6.

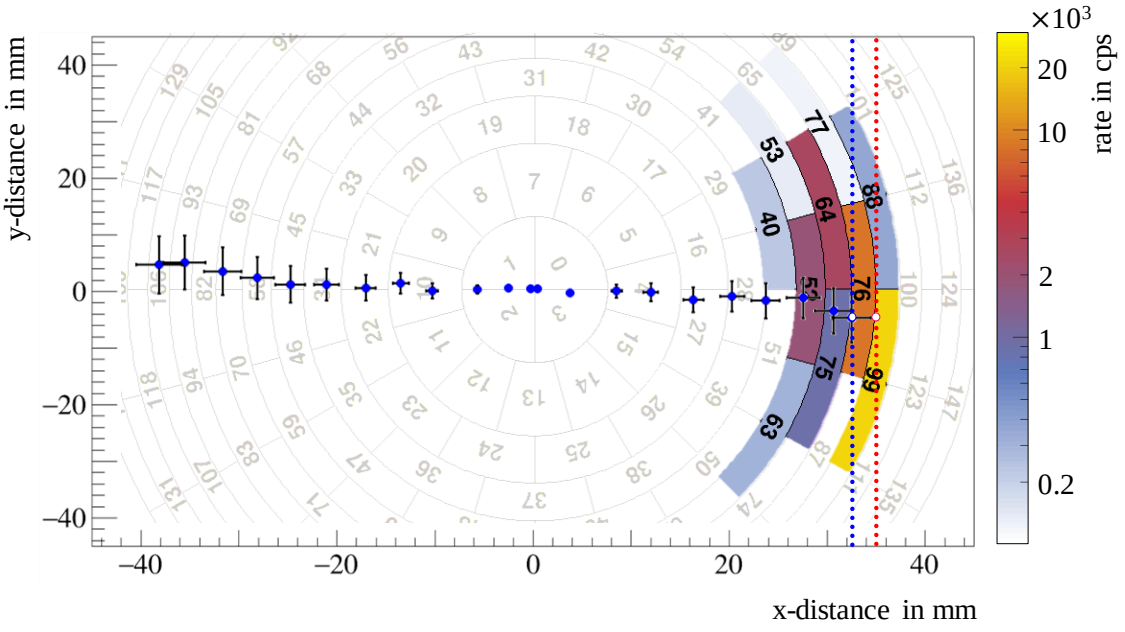

Figure 7.8: The calculated pencil beam centers during a horizontal scan over the wafer. Shown are the calculated pencil beam centers using the CM method for the horizontal scan across the wafer using the dipole coils on the rear part of the WGTS (blue points). The highlighted pixel area shows the halo that surrounds the pencil beam hotspot at an outer radius on the wafer. The significant influence of this halo on the results of the CM method is emphasized by the two dashed lines. The blue line shows the calculated shift in horizontal direction using the CM method. The red line shows the measured pencil beam center, which is comparable with the pencil beam center of the simulation for a dipole current of 16.6 A. It demonstrates that the CM method is noticeably influenced by the halo, since the simulated hit point fits perfectly with the two pixels 76 and 99, which have the largest measured count rate.

7.2.3 Investigation of the magnetic bottlenecks in STS

In this section the alignment of single STS components relative to the detector wafer as well as the global transmission characteristics are discussed. First the transmission characteristics are determined with the pencil beam by scanning the magnetic bottleneck until beam collision with an inner beamline surface is achieved. Since the segmented detector wafer has limited spatial resolution, the measurement data does not include information on the exact point of impingement of the pencil beam onto the wafer. To reach a sub-pixel precision, the linear correlation between dipole current and beam shift has to be used (see section 7.2.2). With calibrated collision currents, an exact position on the detector wafer can be calculated.

The largest collision-free flux tube is projected onto the detector wafer as a "negative image" of the collision points. Its radius can be calculated by analyzing the distance between single collision points and by comparing the image radius with the radii in table 5.1. The center of the "negative image" in comparison to the center of the wafer yields the alignment information between the investigated bottleneck section and the detector wafer. In the case of perfect RW alignment to the investigated bottleneck section, the collision currents would be identical the same for each direction. If not, this is an indication for a relative misalignment between these components. The alignment between the RW and the investigated bottleneck section can then be calculated using the average of collision currents for each direction.

Following the discussions in the section on simulation results, the order of the experimental investigations is identical: first, the bottleneck is created with the WGTS solenoids M2 and M3, then with the DPS solenoids, and finally with the CPS solenoids. To recap briefly: simulations of the bottleneck at the WGTS part of M6 and M7 showed no collisions or constrictions, therefore, due to the limited measurement time an investigation of this part was omitted.

7.2.3.1 Section-wise investigation of the flux tube image

In the following the flux tube transmission characteristics are determined for each single section via the previously introduced collision point identification (CPI) method. At first the measurement results of the measured CPI method are presented, using the measured collision currents and the linear equations 7.1 – 7.4 for the measured linear dependency. These results are compared with the simulated results for the CPI method using simulated collision currents and linear equations 6.1 – 6.4 for the simulated linear behavior. As deviations of the linear fits (see figure 7.6) for measured and simulated pencil beam shift occur, as a result of are due to the systematic uncertainties of the CM method (see section 7.2.2), a combined analysis is performed. Here, the linear equations of the simulations (equation: 6.1 – 6.4) are used together with measured collision currents, hereinafter named "combined CPI method".

To verify the results of the linear fit analysis, another approach is used, the so-called "4 last illuminated pixels" (4LIP) method is used in addition. This method is based on Monte Carlo simulations: first of all, three (out of four) collision pixels with the largest distance to the wafer center are selected and a hit point within each pixel geometry is randomly diced by Monte Carlo. A circle is then calculated to connect all three Monte Carlo hit points. Afterwards, it is calculated whether the fourth collision pixel lies on the calculated circle. The benefit of this analysis approach is that it directly uses the information given by the detector. Due to the pixel size, the result of this 4LIP method is a distribution of the circle radii as well as a distribution of the circle center. These results can be compared with the results of the CPI method.

WGTS

During measurements, the rear section solenoid, as well as magnets M2 and M3 of the WGTS were ramped down to 15 % of their nominal field, while all other magnets were operated at 20 % (see figure 5.4). The pencil beam was then shifted by increasing the dipole currents in 2.0 A steps, starting at 0.0 A, until the beam collided with the WGTS source tube and a rate change is detected. The four collision currents are given in table 7.2 and are compared to corresponding shifts of the pencil beam resulting from the CPI method, as well as simulation results for of the CPI method. Significant deviations between the simulation and measurement CPI results can be traced back to the halo, which causes systematic shifts at the outer detector radii. Using the combined CPI method, the radius of the collision-free magnetic flux tube is 38.7 mm. To verify this result, the previously described 4LIP method is used to calculate the largest collision-free magnetic flux tube.

The results of the 4LIP method are presented in figure 7.9. The radii distribution indicates a WGTS bottleneck image on the detector with radii between 38.0 mm and 39.2 mm. This result is in excellent agreement with the result of the combined CPI method. Both analysis methods indicate that the 210 Tcm^2 flux tube can be guided collision-free through the WGTS (see table 7.2).

Since the four collision points do not include information about collisions in other areas of the circle-shaped flux tube, a fully illuminated electron flux tube was used to investigate these outer areas. In section 7.1 these measurements with the RW serving as a wide beam electron source were discussed. As outlined, they covered an area of the 195 Tcm^2 magnetic flux tube equivalent.

Table 7.2: Collision currents and corresponding collision points for the WGTS bottleneck. The calculated collision points for the measurement data, simulated data and a combined analysis are presented below. The analyzing strategies of the used CPI method were discussed in section 7.2.3. During this measurement, the WGTS solenoids M2 and M3 were operated at 15 % of nominal field, creating the magnetic bottleneck, demonstrated in figure 5.4. The mean radius per axis is given by $\overline{\mathrm{x}}$ and $\overline{\mathrm{y}}$ (eqs. 6.5 and 6.6).

	dipole current (I) in A		displacement ($S(I)$) in mm		
direction	measurement	simulation	measurement	simulation	combined
+x	+19.40	+19.6	$+36.53 \pm 4.77$	$+40.54 \pm 0.11$	$+40.12 \pm 0.68$
−x	−18.00	−20.4	-33.14 ± 4.33	-42.16 ± 0.55	-37.26 ± 0.59
$\overline{\mathrm{x}}$	18.70	20.0	34.84 ± 4.55	41.35 ± 0.33	38.69 ± 0.64
+y	−16.60	−20.0	$+37.70 \pm 4.93$	$+45.33 \pm 0.76$	$+38.19 \pm 0.64$
−y	+21.15	+20.0	-36.15 ± 4.72	-38.89 ± 0.89	-41.33 ± 0.97
$\overline{\mathrm{y}}$	18.88	20.0	36.93 ± 4.82	42.11 ± 0.83	39.76 ± 0.81

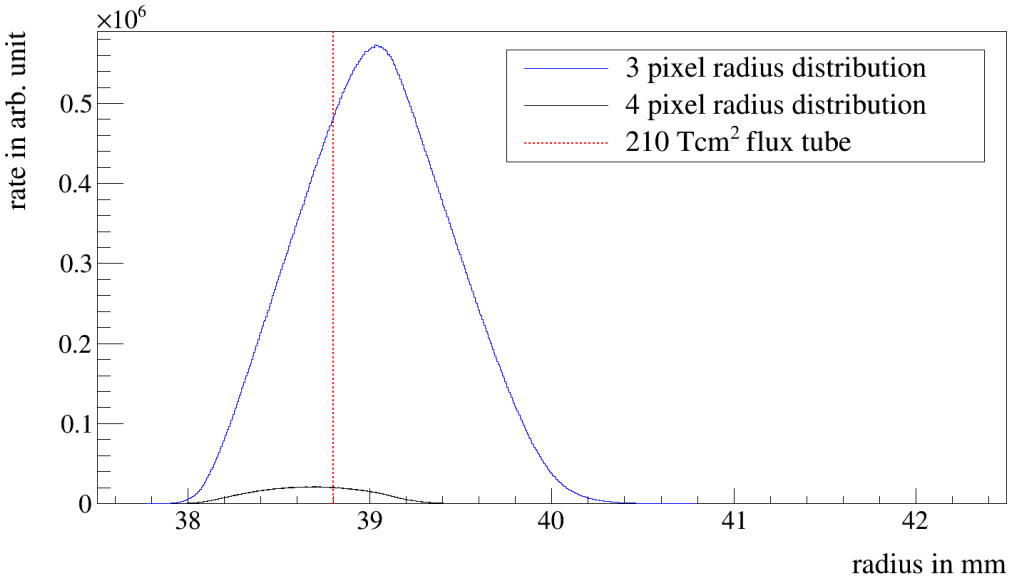

Figure 7.9: Distribution of possible radii of the WGTS flux tube image on the detector wafer. The radii distribution in blue shows the result using the three pixels which have the largest distance to the wafer center. The fourth pixel reduce the radii distribution as shown in black (4LIP method). The expected image radius of the 210 Tcm^2 magnetic flux tube is about 38.8 mm (see table 5.1) and is drawn as a red dashed line. The four pixel radii distribution includes the radius of the 210 Tcm^2 magnetic flux tube.

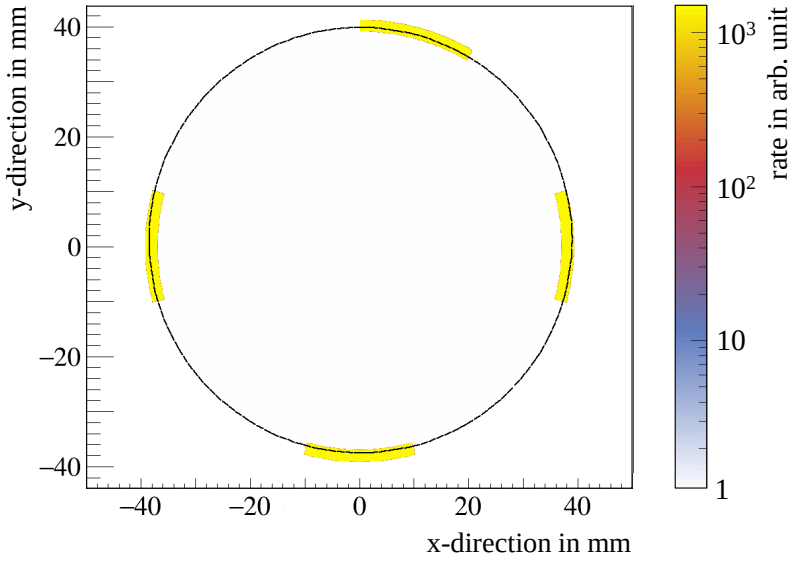

Figure 7.10: Projection of the bottleneck in the WGTS onto the detector wafer. By using the four last illuminated pixels, a Monte Carlo simulation was used to fill the pixel area uniformly with events. The vertical pixels and the pixel on the left side of the figure are used to calculate the radii distribution for three pixels (see figure 7.9). Afterwards the calculated radii distribution was modified by adding the fourth pixel, which is located on the right side of the figure (4LIP method). The mean radius of the four pixel radii distribution was added to the figure, visualizing the projected bottleneck image of the WGTS onto the wafer.

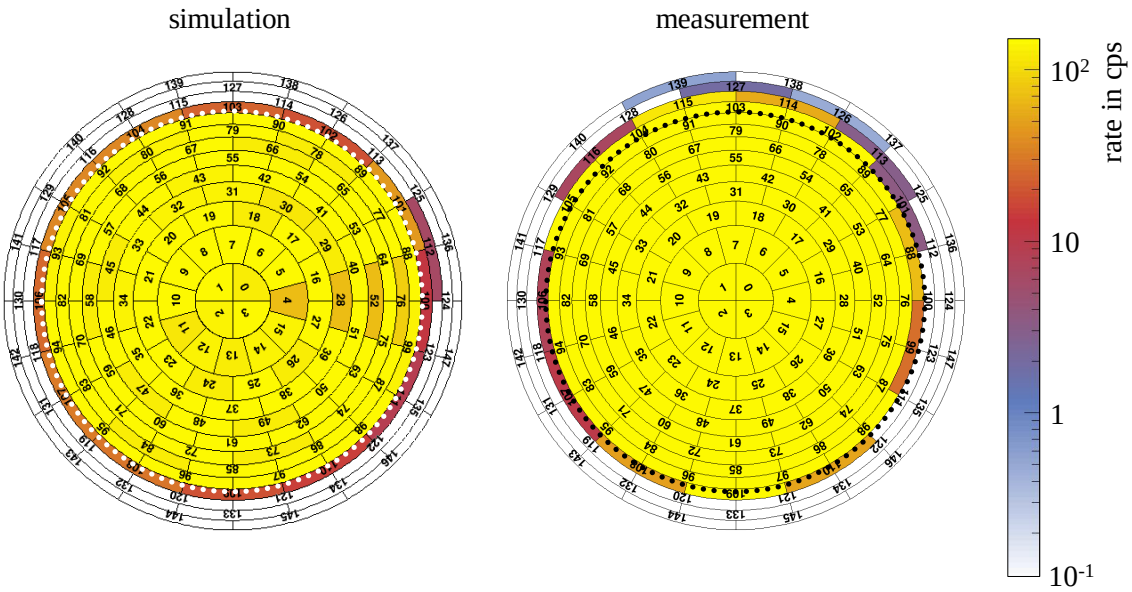

Figure 7.11: Simulation and measurement results of the rear wall image by applying a bottleneck in the WGTS. The left figure shows the wide beam image of the Kassiopeia simulation. Since there is a misalignment in the simulation model of $\sim 3.0\,\mathrm{mm}$ in positive y-direction, but a negligible $< 0.2\,\mathrm{mm}$ in positive x-direction, a current of $+1.6\,\mathrm{A}$ was used for the simulation to center the image on the wafer in vertical direction. A radius of 37.4 mm could be determined and is highlighted as a dashed white circle (see figure 6.4). For the measurement on the right side of the figure, the RW image was also centered on the wafer using the WGTS dipole coils. The resulting image shows some pixels illuminated in the upper part of the wafer, which emphasizes that a part of the UV light had released electrons outside of the active region of the RW. The majority of the count rate, however, can be found in the same area as in the simulations. A radius of $\sim 37.0\,\mathrm{mm}$ was thus determined for the measured circular-shaped image, which is highlighted as black dashed circle. The circle radius is determined by assuming the circle center to correspond to the wafer center. If the circle center is assumed as being independent of the wafer center, as in the case of a not perfectly aligned wide beam image onto the FPD, an image radius of $> 37.0\,\mathrm{mm}$ is possible.

In a first step, the pencil beam and hence the RW image was adjusted to the center of the detector wafer with a dipole current of $+0.7\,\mathrm{A}$ in horizontal and $+2.27\,\mathrm{A}$ in vertical direction (appendix C: FL5). Afterwards, the pencil beam was switched off and the wide beam source was turned on. The detected image on the detector wafer shows no collision points between the beamline and the $195\,\mathrm{Tcm}^2$ magnetic flux tube equivalent, which is illuminated by the wide beam (see figure 7.11). The corresponding simulations show that a collision-free guiding of the RW electrons leads to an image with radius of 37.4 mm on the wafer (see table 6.1). The 4LIP method shows that this radius can be mapped collision-free onto the FPD. Figure 7.11 shows the simulated and measured RW image including the images, radius of 37.4 mm. The shape of the measured wide beam image is not as perfect as the shape of the simulated wide beam image. It is possible that the UV light irradiation at the RW generates additional electrons above the RW disc at the stainless steel RW chamber. As shown in table 5.1, the $191\,\mathrm{Tcm}^2$ flux tube equivalent gives a radius at the detector of $\sim 37.0\,\mathrm{mm}$. Accordingly, the outcome of all measurement and analysis techniques provides unambiguous evidence that the $191\,\mathrm{Tcm}^2$ flux tube can be guided collision-free through the entire source section.

DPS

After the WGTS bottleneck measurements, the DPS solenoids were ramped down to 15 % of their nominal values to create a magnetic bottleneck there. The WGTS solenoids M2 and M3 were still operated at 15 % of their nominal field. First, the collision points were scanned by shifting the pencil beam with the dipole coils of the WGTS, as explained earlier. The results are shown in table 7.3. From the measurement data (CPI method), the largest collision-free magnetic flux is found with radius of (34.02 ± 4.44) mm. A comparison between simulated and measured mean currents yields a near perfect match (see table 7.3). If the combined CPI method is used for analysis of the measured collision currents, a maximum magnetic flux tube with radius of > 37.8 mm is found.

The 4LIP method is used again to cross check these flux-tube radius results. The identified range of possible radii varies between 37.9 mm and 38.2 mm, as shown in figure 7.12. The four illuminated pixels used for the 4LIP method together with the calculated mean radius is given in figure 7.13. The radii distribution confirms the results of the combined CPI analysis of a collision-free 191 Tcm^2 magnetic flux tube guiding. For a detailed investigation of the flux tube shape, the wide beam source was used. To center the wide beam image on the detector, the same correction currents were used as in the WGTS bottleneck case. The mapped RW image is displayed in figure 7.14. RW image on the detector wafer is not completely centered, as pixels on the left side on the last illuminated ring (pixel 105 - 107) show a higher counting rate as pixels on the right side (pixel 99 and 88). A validation for a reduction of the 195 Tcm^2 magnetic flux tube equivalent in horizontal direction has thus not been achieved.

The results of the collision currents and the 4LIP method show that the 210 Tcm^2 magnetic flux tube equivalent cannot be guided collision-free through this beam element. The omega-shaped geometry of the DPS beamline together with the extensive beamline instrumentation, as detailed in section 3.2.4, is the likely source of the reduced magnetic flux tube size, which is most pronounced in horizontal direction. Since the FBM is located in the horizontal part of the 210 Tcm^2 magnetic flux tube of the CPS, a collision in the DPS beamline parts would directly affect the measurement of the source activity (see section 3.3.2.4). Hence, a collision has to be prevented. Therefore, the measurement was repeated with a reduced magnetic bottleneck of 17.5 % of the nominal magnetic field.

Table 7.3: Collision currents and corresponding collision points for the DPS bottleneck. The calculated collision points for the measurement data, simulated data and a combined analysis are presented below. The analyzing strategies of the CPI-method were discussed in section 7.2.3. During this measurement, the DPS solenoids were operated at 15 % of their nominal field, creating a magnetic bottleneck. The mean radius per axis is given by $\overline{\mathrm{x}}$ and $\overline{\mathrm{y}}$ (eqs. 6.5 and 6.6).

	dipole current (I) in A		displacement ($S(I)$) in mm		
direction	measurement	simulation	measurement	simulation	combined
+x	+18.35	+18.4	$+34.53 \pm 4.51$	$+38.06 \pm 0.58$	$+37.96 \pm 0.66$
−x	−18.20	−18.6	-33.51 ± 4.38	-38.48 ± 0.05	-37.67 ± 0.60
$\overline{\mathrm{x}}$	18.28	18.5	34.02 ± 4.44	38.27 ± 0.32	37.81 ± 0.63
+y	−15.80	−19.0	$+36.05 \pm 4.71$	$+43.23 \pm 0.29$	$+36.51 \pm 0.63$
−y	+21.10	+19.0	-36.06 ± 4.71	-36.77 ± 1.18	-41.22 ± 0.97
$\overline{\mathrm{y}}$	18.95	19.0	36.06 ± 4.71	40.00 ± 0.74	38.87 ± 0.80

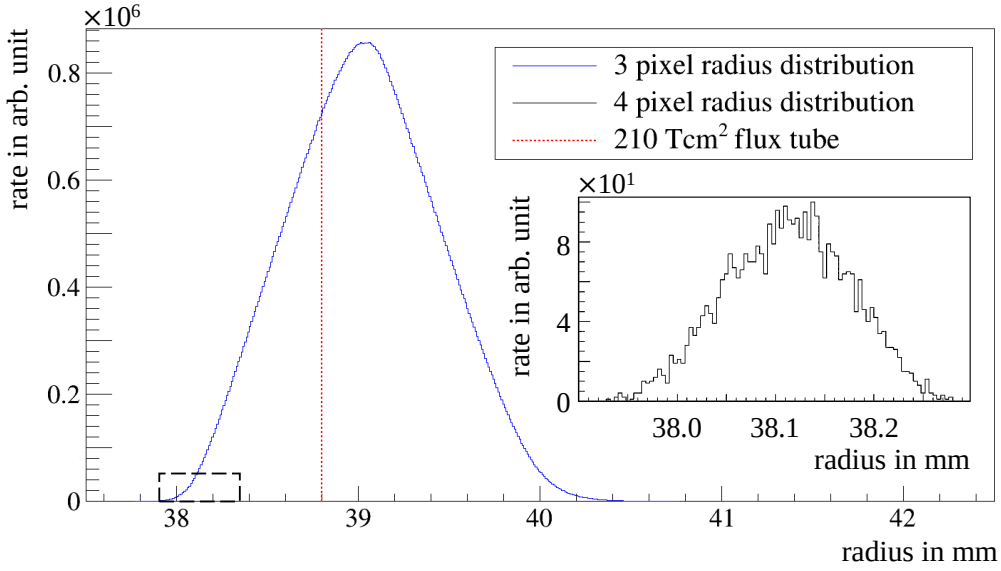

Figure 7.12: Distribution of possible radii of the DPS flux tube image on the detector wafer. The radii distribution in blue shows the result for the three pixels which have the largest distance to the wafer center. The inlet shows the radii distribution for the 4LIP method in black. The radii distribution of the 4LIP method is limited due to the arrangement of the four pixels and especially pixel 88 which has the shortest distance to the wafer center (see figure 7.13). The expected image radius of the 210 Tcm^2 magnetic flux tube equivalent is about 38.8 mm and is drawn as a red dashed line. The four pixel radii distribution includes the radius of the 191 Tcm^2 but not the radius of the 210 Tcm^2 flux tube equivalent.

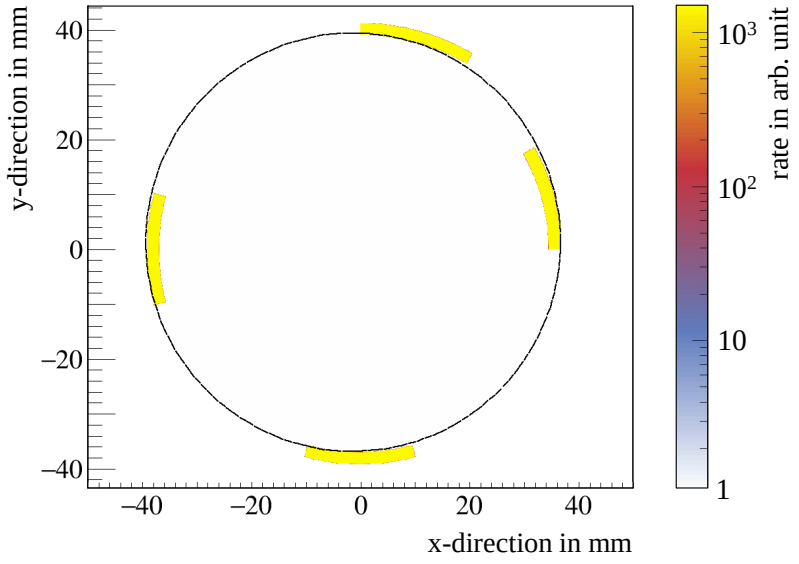

Figure 7.13: Projection of the bottleneck in the DPS onto the detector wafer. By using the four last illuminated pixels, a Monte Carlo simulation is used to fill the pixel area uniformly with events. The vertical pixels and the pixel on the left side of the figure are used to calculate the radii distribution for three pixels (see figure 7.12). Afterwards the calculated radii distribution is narrowed down by adding the fourth pixel (pixel 88), here located on the right side of the figure. The mean radius of the four pixel radii distribution is highlighted as a black circle, visualizing the projected bottleneck image of the DPS onto the detector wafer. The highlighted circle demonstrates the narrowed-down four pixel radii distribution since the circle is located on the outer boundary of the horizontal pixels, which defines the largest radius, and on the inner boundary of the vertical pixels, which defines the smallest radius.

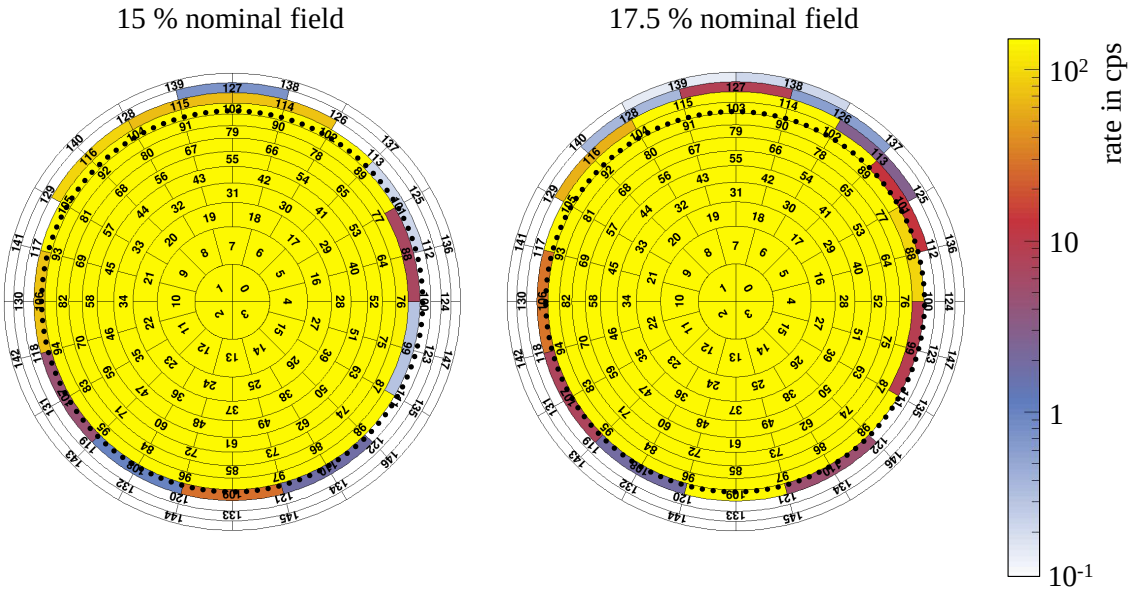

Figure 7.14: Measurement results of the rear wall image when applying two bottlenecks with different magnetic field in the DPS. The left figure shows the wide beam image in combination with a DPS magnetic bottleneck of 15 % nominal field. The radius of the 191 Tcm^2 magnetic flux tube was determined by simulations as well as by calculations ($\sim$ 37.0 mm) and is highlighted a dashed black circle in both pixel patterns of the FPD, see table 6.1. It demonstrates that pixels 88 and 99 detect a lower counting rate in comparison to other illuminated pixels inside the circle. The loss of rate can be caused by a collision. However, the last illuminated pixels on the left side of the wide beam image (pixels 105 - 107) display a higher count rate than expected. A possible explanation is that the image is shifted slightly to the left side without being influenced by collisions. The right figure shows the wide beam image in combination with a DPS magnetic bottleneck of 17.5 % nominal field together with the expected image radius, highlighted as black dashed line. In comparison to the left image, the image is better centered on the wafer, as the right side pixels obtain a larger counting rate while the left side pixels lose counts.

In this case only the collision current of +19.2 A in positive x-direction shows a significant change. Using the combined CPI method, a collision-free magnetic flux tube radius of $>$ 38.6 mm is found. However, the 4LIP method delivers identical results for magnetic bottlenecks of 15 % and 17.5 %, as the four last illuminated pixels remain unchanged. Therefore, the 195 Tcm^2 magnetic flux tube equivalent was illuminated again with RW electrons. As shown in figure 7.14, the two pixels 99 and 88 nearly reaches their nominal counting rate equivalent to the other pixels. Two different explanations are possible, the first one being that the lower magnetic field shifts the RW image slightly to the left side, as explained before. The second is that collisions are eliminated, as the magnetic flux tube is compressed by the higher magnetic field, according to equation 3.8.

The corresponding simulations exhibit nearly the same behavior of a reduction of the magnetic flux tube size in horizontal direction at 15 % of nominal magnetic field, in comparison to the measurement results. The results for all analyzing techniques indicate a collision-free 191 Tcm^2 magnetic flux tube guiding through the DPS beamline part at 15 % of the nominal value. However, the 210 Tcm^2 magnetic flux tube is strongly influenced by collision. Using a slightly higher magnetic field, as is implemented with the magnetic bottleneck of 17.5 % of the nominal value, the measurements still show collisions of the 210 Tcm^2 magnetic flux tube. An unambiguous collision-free magnetic flux tube size could not be provided, since the different measurement and analysis techniques show discrepancies in the results. For future measurements, an even stronger increase in the DPS solenoid

currents should thus be envisaged.

CPS

As shown in the previous section, magnetic bottlenecks in the DPS elements at 15 % and 17.5 % nominal value decrease the radius of the collision-free magnetic flux tube such that it dominates the size of the usable magnetic flux tube in the STS part of KATRIN. To compare the results of the bottleneck measurements of CPS and DPS, the DPS was kept at the last setting of 17.5 %. Then the flux tube scans give mean currents almost identical to the simulated collision currents (see table 7.4). These measured currents show similar results as for the WGTS bottleneck and for the DPS bottleneck at 17.5 % nominal value. By analyzing the collision currents with the CPI method, the maximum collision-free magnetic flux tube is (35.2 ± 4.6) mm. However, for the combined CPI method the maximum collision-free magnetic flux tube is > 38.8 mm. The 4LIP method yields a possible radius range between 38.0 mm and 38.7 mm, as shown in figure 7.15. A mean radius of 37.1 mm is determined and highlighted in figure 7.16.

For a more detailed investigation of the flux tube shape, the wide beam source is used. To center the wide beam image on the detector, the same correction currents are used as in the WGTS bottleneck case. The mapped wide beam image is displayed in figure 7.17, which is complemented by the wide beam image in combination with the DPS magnetic bottleneck at 17.5 % of the nominal value. Almost no difference of the CPS bottleneck on the mapped image in comparison to the DPS bottleneck can be seen. Consequently, it is highly plausible that the 195 Tcm^2 magnetic flux tube equivalent can be guided collision-free through the CPS beamline part.

The combination of the WGTS operated at 15 %, DPS at 17.5 % and CPS at 15 % nominal magnetic field shows that the transmission of the magnetic flux tube for nominal magnetic field setting is affected by the DPS only. All analyzing techniques find that the 191 Tcm^2 magnetic flux tube can be guided collision-free through the CPS beamline part. There is also a high likelihood to guide the 210 Tcm^2 magnetic flux tube collision-free through the CPS beamline part.

Table 7.4: Collision currents and corresponding collision points for the CPS bottleneck. The calculated collision points for the measurement data, simulated data and a combined analysis are presented below. The analyzing strategies of the used CPI method have been discussed in section 7.2.3. During these measurement the CPS solenoids were operated at 15 % nominal field, creating the magnetic bottleneck. The WGTS bottleneck (solenoids M2 and M3) was kept at 15 %, and the DPS solenoids were operated at 17.5 % of nominal field. The mean radius per axis is given by $\overline{\mathrm{x}}$ and $\overline{\mathrm{y}}$ (eqs. 6.5 and 6.6).

	dipole current (I) in A		displacement ($S(I)$) in mm		
direction	measurement	simulation	measurement	simulation	combined
+x	+19.40	+19.4	$+36.53 \pm 4.77$	$+40.12 \pm 0.16$	$+40.12 \pm 0.68$
−x	−18.40	−19.6	-33.88 ± 4.43	-40.52 ± 0.51	-38.08 ± 0.60
$\overline{\mathrm{x}}$	18.90	+19.5	35.21 ± 4.60	40.32 ± 0.33	39.10 ± 0.64
+y	−15.50	−18.0	$+35.43 \pm 4.63$	$+41.13 \pm 0.41$	$+35.88 \pm 0.62$
−y	+21.40	+20.0	-36.62 ± 4.78	-38.89 ± 0.10	-41.86 ± 0.98
$\overline{\mathrm{y}}$	18.85	19.0	36.03 ± 4.71	40.01 ± 0.25	38.87 ± 0.80

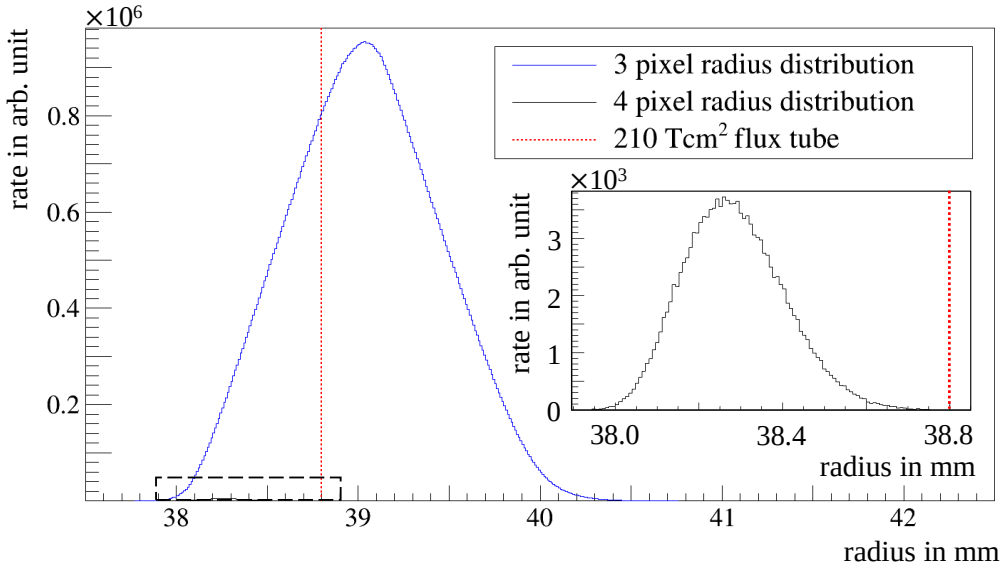

Figure 7.15: Distribution of possible radii of the CPS flux tube image on the detector wafer. The radii distribution in blue shows the result for the three pixels which have the largest distance to the wafer center. The inlet shows again the radii distribution for the 4LIP method in black. The radii distribution of the 4LIP method is more narrow due to the arrangement of the four pixels and especially pixel 99, which is closest to the wafer center (see figure 7.16). The expected image radius of the 210 Tcm^2 magnetic flux tube equivalent is about 38.8 mm and drawn as a red dashed line. The four pixel radii distribution includes the radius of the 191 Tcm^2, but the radius of the 210 Tcm^2 magnetic flux tube equivalent is located virtually at the right tail of the four pixel radii distribution.

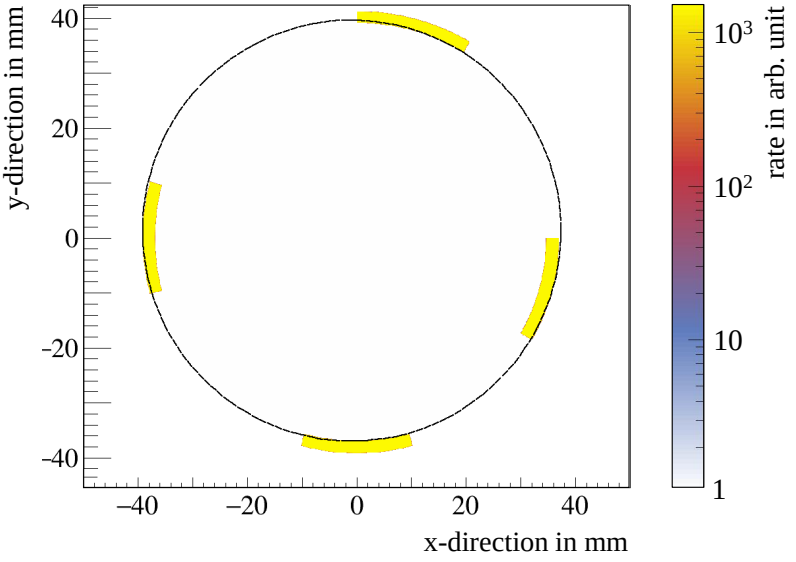

Figure 7.16: Projection of the bottleneck in the CPS onto the detector wafer. By using the four last illuminated pixels, a Monte Carlo simulation was used to fill the pixel area uniformly with events. The vertical pixels and the pixel on the left side of the figure are used to calculate the radii distribution for three pixels (see figure 7.15). Afterwards the calculated radii distribution is narrowed down by adding the fourth pixel (pixel 99), which is located on the right side of the figure (4LIP method). The mean radius of the four pixel radii distribution is highlighted as black circle, visualizing the projected bottleneck image of the CPS onto the detector wafer. The highlighted circle demonstrates the narrow four pixel radii distribution since the circle is located on the outer boundary of the horizontal pixels, which defines the largest radius, and on the inner boundary of the vertical pixels, which defines the smallest radius.

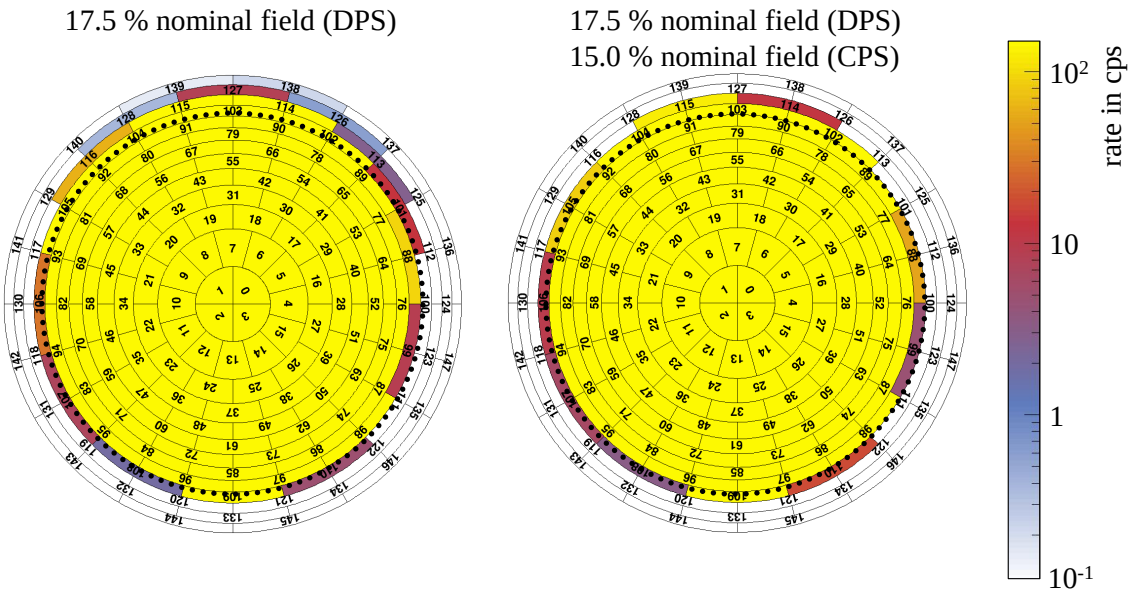

Figure 7.17: Results of measurement of rear wall images by applying a bottleneck in the DPS and in combination with a bottleneck in the CPS. The left figure shows the RW image of the DPS bottleneck at 17.5 % nominal field, the right picture shows the combination of the DPS bottleneck at 17.5 % and the bottleneck at 15 % nominal field. In both figures the radius ($\sim 37.0\,\mathrm{mm}$) of the $191\,\mathrm{Tcm}^2$ magnetic flux tube is highlighted as a dashed black circle, see table 6.1. Comparing the illuminated pixel within the highlighted circle, no significant change of rate can be detected. The upper part of the figures visualizes that the CPS bottleneck reduces the magnetic flux tube size, as illuminated pixels on the upper part of the right pixels get disappeared due to the CPS bottleneck. Hence, the bottleneck in the CPS has an impact on the magnetic flux tube, but not on the inner $191\,\mathrm{Tcm}^2$ magnetic flux tube.

7.2.3.2 Alignment of the single STS components to the detector

In table 7.5 the alignment of the single STS sections with respect to the detector wafer is summarized, where the wafer is used as origin of the coordinate system. Two positions on the wafer are calculated for each direction separately. Since four collision points are to be provide, two collision points are at hand for each axis. Taking the two collision point ($S(I_{+\mathrm{x}})$ & $S(I_{-\mathrm{x}})$ or $S(I_{+\mathrm{y}})$ & $S(I_{-\mathrm{y}})$) of one axis, the image center (x or y) on this axis is half of the difference:

$$\mathrm{x} = \frac{S(I_{+\mathrm{x}}) + S(I_{-\mathrm{x}})}{2}, \tag{7.7}$$

$$\mathrm{y} = \frac{S(I_{+\mathrm{y}}) + S(I_{-\mathrm{y}})}{2}. \tag{7.8}$$

The position of the image center on the wafer center for a) the measurement, b) the simulation and c) the combined method is calculated using calculated collision points from tables 7.2, 7.3 and 7.4. The systematic uncertainty caused by the beam halo (see section 7.2.2) is taken from the measurement positions as well (see table 7.5). There, the combined CPI analysis is displayed. The alignment results of the 4LIP method are shown in figures 7.18, 7.19 and 7.20. They illustrate the distribution of the circle centers for all determined circle radii.

Table 7.5: Results for the alignment between the STS components and the detector wafer. The alignment results summarized below are obtained by analyzing the magnetic bottleneck results from the last section. Here, the analyzed collision points of the measured and simulated bottlenecks at 15 % nominal field of each section are used. Systematic uncertainties of the experimental alignment results are caused by the halo, since these are linked to uncertainties of the determined collision points. In addition, the combined CPI method to calculate the alignment is displayed. The center of the wafer is used as origin of the coordinate system.

		displacement in mm		
section	axis	measurement	simulation	combined
WGTS	x	$+1.70 \pm 4.55$	-0.81 ± 0.44	$+1.43 \pm 0.64$
WGTS	y	$+0.78 \pm 4.82$	$+3.22 \pm 0.86$	-1.57 ± 0.81
DPS	x	$+0.51 \pm 4.44$	-0.21 ± 0.19	$+0.15 \pm 0.63$
DPS	y	-0.01 ± 4.71	$+3.23 \pm 0.96$	-2.36 ± 0.80
CPS	x	$+1.33 \pm 4.60$	-0.20 ± 0.42	$+1.02 \pm 0.64$
CPS	y	$+0.60 \pm 4.71$	$+1.12 \pm 0.18$	-2.99 ± 0.80

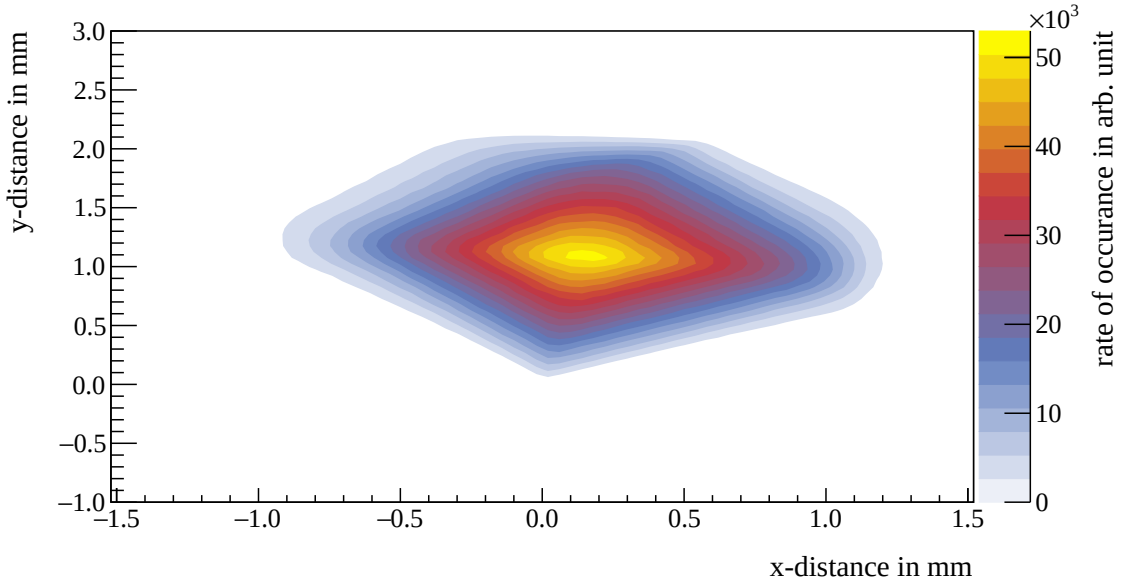

Figure 7.18: Calculated alignment distribution of the four pixel radii distribution of the WGTS bottleneck projection onto the detector wafer. By using the 4LIP method the center of the calculated circle is independent of the wafer center. The figure shows the distribution of the calculated circle centers in relation to the center of the detector wafer.

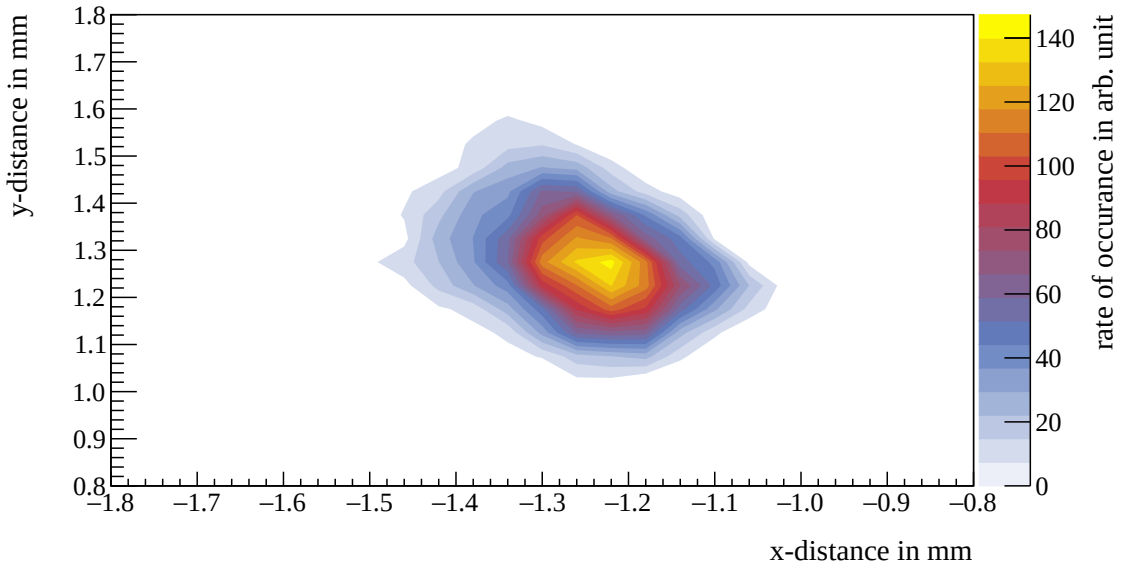

Figure 7.19: Calculated alignment distribution of the four pixel radii distribution of the DPS bottleneck projection onto the detector wafer. By using the 4LIP method the center of the calculated circle is independent of the wafer center. The figure shows the distribution of the calculated circle centers in relation to the center of the detector wafer.

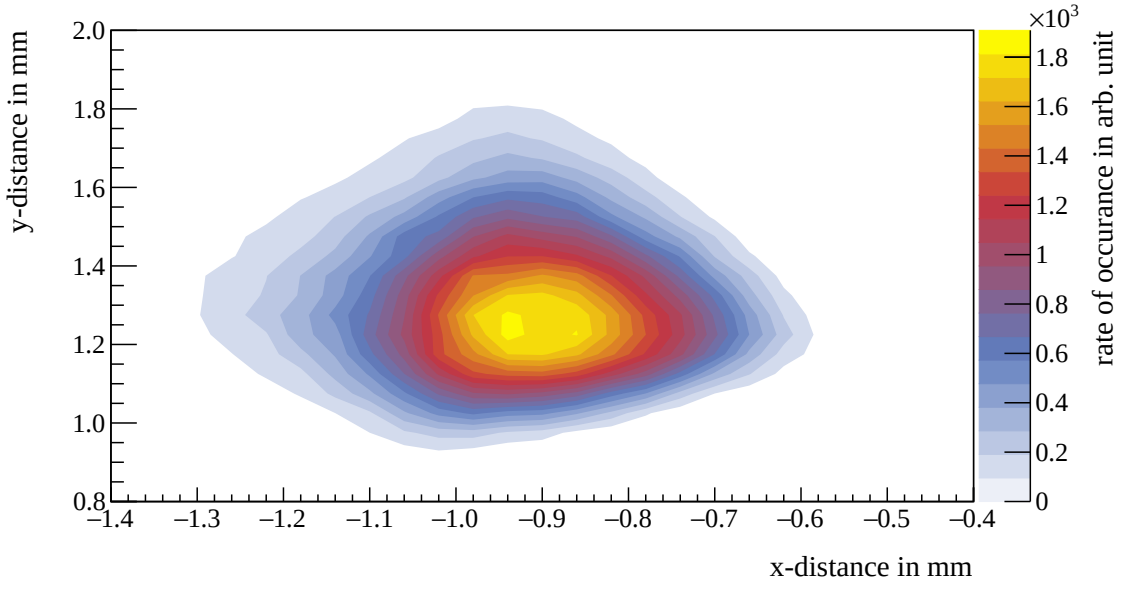

Figure 7.20: Calculated alignment distribution of the four pixel radii distribution of the CPS bottleneck projection onto the detector wafer. By using the 4LIP method the center of the calculated circle is independent of the wafer center. The figure shows the distribution of the calculated circle centers in relation to the center of the detector wafer.

Table 7.6: Alignment of the single STS sections to the rear wall. To obtain comparable alignment results, here the RW center is used as coordinate origin. The second and the third columns present those dipole currents which correspond to collision currents for each direction. In the last three columns the different alignment results are presented, starting with the measured results, followed by simulated results, and finally the combined-analysis results via the CPI method.

		dipole current in A		displacement in mm		
section	axis	measurement	simulation	measurement	simulation	combined
WGTS	x	+0.70	−0.4	$+0.72 \pm 0.21$	-0.46 ± 0.10	$+0.80 \pm 0.04$
WGTS	y	+2.28	±0.0	-2.46 ± 0.72	$\pm 0.00 \pm 0.01$	-2.65 ± 0.14
DPS	x	+0.08	−0.1	$+0.08 \pm 0.02$	-0.11 ± 0.02	$+0.09 \pm 0.00$
DPS	y	+2.65	±0.0	-2.86 ± 0.83	$\pm 0.00 \pm 0.01$	-3.09 ± 0.17
CPS	x	+0.50	−0.1	$+0.51 \pm 0.15$	-0.11 ± 0.02	$+0.56 \pm 0.02$
CPS	y	+2.95	+1.0	-3.18 ± 0.93	-1.16 ± 0.25	-3.44 ± 0.19

7.2.3.3 Alignment of the single STS components to the rear wall

The alignment between single STS sections to the RW center can be calculated using the CPI method, but instead of using the collision currents, the deviation of the current for the two collision currents in each direction of a scan is used. In general, the bottleneck section investigated and the FPD are not operated with identical magnetic fields. Therefore, the shift distance of the pencil beam inside the section does not correspond to the shift distance on the detector wafer. However, due to the conservation of the magnetic flux, the calculated shift on the detector wafer can be translated based into the shift distance inside the bottleneck by using equation 3.8. The calculated shift distance inside the bottleneck then is the relative alignment between the RW and the bottleneck section, and vice versa. These alignment results are outlined in table 7.6. The measured and combined results of the CPI method are in good agreement, apart from the previously mentioned CPS alignment in y-direction.

7.2.4 Rear wall to detector alignment

The overall alignment between the RW and the FPD can be determined by using the workhorse of this thesis, the pencil beam. In doing so, the pencil beam is guided by a global magnetic field setting at 20 % of the nominal value. At first the hit point on the FPD is measured, as presented in figure 7.21. The position of the pencil beam on the detector wafer is calculated with the CM method. The accuracy of this method is limited due to mentioned spatial resolution of the FPD, the extended dimensions of the pencil beam (diameter of about 3.6 mm), and finally by the surrounding halo. To obtain more precise alignment data and to verify the CM method, the s.c. dipoles of the WGTS are used to focus the pencil beam on the "bulls eye" of the wafer, as is visible in figure 7.21. In this case the position on the wafer is known as all "bulls eye" pixels should have an identical count rate. By using the linear equations from section 7.2.2, the dipole currents required to center the pencil beam on the "bulls eye" are used to calculate the position of origin. All measurement results are presented in table 7.7 and are complemented by simulation data. The alignment results achieved are in good agreement.

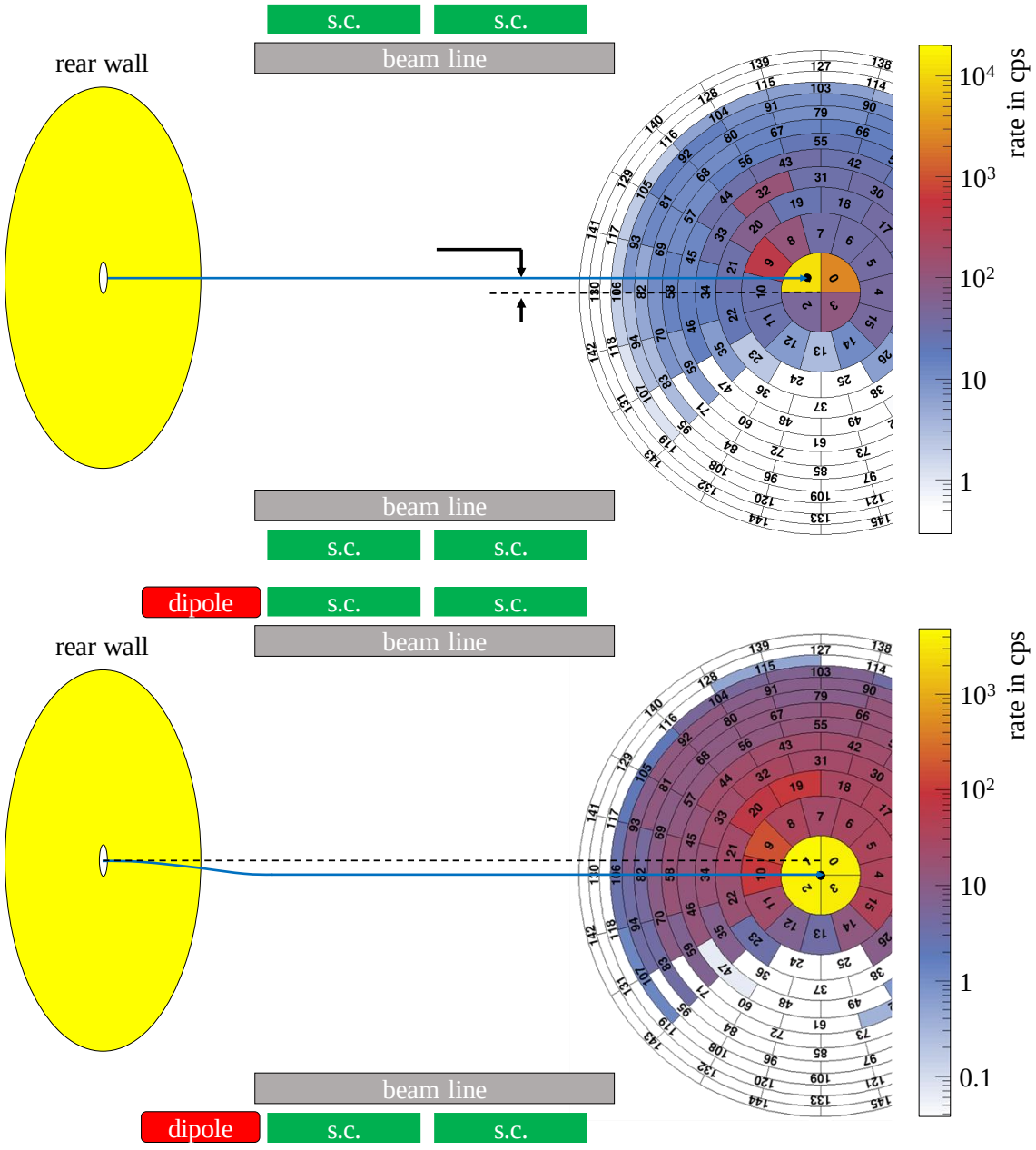

Figure 7.21: Hit point of the electron pencil beam on the FPD and centered electron pencil beam on the FPD by using the s.c. dipole coils of the WGTS. The upper figure displays the case where the global s.c. solenoid system operates at 20 % of nominal field. The electron beam is guided without interference by dipole magnets through the beamline. The center of the impact point, highlighted as black dot, is calculated with the CM method. In the lower figure the global magnetic field is the same as above, but the s.c. dipole coils on the rear part of the WGTS were energized to center the point of impact of the pencil beam on the "bulls eye". Ideally, all four "bulls eye" pixels display the same count rate.

Table 7.7: Measured and simulated alignment between the rear wall and the FPD. The results presented here are generated for a global magnetic field of 20 % of nominal values. The center of the detector wafer is used as origin of the coordinate system. The systematic uncertainties of the CM measurements are given by their RMS value.

	displacement in mm		displacement in mm (linear equation)		
axis	measurement (CM)	simulation	measurement	simulation	combination
x	-1.80 ± 0.40	$+0.03$	-0.34 ± 0.05	-0.15 ± 0.24	-0.89 ± 0.25
y	$+3.30 \pm 0.39$	$+3.38$	$+3.37 \pm 0.33$	$+3.42 \pm 0.29$	$+3.69 \pm 0.41$

7.2.5 Cross check of the alignment results

In the previous section the alignment results in y-direction between the RW and the FPD were shown to be in good agreement for all methods. In case of alignment results for x-direction and measurement (CM) results are neglected, a deviation $< 1\,\text{mm}$ is determined. Hence, the data set represents the best alignment values to be achieved. Since the alignment values of each STS section are determined relative to the FPD and to the RW, the two alignment results can be used to calculate the alignment between the FPD and the RW. The basis of this calculation is given by the CPI method, making use of the collision points. Consequently, the calculated alignment between the FPD and the RW is used to verify the overall CPI method. This is possible since the alignment values determined in the previous section is based on using different techniques. The results are presented in table 7.8 and can be compared with the results in table 7.7. This demonstrates that the measured results are in good agreement in view of the rather large systematic uncertainties. However, the simulated results are in very good agreement. The combined method, however, shows a significant deviation.

This demonstrates that the results of the measurements are strongly influenced by systematic effects caused by the beam halo. The combined CPI method include an unaccounted uncertainty. Nevertheless, the cross check method can be used to verify the CPI method since the achieved simulation results for all techniques are perfectly comparable.

7.2.6 Discussion of the results

Two key objectives of this thesis have been discussed in this section: to obtain transmission characteristics for each single STS unit and to quantify its alignment with respect to the detector. For both analyses the linear dependence between the dipole current and the shift of the pencil beam was of paramount importance. The achieved results for the linear dependence in case of experimental data show noticeable deviations in comparison to simulated data. As was mentioned earlier in section 7.2.2, this deviation likely originates from an extended beam halo that surrounds the pencil beam. In particular, it significantly influences the calculated positions of the pencil beam on the detector wafer, causing systematic uncertainties when using the CM method. However, when taking into account this systematic uncertainty, measured and the simulated linear parameter values are comparable.

An in-depth investigation of each single STS section was performed by deliberately creating magnetic bottlenecks in the corresponding sections (see section 7.2.3). In this process, the electron beam was shifted across the flux tube to find four collision points for each bottleneck to determine the largest collision-free magnetic flux tube. The bottleneck results of the source section have nicely confirmed the corresponding simulation results indicating that the $210\,\text{Tcm}^2$ magnetic flux tube can be guided collision-free through the WGTS with high probability.

Table 7.8: The results of the alignment between the rear wall and the FPD based on the alignment results of single STS components. The single STS alignment results given in table 7.5 and table 7.6 from the linear equation are used to calculate the RW-to-FPD alignment. The center of the detector wafer is used as origin of the coordinate system.

		displacement in mm		
section	axis	measurement	simulation	combination
WGTS	x	$+0.98 \pm 4.76$	-0.35 ± 0.43	$+0.63 \pm 0.67$
WGTS	y	$+3.24 \pm 5.54$	$+3.22 \pm 0.06$	$+1.08 \pm 0.95$
DPS	x	$+0.43 \pm 4.47$	-0.10 ± 0.29	$+1.14 \pm 0.63$
DPS	y	$+2.86 \pm 5.54$	$+3.23 \pm 0.44$	$+0.73 \pm 0.96$
CPS	x	$+0.81 \pm 4.75$	-0.09 ± 0.36	-0.61 ± 0.67
CPS	y	$+2.59 \pm 5.63$	$+2.28 \pm 0.50$	$+0.45 \pm 0.98$

The simulation results already indicate specific potential constrictions in the beamline part of the DPS and CPS. Indeed it could be shown that the DPS instrumentation reduces the transmission of the flux tube in the STS beamline significantly. With respect to the collision points which are obtained by the CPI method, in combination with the measured collision currents, there is a non-zero possibility that the 191 Tcm^2 magnetic flux tube will collide with the beamline. However, it could be shown that the CPI method is perturbed by the beam halo, resulting in non-negligible uncertainties. However, all other analyzing methods point to the fact that collisions will occur only in 210 Tcm^2 magnetic flux tube.

Therefore, the magnetic field in the DPS was increased to 17.5 % of its nominal value to repeat the investigation with a less pronounced bottleneck. The analysis showed that most collisions vanished, but the full design transmission of 210 Tcm^2 could not be achieved. Hence, the CPS bottleneck had to be investigated with the DPS still at 17.5 % of its nominal field, resulting in negligible changes in transmission characteristics. From this it can be concluded that the DPS alone is limiting the transmission properties of the magnetic flux tube in the STS part of the KATRIN beamline. By operating the DPS on a sufficient high magnetic field the 210 Tcm^2 magnetic flux tube will be guided collision-free as well.

The alignment results of the STS components to the detector wafer are in good agreement based on data from measurement, simulation, and a combined analysis. The same applies for the alignment results of the STS components relative to the RW at the opposite end. The CPI method was used to calculate the alignment between the STS components and the FPD, as well as the alignment between the RW and the STS components. Hence it is possible to calculate the RW to FPD alignment based on experimental results. A direct investigation of this alignment shows a near-perfect agreement for the diverse set of measurement and analysis techniques. This outcome can be treated as good verification of the CPI method in combination with collision currents.

7.3 Alignment measurements in SDS

The first alignment measurements between the main spectrometer and the detector wafer by making use of an asymmetric MS magnetic field configuration were pionered by J. Schwarz during the SDS-I campaign [Sch14]. Due to a then misalignment along the SDS beam tube between MS and the FPD, the magnetic flux tube collided with parts of the beamline, producing a shadow at the FPD. Due to the shadow, a total of 22 detector channels could not be used for the initial analysis in SDS-I. During the subsequent measurement campaign SDS-II, the alignment measurements were refined by F. Harms

[Har15]. Mechanical position measurements at the FPD carried out in advance enabled a precise alignment of the system, guaranteeing the usability of all wafer pixels. However, even the very careful positioning and alignment measurements carried out during SDS-II showed a non-negligible deviation in comparison to simulated results from Kassiopeia.

Since then the detector system was disassembled and reconstructed and the extensive and time-consuming mechanical alignment procedures had to be repeated. In addition, the pre-spectrometer alignment was studied for the first time. All mechanical alignment data have now been implemented into Kassiopeia and first global alignment simulations were carried out in this thesis (see section 6.3.2).

The following section gives an overview of the alignment measurement principles in SDS in section 7.3.1. In section 7.3.2 the asymmetric magnetic field settings are explained in detail, followed by a summary of the alignment results in section 7.3.3. Finally, the global results are discussed in section 7.3.4.

7.3.1 Overview

As mentioned in section 6.3.2, in the SDS campaign alignment measurements were based on the inner wire electrode system of the spectrometers which served as electron source via electron field emission and by secondary electron emission. Accordingly, the structure of the electrode system can be mapped onto the detector resulting in two ring structures. The alignment between the electrode system and the detector can then be determined by fitting the ring structures and determine the shift between the ring centers and the detector wafer center. A rather precise analysis is possible, since the position of the individual wire modules was determined by laser tracker and is known to an accuracy much more better than $\leq 1\,\mathrm{mm}$ [Hil11, Pra11].

7.3.2 Asymmetric magnetic field measurements

To measure the alignment between the main spectrometer and the FPD, a magnetic field configuration identical to the Kassiopeia simulations in section 6.3.2.1 is used. The inner wire electrode (IE) system is set to $-120\,\mathrm{V}$ with all other electrodes, including the main spectrometer vessel being grounded, to generate the required conditions to ignite electron field emission (appendix C: FL8).

The alignment between the PS and the detector is measured with a magnetic field configuration equal to the simulations of section 6.3.2.1. Here, the wire electrodes in the PS are elevated to $-100\,\mathrm{V}$, and its upstream electrode to an even larger potential $-120\,\mathrm{V}$. All other electrodes including the spectrometer vessels are grounded. The EMCS is kept at identical parameters as during the alignment measurement.

7.3.3 Spectrometer to detector alignment

To analyze an electron field emission based ring structure, a Monte-Carlo simulation is implemented first which to randomly distributes an overall the measured count rate over a ring to each pixel across its geometry. The resulting uncertainty of the ring-fits is of the order of $\sim 1\,\mathrm{mm}$. The determined alignment results are stated relative to the center of the detector wafer, which also serves as origin of the coordinate system. The mean value of the computed ring centers which indicates the alignment between the MS and the FPD is at $\langle \mathrm{x} \rangle = -0.80\,\mathrm{mm}$ and $\langle \mathrm{y} \rangle = -1.75\,\mathrm{mm}$. For the PS to FPD alignment a corresponding displacement of $\langle \mathrm{x} \rangle = -1.25\,\mathrm{mm}$ and $\langle \mathrm{y} \rangle = -2.50\,\mathrm{mm}$ is found.

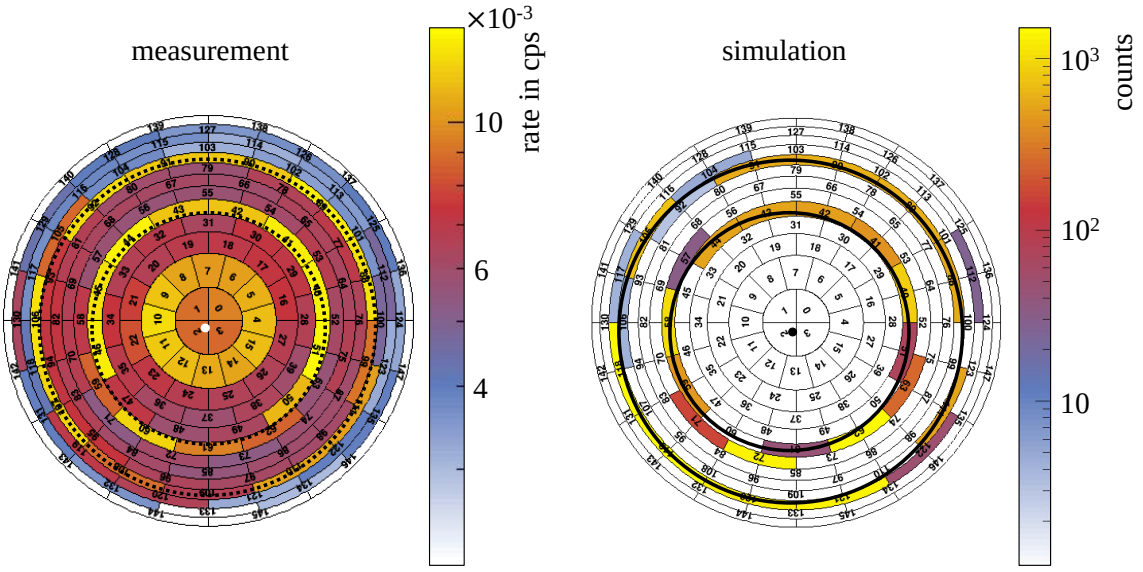

Figure 7.22: Measured and simulated detector view of the main spectrometer electrode system mapped on the FPD pixels via an asymmetric magnetic field setting. The left figure shows the inner wire comb structure of the main spectrometer mapped onto the FPD. The inner ring corresponds to the structural points z2, while the outer rings corresponds to the structural points z3 in figure 6.14. The structural point z1 produces the fully illuminated circle at the "bulls eye" and the following pixel ring. Due to its broad structure it is not used for the alignment analysis. On the right side the corresponding simulation results are contrasted including the two rings and the mean circle center.

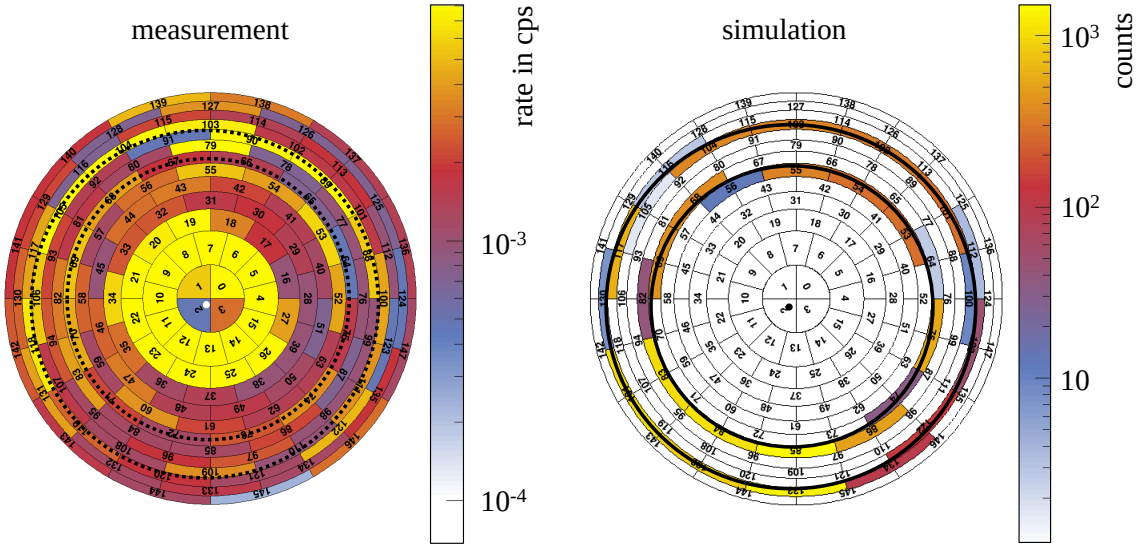

Figure 7.23: Measured and simulated detector view of the pre-spectrometer electrode system mapped on the FPD via an asymmetric magnetic field setting. The left figure shows the inner wire comb structure of the pre-spectrometer mapped onto the FPD. Here, it is assumed that the lower part of the mapped image is influenced by an electrostatic potential (see section 7.1.1) as the structure is not completely mapped onto the pixels at the lower bottom left side. The location of the electron field emission is given in figure 6.15. The inner ring corresponds to the structural points k1, while the outer ring corresponds to the structural points k2 (see figure 6.15). The mean circle center is highlighted as white dot located next to the center of the wafer. It is presumed that the fully illuminated circle at the "bulls eye" and the following pixel ring are generated by the upstream part of the wire electrode. Due to its size it is not used for the alignment analysis. On the right side the corresponding simulation results are presented.

Table 7.9: Results of the alignment of the MS and PS relative to the FPD. The alignment results below were obtained with an asymmetric SDS magnetic field configuration. An uncertainty of about 1 mm for the measured alignment has to be taken in account due to the ring-fit algorithm employed. Since two ring structures are fitted for each spectrometer, the average of both results is given.

		displacement in mm	
section	axis	measurement	simulation
main spectrometer	x	−0.80	−0.99
main spectrometer	y	−1.75	−2.50
pre-spectrometer	x	−1.25	−1.44
pre-spectrometer	y	−2.50	−2.89

7.3.4 Discussion of the results

The simulation and the measurement results of the SDS part of KATRIN are summarized in table 7.9. The maximum observed deviation of 0.75 mm between simulation and measurement between MS and the FPD demonstrates excellent agreement when taking into account systematic uncertainties of the applied ring fits of ~ 1 mm. During the SDS-II campaign, the alignment between the MS and FPD was determined to be $x = +1.75$ mm and $y = -2.13$ mm. Comparing these SDS-II results to the above quoted First Light alignment results of the MS, a significant deviation appears in x-direction, which cannot be explained by uncertainties. This deviation is caused by the readjustment of the FPD during installation work at the system in between the SDS-II and First Light measurement campaigns. Therefore, a careful asymmetric magnetic field measurement to determine the actual alignment of both components is required after each reinstallation at the beamline.

7.4 Discussion of the global magnetic flux tube alignment

The final measurement campaign SDS-II could clearly demonstrate that the modifications that were carried out to improve mechanical alignment of the FPD indeed did remove several collisions of the flux tube between the MS and the FPD that were observed previously during SDS-I [Sch14, Har15, Erh16, Mue16]. By analyzing the mapped wire electrode structure image, the alignment between the two components was determined. Furthermore, these results were verified by detailed simulations with the Kassiopeia simulation tool. Numerous alignment measurements have been performed during the commissioning including several hardware improvements and further refinements of the FPD system. There is a clear evidence that each service phase of the FPD significantly altered the actual alignment [Sch14, Har15, Erh16, Mue16]. Accordingly, each hardware change at the system requires a new alignment measurement before a subsequent measurement campaign. The mechanical alignment measurements were continuously developed further and improved, resulting in a detailed geometry data base which was implemented to optimize the Kassiopeia code [Def17]. Latest alignment results of the main spectrometer together with the impact of external magnetic fields from magnetization of the reinforced concrete of the spectrometer hall can be found in [Erh16].

For the First Light measurement campaign, the alignment measurements in the SDS part of KATRIN were repeated in the framework of this thesis, including the first ever pre-spectrometer alignment. For both spectrometers, asymmetric magnetic field configurations were used, and measured and simulated results are in good agreement. The transmission characteristics of the SDS (and STS parts as well as globally) were investigated with a fully illuminated magnetic flux tube. The detected flux tube collisions between the PS and MS

were identified as being due to electrostatic blocking from a negatively charged component at the flapper valve. Since only electrons with energies below 110 eV are blocked, the high-energy β-decay electrons are not influenced. However, this electrostatic potential blocks low-energy electrons used for alignment measurements in the lower part of the magnetic flux tube. This result in a reduced observability of the spatial distribution of low-energy background in the STS part.

To determine the alignment and transmission in the STS part of KATRIN, a various magnetic bottleneck configurations were used. Previously implemented simulations of the distance between the magnetic flux tube and the beamline pointed to the existence of significant constrictions for the DPS and CPS beam tubes (see section 6.1.4). The DPS instrumentation and tube geometry was identified as critical element to reduce the magnetic flux tube size and to constrain collision-free transmission. The measurements were confirmed by simulation results in the STS beamline. A major result is that the 210 Tcm^2 flux tube is guided collision-free through the WGTS and CPS beamlines. Moreover, the measured alignment of the WGTS and CPS to the detector wafer are in good agreement. For the DPS transmission indications for a collision of the 191 Tcm^2 magnetic flux tube with the beamline were found. The simulations and the measurements could demonstrate that a moderate increase of the magnetic field in the DPS elements compared to the fixed layout of the other beamline solenoids eliminate collisions in the relevant flux tube parts up to 210 Tcm^2.

7.5 Ways to improve the magnetic flux tube alignment

As discussed above the DPS beam tube elements are the most critical sections of the KATRIN beamline in terms of alignment as they limit the transmission properties during standard operation mode. A major outcome of this thesis is the clear and strong recommendation to improved the transmission by higher magnetic field in the DPS compared to the global magnetic field setting. Under nominal magnetic field conditions, an increase by $17 - 20\,\%$ would imply that the DPS solenoids have to operated at a field of 5.8 T, instead of 5.0 T. In view to the specified design limit of 5.5 T this is not feasible. Due to limitations of the allowed current setting of the CPS, the global magnetic field setting, however, is reduced to 70.0 % (see section 4.3.2). Accordingly, the DPS can be operated at higher fields of beyond 20 %. At 18.6 % higher magnetic field in a setting with reduced global magnetic field ratio of 70.0 %, this would result in a 4.15 T magnetic field of the DPS solenoids. The pinch solenoid is foreseen to provide the strongest magnetic field along the KATRIN beamline as it reduces the background rate on the FPD (see section 3.1.2). However, its magnetic field of now 4.2 T is still higher than the increased DPS field, thus the field of the pinch magnet can stay at this value. Nevertheless an in-depth detailed investigation of the transmission of the DPS elements has to be performed via the magnetic bottleneck method for each s.c. DPS solenoid, to provide information about potential collision points along each DPS beam tube. If corresponding beamline parts would be identified, a mechanical alignment modification could be initiated in view of the modular setup of the DPS element. However, this mechanical alignment is rather time-consuming and its outcome is to be verified due to the complex geometry of the DPS beamline and its instrumentation. Thus, at this point it is recommended to repeat the above discussed alignment measurements with a more precise EGUN in combination with an increased magnetic field of the DPS solenoids.

7.6 Implication for the neutrino mass measurements

A key objective of this thesis was to determine if the 191 Tcm^2 flux tube can be transported undisturbed through the entire experiment. This is of major importance since it determines

that β-electrons propagate undisturbed and without energy losses. These have to be avoided at all costs in view of their danger to spoil the neutrino mass analysis. The present setup has to be improved in view of the possibility that the 191 Tcm^2 flux tube collides with the DPS beamline elements. The alignment results achieved here have to be verified by future measurements, which offer the possibility to use a high-precision EGUN at the RS to generate an electron beam with a radius < 0.1 mm. If the determined reduction of the DPS transmission properties is confirmed, it is strongly recommended to increase the magnetic field at the DPS for the neutrino mass measurement so that no collisions of the 210 Tcm^2 flux tube and the beamline occur at DPS. This extended flux tube is essential for the online monitoring of the source activity with the FBM located at pump port 2 of the CPS. The rear part of the WGTS beamline surrounded by the s.c. solenoids M5 and M6 could not be investigated by the bottleneck method yet. Since this part is of great importance to control and stabilize the source plasma via RW electrons, it is recommended to investigate this part during the next alignment measurement campaign as well.

7.7 Suggestions for future alignment measurements

The alignment and transmission measurement techniques developed in the framework of this thesis are based on using an electron beam to scan artificial and pre-existing bottlenecks inside the STS part of KATRIN. They serve as ideal template for future measurement campaigns. The same token applies to the asymmetric magnetic field measurements in the SDS part. A major improvement for the STS measurements will be achieved once the EGUN of the rear section is available for the final alignment investigations. Currently, these are scheduled for the first half of 2018. With an electron beam diameter of 177 µm inside the WGTS, the corresponding diameter at the FPD will be about 185 µm [Bab14]. The overall rate to be delivered will depend on the precision mode of the EGUN. Typically it is specified with 10^5 – 10^6 electrons per second [Bab14]. In addition, a variety of tasks of the rear section EGUN require a halo-free operation. Also, the vacuum performance of the global KATRIN beamline will significantly surpass the First Light vacuum performance, since all TMPs will be operational then. Accordingly, the collision probability of electrons with the residual gas molecules will be reduced by a huge factor so that an expansion of the electron beam size and the formation of a halo will be suppressed. This high-precision electron beam will allow to focus on single pixel boundaries to improve on the position resolution by a huge amount. During the measurements of the linear dependence between the currents of the WGTS dipole coils and the resulting electron beam shift, these boundaries can be used as the ultimate means to localize the beam spot on the detector wafer. Moreover, the electron rate can be used as powerful position indicator, since a perfect hit of a pixel boundary is detected as two-pixel event with equal count rate. The radial distance to the FPD center is given by the ring-shaped pixel boundaries and the dipole current in use. To minimize tangential offset, the pixel boundaries in radial direction should be targeted in the beginning. Hence, the uncertainty of the electron beam position on the FPD will be greatly improved. If both magnetic dipoles are used to obtain a simultaneous shift of the electron beam on the detector wafer in both x- or y-direction, a potential tilt between the detector wafer and the dipole magnets can be determined as well.

A precision electron beam will allow to determine the collision points in a very precise way, since a collision would cause an abrupt decrease of the electron count rate. Alternatively, it may be feasible to measure the alignment of single components of the beamline instrumentation of the DPS. Furthermore, the tilt around the beam axis of the electric dipole electrodes of the DPS relative to each other could be determined, since small lobules are welded to the inner side of the dipole electrodes. The knowledge of this tilt is important as it strongly influences the ion removal efficiency. These measurements can be performed

due to the fact that each single DPS solenoid current can be controlled separately, allowing to apply the bottleneck method for each beam tube element of DPS. In this way it will be possible to determine the alignment of the FT-ICR unit in beam tube five, which is of key importance to assess the sensitivity of this device. Finally, the position of the FBM can be determined for different monitoring positions, including illumination tests of the sensitive part of the detector array.

CHAPTER 8

Summary and outlook

The thesis at hand describes works performed during the First Light measurement campaign, which were targeted to examine the magnetic flux tube alignment inside the 70-m long KATRIN beamline. A second major objective of this thesis was to investigate the temperature stability and homogeneity of the source tube during the commissioning of the WGTS cryostat. The results obtained are essential prerequisites so that the experiment can reach an absolute neutrino mass scale with a sensitivity of 200 meV (90 % C.L.) and a 5σ discovery potential of 350 meV.

The Standard Model of particle physics describes the neutrinos as massless, neutral and weakly interacting particles. However, the discovery of neutrino oscillations has provided irrefutable evidence that neutrinos possess a non-vanishing mass. Relic neutrinos from the Big Bang are the most abundant massive particles in the universe, with each cm^3 containing 339 of these enigmatic particles. Due to their non-vanishing mass and their free-streaming property, they have influenced the formation and evolution of large-scale structures in the early universe. A direct and model-independent determination of the absolute neutrino mass scale would allow to pin down one of the key input parameters of cosmological models. Additionally, the observation of the absolute neutrino mass scale could provide a first hint at how masses are generated beyond the Higgs mechanism. Therefore it is of key importance for cosmology and particle physics to determine the absolute scale of neutrino masses. The high-precision spectroscopy of tritium β-decay close to its 18.6 keV endpoint is well-suited to determine the fundamental neutrino mass scale, since even sub-eV neutrino masses cause a distinct distortion of the spectral shape a few eV below the endpoint. The KATRIN experiment is the leading next-generation tritium neutrino mass experiment, which will surpass the previous experiments at Mainz and Troitsk by one order of magnitude in sensitivity. This ambitious objective requires to increase statistics by a factor 100, while at the same time reducing systematic uncertainties by two orders of magnitude. This will be achieved by combining the well-established technique of a windowless gaseous tritium source and a retarding spectrometer based on the MAC-E filter technique.

The KATRIN source is designed to provide an activity of 10^{11} β-electrons per second. Since only a tiny fraction of 2×10^{-13} of all β-decays occur in the last 1 eV interval below the endpoint, a signal count rate of a few cps is expected in a region of a few eV below E_0. Hence, three net years of data taking, corresponding to five calender years of experimental run time, are necessary to reach the required statistics for the aspired neutrino mass sensitivity. As fluctuations of the activity in the windowless gaseous tritium source lead to systematic uncertainties, it has to be stabilized on the 0.1 % level. This requirement necessitates similar stability levels for several parameters: the injection pressure of the tritium

gas into the source tube, the pumping efficiency of the TMPs, and most challengingly, the temperature of the source tube. To minimize the tritium throughput and mitigate the effect of thermal Doppler broadening of β-electron energies, the source gas and the surrounding beam tube have to be cooled to 30 K. One key objective of this thesis was to determine if this specific temperature regime can be reached, and, more importantly, whether an 0.1 % level of stability can be achieved.

In autumn 2015 the assembly of the WGTS cryostat was completed and the large unit was delivered to KIT to complete the beamline of source-related components. The commissioning of the WGTS included to operate the source tube cooling system and to calibrate the temperature sensors. The long-term temperature measurements of the source tube could demonstrate that the design operating temperature of 30 K can be achieved. The average value of the temperature stability of (3.28 ± 1.68) mK/h recorded over a time period of 16 days is one order of magnitude better than the specified temperature stability of 30 mK/h. This allows to operate the WGTS well within its uncertainty budget. The required temperature homogeneity along the 10-m long source tube exceed specification tough, as the temperature on the rear end is about 500 mK higher in comparison to the center and the front end of the source tube. However, based on the excellent results for the temperature stability, this inhomogeneity can be implemented into the source model, avoiding systematic effects in the neutrino mass analysis.

To exclude systematic from energy losses of signal electrons due to the wall interactions, the magnetic flux tube within the beamline has to guide β-electrons adiabatic and collision-free from their point of origin through the 70-m long setup to be counted at the detector. In this context two magnetic flux tube sizes have to be distinguished. First, the flux tube value of 191 Tcm^2, guides all signal β-electrons to be used in the analysis. Second, the larger flux value of 210 Tcm^2 serves as buffer area, "shielding" the 191 Tcm^2 magnetic flux from collisions due to misalignment. In addition, it is of key importance to monitor the source activity via the FBM unit located at the outermost rim tube in downstream direction at the CPS. The main objective of this thesis was to investigate the adequate alignment of the magnetic flux tubes within the beamline. In particular it should be determined if β-electrons can be guided without collision or interception in both flux tubes to minimize systematics.

The integration of the STS components to a 70-m long beamline was finished in early 2016, in parallel to the commissioning of each component. In this context, the main spectrometer and detector system, forming a major part of SDS, were already commissioned during two previous measurement campaigns, SDS-I and SDS-II, between 2012 and 2016. The last missing component to complete SDS and hence the global KATRIN beamline was integrate the pre-spectrometer in summer 2016. Due to the parallel commissioning of the individual sections, the s.c. solenoids could be operated together for the first time to form a global magnetic flux tube over 70 m. In fall 2016 two artificial electron sources, providing a pencil beam and a wide beam, were installed at the rear part of the beamline, to enable a first detailed alignment measurement campaign of the magnetic flux tube.

Due to the very detailed mechanical alignment of individual KATRIN components during construction and commissioning it was possible to create a realistic data set and model of the entire beamline as input for the Kassiopeia software package. Based on actual "as-built" geometries of the solenoids, it allows to perform precise tracking of electrons along magnetic field lines. In combination with the implemented electron pencil beam, these tracking simulations allow to verify and assess experimental findings. A novel technique introduced and pioneered by this thesis is the pencil beam scanning of the magnetic flux tube. To this end, the s.c. dipole magnets in the rear part of the WGTS were operated for the first time. The linear dependence between the lateral shift of the pencil beam at the

surface of the detector wafer and the dipole current was used for a variety of alignment investigations. At first the pencil beam was centered to the center of the wafer. This is an essential prerequisite for the so-called magnetic bottleneck method, where the magnetic field in the section investigated is reduced. This allows to search for collision points. To do so, the specific bottleneck between the magnetic flux tube and the inner beamline surface is scanned via the pencil beam. Mapping of the pencil beam shift until disappearance on the detector wafer allows to test the alignment of the investigated section relative to the FPD. Most importantly the collision-free guiding of the magnetic flux tube can be verified after the shift displacement is calibrated. The corresponding simulations verify that the 191 Tcm^2 magnetic flux tube can indeed be guided collision-free through the entire beamline. However, the 210 Tcm^2 magnetic flux tube is intercepted horizontally within the DPS beamline. By operating the solenoids of the DPS at a slightly higher magnetic field as designed, collision of the 210 Tcm^2 magnetic flux tube can be avoided, resulting in a collision-free guiding through the entire setup and enabling monitoring by the FBM.

The alignment between the spectrometers and the detector was investigated by using the "asymmetric magnetic field method". It is based in deenergizing the upstream solenoid of the investigated spectrometer, resulting in a widening of the magnetic flux. This allows to detect field-emission electrons from the inner electrodes of the spectrometer. The resulting ring-shaped image on the detector wafer allows to obtain precision information of the alignment between the investigated spectrometer and the FPD. A key constrain for the investigations of this thesis was the fact the magnetic field had to be reduced for the "First Light" measurements. Simulations performed at different field settings have verified that the alignment measurements are independent of the absolute global magnetic field, as long as all coils are reduced by the same factor. A variety of complex measurement strategies was successfully used to determine the alignment of the magnetic flux tube during First Light.

A key result was the verification of the excellent linear dependence between the pencil beam shift on the wafer and the WGTS dipole current. Due to the non-optimum vacuum conditions then, the measurement was influenced by a halo surrounding the pencil beam. This has induced systematic effects and introduced significant uncertainties in several alignment results. Despite this, the experimental alignment results obtained are similar to the simulation results. The key message of both experiment and simulation is that only the DPS reduces the magnetic flux tube size horizontally. This limits transmission to the inner 191 Tcm^2 magnetic flux tube, which is guided collision-free through the entire beamline at nominal magnetic field settings. By operating the DPS at a slightly higher magnetic field, the collisions of the larger 210 Tcm^2 magnetic flux tube can be avoided completely. Hence it should be possible to monitor the source activity in the outer rim of the 210 Tcm^2 magnetic flux tube by the FBM. Individual sections of both STS and SDS showed no significant misalignment with respect to the FPD. Hence, a mechanical realignment of individual sections or a magnetic flux tube alignment by using the s.c. dipole magnets of the WGTS is not required. This alignment result, in combination with the verified integrity of the 210 Tcm^2 buffer area, "shields" the signal electrons in the entire beamline and mitigates dangerous energy losses from small angle scattering at the inner beam tube surface.

By using a wide beam of low-energy photoelectrons, the transport characteristics of the magnetic flux tube over its entire length of 70 m could be measured for the first time. The initial result was the surprising observation of a shadow visible on the bottom part of the detector wafer. Further investigations revealed the shadow to be caused by an electrostatic potential located at the flapper valve between the pre- and the main spectrometer. It reflects low-energy electrons with energies below 100 eV. Since electrons from tritium β-

decay feature energies in the keV regime, they will not be influenced by this electrostatic potential. However, the electrostatic potential influences and limits the investigation of background electrons generated along the STS beamline as well as in the pre-spectrometer. Further investigations are necessary to identify the exact cause of the potential so that the component can be modified to remove the electrostatic potential.

The upcoming commissioning phase III of KATRIN in the first half of 2018 will allow to investigate the alignment of the magnetic flux tube in even more detailed. This will be possible after the EGUN of the rear section becomes available and UHV conditions in the beamline prevail, which provide a halo-free electron beam with sharp geometric edge and a lateral beam size in the sub-mm range. It will yield a more detailed picture of the magnetic flux tube alignment inside the beamline by using the established magnetic bottleneck method.

Finally, during the writing of this thesis the assembly and installation of the extended beamline instrumentation was completed. Based on the results of this thesis, the magnetic flux tube can be expected to fulfill all requirements to measure the effective neutrino mass with a sensitivity of 200 meV at 90 % C.L. over five calendar years.

Appendix

A Setup of the DPS beamline during First Light

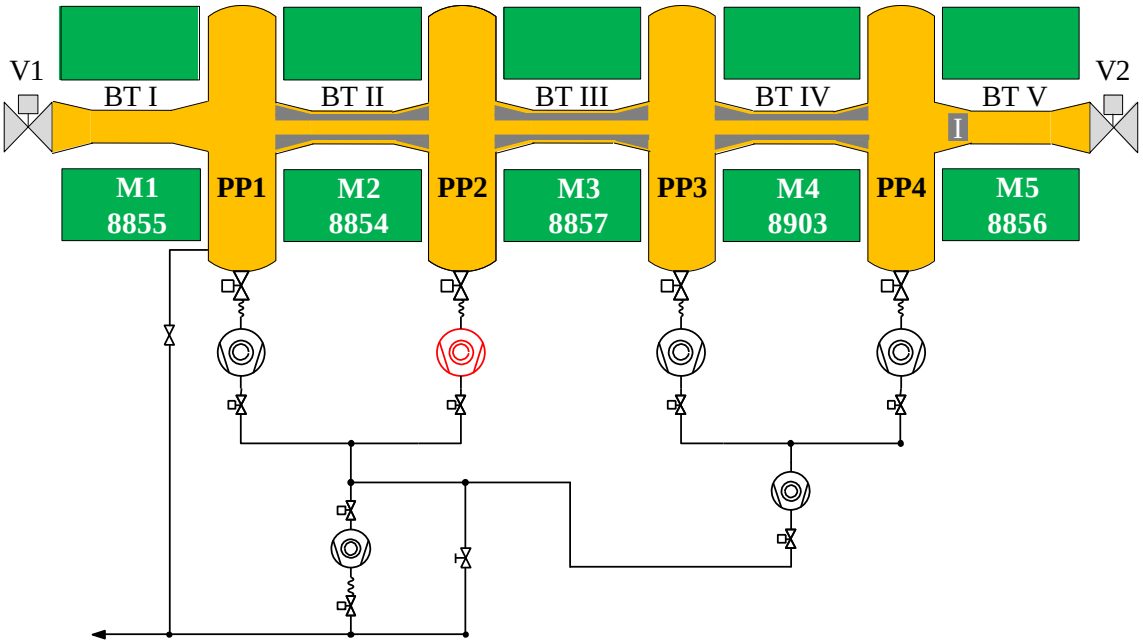

Figure A.1: Construction progress of the DPS beamline instrumentation during First Light. The DPS beamline was evacuated during First Light with one TMP, which is highlighted in red. A system consisting of three dipole electrodes located in beam tubes 2 – 4 (BT II-IV) and one ring electrode (I) located in beam tube 5 (BT V) were already installed.

B Single runs of the pencil beam scan

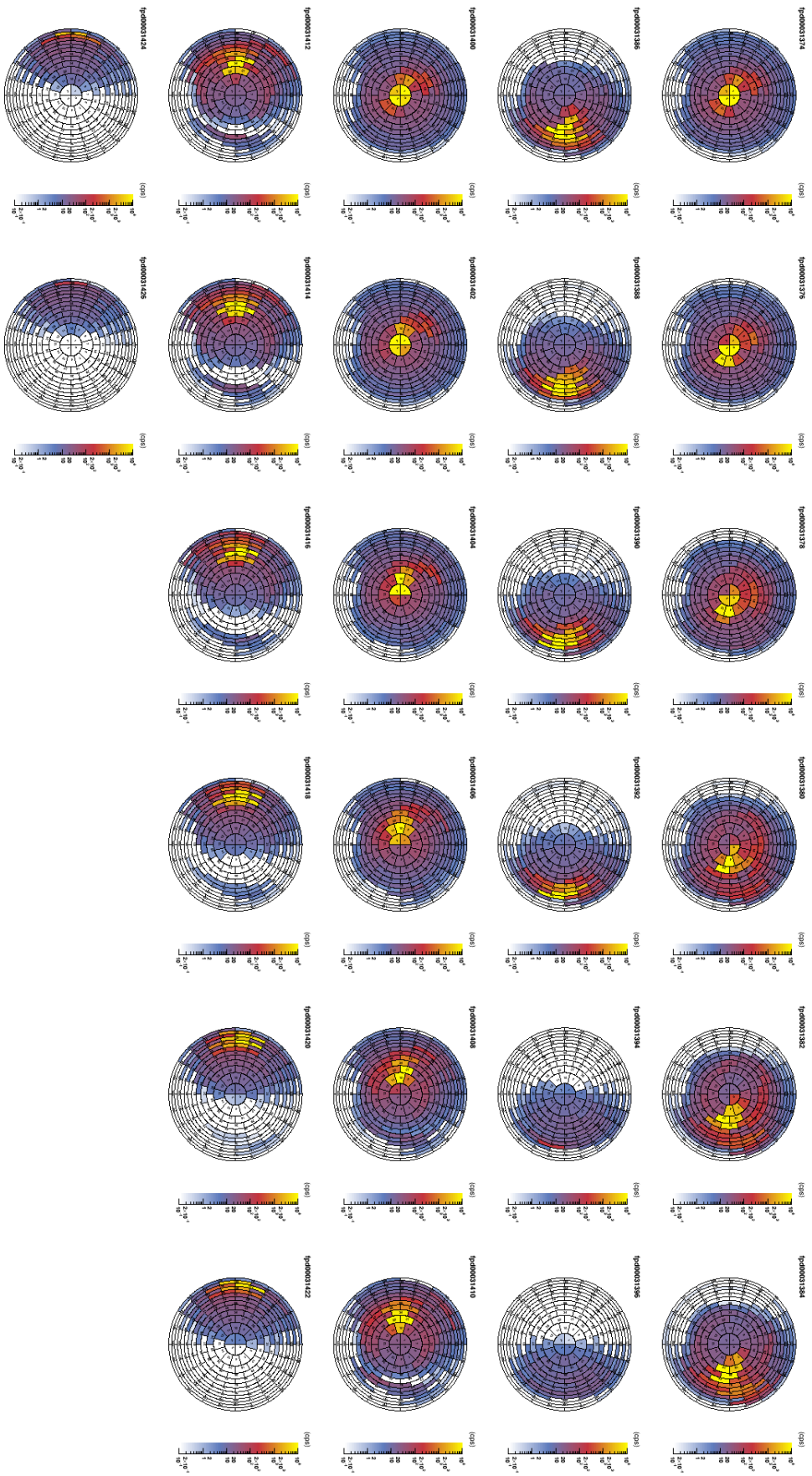

Figure B.2: Pencil beam scanning in horizontal direction.

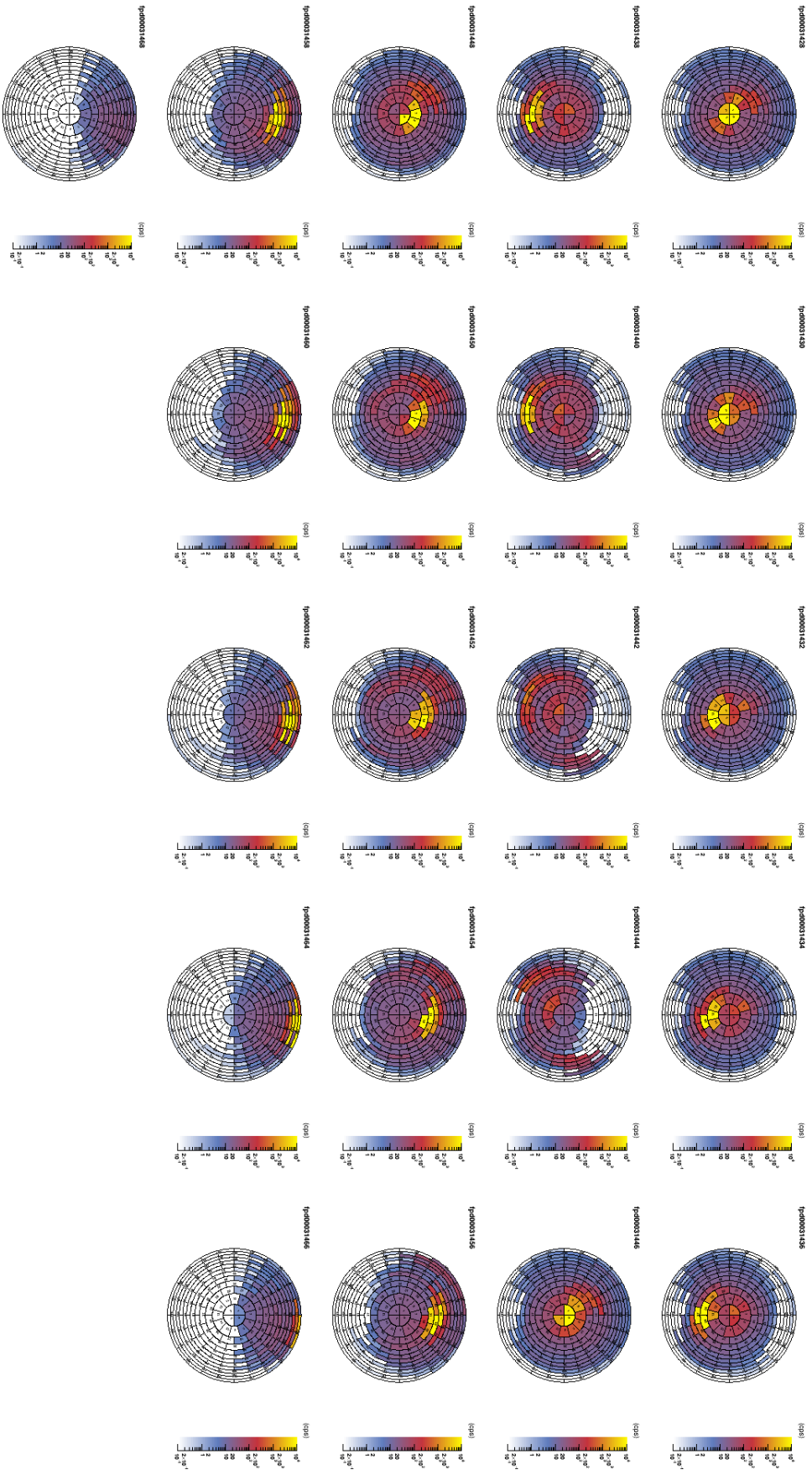

Figure B.3: Pencil beam scanning in vertical direction.

C Internal bibliography

The sources listed below are only available for the KATRIN collaboration. These are the electronic logbook (ELOG) and the Basic Support of Cooperative Work (BSCW) server of the state education server. If you have any questions about the sources below, please contact the author of this work: Moritz Hackenjos, moritz.hackenjos@kit.edu.

C.1 ELOG - First Light

FL1 ELOG, FirstLightPlus, Message ID: 5

FL2 ELOG, FirstLightPlus, Message ID: 8

FL3 ELOG, FirstLightPlus, Message ID: 14

FL4 ELOG, FirstLightPlus, Message ID: 19

FL5 ELOG, FirstLightPlus, Message ID: 31

FL6 ELOG, FirstLightPlus, Message ID: 32

FL7 ELOG, FirstLightPlus, Message ID: 34

FL8 ELOG, SDS-Measurements Phase 3, Message ID: 1

C.2 ELOG - Main Detector

MD1 ELOG, Main Detector, Message ID: 47

MD2 ELOG, Main Detector, Message ID: 51

C.3 ELOG - DPS

DP1 ELOG, DPS, Message ID: 179

C.4 BSCW

BW1 95 General Meetings and Review Panels, Collaboration Meetings, 31. Collaboration Meeting, Parallel A2, 95-TRP-6111-A2-KSchoenung.pptx

BW2 95 General Meetings and Review Panels, Collaboration Meetings, 32. Collaboration Meeting, Plenary 5, 95-TRP-6221-P5-MKlein.pptx

BW3 95 General Meetings and Review Panels, Collaboration Meetings, 32. Collaboration Meeting, Plenary 2, 95-TRP-6206-P2-MSteidl.pptx

BW4 95 General Meetings and Review Panels, Collaboration Meetings, 32. Collaboration Meeting, Plenary 3, 95-TRP-6210-P3-WGil.pptx

C.5 Design Reports

DR1 KATRIN DPS Cryostat Design, CMI, Confidential Report

DR2 Superconducting Magnet Systems for the Differential Pumping Section (DPS), Cryostat Heat Load Calculations, CMI, Confidential Report

DR3 Design Report CPS

List of acronyms

AC	**A**ir **C**oil
AGS	**A**lternating **G**radient **S**ynchrotron
ALEPH	**A**pparatus for **LEP ph**ysics
ATLAS	**A T**oroidal **L**HC **A**pparatu**s**
BIXS	**B**eta-**I**nduced **X**-ray **S**pectrometry
BSCW	**B**asic **S**upport of **C**ooperative **W**ork
CAD	**C**omputer-**a**ided **d**esign
CERN	**C**onseil **E**uropéen pour la **R**echerche **N**ucléaire
CP	**C**harge and **P**arity
CPS	**C**ryogenic **P**umping **S**ection
cps	**c**ounts **p**er **s**econd
CM	**C**enter-of-**m**ass
CMI	**C**ryo**m**agnetics, **I**nc.
CMS	**C**ompact **M**uon **S**olenoid
CPI	**C**ollision **p**oint **i**dentification
DONUT	**D**irect **o**bservation of the **nu t**au
DPS	**D**ifferential **P**umping **S**ection
EC	**E**lectron **C**apture
ECHo	**E**lectron **C**apture ^{163}**Ho**
EGUN	**E**lectron **gun**
ELIOTT	**E**lectron Impact **IO**n Source **T**o **T**est the DPS
ELOG	**El**ectronic **Lo**gbook
EMCS	**E**arth **M**agnetic field **C**ompensation **S**ystem
FBM	**F**orward **B**eam **M**onitor
FPD	**F**ocal-**P**lane **D**etector
FT-ICR	**F**ourier **T**ransform-**I**on **C**yclotron **R**esonance
HV	**H**igh **v**oltage
IE	**I**nner **e**lectrode

KATRIN	**Ka**rlsruhe **Tri**tium **N**eutrino
KIT	**K**arlsruhe **I**nstitute of **T**echnology
LARA	**La**ser **Ra**man
LEP	**L**arge **E**lectron-**P**ositron Collider
LFCS	**L**ow-**F**ield **C**orrection **S**ystem
LHe	**L**iquid **he**lium
LN_2	**L**iquid **n**itrogen
MAC-E	**M**agnetic-**a**diabatic **c**ollimation combined with an **e**lectrostatic
MS	**M**ain **S**pectrometer
MSW	**M**ikheyev-**S**mirnov-**W**olfenstein
M1	**M**agnet number 1 of the WGTS
M2	**M**agnet number 2 of the WGTS
M3	**M**agnet number 3 of the WGTS
M4	**M**agnet number 4 of the WGTS
M5	**M**agnet number 5 of the WGTS
M6	**M**agnet number 6 of the WGTS
M7	**M**agnet number 7 of the WGTS
NMR	**N**uclear-**m**agnetic **r**esonance
PMNS	**P**ontecorvo-**M**aki-**N**akagawa-**S**akata
PMT	**P**hoto-**m**ultiplier **t**ube
PS	**P**re-**S**pectrometer
PS1	**P**re-**S**pectrometer magnet **1**
PS2	**P**re-**S**pectrometer magnet **2**
QED	**Q**uantum **E**lectro**d**ynamics
RMS	**R**oot-**M**ean-**S**quare
RS	**R**ear **S**ection
SDD	**S**ilicon **d**rift **d**etector
SDS	**S**pectrometer and **D**etector **S**ection
SDS-I	**1**st commissioning phase of the **S**pectrometer and **D**etector **S**ection
SDS-II	**2**nd commissioning phase of the **S**pectrometer and **D**etector **S**ection
SDS-IIA	**SDS-II** - part **A**
SDS-IIB	**SDS-II** - part **B**
SDSS	**S**loan **D**igital **S**ky **S**urvey
SLC	**S**tanford-**L**inear **C**ollider
SM	**S**tandard **M**odel

SNLS	**S**uper**n**ovae **L**egacy **S**urvey
SSM	**S**tandard **s**olar **m**odel
STS	**S**urce and **T**ransport **S**ection
RW	**R**ear **W**all
T2K	**T**okai **to K**amioka
TLK	**T**ritium **L**aboratory **K**arlsruhe
TMP	**T**urbo**m**olecular **p**ump
UHV	**U**ltra-**h**igh **v**acuum
UV	**U**ltra **v**iolet
WGTS	**W**indowless **G**aseous **T**ritium **S**ource
WGTS-R	**W**indowless **G**aseous **T**ritium **S**ource-**R**ear
WGTS-F	**W**indowless **G**aseous **T**ritium **S**ource-**F**ront
XML	E**x**tensible **M**arkup **L**anguage
4LIP	**4** **l**ast **i**lluminated **p**ixels

List of figures

List of tables

Bibliography

[Aad12] G. Aad et al. (ATLAS Collaboration): *Observation of a new particle in the search for the Standard Model Higgs boson with the ATLAS detector at the LHC.* Physics Letters B, 716:1–29, 2012.

[Abd02] J. N. Abdurashitov et al.: *Solar neutrino flux measurements by the Soviet-American gallium experiment (SAGE) for half the 22-year solar cycle.* Journal of Experimental and Theoretical Physics, 95(2):181–193, 2002.

[Abe93] H. Abele et al.: *On the origin of the 17 keV neutrino signals, and a loss-free measurement of the* ^{35}S *β-spectrum.* Physics Letters B, 316(1):26 – 31, 1993.

[Abe08] S. Abe et al. (KamLAND Collaboration): *Precision Measurement of Neutrino Oscillation Parameters with KamLAND.* Physical Review Letters, 100:221803, 2008.

[Abe11] K. Abe et al. (Super-Kamiokande Collaboration): *Search for Differences in Oscillation Parameters for Atmospheric Neutrinos and Antineutrinos at Super-Kamiokande.* Phys. Rev. Lett., 107:241801, 2011.

[Abe12] Y. Abe et al.: *Reactor* $\overline{\nu}_e$ *disappearance in the Double Chooz experiment.* Physical Review D, 86:052008, 2012.

[Abe15] K. Abe et al. (T2K Collaboration): *Measurements of neutrino oscillation in appearance and disappearance channels by the T2K experiment with* 6.6×10^{20} *protons on target.* Phys. Rev. D, 91:072010, 2015.

[Ack13] K. Ackermann et al.: *The GERDA experiment for the search of* $0\nu\beta\beta$ *decay in* ^{76}Ge. The European Physical Journal C, 73(3):2330, 2013.

[Ada13] P. Adamson et al. (MINOS Collaboration): *Measurement of Neutrino and Antineutrino Oscillations Using Beam and Atmospheric Data in MINOS.* Phys. Rev. Lett., 110:251801, 2013.

[Ada16a] P. Adamson et al. (NOvA Collaboration): *First measurement of muon-neutrino disappearance in NOvA.* Phys. Rev., D93(5):051104, 2016.

[Ada16b] P. Adamson et al. (NOvA Collaboration): *First measurement of electron neutrino appearance in NOvA.* Phys. Rev. Lett., 116(15):151806, 2016.

[Ada17] P. Adamson et al. (NOvA Collaboration): *Measurement of the neutrino mixing angle* θ_{23} *in NOvA.* Phys. Rev. Lett., 118(15):151802, 2017.

[Ade16] P. Ade et al. (Planck Collaboration): *Planck 2015 results-XIII. Cosmological parameters.* Astronomy & Astrophysics, 594:A13, 2016.

[Aga11] S. Agarwal and H. Feldman: *The effect of massive neutrinos on the matter power spectrum.* Monthly Notices of the Royal Astronomical Society, 410(3):1647–1654, 2011.

[Ago03] S. Agostinelli et al.: *Geant4 - a simulation toolkit.* Nuclear Instruments and Methods in Physics Research Section A: Accelerators, Spectrometers, Detectors and Associated Equipment, 506(3):250 – 303, 2003.

[Ago13] M. Agostini et al.: *Results on Neutrinoless Double-β Decay of ^{76}Ge from Phase I of the GERDA Experiment.* Physical Review Letters, 111(12):122503, 2013.

[Aha05] B. Aharmim et al. (SNO Collaboration): *Electron energy spectra, fluxes, and day-night asymmetries of ^{8}B solar neutrinos from measurements with NaCl dissolved in the heavy-water detector at the Sudbury Neutrino Observatory.* Phys. Rev. C, 72(1):055502, 2005.

[Aha13] B. Aharmim et al. (SNO Collaboration): *Combined analysis of all three phases of solar neutrino data from the Sudbury Neutrino Observatory.* Phys. Rev. C, 88:025501, Aug 2013.

[Ahm01] Q. R. Ahmad et al. (SNO Collaboration): *Measurement of the Rate of $\nu_e + d \rightarrow p + p + e^-$ Interactions Produced by ^{8}B Solar Neutrinos at the Sudbury Neutrino Observatory.* Phys. Rev. Lett., 87(7), 2001.

[Ahm02] Q. R. Ahmad et al. (SNO Collaboration): *Direct Evidence for Neutrino Flavor Transformation from Neutral-Current Interactions in the Sudbury Neutrino Observatory.* Phys. Rev. Lett., 89(1), 2002.

[Ahn06] M. H. Ahn et al. (K2K Collaboration): *Measurement of neutrino oscillation by the K2K experiment.* Physical Review D, 74:072003, 2006.

[Ahn12] J. K. Ahn et al. (RENO Collaboration): *Observation of Reactor Electron Antineutrinos Disappearance in the RENO Experiment.* Physical Review Letters, 108:191802, 2012.

[Alb14] J. Albert et al. (EXO-200 Collaboration): *Search for Majorana neutrinos with the first two years of EXO-200 data.* Nature, 510(7504):229–234, 2014.

[Alt05] M. Altmann et al. (GNO Collaboration): *Complete results for five years of GNO solar neutrino observations.* Physics Letters B, 616(3-4):174–190, 2005.

[An 12] F. An et al. (Daya Bay Collaboration): *Observation of Electron-Antineutrino Disappearance at Daya Bay.* Physical Review Letters, 108:171803, 2012.

[An 14] F. An et al. (Daya Bay Collaboration): *Independent measurement of the neutrino mixing angle θ_{13} via neutron capture on hydrogen at Daya Bay.* Physical Review D, 90(7):071101, 2014.

[Ang05] J. Angrik et al. (KATRIN Collaboration): *KATRIN Design Report.* FZKA scientific report, 7090, 2005.

[Asa16] K. Asakura et al.: *Search for double-beta decay of ^{136}Xe to excited states of ^{136}Ba with the KamLAND-Zen experiment.* Nuclear Physics A, 946:171–181, 2016.

[Ase11] V. N. Aseev et al.: *Upper limit on the electron antineutrino mass from the Troitsk experiment.* Physical Review D, 84:112003, 2011.

[Ash17] A. Ashtari Esfahani et al. (Project 8 Collaboration): *Determining the neutrino mass with Cyclotron Radiation Emission Spectroscopy - Project 8.* J. Phys. G, 2017.

[Asn15] D. Asner et al. (Project 8 Collaboration): *Single electron detection and spectroscopy via relativistic cyclotron radiation.* Phys. Rev. Lett., 114(16):162501, 2015.

[Bab12] M. Babutzka et al.: *Monitoring of the operating parameters of the KATRIN Windowless Gaseous Tritium Source.* New Journal of Physics, 14:103046, 2012.

[Bab14] M. Babutzka: *Design and development for the Rearsection of the KATRIN experiment.* PhD Thesis, Karlsruhe Institute of Technology, 2014.

[Bae11a] O. Baeyer et al.: *Magnetische Spektren der β-Strahlen des Radiums.* Physikalische Zeitschrifthys. Zeit, 12:1099–1101, 1911.

[Bae11b] O. Baeyer et al.: *Nachweis von β-Strahlen bei Radium D.* Physikalische Zeitschrift, 12:378–379, 1911.

[Bah64a] J. Bahcall: *Solar Neutrino Cross Sections and Nuclear Beta Decay.* Phys. Rev., 135:B137–B146, 1964.

[Bah64b] N. Bahcall: *Solar Neutrinos. I. Theoretical.* Phys. Rev. Lett., 12:300–302, 1964.

[Bah76] J. Bahcall et al.: *Solar neutrinos: a scientific puzzle.* Science, 191:264–267, 1976.

[Bah82] J. Bahcallet al.: *Standard solar models and the uncertainties in predicted capture rates of solar neutrinos.* Rev. Mod. Phys., 54:767–799, 1982.

[Bah05] John N. Bahcall et al.: *New Solar Opacities, Abundances, Helioseismology, and Neutrino Fluxes.* The Astrophysical Journal Letters, 621(1):621, 2005.

[Bar98] H. Barth et al.: *Status and perspectives of the Mainz neutrino mass experiment.* Progress in Particle and Nuclear Physics, 40:353–376, 1998.

[Bea80] G. Beamson et al.: *The collimating and magnifying properties of a superconducting field photoelectron spectrometer.* Journal of Physics E: Scientific Instruments, 13(1):64, 1980.

[Bel03] E. Bellotti and Società italiana di fisica: *Neutrino Physics.* Nummer Bd. 152 in *International School of Physics Enrico Fermi Series.* IOS Press, Amsterdam, Netherlands, 2003, ISBN 9781586033859.

[Bel10] G. Bellini et al.: *Measurement of the solar* ^{8}B *neutrino rate with a liquid scintillator target and 3 MeV energy threshold in the Borexino detector.* Phys. Rev. D, 82:033006, 2010.

[Bel12] G. Bellini, et al. (Borexino Collaboration): *First Evidence of pep Solar Neutrinos by Direct Detection in Borexino.* Phys. Rev. Lett., 108:051302, 2012.

[Ber12] J. Beringer et al.: *Review of Particle Physics.* Phys. Rev. D, 86:010001, 2012.

[Bet34] H. Bethe and R. Peierls: *The Neutrino.* Nature, 133:532, 1934.

[Bet14a] M. Betoule et al.: *Improved cosmological constraints from a joint analysis of the SDSS-II and SNLS supernova samples.* Astronomy & Astrophysics, 568:A22, 2014.

[Bet14b] A. Bettini: *Introduction to Elementary Particle Physics.* Cambridge University Press, London, UK, 2014, ISBN 978-1-107-05040-2.

[Beu11] F. Beutler et al.: *The 6dF Galaxy Survey: baryon acoustic oscillations and the local Hubble constant.* Monthly Notices of the Royal Astronomical Society, 416(4):3017–3032, 2011.

[Bio87] R. Bionta et al.: *Observation of a neutrino burst in coincidence with supernova 1987A in the Large Magellanic Cloud.* Physical Review Letters, 58(14):1494, 1987.

[Bor17] L. Bornschein et al.: *Status of the Karlsruhe Tritium Neutrino Mass Experiment KATRIN.* Fusion Science and Technology, 71(4):485–490, 2017.

[Cha14] J. Chadwick: *Intensitätsverteilung im magnetischen Spektrum der β-Strahlen von Radium B + C / The Intensity Distribution in Magnetic Spectrum of β-Rays of Radium B + C.* Verhandl. Dtsch. phys. Ges., 16:383, 1914.

[Cha12] S. Chatrchyan et al.: *Observation of a new boson at a mass of 125 GeV with the CMS experiment at the LHC.* Physics Letters B, 716(1):30 – 61, 2012.

[Cha15] M. Chavez-Estrada and A. Aguilar-Arevalo: *Antineutrino Flux from the Laguna Verde Nuclear Power Plant.* Advances in High Energy Physics, 2015(109738), 2015.

[Col17] R. Leitner (Daya Bay Collaboration): *Recent results of Daya Bay reactor neutrino experiment.* Nuclear and Particle Physics Proceedings, 285(Supplement C):32 – 37, 2017.

[Cow56] C. L. Cowan et al.: *Detection of the Free Neutrino: A Confirmation.* Science, 124:103–104, Juli 1956.

[Dan62] G. Danby et al.: *Observation of High-Energy Neutrino Reactions and the Existence of Two Kinds of Neutrinos.* Phys. Rev. Lett., 9(1):36 – 44, 1962.

[Dav55] R. Davis: *Attempt to Detect the Antineutrinos from a Nuclear Reactor by the* $Cl^{37}(\overline{\nu}, e^-)A^{37}$ *Reaction.* Phys. Rev., 97:766–769, 1955.

[Dav64] R. Davis: *Solar neutrinos. II: Experimental.* Phys. Rev. Lett., 12:303–305, 1964.

[Dav68] R. Davis et al.: *Search for Neutrinos from the Sun.* Phys. Rev. Lett., 20:1205–1209, 1968.

[Dav79] R. Davis et al.: *The solar neutrino problem.* AIP Conference Proceedings, 52(1):17–27, 1979.

[Dav94] R. Davis: *A review of the Homestake solar neutrino experiment.* Prog. Part. Nucl. Phys., 32:13–32, 1994.

[DeC89] D. DeCamp et al. (ALEPH Collaboration): *Determination of the number of light neutrino species.* Physics Letters B, 231(4):519–529, 1989.

[Def17] M. Deffert: *Simulation of the global beamline alignment of the KATRIN experiment.* Master's Thesis, Karlsruhe Institute of Technology, 2017.

[Dir27] Paul Dirac: *The Quantum Theory of the Emission and Absorption of Radiation.* Proceedings Royal Society A, 114:243, 1927.

[Dob56] E. Dobbs et al.: *Density and expansivity of solid argon.* Nature, 178(4531):483–483, 1956.

[DON01] DONUT Collaboration: *Observation of Tau Neutrino Interactions.* Phys. Lett. B, 504(3):218 – 224, 2001.

[Dos06] N. Doss et al.: *Molecular effects in investigations of tritium molecule β decay endpoint experiments.* Phys. Rev. C, 73:025502, 2006.

[Dos08] N. Doss et al.: *Excitations to the electronic continuum of* $^3HeT^+$ *in investigations of* T^2 *β-decay experiments.* Journal of Physics B: Atomic, Molecular and Optical Physics, 41(12):125701, 2008.

[Dre13] G. Drexlin et al.: *Current Direct Neutrino Mass Experiments.* Advances in High Energy Physics, 2013, 2013.

[Dwy15] D. Dwyer: *Antineutrinos from nuclear reactors: recent oscillation measurements.* New Journal of Physics, 17(2):025003, 2015.

[Eic08] F. Eichelhardt et al.: *First Tritium Results of the KATRIN Test Experiment Trap.* Fusion Science and Technology, 54(2):615–618, 2008.

[Ell27] C. Ellis and W. Wooster: *The average energy of disintegration of radium E.* Proceedings of the Royal Society of London. Series A, Containing Papers of a Mathematical and Physical Character, 117(776):109–123, 1927.

[Ell17] E. Ellinger et al.: *Monitoring the KATRIN source properties within the beamline.* Journal of Physics: Conference Series, 888:012229, 2017.

[Eng64] F. Englert and R. Brout: *Broken Symmetry and the Mass of Gauge Vector Mesons.* Phys. Rev. Lett., 13:321–323, 1964.

[Erh16] M. Erhard: *Influence of the magnetic field on the transmission characteristics and the neutrino mass systematic of the KATRIN experiment.* PhD Thesis, Karlsruhe Institute of Technology, 2016.

[Fer34] E. Fermi: *Versuch einer Theorie der β-Strahlen.* Zeitschrift für Physik, 88(3–4):161–177, 1934.

[Fey58] R. Feynman and M. Gell-Mann: *Theory of the Fermi Interaction.* Phys. Rev., 109:193–198, 1958.

[Fis10] T. Fischer et al.: *Protoneutron star evolution and the neutrino-driven wind in general relativistic neutrino radiation hydrodynamics simulations.* Astronomy & Astrophysics, 517:A80, 2010.

[Fis11] S. Fischer et al.: *Monitoring of tritium purity during long-term circulation in the KATRIN test experiment LOOPINO using laser Raman spectroscopy.* Fusion Science and Technology, 60(3):925–930, 2011.

[Fis14] S. Fischer: *Commissioning of the KATRIN Raman system and durability studies of optical coatings in glove box and tritium atmospheres.* PhD Thesis, Karlsruhe Institute of Technology, 2014.

[Fow28] R. Fowler and L. Nordheim: *Electron Emission in Intense Electric Fields.* Proceedings of the Royal Society of London A: Mathematical, Physical and Engineering Sciences, 119(781):173–181, 1928.

[Fra10] F. M. Fraenkle: *Background Investigations of the KATRIN Pre-Spectrometer.* PhD Thesis, Karlsruhe Institute of Technology, 2010.

[Fra17] F. Fraenkle et al. (KATRIN Collaboration): *Background processes in the KATRIN main spectrometer.* Journal of Physics: Conference Series, 888(1):012070, 2017.

[Fri17] F. Friedel: *Studien zur Inbetriebnahme der kryogenen Pumpstrecke des KATRIN Experiments.* Master's Thesis, Karlsruhe Institute of Technology, 2017.

[Fuk94] Y. Fukuda et al. (Kamiokande Collaboration): *Atmospheric $\nu\mu\nu e$ ratio in the multi-GeV energy range.* Physics Letters B, 335(2):237–245, 1994.

[Fuk96] Y. Fukuda et al.: *Solar neutrino data covering solar cycle 22.* Physical Review Letters, 77(9):1683, 1996.

[Fuk98a] Y. Fukuda et al. (Super-Kamiokande Collaboration): *Measurements of the Solar Neutrino Flux from Super-Kamiokande's First 300 Days.* Phys. Rev. Lett., 81:1158, 1998.

[Fuk98b] Y. Fukuda et al. (Super-Kamiokande Collaboration): *Evidence for Oscillation of Atmospheric Neutrinos.* Phys. Rev. Lett., 81(8):1562 – 1567, 1998.

[Fuk02] S. Fukuda et al.: *Determination of solar neutrino oscillation parameters using 1496 days of Super-Kamiokande-I data.* Physics Letters B, 539(3):179–187, 2002.

[Fuk03] S. Fukuda et al.: *The Super-Kamiokande detector.* Nuclear Instruments and Methods in Physics Research Section A: Accelerators, Spectrometers, Detectors and Associated Equipment, 501(2 - 3):418 – 462, 2003.

[Fur39] W. Furry: *On transition probabilities in double beta-disintegration.* Physical Review, 56(12):1184, 1939.

[Fur17] D. Furse et al.: *Kassiopeia: A modern, extensible C++ particle tracking package.* New Journal of Physics, 19(5):053012, 2017.

[Gar51] Milan Wayne Garrett: *Axially symmetric systems for generating and measuring magnetic fields. Part I.* Journal of Applied Physics, 22(9):1091–1107, 1951.

[Gas14] L. Gastaldo et al.: *The Electron Capture^{163} Ho Experiment ECHo.* Journal of low temperature physics, 176(5-6):876–884, 2014.

[Gil17] W. Gil et al.: *The KATRIN Superconducting Magnets: Overview and First Performance Results.* to be published in *Journal of Instrumentation*, 2017.

[Gla61] S. L. Glashow: *Partial-symmetries of weak interactions.* Nuclear Physics, 22(4):579 – 588, 1961.

[Gla15] I. Glasner: *Magnetfeldmessungen an der differentiellen Pumpstrecke am KATRIN-Experiment.* Master's Thesis, Karlsruhe Institute of Technology, 2015.

[Glu11] Ferenc Gluck: *Axisymmetric magnetic field calculation with zonal harmonic expansion.* Progress In Electromagnetics Research B, 32:351–388, 2011.

[Glu13] F. Glueck et al.: *Electromagnetic design of the large-volume air coil system of the KATRIN experiment.* New Journal of Physics, 15:083025, 2013.

[Goe35] M. Goeppert-Mayer: *Double beta-disintegration.* Physical Review, 48(6):512, 1935.

[Goe14] S. Goerhardt: *Background Reduction Methods and Vacuum Technology at the KATRIN Spectrometers.* PhD Thesis, Karlsruhe Institute of Technology, 2014.

[Gol58] M. Goldhaber et al.: *Helicity of Neutrinos.* Phys. Rev., 109:1015–1017, 1958.

[Gri69] V. Gribov et al.: *Neutrino astronomy and lepton charge.* Physics Letters B, 28(7):493–496, 1969.

[Gri04] D. Griffiths: *Introduction to Elementary Particles*, Seiten 26–27. Wiley-VCH, Weinheim, Germany, 2004, ISBN 9780471603863.

[Gro08] S. Grohmann: *CRYOGENIC DESIGN OF THE KATRIN SOURCE CRYOSTAT.* AIP Conference Proceedings, 985(1):1277–1284, 2008.

[Gro09] S. Grohmann: *Stability analyses of the beam tube cooling system in the KATRIN source cryostat.* Cryogenics, 49(8):413–420, 2009.

[Gro11] S. Grohmann: *Precise temperature measurement at 30 K in the KATRIN source cryostat.* Cryogenics, 51(8):438–445, 2011.

[Gro13] S. Grohmann: *The thermal behaviour of the tritium source in KATRIN.* Cryogenics, 55:5–11, 2013.

[Gro15] S. Groh: *Modeling of the response function and measurement of transmission properties of the KATRIN experiment.* PhD Thesis, Karlsruhe Institute of Technology, 2015.

[Hab09] F. Habermehl: *Electromagnetic Measurements with the KATRIN Pre-Spectrometer.* PhD Thesis, Karlsruhe Institute of Technology, 2009.

[Hac15] M. Hackenjos: *Die differentielle Pumpstrecke des KATRIN-Experiments - Inbetriebnahme und Charakterisierung des supraleitenden Magnetsystems.* Master's Thesis, Karlsruhe Institute of Technology, 2015.

[Ham99] W. Hampel et al. (GALLEX Collaboration): *GALLEX solar neutrino observations: results for GALLEX IV.* Physics Letters B, 447:127–133, 1999.

[Har15] F. Harms: *Characterization and minimization of background processes in the KATRIN main spectrometer.* PhD Thesis, Karlsruhe Institute of Technology, Karlsruhe, 2015.

[Hig64] P. Higgs: *Broken Symmetries and the Masses of Gauge Bosons.* Phys. Rev. Lett., 13:508–509, 1964.

[Hig07] H. Higaki et al.: *Properties of non-neutral electron plasmas confined with a magnetic mirror field.* Physical Review E, 75(6):066401, 2007.

[Hig08] H. Higaki et al.: *Electrons confined with an axially symmetric magnetic mirror field.* AIP Conference Proceedings, 1037(1):106–114, 2008.

[Hil11] B. Hillen: *Untersuchung von Methoden zur Unterdrueckung des Spektrometeruntergrunds beim KATRIN Experiment.* PhD Thesis, Westfälische Wilhelms-Universität Münster, 2011.

[Him89] A. Hime and J. Simpson: *Evidence of the 17-keV neutrino in the β spectrum of* ^{3}H. Phys. Rev. D, 39:1837–1850, 1989.

[Him91] A. Hime et al.: *New evidence for the 17 keV neutrino.* Physics Letters B, 257(3-4):441–449, 1991.

[Him93] A. Hime: *Do scattering effects resolve the 17-keV conundrum?* Physics Letters B, 299(1):165 – 173, 1993.

[Hir88] K. Hirata et al.: *Observation in the Kamiokande-II detector of the neutrino burst from supernova SN1987A.* Physical Review D, 38(2):448, 1988.

[Hoe12] M. Hoetzel: *Simulation and analysis of source-related effects for KATRIN.* PhD Thesis, Karlsruhe Institute of Technology, 2012.

[Hu 15] B. Hu et al. (Daya Bay Collaboration): *Recent Results from Daya Bay Reactor Neutrino Experiment.* arXiv preprint hep-ex, 2015.

[Hub29] E. Hubble: *A relation between distance and radial velocity among extra-galactic nebulae.* Proceedings of the National Academy of Sciences, 15(3):168–173, 1929.

[Hug08] K. Hugenberg: *Design of the electrode system for the KATRIN main spectrometer.* Diploma Thesis, Westfälische Wilhelms-Universität Münster, 2008.

[Hug10] K. Hugenberg: *An angular resolved pulsed UV LED photoelectron source for KATRIN.* Progress in Particle and Nuclear Physics, 64(2):288–290, 2010.

[Jan15] A. Jansen: *The crypgenic pumping section of the KATRIN experiment - Design studies and experiments for the commissioning.* PhD Thesis, Karlsruhe Institute of Technology, 2015.

[Jol34] F. Joliot and I. Curie: *Artificial Production of a New Kind of Radio-Element.* Nature, 133(3354):201–202, 1934.

[Kaz08] O. Kazachenkoet al.: *TRAP - a cryo-pump for pumping tritium on pre-condensed argon.* Nuclear Instruments and Methods in Physics Research Section A: Accelerators, Spectrometers, Detectors and Associated Equipment, 587(1):136–144, 2008.

[Kir69] T. Kirsten et al.: *Observation of* ^{82}Se *double-beta decay in selenium ores.* Earth and Planetary Science Letters, 6(4):271–274, 1969.

[Kle14] M. Kleesig: *A Data-Analysis and Sensitivity-Optimization Framework for the KATRIN Experiment.* PhD Thesis, Karlsruhe Institute of Technology, 2014.

[Kle18] M. Klein: *Tritium ions in KATRIN – Detection, blocking and removal.* PhD Thesis, Karlsruhe Institute of Technology, 2018. to be published.

[Kos12] A. Kosmider: *Tritium Retention Techniques in the KATRIN Transport Section and Commissioning of its DPS2-F Cryostat.* PhD Thesis, Karlsruhe Institute of Technology, 2012.

[Kra05] C. Kraus et al.: *Final results from phase II of the Mainz neutrino mass search in tritium β decay.* The European Physical Journal C - Particles and Fields, 40(4):447–468, 2005.

[Kra16] M. Kraus: *Energy-Scale Systematics at the KATRIN Main Spectrometer.* PhD Thesis, Karlsruhe Institute of Technology, 2016.

[Kru83] P. Kruit et al.: *Magnetic field paralleliser for 2π electron-spectrometer and electron-image magnifier.* Journal of Physics E: Scientific Instruments, 16(4):313, 1983.

[Kuc16] L. Kuckert: *The Windowless Gaseous Tritium Source of the KATRIN Experiment - Characterisation of Gas Dynamical and Plasma Properties.* PhD Thesis, Karlsruhe Institute of Technology, 2016.

[Lee56] T. Lee and C. Yang: *Question of Parity Conservation in Weak Interactions.* Phys. Rev., 104:254–258, 1956.

[Lei14] B. Leiber: *Investigations of background due to secondary electron emission in the KATRIN-experiment.* PhD Thesis, Karlsruhe Institute of Technology, 2014.

[Les12] J. Lesgourgues et al.: *Neutrino mass from Cosmology.* Advances in High Energy Physics, 2012, 2012.

[Lin15] J. Linek: *Investigation of the muon induced background at the KATRIN main spectrometer.* Master's Thesis, Karlsruhe Institute of Technology, 2015.

[Lob85] V. Lobashev et al.: *A method for measuring the electron antineutrino rest mass.* Nuclear Instruments and Methods in Physics Research Section A: Accelerators, Spectrometers, Detectors and Associated Equipment, 240(2):305 – 310, 1985.

[Lor02] T. Loredo et al.: *Bayesian analysis of neutrinos observed from supernova SN 1987A.* Physical Review D, 65(6):063002, 2002.

[Lub17] M. Lubej: *Standard model of the particle physics*, 2017.

[Luc00] L. Lucas et al.: *Comprehensive Review and Critical Evaluation of the Half-Life of Tritium.* Journal of Research of the National Institute of Standards and Technology, 105(4):541 – 549, 2000.

[Luk11] S. Lukic et al.: *Ion source for tests of ion behavior in the Karlsruhe tritium neutrino experiment beam line.* Review of Scientific Instruments, 82(1):013303, 2011.

[Luk12] S. Lukic et al.: *Measurement of the gas-flow reduction factor of the KATRIN DPS2-F differential pumping section.* Vacuum, 86(8):1126–1133, 2012.

[Luo08] X. Luo et al.: *Test particle Monte Carlo study of the cryogenic pumping system of the Karlsruhe tritium neutrino experiment.* Journal of Vacuum Science & Technology A: Vacuum, Surfaces, and Films, 26(5):1319–1325, 2008.

[Maj37] E. Majorana: *Teoria simmetrica dell´elettrone e del positrone.* Il Nuovo Cimento (1924-1942), 14(4):171, 1937.

[Mak62] Z. Maki et al.: *Remarks on the Unified Model of Elementary Particles.* Progress of Theoretical Physics, 28(5):870, 1962.

[Mar02] E. Marquardt et al.: *Cryogenic material properties database*, Seiten 681–687. Springer, Boston, USA, 2002.

[Mar17] A. Marsteller: *Measurements of temperature stability and homogeneity of the KATRIN WGTS cryostat.* Master's Thesis, Karlsruhe Institute of Technology, 2017.

[Mas07] S. S. Masood et al.: *Exact relativistic β decay endpoint spectrum.* Physical Review C, 76:045501, 2007.

[Mei13] L. Meitner et al.: *Das magnetische Spektrum der β-Strahlen von Radioaktinium und seiner Zerfallsprodukte.* Physikalische Zeitschrift, 14:321–323, 1913.

[Mei30] L. Meitner and W. Orthmann: *Über eine absolute Bestimmung der Energie der primären β-Strahlen von Radium E.* Zeitschrift für Physik A Hadrons and Nuclei, 60(3):143–155, 1930.

[Men11] G. Mentionet al.: *Reactor antineutrino anomaly.* Phys. Rev. D, 83:073006, Apr 2011.

[Mer12] S. Mertens: *Study of Background Processes in the Electrostatic Spectrometers of the KATRIN experiment.* PhD Thesis, Karlsruhe Institute of Technology, 2012.

[Mik85] S. Mikheev et al.: *Resonance Amplification of Oscillations in Matter and Spectroscopy of Solar Neutrinos.* Sov. J. Nucl. Phys., 42:913–917, 1985.

[Mik86] S. Mikheev et al.: *Resonant amplification of ν oscillations in matter and solar-neutrino spectroscopy.* Il Nuovo Cimento C, 9(1):17–26, 1986.

[Mue16] A. Mueller: *Investigation of the secondary electron emission characteristics of the KATRIN main spectrometer.* Master's Thesis, Karlsruhe Institute of Technology, 2016.

[Nag06] Sz. Nagy et al.: *On the Q-value of the tritium β-decay.* Europhysics Letters, 74(3):404–410, 2006.

[Nep05] S. Nepijko et al.: *Morphology of Frozen Rare-Gas Layers.* ChemPhysChem, 6(2):235–238, 2005.

[Ott08] E. W. Otten et al.: *Neutrino mass limit from tritium β decay.* Reports on Progress in Physics, 71(8):086201, 2008.

[Pat16] C. Patrignani et al.: *Review of Particle Physics.* Chin. Phys., C40(10):100001, 2016.

[Pau30a] W. Pauli: *The Neutrino Invention*, 1930.

[Pau30b] W. Pauli: *Symmetry: A joint Fermilab/SLAC publication*, 1930. Offener Brief an die Gruppe der Radioaktiven bei der Gauvereinstagung zu Tübingen (datiert 4. Dez. 1930).

[Pen00] R. Penzhorn et al.: *Status and research progress at the Tritium Laboratory Karlsruhe.* Fusion engineering and design, 49:753–767, 2000.

[Per75] M. L. Perl et al.: *Evidence for Anomalous Lepton Production in $e^+ - e^-$ Annihilation.* Phys. Rev. Lett., 35(22):1489 – 1492, 1975.

[Per09] D. Perkins: *Particle astrophysics.* Nummer 10. Oxford University Press, New York, USA, 2009.

[Pet66] O. Peterson et al.: *Measurements of X-ray lattice constant, thermal expansivity, and isothermal compressibility of argon crystals.* Physical Review, 150(2):703, 1966.

[Pic92] A. Picard et al.: *A solenoid retarding spectrometer with high resolution and transmission for keV electrons.* Nuclear Instruments and Methods in Physics Research Section B: Beam Interactions with Materials and Atoms, 63(3):345–358, 1992.

[Pon57] B. Pontecorvo: *Mesonium and anti-mesonium.* Sov. Phys. JETP, 6:429, 1957.

[Pon58] B. Pontecorvo: *Inverse beta processes and nonconservation of lepton charge.* Sov. Phys. JETP, 7:172–173, 1958.

[Pon68] B. Pontecorvo: *Neutrino experiments and the problem of conservation of leptonic charge.* Sov. Phys. JETP, 26(984):25, 1968.

[Pon91] B. Pontecorvo: *Inverse beta process.* Camb. Monogr. Part. Phys. Nucl. Phys. Cosmol., 1:25–31, 1991.

[Pra11] M. Prall: *Background Reduction of the KATRIN Spectrometers: Transmission Function of the Pre-Spectrometer and Systematic Test of the Main-Spectrometer Wire Electrode.* PhD Thesis, Westfälische Wilhelms-Universität Münster, 2011.

[Pra12] M. Prall et al.: *The KATRIN pre-spectrometer at reduced filter energy.* New Journal of Physics, 14:073054, 2012.

[Pri13] F. Priester et al.: *TriToP - A compatibility experiment with turbomolecular pumps under tritium atmosphere.* Vacuum, 98(0):22–28, 2013.

[Pri15] F. Priester et al.: *Commissioning and detailed results of KATRIN inner loop tritium processing system at Tritium Laboratory Karlsruhe.* Vacuum, 116:42–47, 2015.

[Rac37] G. Racah: *Sulla simmetria tra particelle e antiparticelle.* Il Nuovo Cimento (1924-1942), 14(7):322–328, 1937.

[Ran17] P. Ranitzsch et al.: *Characterization of the ^{163}Ho Electron Capture Spectrum: A Step Towards the Electron Neutrino Mass Determination.* Physical Review Letters, 119(12):122501, 2017.

[Rei53] F. Reines and Cowan, C.L.: *Detection of the Free Neutrino.* Physical Review, 92:830–831, 1953.

[Rei56a] F. Reines and C. Cowan: *Telegram from Frederick Reines and Clyde Cowan to Wolfgang Pauli announcing the detection of the neutrino*, 1956.

[Rei56b] F. Reines and Cowan, C.L.: *The neutrino.* Nature, 178(4531):446–449, 1956.

[Rei09] S. Reimer: *Ein elektrostatisches Dipolsystem zur Eliminierung von Ionen in der DPS2-F des KATRIN Experimentes.* Diplomarbeit, Karlsruhe Institute of Technology, 2009.

[Rob88] R. G. H. Robertson et al.: *Direct Measurements of Neutrino Mass.* Annual Review of Nuclear and Particle Science, 38(1):185–215, 1988.

[Roe13] M. Roellig et al.: *Activity monitoring of a gaseous tritium source by beta induced X-ray spectrometry.* Fusion Engineering and Design, 88(6-8):1263–1266, 2013.

[Roe15] M. Roellig: *Tritium analytics by beta induced X-ray spectrometry.* PhD Thesis, Karlsruhe Institute of Technology, 2015.

[Roe16] C. Roettele: *Simulationen zu den Inbetriebnahmemessungen mit der kryogenen Pumpstrecke CPS des KATRIN Experiments.* Master's Thesis, Karlsruhe Institute of Technology, 2016.

[Roe17] C. Roettele: *Results of the first Cool-down of the KATRIN Cryogenic Pumping Section.* Journal of Physics: Conference Series, 888(1):012228, 2017.

[Rut10] E. Rutherford and J. Chadwick and C. D. Ellis: *Radiations from radioactive substances.* Cambridge University Press, London, UK, 2010.

[Sac15] R. Sack: *Aufbau einer Ionenquelle und Simulation der Transporteigenschaften der DPS und CPS am KATRIN Experiment.* Master's Thesis, Karlsruhe Institute of Technology, 2015.

[Sal64] A. Salam and J. C. Ward: *Electromagnetic and weak interactions.* Physics Letters, 13(2):168 – 171, 1964.

[Sal68] A. Salam: *Weak and Electromagnetic Interactions.* Conf. Proc., C680519:367–377, 1968.

[Sch11] M. Schloesser et al.: *Design Implications for Laser Raman Measurement Systems for Tritium Sample-Analysis, Accountancy or Process-Control Applications.* Fusion Science and Technology, 60(3):976–981, 2011.

[Sch12] M. Schloesser et al.: *Accuracy of the Laser Raman system for KATRIN.* arXiv preprint physics, 2012.

[Sch13a] M. Schloesser: *Accurate calibration of the Raman system for the Karlsruhe Tritium Neutrino Experiment.* PhD Thesis, Karlsruhe Institute of Technology, 2013.

[Sch13b] M. Schloesser et al.: *Evaluation method for Raman depolarization measurements including geometrical effects and polarization aberrations.* Journal of Raman Spectroscopy, 44(3):453–462, 2013.

[Sch13c] M. Schloesser et al.: *In-Line Calibration of Raman Systems for Analysis of Gas Mixtures of Hydrogen Isotopologues with Sub-Percent Accuracy.* Analytical Chemistry, 85(5):2739–2745, 2013.

[Sch14] J. Schwarz: *The Detector System of the KATRIN Experiment - Implementation and First Measurements with the Spectrometer.* PhD Thesis, Karlsruhe Institute of Technology, 2014.

[Sch15] M. Schloesser et al.: *Raman Spectroscopy at the Tritium Laboratory Karlsruhe.* Fusion Science and Technology, 67(3):555–558, 2015.

[Sch16] K. Schoenung: *Development of a Rear Wall for the KATRIN Rear Section and investigation of tritium compatibility of Rear Section components.* PhD Thesis, Karlsruhe Institute of Technology, 2016.

[Sch17] L. Schimpf: *Untersuchung thermischer und radioaktiver Einflüsse auf den Tritium-Rückhaltefaktor der kryogenen Pumpstrecke von KATRIN.* Master's Thesis, Karlsruhe Institute of Technology, 2017.

[Sco35] F. A. Scott: *Energy Spectrum of the Beta-Rays of Radium E.* Phys. Rev., 48(5):391 – 395, 1935.

[Sim89] J. Simpson et al.: *Evidence of the 17-keV neutrino in the β spectrum of ^{35}S.* Phys. Rev. D, 39:1825–1836, 1989.

[Sis04] M. Sisti et al.: *New limits from the Milano neutrino mass experiment with thermal microcalorimeters.* Nuclear Instruments and Methods in Physics Research Section A: Accelerators, Spectrometers, Detectors and Associated Equipment, 520(1):125 – 131, 2004.

[Stu10] M. Sturm: *Aufbau und Test des Inner-Loop-Systems der Tritiumquelle von KATRIN.* PhD Thesis, Karlsruhe Institute of Technology, 2010.

[Sud58] E. Sudarshan and R. Marshak: *Chirality Invariance and the Universal Fermi Interaction.* Phys. Rev., 109:1860–1862, 1958.

[Sur91] B. Sur et al.: *Evidence for the emission of a 17-keV neutrino in the β decay of ^{14}C.* Phys. Rev. Lett., 66:2444–2447, 1991.

[Sut16] C. Sutton: *Ghosts in the machine.* CERN Courier, 2016.

[Tel15] Neutrino Telescopes: *Poster Excerpt 14: HOLMES, an experiment for a direct measurement of neutrino mass*, 2015.

[The06] The SLD and Groups, Heavy Flavour and ALEPH Collaboration and DELPHI Collaboration and L3 Collaboration and OPAL Collaboration and SLD Collaboration and LEP Electroweak Working Group and others: *Precision electroweak measurements on the Z resonance.* Physics Reports, 427(5):257–454, 2006.

[Thu11] T. Thuemmler et al.: *Direct neutrino mass measurements.* Physics of Particles and Nuclei, 42(4):590, 2011.

[Val09] K. Valerius: *Spectrometer-related background processes and their suppression in the KATRIN experiment.* PhD Thesis, Westfälische Wilhelms-Universität Münster, 2009.

[Val10] K. Valerius: *The wire electrode system for the KATRIN main spectrometer.* Progress in Particle and Nuclear Physics, 64(2):291 – 293, 2010.

[Vir16] T. S. Virdee: *Beyond the standard model of particle physics.* Philosophical Transactions of the Royal Society of London A: Mathematical, Physical and Engineering Sciences, 374(2075), 2016.

[Wan97] C. Wang et al.: *A two-stage pulse tube cooler operating below 4 K.* Cryogenics, 37(3):159–164, 1997.

[Wan13] N. Wandkowsky: *Study of background and transmission properties of the KATRIN spectrometers.* PhD Thesis, Karlsruhe Institute of Technology, 2013.

[Wec17] M. Wecker: *Development and setup of an experiment to characterize surfaces of KATRIN rear wall candidates with UV light.* Master's Thesis, Karlsruhe Institute of Technology, 2017.

[Wei35] C. Weizsaecker: *Zur Theorie der Kernmassen.* Zeitschrift für Physik A Hadrons and Nuclei, 96(7):431–458, 1935.

[Wei67] S. Weinberg: *A Model of Leptons.* Phys. Rev. Lett., 19:1264–1266, 1967.

[Wei99] C. Weinheimer et al.: *High precision measurement of the tritium β spectrum near its endpoint and upper limit on the neutrino mass.* Physics Letters B, 460(1 - 2):219 – 226, 1999.

[Wei05] C. Weinheimer: *Direct determination of the neutrino masses.* Comptes Rendus Physique, 6(7):768–777, 2005.

[Wen10] R. Wendell et al. (Super-Kamiokande Collaboration): *Atmospheric neutrino oscillation analysis with subleading effects in Super-Kamiokande I, II, and III.* Physical Review D, 81:092004, 2010.

[Win11] A. Windberger: *Berechnungen und Simulationen zum Verhalten von Ionen in der differenziellen Pumpstrecke des KATRIN-Experiments.* Diplomarbeit, Karlsruhe Institute of Technology, 2011.

[Wol78] L. Wolfenstein: *Neutrino oscillations in matter.* Phys. Rev. D, 17:2369–2374, 1978.

[Wu 57] C. Wu et al.: *Experimental Test of Parity Conservation in Beta Decay.* Phys. Rev., 105:1413–1415, 1957.

[Zac09] M. Zacher: *Electromagnetic design and field emission studies for the inner electrode system of the KATRIN main spectrometer.* Diploma Thesis, Westfälische Wilhelms-Universität Münster, 2009.

[Zha11] Y. Zhang et al.: *Corrected Values for Boiling Points and Enthalpies of Vaporization of Elements in Handbooks.* Journal of Chemical and Engineering, 56(2):328–337, 2011.

[Zub11] Kai Zuber: *Neutrino physics.* CRC press, Boca Raton, USA, 2011, ISBN 978-1-4200-6471-1.

Danksagung

An dieser Stelle möchte ich zuerst allen Personen danken, die mich während meiner Promotion unterstützt und begleitet haben und somit zum Gelingen meiner Promotion beigetragen haben. Folgenden Personen gebührt dabei ein ganz besonderes Dankeschön.

Vielen Dank Prof. Dr. Drexlin, für die Möglichkeit meine Promotion im Umfeld des Großforschungsprojekts KATRIN durchzuführen. Ich möchte ihm für die stets offenen Konversationen sowie die motivierenden Gespräche danken und dafür, dass er durch seine Vorlesungen meine Begeisterung für die Astroteilchenphysik geweckt hat.

Vielen Dank Prof. Dr. Holzapfel für die Begutachtung dieser Arbeit als Korreferent sowie die freundlichen Gespräche und die Unterstützung.

Dr. Beate Bornschein danke ich für ihre konstruktive Kritik, welche mich dazu bewegt hat, mich stetig zu verbessern und meine wissenschaftliche Arbeit kritisch zu hinterfragen. Außerdem möchte ich ihr für ihr überdurchschnittliches Engagement im Bereich des wissenschaftlichen Schreibens danken.

Ebenfalls möchte ich Dr. Michael Sturm für sein Engagement und für die wissenschaftliche Betreuung während meiner Promotion danken.

Danke Dr. Lutz Bornschein, Alexander Marsteller, Dr. Alexander Jansen, Steffen Lichter, Heike Bolz und Luisa La Cascio für die schöne und spannende Zeit im Labor. Zusätzlich danke ich euch sowie Dr. Beate Bornschein und Dr. Michael Sturm, dass ihr mir in den letzten Monaten den Rücken frei gehalten habt und ich mich somit vollständig auf das Schreiben konzentrieren konnte.

Ein besonderer Dank geht an Dr. Fabian Harms für seine Unterstützung und Hilfestellung in Sachen Programmierung aber vor allem für die witzigen Erlebnisse egal ob im Büro oder in der Freizeit.

Vielen Dank Dr. Joachim Wolf, Dr. Ferenc Glück, Dr. Florian Fränkle, Dr. Jan Behrens, Dr. Thomas Thümmler, Marco Deffert, Dr. Markus Steidl und Nikolaus Trost für die zahlreichen wissenschaftlichen Diskussionen und das Feedback.

Vielen Dank Simon Niemes, Dr. Marco Röllig, Dr. Florian Priester und Woo-Jeong Baek für die unterhaltsame Arbeitsatmosphäre.

Vielen Dank Caroline Rodenbeck für die Organisation der Kaffeekasse und meinen konstant hohen und nicht oszillierenden Coffee Flavor.

Ein besonderer Dank geht an das Werkstattteam Klaus Mehret, Bernard Bender, Hendrik Weingardt, Alan Kumb, Holger Frenzel und Monika Kaiser für die exzellenten Installationsarbeiten und ihren stets motivierten Arbeitseinsatz.

Ebenfalls ein besonderer Dank geht an die Mess- und Automatisierungstechniker Arne Felden, Jürgen Grimm unter der Leitung von Thomas Höhn, für die elektronische Anbindung aller Solenoide an die Hallen-Infrastruktur und die überdurchschnittlich schnellen Hilfestellungen.

Vielen Dank Dr. Uwe Besserer, Dr. Jürgen Wendel und Dirk Osenberg für den reibungslosen Betrieb des Tritiumlabors.

Danke Michaela Meloni und Rolf Rinderspacher für das Erstellen der zahlreichen CAD Zeichnungen.

Rainer Gumbsheimer möchte ich für die exzellente technische Koordination und die ausführlichen Informationen zu all meinen technischen Detailfragen danken.

Danke Dr. Kathrin Valerius, Hendrik Seitz-Moskaliuk und Carsten Röttele für die Aufnahme in eure Laufgruppe und das Organisieren der Wettkämpfe.

Vielen Dank Katharina Fischer und Eva Porter für die Unterstützung im Bereich der Administration.

Danke Anton Huber, Jan Bondy, Isabel Arnst, Florian Heizmann, Philipp Gasch, Malte Langenhorst, Max Reimer, Max Zanner, Michael Jenne und Rainer Kraft für die gemeinsame Zeit im Studium und die produktiven Lerngruppen. Wer meint er hätte nicht die rockigste Zeit seines Lebens während dem Studium gehabt, der hat definitiv nicht mit euch studiert.

Vielen Dank Christian Günter, Lorenz Zimmermann, Sebastian Köhl, Mirco Quednau, Sebastian Gack und Fabian Ziegler für zwanzig Jahre Freundschaft sowie für die legendären Abende auf´m Stöckle.

Meinen Eltern Linda Hackenjos und Thomas Besch möchte ich für die Motivation sowie die liebevolle Unterstützung danken, die ich fortwährend von ihnen erfahre und dafür, dass sie immer an mich geglaubt haben.

Meiner Freundin Sabine Enderle gebührt der größte Dank, nicht nur für ihre ununterbrochene Unterstützung sondern ganz besonders für die wundervollen gemeinsamen Momente, welche mich vorübergehend den Stress der Promotion vergessen ließen.